Study of Crystallographic Texture during Thermo-mechanical processing of Boron modified Ti-alloys

Principal Investigators

Dr. Satyam Suwas, Assistant Professor, Department of Materials Engineering, Indian Institute of Science, Bangalore 560012, India

Dr. D.B. Miracle, Air Force Research Laboratory, Materials and Manufacturing Directorate, Building 655, 2230 Tenth Street, Wright-Patterson Air force Base, OH 45433, USA

Dr. S. Tamirisakandala, Department of Mechanical Engineering, Ohio University, Athens, OH 45701, USA

Prof. R. Srinivasan, Department of Mechanical and Materials Engineering, 209 Russ Engineering Center, Wright State University, 3640 Col. Glenn High way, Dayton Ohio 45435, USA

Other Investigator

Shibayan Roy, *Research Scholar, Department of Materials Engineering, Indian Institute of Science, Bangalore 560012, India*

Report Documentation Page

Form Approved
OMB No. 0704-0188

1. REPORT DATE	2. REPORT TYPE	3. DATES COVERED
15 JUL 2009	**FInal**	**07-02-2007 to 06-03-2008**

4. TITLE AND SUBTITLE
Study of crystallographic texture during thermo-mechanical processing of boron modified Ti-alloys

5a. CONTRACT NUMBER
FA48690714002

5b. GRANT NUMBER

5c. PROGRAM ELEMENT NUMBER

6. AUTHOR(S)
Satyam Suwans

5d. PROJECT NUMBER

5e. TASK NUMBER

5f. WORK UNIT NUMBER

7. PERFORMING ORGANIZATION NAME(S) AND ADDRESS(ES)
Indian Institute of Science,Indian Institute of Science, Dept. of Metallurgy,Bangalore 560 012,India,In,560 012

8. PERFORMING ORGANIZATION REPORT NUMBER
N/A

9. SPONSORING/MONITORING AGENCY NAME(S) AND ADDRESS(ES)
AOARD, UNIT 45002, APO, AP, 96337-5002

10. SPONSOR/MONITOR'S ACRONYM(S)
AOARD

11. SPONSOR/MONITOR'S REPORT NUMBER(S)
AOARD-074002

12. DISTRIBUTION/AVAILABILITY STATEMENT
Approved for public release; distribution unlimited

13. SUPPLEMENTARY NOTES

14. ABSTRACT
This project developed a processing strategy for boron-modified titanium alloy Ti-6Al-4V, and developed an understanding of the deformation and transformation mechanisms as a function of the boron addition.

15. SUBJECT TERMS
Titanium Alloy, Processing, deformation

16. SECURITY CLASSIFICATION OF:			17. LIMITATION OF ABSTRACT	18. NUMBER OF PAGES	19a. NAME OF RESPONSIBLE PERSON
a. REPORT	b. ABSTRACT	c. THIS PAGE			
unclassified	**unclassified**	**unclassified**	**Same as Report (SAR)**	**129**	

Content

Project Synopsis

Title of the project:

Study of crystallographic texture during thermo-mechanical processing of boron modified Ti-alloys

Principal Investigators

1. Dr. Satyam Suwas, Assistant Professor, Department of Metallurgy, Indian Institute of Science, Bangalore 560012, India
2. Dr. D.B. Miracle, Air Force Research Laboratory, Materials and Manufacturing Directorate, Building 655, 2230 Tenth Street, Wright-Patterson Air force Base, OH 45433, USA
3. Dr. S. Tamirisakandala, Department of Mechanical Engineering, Ohio University, Athens, OH 45701, USA
4. Prof. R. Srinivasan, Department of Mechanical and Materials Engineering, 209 Russ Engineering Center, Wright State University, 3640 Col. Glenn High way, Dayton Ohio 45435, USA

Other Investigator

Shibayan Roy, Research Scholar, Department of Materials Engineering, Indian Institute of Science, Bangalore 560012, India

Project Summary

Titanium and its alloys are extensively used for the manufacture of lighter but stronger components in aerospace applications. Trace boron addition (~0.1 wt.%) to certain Ti–alloys produces a reduction in the as-cast grain size by roughly an order of magnitude compared to boron-free alloy. The boron modified titanium alloys are found to be more ductile than boron-free one and also exhibit higher stiffness and strength plus good fracture resistance. Due to these special attributes, these alloys have attracted attention in the recent years, which are primarily aimed for enhancing structural efficiency.

The processing of titanium alloys for engineering application involves a suitable combination of deformation processing and thermal or thermo-mechanical treatments. The mechanical properties of such products/ components depend on the type of crystallographic texture present, especially in the case of h.c.p. materials. By proper control of processing variables, specific textures can be tailored in the material that can act as a means of strengthening and this in turn can be utilized to fabricate components having higher strengths along particular direction.

The effect of boron addition on deformation behavior and therefore, on the evolution of deformation texture, is not known yet. Titanium alloys are generally processed through thermo-mechanical treatments (TMT) involving processing at different temperature regimes corresponding to different phase fields, for example near α, α + β and β, which gives rise to characteristic textures. So far, there has been no effort made for optimizing the processing parameters for alloys containing boron. This project is, therefore, very unique in this sense.

Objectives decided:

1. To develop the processing strategy for boron modified titanium alloy Ti-6Al-4V
2. To understand the deformation and transformation mechanisms as a function of boron addition to Ti-6Al-4V

Milestones Set:

(i) Understanding the solidification texture and its relation with grain refinement due to boron addition

Progress made: This goal is achieved successfully and is presented in the first section of the report.

(ii) Optimization of deformation processing parameters and determination of deformation texture

Progress made: This goal is also achieved successfully and is presented in the second section of the report.

(iii) Thermal stability of deformation texture

Progress made: This work is continuing so far and sufficient progress has been made in this direction. However, the detailed study will take some more time and the progress report will be send as an addendum.

Methodology Followed:

(I) Material:

Material was received from the US counterparts in the form of,

(1) Induction skull melted as cast ingots (two numbers) of normal and boron modified Ti-6Al-4V.

(2) Beta extruded rods from as cast materials (two numbers)

(II) Experimental Phase 1:

Characterization of microstructure using optical and electron microscopy techniques and texture using EBSD technique of the initial as cast and the extruded materials was carried out.

(III) Experimental Phase 2:

a) The high temperature deformation behaviour of as cast material was studied using uniaxial plane strain compression experiments under various temperature-strain rate conditions. These experiments provide sufficient insight regarding the deformation behaviour of the normal and boron modified alloys which will be used in optimising the hot rolling conditions of these materials.

b) Texture evolution of the deformed materials was studied using EBSD technique.

Abstract

Owing to their high strength-to-weight ratio, excellent mechanical properties and corrosion resistance, titanium (Ti) and its alloys, especially (α+β) alloys like Ti-6Al-4V, are the backbone materials for aerospace, energy, and chemical industries. Pure titanium has hexagonal (α) crystal structure at room temperature, which transforms to bcc (β) structure at ~885℃ following specified orientation relationship. The basis for tailoring a suitable texture and microstructure uring heat treatment of titanium alloys, therefore, depends strongly on the β to α transformation. The same is applicable for (α+β) titanium alloys. Trace boron addition (~0.1 wt. %) to the alloy Ti-6Al-4V produces a reduction in as-cast grain size by roughly an order of magnitude. Special attributes of Boron addition includes enhanced ductility, higher stiffness and strength in addition to good fracture resistance. Recently, Ti-alloys have been produced by Induction skull melting (ISM) technique, which offers number of advantages in terms of improved ingot quality. Boron addition as well as ISM technique could affect the evolution of texture and microstructure in the material both in the as-cast and wrought conditions. Additionally, the deformation behavior / processing response during thermo-mechanical processing and subsequently, the microstructure and is expected to vary as a result of boron addition. A research program has been developed in order to study different aspects of texture evolution in ISM processed boron modified Ti-6Al-4V.

The solidification microstructure of Boron free as well as Boron containing Ti-6Al-4V after ISM processing are found to be almost homogeneous from periphery towards the center of as-cast ingot in terms of both α-colony size and distribution. Boron addition substantially reduces α-colony size (~50-80 μm). Needle shaped Ti-B particles segregate at the grain boundary. A gradual change in α texture from periphery towards the center has been observed with orientations close to specific texture components suggesting the formation of texture zones. The deformation of boron modified Ti-6Al-4V alloy in the limited temperature range of 750°-900°C and strain rate of 10^{-3} to 1 S^{-1} shows steady state flow and substantial flow softening for low strain rates at all temperatures and for high strain rates at high temperatures. Kinetic analysis reveals the possibility of dynamic recovery in the alpha phase during low strain rate deformation as well as dynamic recrystallization at higher strain rate and temperature. The noticeable observation is the absence of instability during the deformation of Ti64+B, possibly due to the ease of nucleation at boride particles during dynamic recrystallization.

Characterization of Texture of the Initial Cast and Beta-Extruded Materials

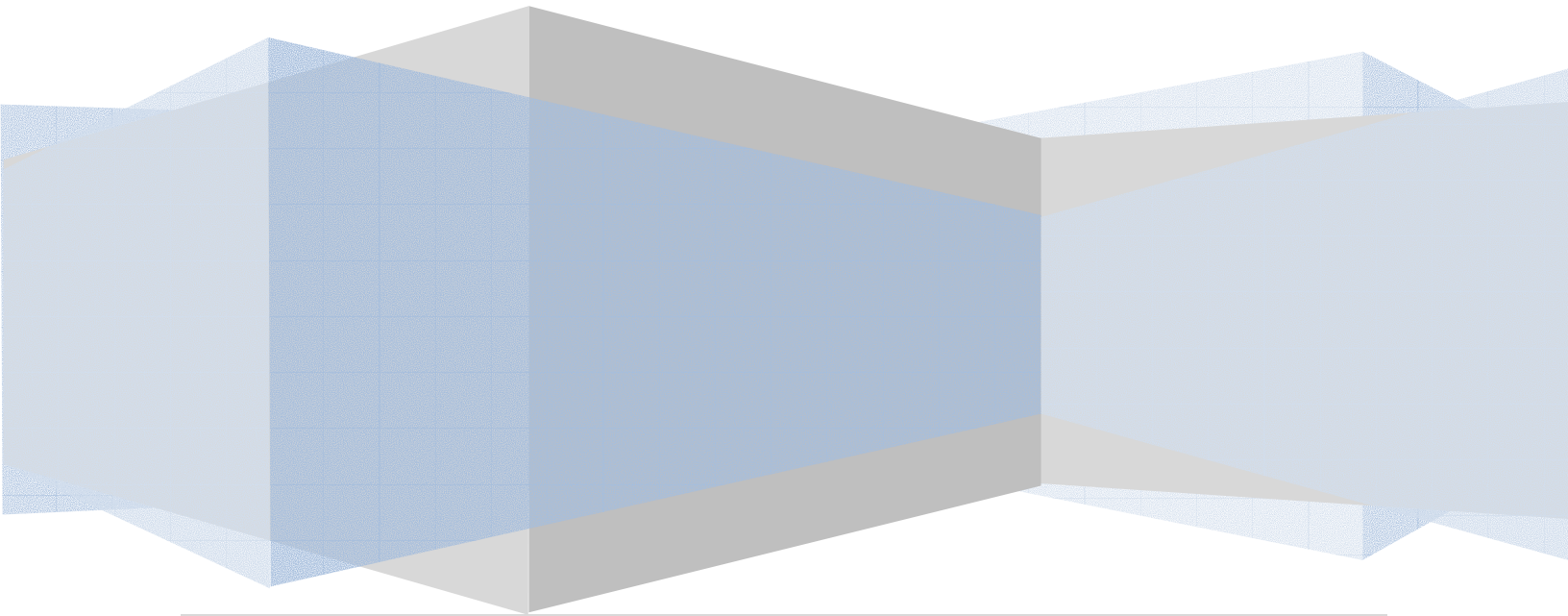

1. Introduction:

Since the introduction of titanium and titanium alloys in the early 1950s, these materials have in a relatively short time become backbone materials for the aerospace, energy, and chemical industries. They are very useful light materials that exhibit high specific strength and fracture toughness with a good corrosion resistance for temperatures up to 550–800 K[i]. The basis for microstructural and textural manipulation during heat treatment of titanium and titanium alloys centers on the β (body-centered cubic) to α (hexagonal close packed) transformation at ~885℃. The crystallography of the two phases is commonly found to be related by the Burgers orientation relationship (OR) where close packed planes [0001]α = [110]β and close packed directions [11-20]α = [111]β are parallel[ii, iii]. Seward et al[iv] have made in situ observations (above 900°C) of the α→β phase transformation in commercially pure titanium using EBSD and found that the strong components in the beta crystallographic texture can be correlated directly to the initial α texture via the Burger OR. The most widely used titanium alloy is the Ti-6Al-4V (α+β) alloy which is most commonly used in the annealed condition[1]. Microstructure and texture evolution in this alloy was studied with great details by many researchers. Kobryn et al[v] have found that metal-mold-cast Ti–6Al–4V tends to have equiaxed prior-beta grain morphology, while direct-laser-fabricated Ti–6Al–4V usually have a columnar morphology. The alpha-phase texture in direct-laser-fabricated Ti– 6Al–4V was found to be fairly weak (i.e. maximum IPF intensity of ~ 1.6 times random). In another study, Kalinyuk et al[vi] [ref] showed that the microstructure of two electron beam melted Ti-6Al-4V ingots at all locations are identical and characterized by coarse beta grains decorated by a layer of grain-boundary alpha. The texture of both the ingots are found to be completely random suggesting the possibility that the texture distribution not being affected by anisotropy in grain growth during solidification. In a vacuum arc melted Ti-6Al-4V ingot, Glavicic et al[vii] have utilized the room temperature measured orientations of alpha-phase variants from a number of prior-beta grains to generate the prior beta texture. The results of the analysis demonstrated that the solidification of the beta phase produces columnar grains in the ingot along <100> preferred-growth directions, where the texture of the beta phase was inherited by the alpha phase in a manner consistent with the burgers relationship; in contrast to the equiaxed grains at the center of the ingot having random alpha and beta phase textures.

The primary problem for any titanium metallurgist is the large grain size (often in the millimeter range) that evolves during the solidification of the as-cast titanium ingot. Extensive hot working in the β-phase field followed by recrystallization is an effective industrial practice for

reducing the grain size of the wrought product. This process, popularly known as 'ingot breakdown' increases the production cost of the finished titanium products and restricts its extensive use to some extent. Any development in terms of grain refinement in as-cast titanium and its alloys will certainly popularize its massive use. Recently, Zhu et al[viii] have observed that small amount (~0.086 to 0.14 mass%) of boron addition induces a significant refinement of as-cast structure and improvement of mechanical properties like tensile ductility, strength and hardness for cast CP Titanium and Ti-0.5Si alloys. Similar observations are reported by other researchers[ix, x, xi]. Tamirisakandala et al[9] have shown a grain size reduction of as-cast Ti-6Al–4V by about an order of magnitude (from 1700 to 200 μm) with an addition of only 0.1wt.% boron, while much weaker dependence is observed for boron additions from >0.1% to 1.0%. The concept of boron addition for grain refinement is, however, not a new thought and is quite frequently being adopted for aluminium alloys[xii, xiii, xiv]. The grain refinement of cast Ti alloys via boron addition are hypothesized as the effect of constitutional super-cooling, caused by the boron rejection from the primary β-Ti grains into the liquid ahead of the solidification front, which in turn increases the nucleation rate but prevents the nucleus to grow[9]. Wherein Zhu et al[8] have reported that the tensile ductility of cast Ti- 6Al- 4V alloy cannot be improved with boron addition, a more recent study by Sen et al[11] have shown that with the refinement in the microstructure, the yield and ultimate tensile strengths increase whereas the fracture toughness and the threshold for fatigue crack propagation decreases. All these experimental findings leads to the increasing importance of the boron modified Ti-alloys. The texture evolution of as cast boron modified Ti-6Al-4V alloy is, however, still lacking, which is the prima facie of the present work.

2. Experimental:

2.1 Material

The materials used in this present study are the widely used Ti alloys, Ti–6Al–4V, with and without the boron addition (referred to hereafter as Ti64 and Ti64-B, respectively). The detailed composition in terms of weight per cent is given in Table-1. The partial phase diagram of Titanium-boron is shown in Fig. 1. The present composition lies in the hypoeutectic side of the phase diagram. Ingots from each of these compositions were melted at Flowserve Corporation, Dayton, OH in an induction skull melting chamber and cast into graphite molds. The cast ingot dimensions were 70 mm diameter X 500 mm length. The boron was added in the form of elemental boron that completely dissolved in the liquid melt. All the ingots were subjected to a standard hot isostatic pressing (HIP) treatment at 900^{o}C and 100 MPa for 2 hours. Since the HIP temperature is well below the β-transus temperature (~1000^{o}C), the microstructural features of as-cast and cast + HIP will be essentially identical. The ingots were radiographed after HIP and confirmed to be free from porosity. Both the ingots were extruded using a servo-hydraulic extruder at 1100^{o}C (i.e. in the beta phase field) with an extrusion ratio of 1:12. This extrusion ration is equivalent to a true strain value of 1.08. The extruded rod is of 2.5cm in diameter and 10cm in length.

2.2 Microstructural Characterization

In case of as-cast initial material, a thin strip of dimension 35mm (length) X 7mm (width) X 5mm (thickness) was cut from the periphery to the center of the as-cast ingot as shown in Fig. 2. This thin strip was then divided into six equal pieces. For the extruded samples, specimens were sectioned (i.e. the top surface of the extruded rod) as well as parallel to the extrusion axis. The microstructures of the samples were characterized by scanning electron microscopy[1]. The samples were first metallographically polished up to 2500 grit sized silicon carbide paper and finally electro-polished using Struers® Lectropol-5[2]. The electrolyte contains 600ml methanol,

[1] *QUANTA 200, FEI, The Netherlands*
[2] *Struers A/S, Germany*

360ml butoxyethanol and 60ml of perchloric acid. The samples were etched with a custom made etchant containing 5% HF, 10%HNO_3 and rest water for 30 seconds.

2.3 Textural Characterization

Each of the pieces from the original as cast thin strip as well as the vertical faces of extruded Ti64 and Ti64+B were subjected to Orientation Imaging Microscopy using a Field Emission Gun Scanning Electron Microscope[3] with Electron Back-Scattered Diffraction (EBSD) facility. All the samples were metallographically prepared in the same way as described above for SEM observations without doing any etching. They were ultrasonically cleaned at every step of polishing and degassed completely before using for the EBSD scan. In case of as-cast initial material, in each of the samples, an area of 1mm X 4mm was scanned with a step size of 5 µm. for extruded samples, a scanning area of 750µm X 1000 µm for Ti64 and 1500 µm X 1500µm for Ti64+B with a step size of 1.5 µm were illuminated. The accelerating voltage used was 20 KV and minimum boundary misorientation was taken to be 2^o. Titanium alloys, as reported in the literature, are very prone to oxidation in the normal condition so that sufficient care was taken before putting the samples for EBSD scan. Textural analysis (inverse pole figures, IPF maps, misorientation calculation etc.) was done using OIM™ Analysis Software[4]. In the entire study, only alpha textures have been studied though these alloys contain substantial amount of beta phase (~10%). This is because of the fact that beta phase is actually present between alpha laths as a thin layer and hence very small step size (~0.5 µm) is needed in EBSD scans to detect beta phase texture efficiently. However, in order to get a quantitative estimate of alpha texture, larger area needs to be scanned that in turn makes impractical to detect beta phase using a smaller step size. Hence, the entire study is focused on the texture of the alpha phase that constitutes about 90% of these alloys. Another important point to ponder over is the comparability between the sizes of the prior β grains and in turn the α-colony size with the area used for EBSD scans (4 square mm). As has been observed by in an earlier study of one of the authors, for Ti64, prior β grain size is ~1.7mm. It may so appear that the area scanned in EBSD is insufficient to capture too many β grains. In order to increase statistical significance, therefore, a suitable area where at least 3-4 prior β grains meet is selected. This difficulty, however, is not critical for Ti64-B as boron addition reduces β grain size to ~0.2mm, so that sufficient number of β grains does interact with the EBSD scanning area.

[3] *FEG-SEM, Sirion XL-40, FEI, The Netherlands*
[4] *TSL Crystallography, AMETEK Inc., USA*

3. Results and Discussions:

3.1 Microstructural Characterization

Fig. 3 and Fig. 4 show the microstructural mapping of the as-cast Ti64 vis-à-vis Ti64-B starting from the periphery towards the center of the ingot. In both these materials, the microstructure is completely homogenous and uniform throughout in terms of all kinds of microstructural length scales (prior β grain size as well as α-colony size). This observation is quite consistent with the earlier work by different researchers [9, 10] and can be attributed to the lower solidification rate during the induction skull melting process which ensures the formation of equiaxed beta grains instead of columnar grains[xv]. Both the materials are composed of Widmanstäten colonies of alpha lamellae with beta phase being sandwiched in between alpha lamellae and at the grain boundaries. Comparison between Fig. 3 and Fig. 4 clearly shows the microstructural refinement in Ti64 due to boron addition. In case of Ti64, the size of the prior β grains are typically in the millimeter range, with the α-colonies covers several hundreds of microns. In contrast, the prior β grain size is only ~200 microns with the alpha colonies being finer than 50 microns in case of Ti64-B. Hexagonal TiB crystals can be seen sitting at the grain boundary (see Fig. 3a inset) and forming a typical 'necklace' structure (see Fig. 3c inset), as has also been observed by earlier researchers[8, 9, 10]. Additional evidence can be deduced from the inverse pole figure maps generated from EBSD analysis, which supports both the facts that boron refines the grain size tremendously as well as induction skull melting produces an uniform macro as well as microstructure throughout the ingot.

3.2 Textural Characterization

The texture data for the boron modified Ti64 is given in Fig. 5 in terms inverse pole figures vis-à-vis normal Ti64. To estimate the gradient in the texture of the solidified ingot, bulk texture measurement using XRD is inefficient as it fails to give localized information. The only way to study texture gradient is by using EBSD; however large areas need to be scanned in order to get statistically significant information. When brought to the same intensity level, the pole figures for Ti64-B actually show less number of contour lines than that of Ti64. Also, the number of intensity maxima is relatively high for Ti64-B. This randomness in the solidification

texture of the as-cast material can be attributed to the basic grain refinement mechanism by boron addition in titanium alloys. As discussed earlier, boron addition increases β nucleation and suppresses its growth. In the process, it not only reduces the prior β grain size, but also increases the number of alpha colonies in a given sampling area as compared to Ti64. From a single β orientation, 12 different α orientations of {0001} type can be generated consistent with the Burger's orientation relationship[xvi]. Thus, any refinement in the prior β grain size will also refine the alpha colony size that can lead to randomization in the alpha phase texture, unless a variant selection process takes place during the transformation. The inverse pole figures show that in general, the intensity levels are lower for the Ti64-B samples than Ti64 (see Fig. 5). This indicates that boron addition leads to a weaker texture. Also, there are no strong components present in any of the samples. On the other hand, the samples without boron shows higher intensity for certain texture components in different cuts. Boron addition thus not only refines the microstructure but also considerably weakens the texture and makes it more homogeneous.

The α phase texture that is investigated in the present study has its origin in the solidification texture of β phase which in turn undergoes phase transformation to α phase. Thus, the solidification texture of α phase and the transformation texture during β to α transformation govern the final texture. The increase in nucleation rate of β due to rejection of boron leads to a more random beta texture. During transformation from beta to alpha phase, each beta orientation can be transformed to 12 equivalent α orientations with same probability. However, under certain conditions, only some of these alpha orientations are formed. This phenomenon is known as variant selection. In the present case, TiB needles are found to be present at the prior β grain boundary and hence it can act as an additional site for the nucleation of α from β during phase transformation. This further contributes to weakening the α texture upon transformation. Thus, the addition of boron has two fold effects on the texture evolution in Ti64; firstly, it affects the solidification texture of β phase and secondly it again alters the β to α transformation texture.

3.3 Microstructure and Texture Evolution in Extrusion

The microstructure of the extruded samples is shown from Fig 6 to Fig. 9. In cases of Ti64 and Ti64+B, the microstructure is typical beta worked equiaxed structure characterized by the presence of fine acicular alpha phase. This acicular alpha structure is due to the faster rate of cooling that was experienced during the extrusion operation. The pre-existing beta grain boundaries are quite clearly prominent in both the materials. In case of Ti64, the beta grain size

is around 100 µm and alpha colony size is around 10-15 µm (see Fig. 6 and 7). This refinement in microstructural size is again quite frequently observed and it is a direct consequence of the dynamic recrystallization during extrusion in the beta phase field. For Ti64+B, an even finer microstructure can be observed with beta grain size being around 50 µm and alpha colony size being 5-10 µm (see Fig. 8 and 9). The TiB particles, tends to align themselves in the direction of extrusion (see Fig. 9). The location of these particles actually signifies for the grain boundaries of the original beta phase in the as cast material. As can be observed from Fig. 9a, the original beta grains initially elongates along the extrusion direction. They then dynamically recrystallized and form the equiaxed microstructure.

Although, the SEM micrographs show completely equiaxed microstructure in case of Ti64 after extrusion, the inverse pole figure maps generated from the EBSD scans shows large elongated grain structure still persisting in this material (see Fig. 10a). This feature indicates that dynamic recrystallization is not completed during extrusion. Smaller equiaxed tend to form at the grain boundaries of the original beta grain boundaries. However, in case of Ti64+B, a completely equiaxed a s well as finer structure can be observed from the IPF map indicating sufficient dynamic recrystallization to occur during extrusion (see Fig. 10b). This difference in the microstructure as well microstructural size is due to the presence of hard and brittle TiB particles. During extrusion, these unreformed particles accumulate sufficient strain around them, which then helps in nucleating recrystallized grains at these points. Therefore faster dynamic rcrystallization as well as finer dynamically recrystallized beta grains are possible in Ti64+B, which leads to finer beta grain size. Figure 11 shows the inverse pole figures for these two materials. It can be observed that the texture of the two materials is markedly different with Ti64+B extruded material showing comparatively weaker texture. Wherein Ti64 shows the presence of {11-20> as the main texture component, in case of Ti64+B, the texture component of {10-11> is present in addition to the presence of slightly rotated {11-21> texture component.

4. Conclusion:

The microstructural and micro texture evolution during solidification of EBM Ti64 and Ti64-B ingot has been studied using EBSD. It is concluded that addition of boron refines the microstructure as well as modifies/weakens the texture of the solidified ingot. The uniform finer grain size along with a weaker texture for Ti64+B is expected to facilitate further thermo-mechanical processing of the ingot to finished products. This prediction is indeed found true in case of extrusion of the boron modified material with the presence of TiB particles successfully producing a fine equiaxed microstructure after extrusion.

References:

[i] ASM Metals Handbook Volume 2, "Properties and selection of nonferrous alloys and special purpose materials", ASM International, Tenth Edition

[ii] E. W. Collings, "The Physical Metallurgy of Titanium Alloys," American Society for Metals, Metals Park, OH 44073

[iii] G. Lütjering, and J. C. Williams, "Titanium", Springer-Verlag Berlin Heidelberg 2003

[iv] G. G. E. Seward , S. Celotto, D. J. Prior, J. Wheeler, and R.C. Pond, "In situ SEM-EBSD observations of the hcp to bcc phase transformation in commercially pure titanium," *Acta Materialia,* **52**, 821–832 (2004)

[v] P. A. Kobryn, S. L. Semiatin, "Microstructure and texture evolution during solidification processing of Ti–6Al–4V," *Journal of Materials Processing Technology,* **135**, 330–339 (2003)

[vi] A. N. Kalinyuk, N. P. Trigu, V. N. Zamkov, O. M. Ivasishin, P. E. Markovsky, R. V. Teliovich, and S. L. Semiatin, "Microstructure, texture, and mechanical properties of electron-beam melted Ti-6Al-4V," Materials Science and Engineering A, **346,** 178-188 (2003)

[vii] M. G. Glavicic, P. A. Kobryn, F. Spadafora, and S. L. Semiatin, "Texture evolution in vacuum arc remelted ingots of Ti-6Al-4V," Materials Science and Engineering A, **346**, 8-18 (2003)

[viii] J. Zhu, A. Kamiya, T. Yamada, W. Shi, and K. Naganuma, "Influence of boron addition on microstructure and mechanical properties of dental cast titanium alloys," Materials Science and Engineering A, **339,** 53-62 (2003)

[ix] S. Tamirisakandala, R. B. Bhat, J. S. Tiley, and D. B. Miracle, "Grain refinement of cast titanium alloys via trace boron addition," Scripta Materialia, **53**, 1421–1426(2005)

[x] S. Tamirisakandala, R. B. Bhat, D. B. Miracle, S. Boddapati, R. Bordia, R. Vanover, and V. K. Vasudevan, "Effect of boron on the beta transus of Ti–6Al–4V alloy," Scripta Materialia, **53,** 217–222 (2005)

[xi] I. Sen, S. Tamirisakandala, D. B. Miracle, and U. Ramamurty, "Microstructural effects on the mechanical behavior of B-modified Ti–6Al–4V alloys," Acta Materialia, **55**, 4983-4993 (2007)

[xii] B. Hu, and H. Li, "Grain refinement of DIN226S alloy at lower titanium and boron addition levels," Journal of Materials Processing Technology, **74,** 56–60 (1998)

[xiii] H. Li, T. Sritharan, and H. P. Seow, "Grain refinement in DIN226 alloy at high titanium and boron inoculotion levels," Scripta Materialia, **35(7)**, 869-872 (1996)

[xiv] M. Wang, S Wang, Z. Liu, Z. Liu, T. Song, and X. Zuo, "Effect of B/Ti mass ratio on grain refining of low-titanium aluminum produced by electrolysis," Materials Science and Engineering A, **416**, 312–316 (2006)

[xv] J. P. Kuang, R. A. Harding, and J. Campbell, "Microstructures and properties of investment castings of γ-titanium Aluminide," Materials Science and Engineering A, **329–331,** 31–37 (2002)

[xvi] L. Zeng, T. R. Bieler, "Effects of working, heat treatment, and aging on microstructural evolution and crystallographic texture of α, α', α" and β phases in Ti–6Al–4V wire," Materials Science and Engineering A, **392**, 403–414 (2005)

Table-1: Chemical compositions (in wt. %) of boron modified Ti alloys used in the study

Alloy	Al	V	B	O	H	C	N	Fe	Ti
Ti64	6.6	4.1		0.18	0.008	0.02	0.01	0.23	Balance
Ti64+B	6.0	4.0	0.1	0.15	0.005	0.02	0.01	0.13	Balance

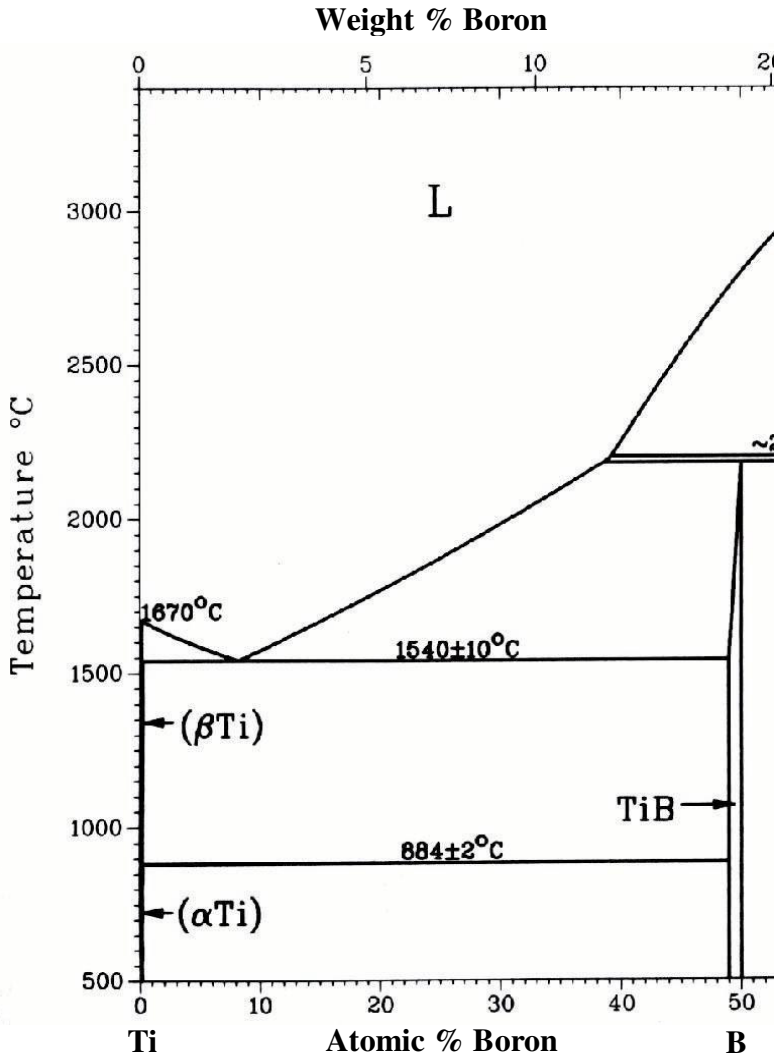

Fig. 1: Titanium-boron partial phase diagram.

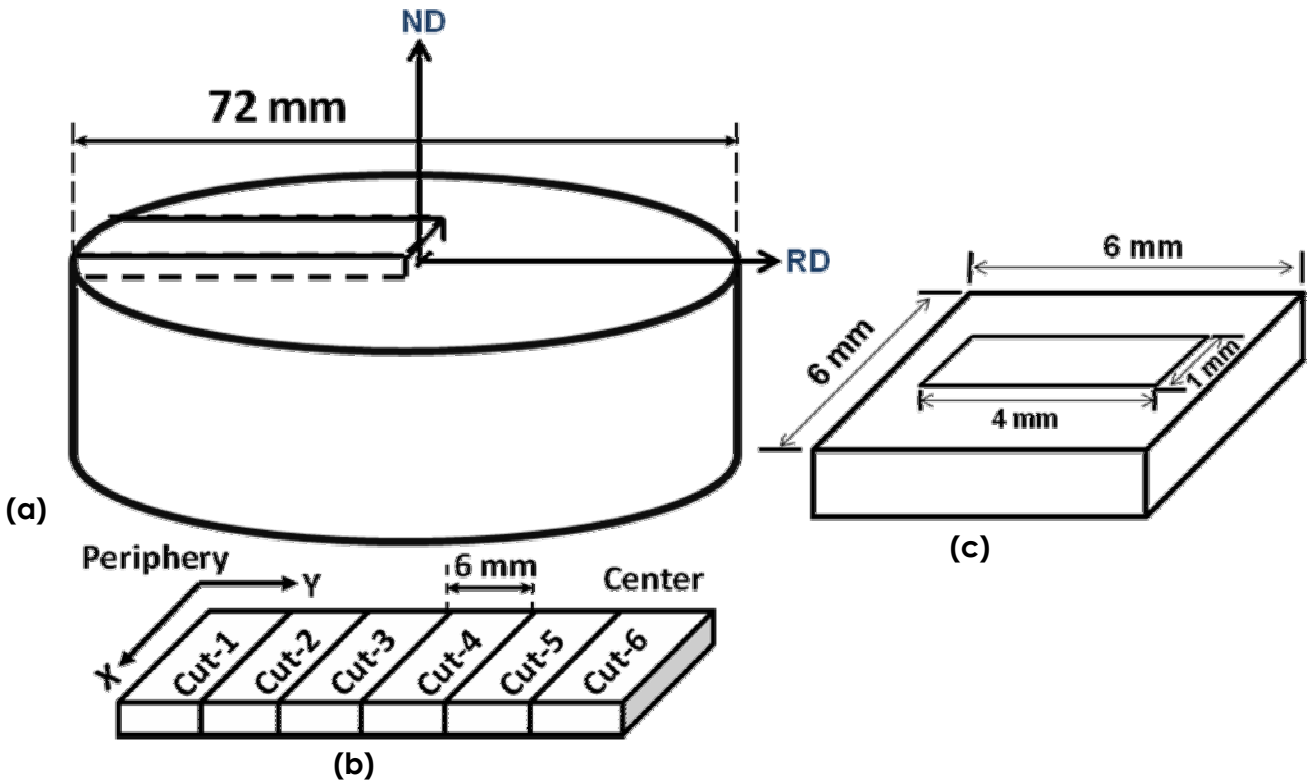

Fig. 2: Experimental procedure showing (a) a bar is cut from the as-cast ingot and (b) the bar is divided into six equal pieces for texture measurement. This method is applied for both Ti64 and Ti64-B.

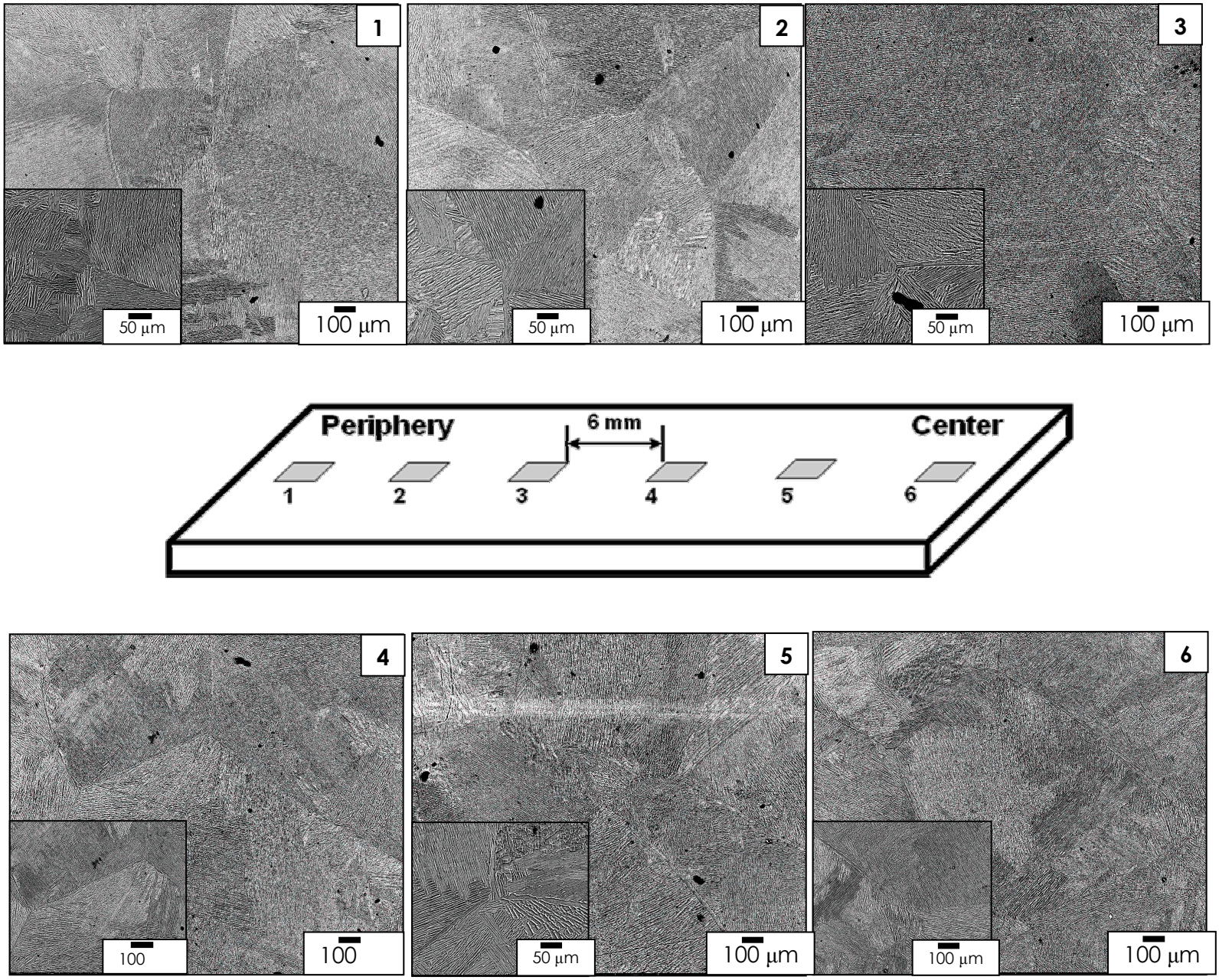

Fig. 3: Microstructural mapping of the as-cast Ti64 from the periphery towards the center. BSE micrographs shows coarse grained microstructure with grain size in millimeter range and almost identical microstructural features throughout the as-cast ingot.

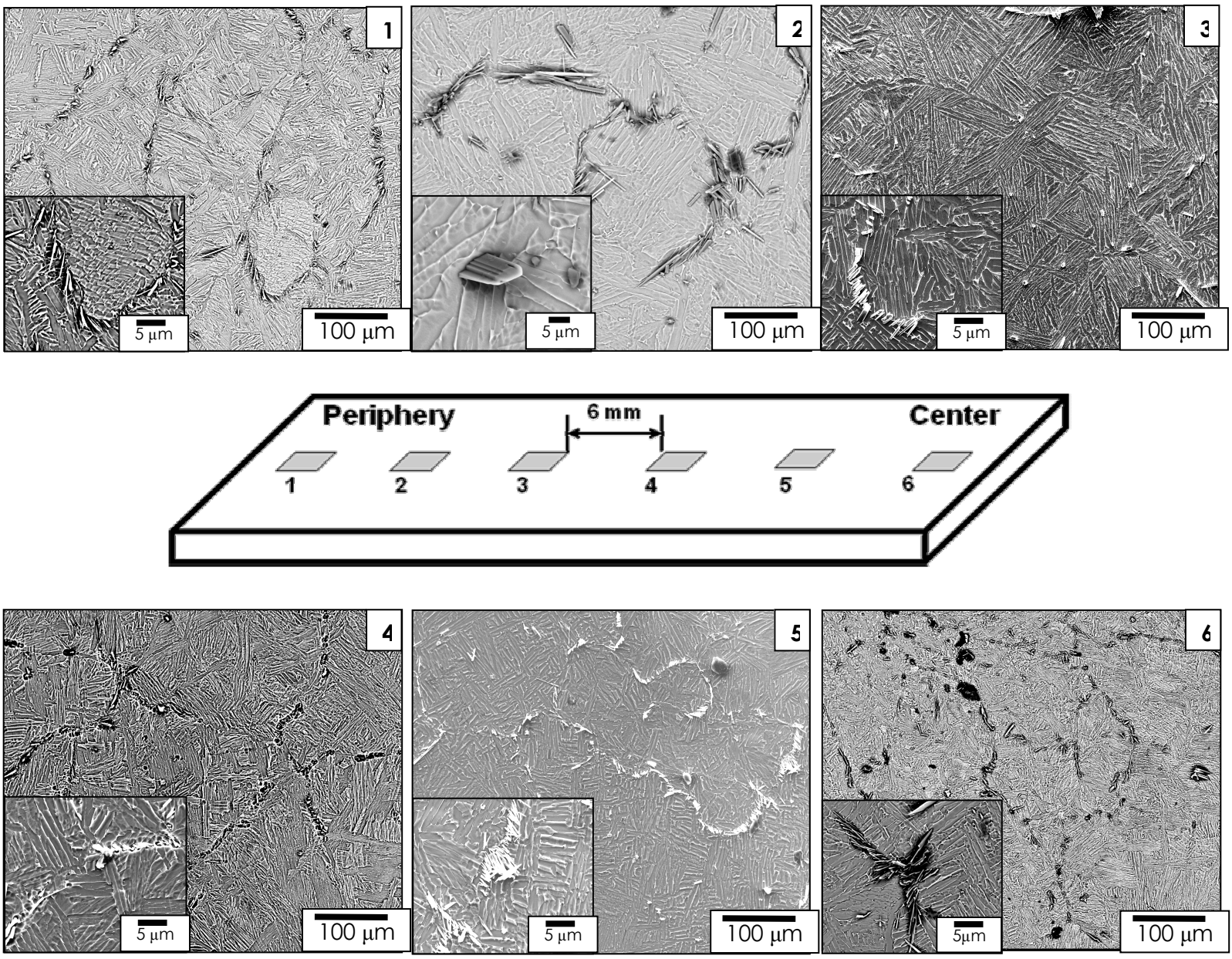

Fig. 4: Microstructural mapping of the as-cast boron containing Ti64 sample from the periphery towards the center. BSE micrographs shows grain refined grained microstructure with grain size in several hundreds of microns range. The microstructure is almost homogeneous in terms of both prior β grain size and α colony size throughout the as-cast ingot. Hexagonal TiB crystals are frequently found along a grain or colony boundary, forming the typical 'necklace' structure at the prior β grain boundary.

	Ti64	Ti64+B
Cut-1	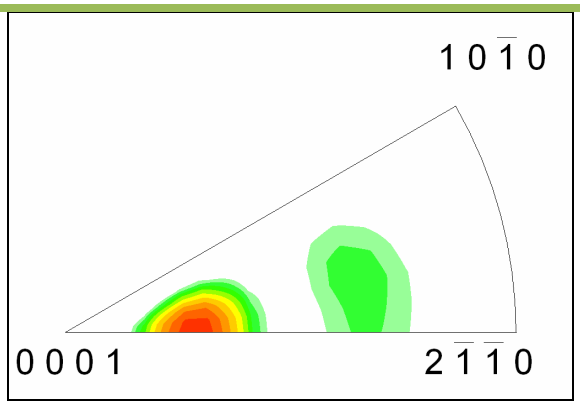	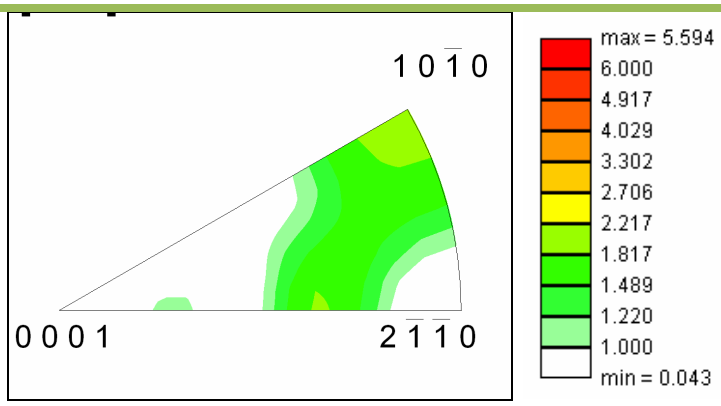
Cut-2	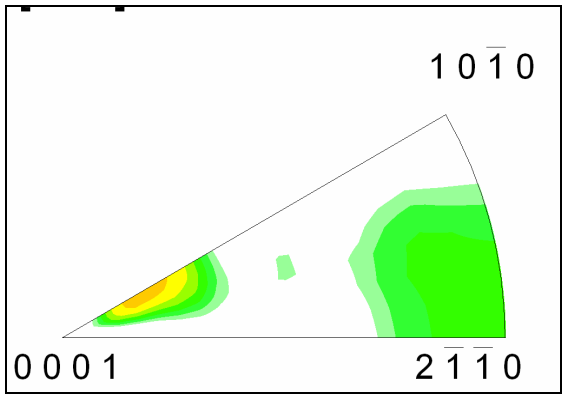	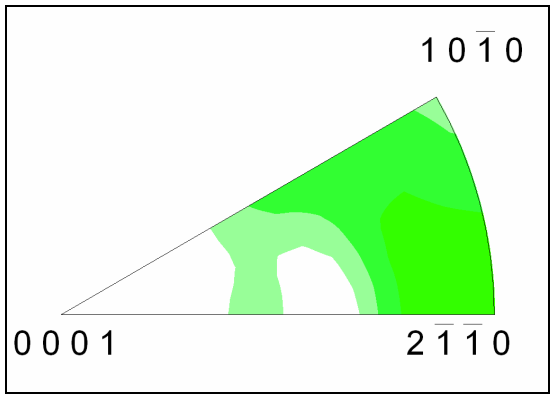
Cut-3	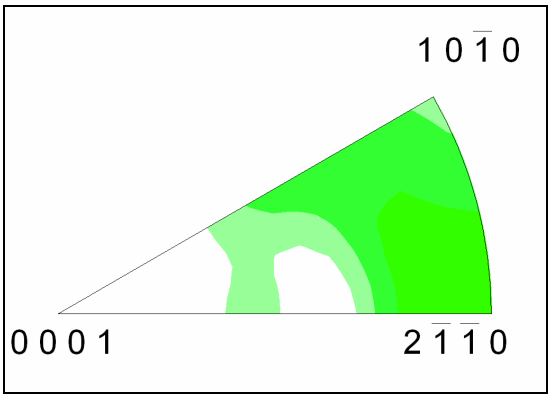	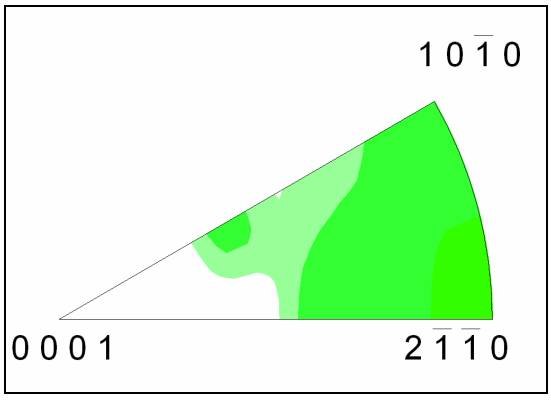

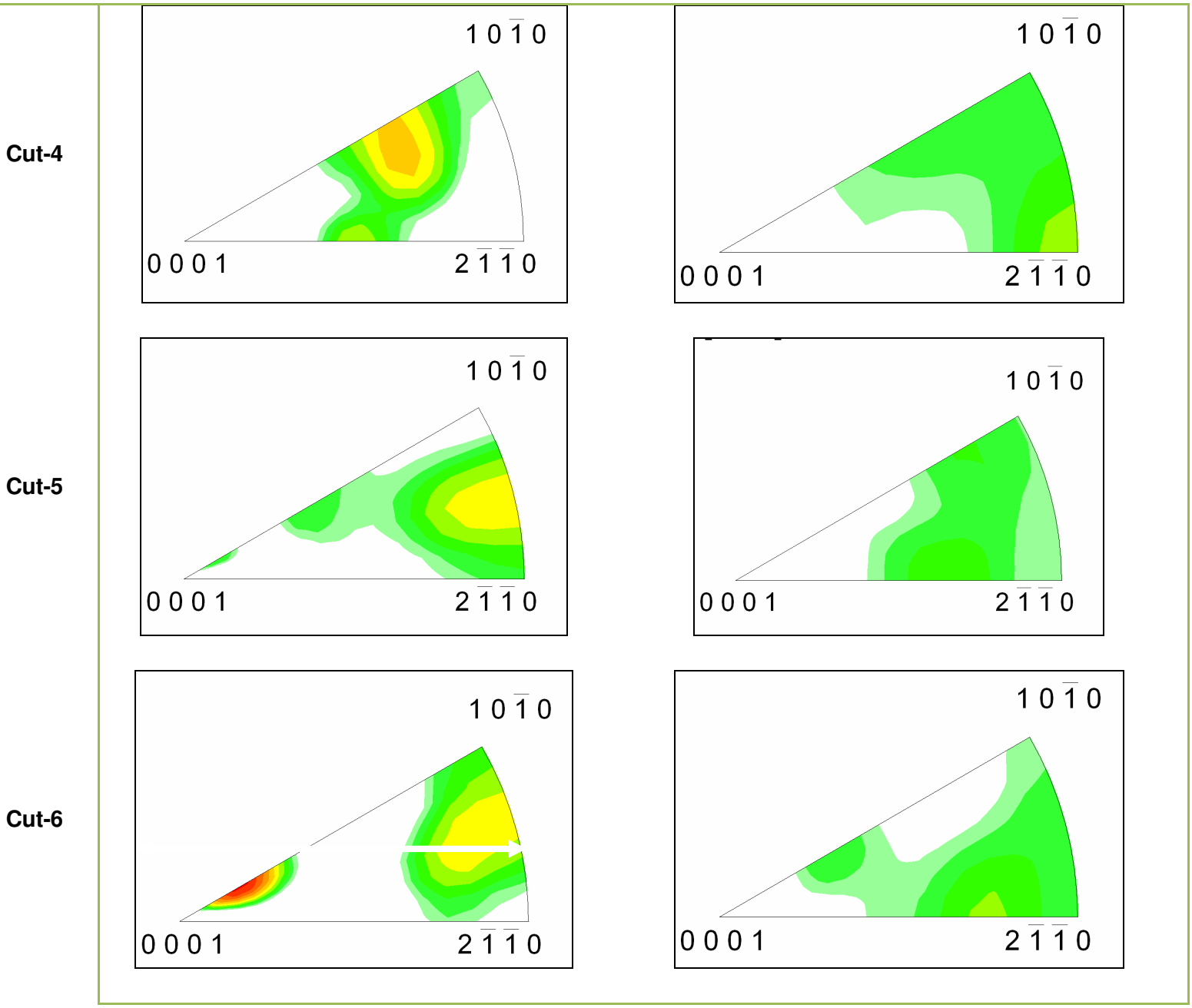

Fig. 5: (0001) pole figures of α-phase for as-cast Ti64-B vis-à-vis as-cast Ti64 with boron addition. Both types of pole figures are expressed in terms of similar intensity levels.

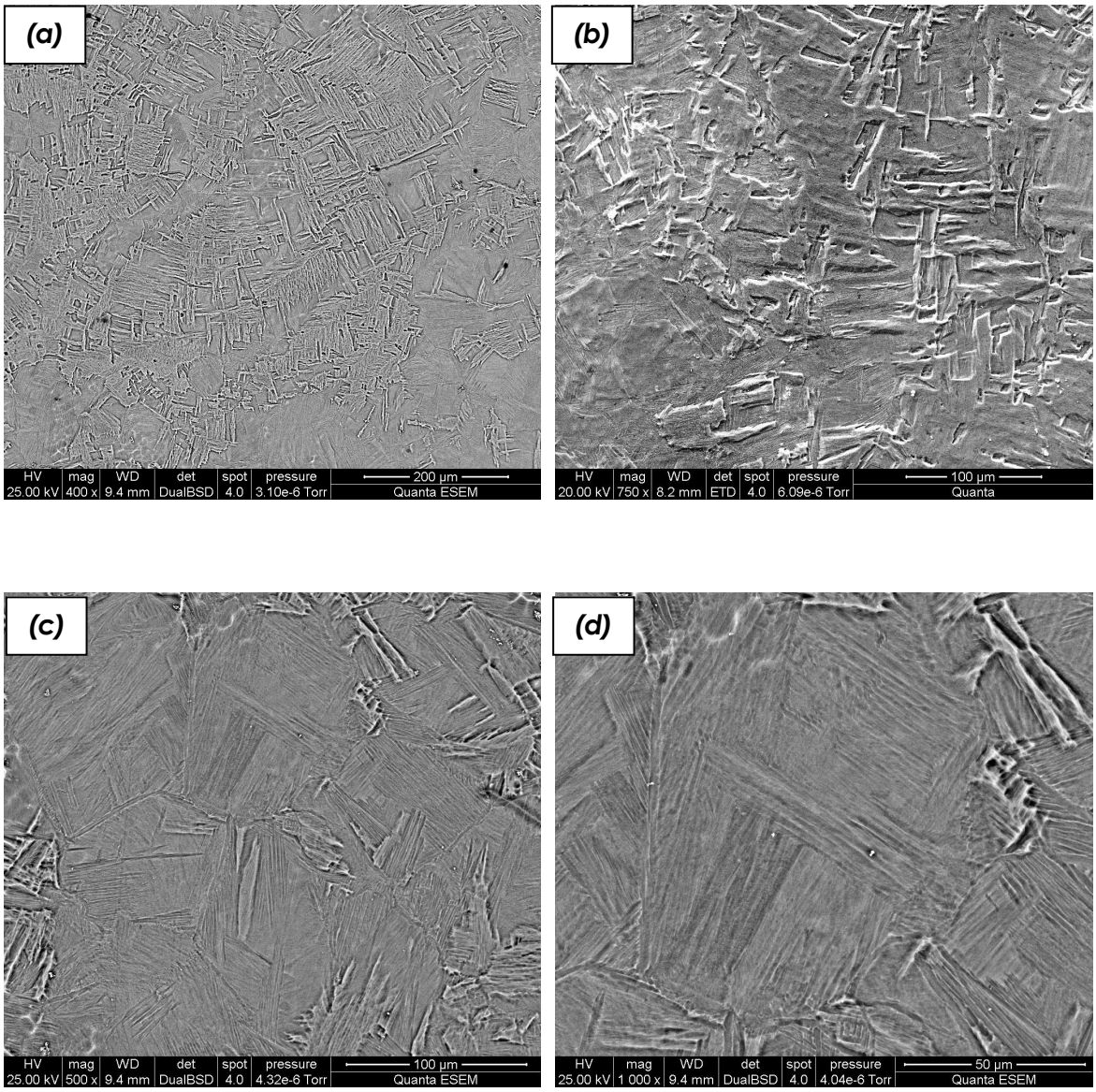

Fig. 6: SEM micrographs showing the top surface of the extruded samples of Ti64.

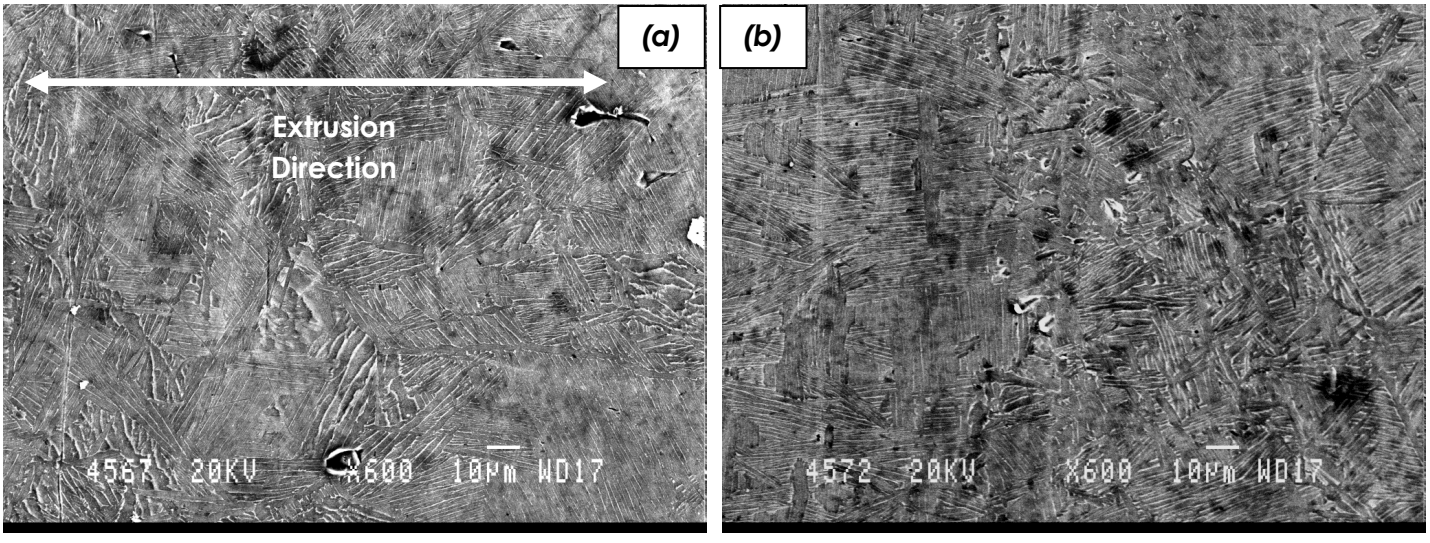

Fig. 7: SEM micrographs showing the vertical surface of the extruded samples of Ti64.

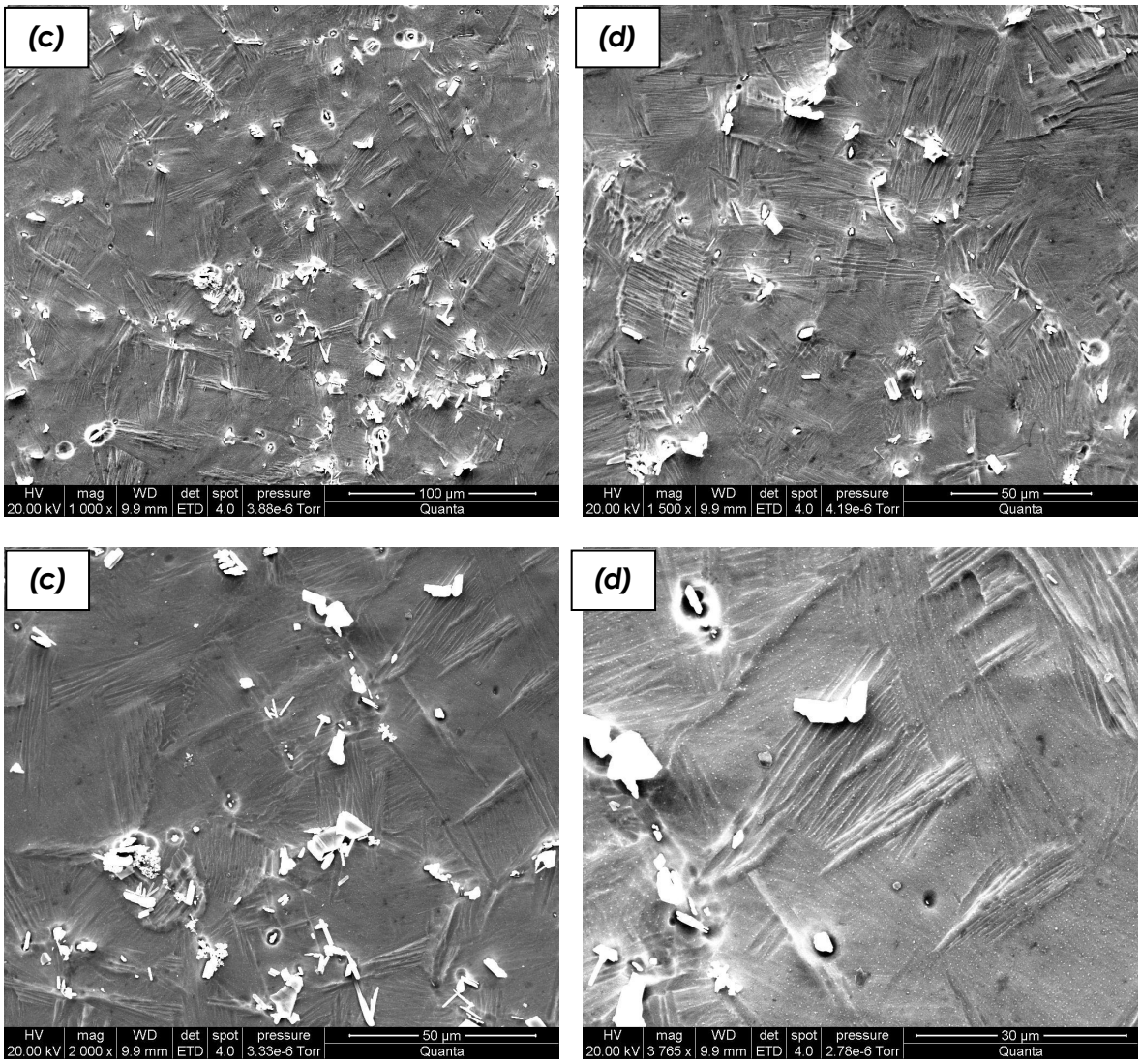

Fig. 8: SEM micrographs showing the top surface of the extruded samples of Ti64+B.

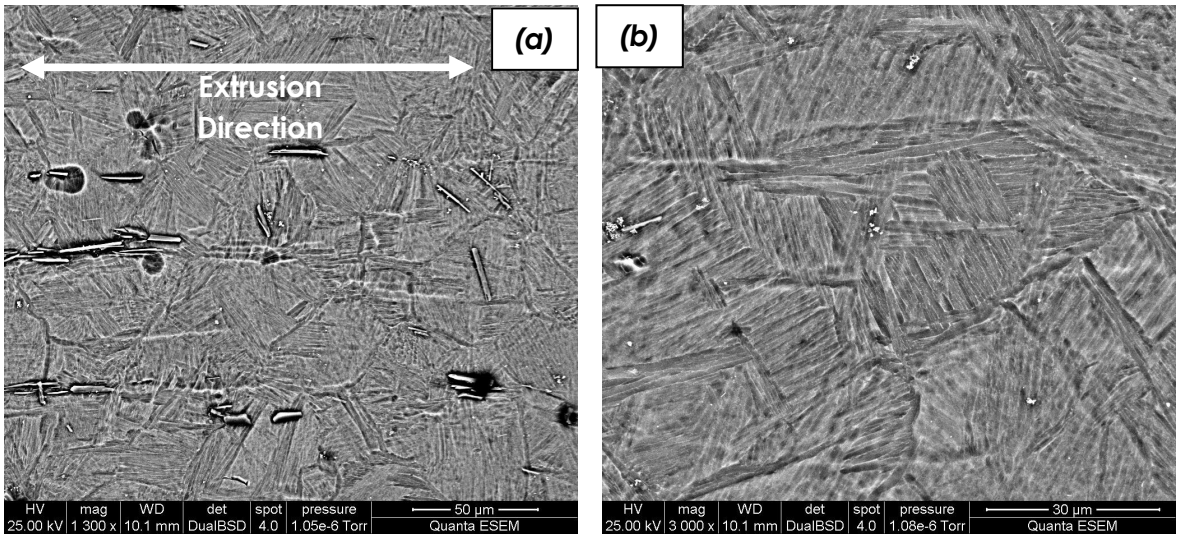

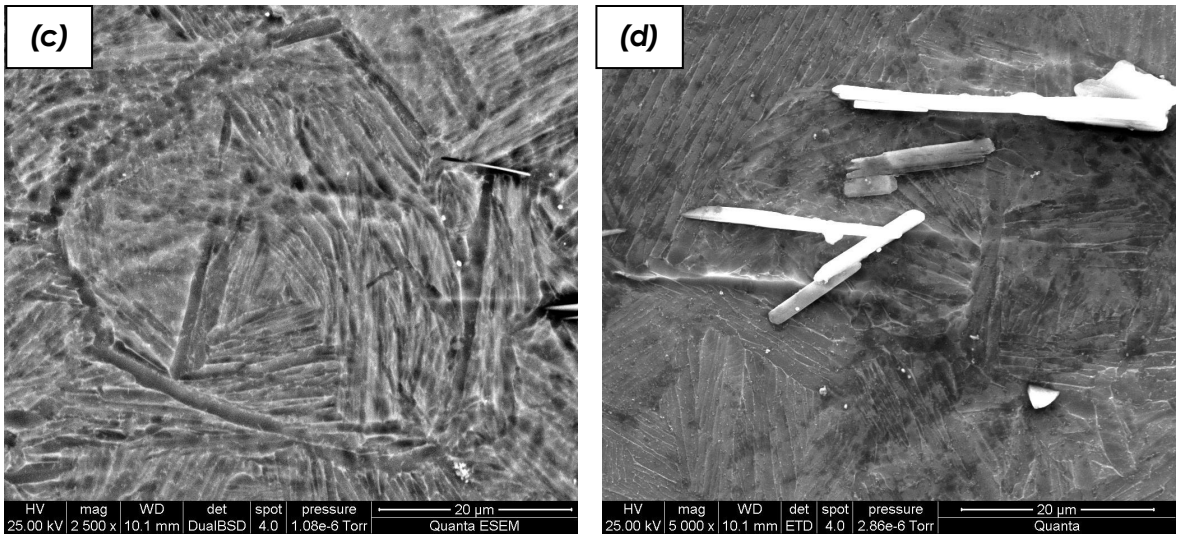

Fig. 9: SEM micrographs showing the vertical surface of the extruded samples of Ti64+B.

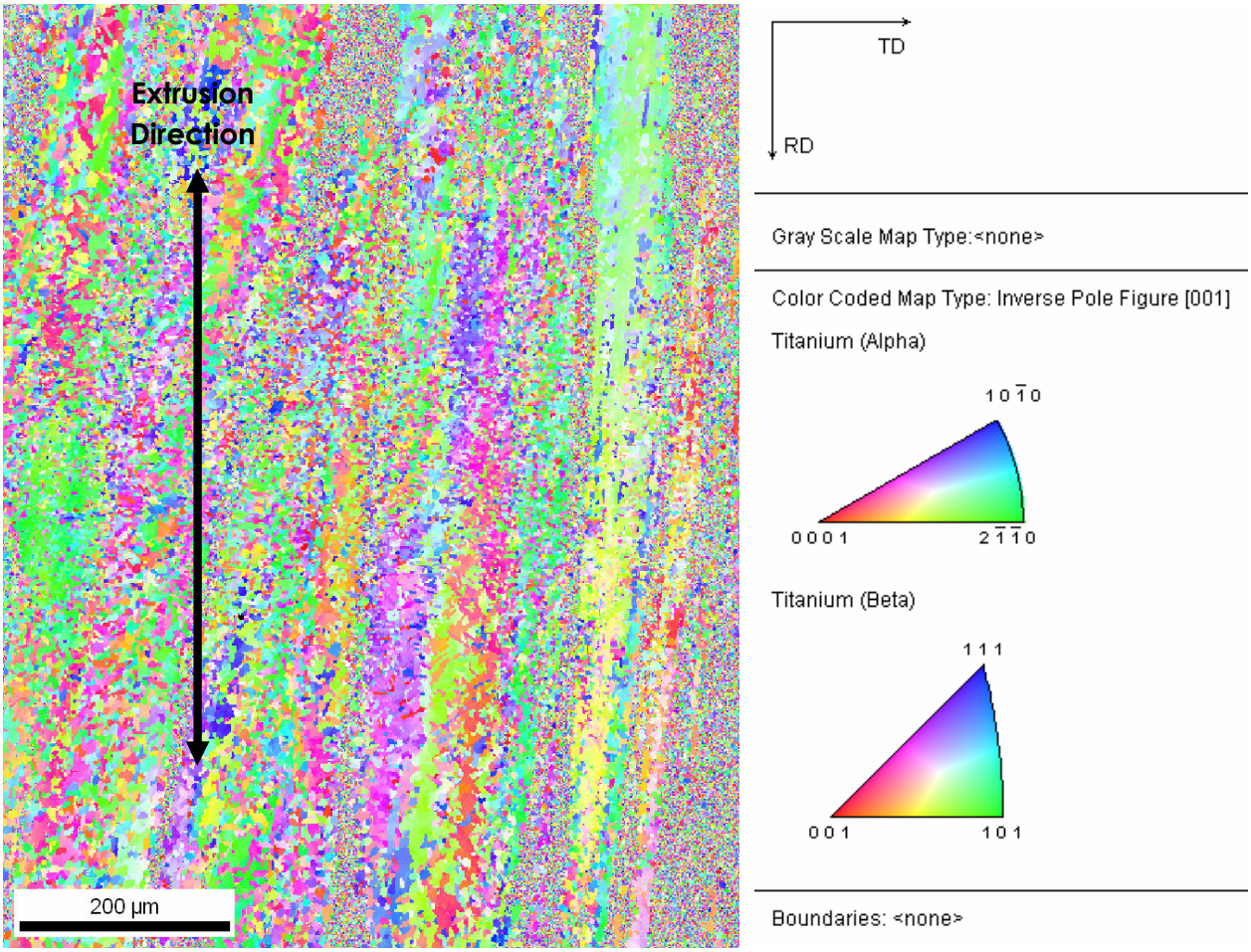

(a)

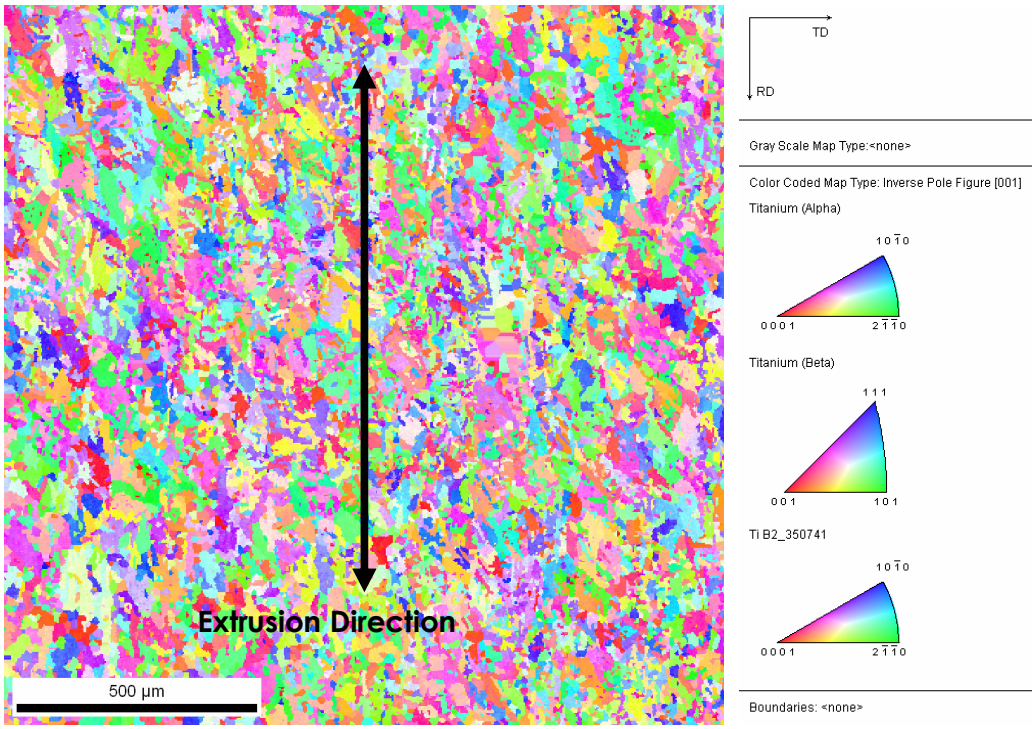

(b)

Fig. 10: Inverse pole figure maps obtained from EBSD analysis of extruded samples of (a) Ti64, and (b) Ti64+B.

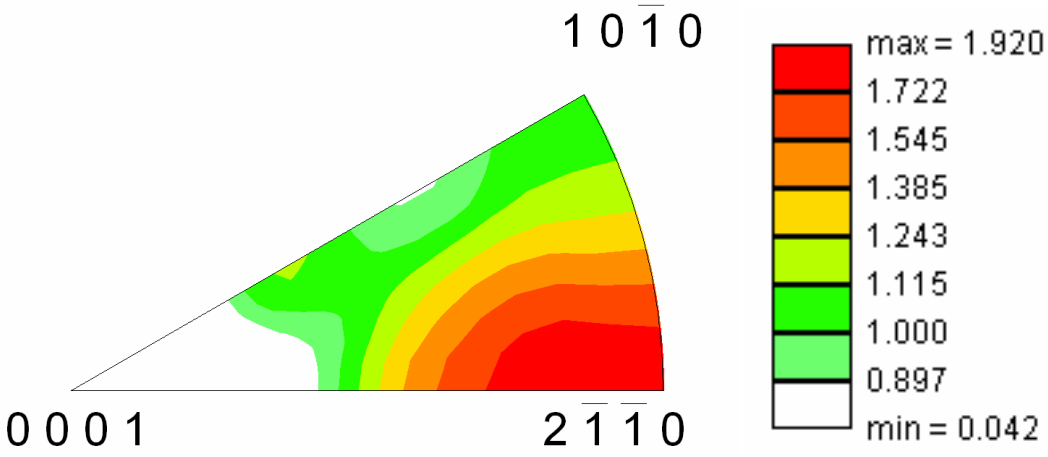

(a)

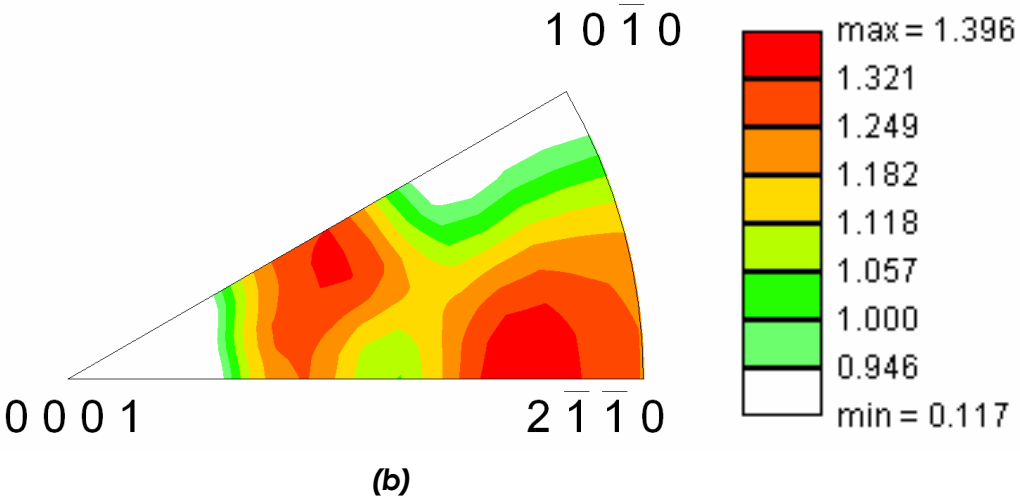

Fig. 11: Inverse pole figure plots obtained from EBSD analysis of extruded samples of (a) Ti64, and (b) Ti64+B.

Study of Deformation Behaviour of Cast Material using Plane Strain Compression Experiments

1. Introduction:

Metalworking of titanium and its alloys generally involves a series of thermo-mechanical processing steps to modify the as-cast microstructure into an equiaxed microstructure. These include upsetting/side pressing, cogging or extrusion at temperatures above or close to the beta transus (the temperature at which alpha phase transforms to beta and vice versa). This thermo-mechanical processes needs precise process control to avoid the occurrence of microstructural defects like wedge cracks and flow localization [1]. The working response of the newly developed boron modified Ti-6Al-4V alloy during hot working will be of particular interest in designing industrial hot working schedules for microstructural conversion without defect generation. The objective of this study is to characterize the hot deformation behavior of Ti-6Al-4V with and without boron modification over wide temperature and strain rate ranges with a view to model the microstructural mechanisms of hot deformation in mostly the alpha-beta phase fields. A wider strain rate range is selected which covers the speeds encountered in majority of the bulk metal working processes including forging, extrusion, and rolling. Materials modeling techniques involving kinetic analysis of flow stress data were used to achieve this objective and the results were correlated with microstructural observations.

An important and typical restoration mechanism in titanium and its alloys during hot working is called globularization, which plays crucial role in transforming the microstructure froma deformed one to a dynamically restored one. Semiatin et al [2] attempted to quantify the kinetics of globularization and found that dislocation glide/climb processes control the hot deformation of a colony structure. Seshacharyuly et al [3] have summarized the process of globularization to be consisted of four steps (see Fig. 1), like (i) Shearing of laths due to imposed shear strain: Initially, a few colonies that are favorably oriented with respect to the applied stress will participate in the shearing process, which will rotate the neighboring colonies to favorable orientations facilitating further shear; (ii) Generation of dislocations of both signs along the line of shear; (iv) Simultaneous recovery by cross-slip leading to annihilation of opposite sign dislocations on intersecting slip planes and leaving behind groups of dislocations with same sign to nucleate an interface along the line of shear and (iv) Migration of interfaces by diffusion to minimize the surface energy forming the globules. To conclude, they have explained the globularization process to be regarded as a type of dynamic recrystallization since it also involves two competitive processes viz., rate of nucleation and rate of migration.

Another important mechanism which dictates the workability of titanium and its alloys during hot working is the formation of microstructural instabilities (e.g. strain induced porosity consisted of wedge cracks and pores along the prior beta grain boundaries). Nicolaou et al [4] conducted a detailed investigation on prior beta boundary cavitation phenomenon and correlated the observations with the available continuum models for plasticity-controlled cavity growth and cavity coalescence. Formation of instabilities in ELI grade Ti-6Al-4V with beta transformed Widmanstatten structure (consists of lamellar alpha colonies, primary alpha at the prior beta grain boundaries and a thin layer of beta in-between the colony boundary and the primary alpha layer) has been briefly summarized by Seshacharyuly et al [5]. During deformation sliding of the prior beta boundary occurs across the soft beta layer and produces stress concentration at the primary alpha-thin beta interface. This stress concentration leads to cracks along the interface under mixed mode stress conditions (shear-tensile). At much higher temperatures and lower strain rates, the alpha phase is likely to undergo dynamic recrystallization (DRX) which softens the boundary layer and prevents cracking totally.

Seshacharyulu et al [1] have studied the hot deformation behavior of commercial grade Ti–6Al–4V with a lamellar starting microstructure in the temperature range 750–1100℃ and strain rate range 3×10^{-4} to $10S^{-1}$. They observed cracking at the prior beta grain boundaries when deformed in the lower alpha-beta temperature regime (<900℃) and slower strain rates (~10^{-1} S^{-1}). Also, globularization of lamellar structure occurs by cross slip in the temperature range 800–975℃ and strain rates slower than 10^{-2} S^{-1}. The beta phase undergoes dynamic recrystallization at higher temperatures (>1100℃) and slower strain rates (10^{-1} S^{-1} by self diffusion in the beta phase. At strain rates higher than 10^{-1} S^{-1} in the alpha-beta phase field, the material exhibits wide regime of flow instability manifested by adiabatic shear bands and lamellae kinking. At very high strain rates (~$1S^{-1}$) intense flow localization occur which causes cracking along the bands. In another study with equiaxed alpha-beta perform microstructure, the same researchers have observed [6] fine-grained super-plasticity controlled by dynamic recovery of grain boundary beta in the temperature range 750–950℃ and strain rates slower than 0.002 S^{-1}. Wherein the beta phase undergoes DRX at higher temperatures (~1050 C) through self-diffusion in beta phase, a wide regime of flow instabilities at strain rates higher than 0.1 S^{-1} is observed in their study. In a different study on ELI grade lamellar Ti-6Al-4V alloy, Seshacharyulu et al [5] observed globularization in the alpha-beta phase field while the beta phase deforms by the mechanism of large-grained super-plasticity.

2. Experimental Procedure:

2.1 Material

The materials used for the study are induction skull melted as cast and hipped ingots of Ti-6Al-4V, with and without boron addition (referred to hereafter as Ti64 and Ti64+B, respectively). Details about the composition of the materials can be found in Table 1 of part 1. As has been shown in part 1, in both these materials, the microstructure is completely homogenous and uniform throughout in terms of all kinds of microstructural length scales (prior β grain size as well as α-colony size). Both the materials are composed of Widmanstäten colonies of alpha lamellae with beta phase being sandwiched in between alpha lamellae and at the grain boundaries. In case of Ti64, the size of the prior β grains are typically in the millimeter range, with the α-colonies covers several hundreds of microns. In contrast, the prior β grain size is only ~200 microns with the alpha colonies being finer than 50 microns in case of Ti64-B. Hexagonal TiB crystals can be seen sitting at the grain boundary (see Fig. 3a inset) and forming a typical 'necklace' structure. Detailed description about the microstructure of these two materials can be found in the results section of part 1 of this report.

2.2 Hot Compression Test:

Compression specimens of 9 mm height and 6 mm diameter were machined from as cast ingots (see Fig. 1b and 1c). In case of Ti64, the compression axis was always parallel to the axis of the ingot. In case of Ti64+B, samples were made in two different sets (see Fig. 1a), one set with their compression axis being parallel to the ingot axis (referred to as Ti64+B-axial hereinafter) and another set with their compression axis being perpendicular to the ingot axis (referred to as Ti64+B-radial hereinafter). Concentric grooves of 0.5 mm depth were made on the top and bottom faces of the specimens to trap the lubricant and assist in reducing friction. A

1-mm 45° chamfer was provided on the specimen edges to avoid fold-over of the material during the initial stages of compression. Isothermal hot compression tests were conducted using a computer-controlled servo-hydraulic testing machine between two Ni-based super-alloy platens. A resistance heating split furnace with SiC elements was used to surround the platens and specimen. The specimens were coated with a borosilicate glass paste for lubrication and environmental protection. The detailed compression test matrix is given in table 1. It consists of a temperature range of 750°–1000°C at 50°C intervals. The crosshead motion of this machine was controlled to impose constant true strain rates of 10^{-3}, 10^{-2}, 10^{-1}, 1, and 10 S^{-1}. A chromel–alumel thermocouple was wrapped around the mid height of the specimen to monitor the actual temperature of the specimen as well as to measure any adiabatic temperature rise during testing. Isothermal condition was maintained inside the furnace within 2°C fluctuation in temperature during the whole test. The specimens were heated to test temperature and soaked for 5 minutes before compression. The specimens were deformed to 50% of their original height in each case to impose a true strain of about 0.7. The samples were air-cooled to room temperature after deformation by forced-convection cooling. The cooling rates affected by this were of the order of 25°C per seconds, resulting in cooling times that were much shorter than those that could give rise to the initiation of static globularization [ref]. The load-stroke data obtained in compression were converted to true stress-true plastic strain curves using the standard method. The flow stress data at different temperatures were corrected for adiabatic temperature rise (significant at strain rates higher than 10^{-3} S^{-1} and below 900°C) according to the temperature dependence of flow stress at constant strain and strain rate.

2.3 Microstructural Characterization

Deformed specimens were sectioned parallel to the compression axis (see Fig. 2b).The cut surfaces were first metallographically polished up to 2500 grit sized silicon carbide paper and finally electro-polished using Struers® Lectropol-5[1]. The electrolyte contains 600ml methanol, 360ml butoxyethanol and 60ml of perchloric acid. The samples were etched with a custom made etchant containing 5% HF, 10%HNO_3 and rest water for 30 seconds. The microstructures

[1] *Struers A/S, Germany*

of the samples were characterized by scanning electron microscopy[2]. In order to avoid to avoid the friction effected zones in the top and bottom sides of the deformed specimens, all microstructural characterization was carried out at the middle of the cut surfaces (i.e. at the mid thickness of the deformed specimens), where only true plane strain condition prevails (see Fig. 3c). Additional micrographs were taken from the two sides of the cut surfaces to capture the effect of secondary tensile stresses. Noteworthy to mention here that the instabilities like cavitation, shear cracking etc can be found typically in this zone.

2.4 Textural Characterization

The deformed samples were subjected to Orientation Imaging Microscopy using a Field Emission Gun Scanning Electron Microscope[3] with Electron Back-Scattered Diffraction (EBSD) facility. All the samples were metallographically prepared in the same way as described above for SEM observations without doing any etching. They were ultrasonically cleaned at every step of polishing and degassed completely before using for the EBSD scan. From each of the samples, an area of 750µm X 750µm was scanned with a step size of 1.5 µm. The accelerating voltage used was 20 KV and minimum boundary misorientation was taken to be 2^{o}. Titanium alloys, as reported in the literature, are very prone to oxidation in the normal condition so that sufficient care was taken before putting the samples for EBSD scan. Textural analysis (inverse pole figures, IPF maps, misorientation calculation etc.) was done using OIM™ Analysis Software[4]. In the entire study, only alpha textures have been studied though these alloys contain substantial amount of beta phase (~10%). This is because of the fact that beta phase is actually present between alpha laths as a thin layer and hence very small step size (~0.5 µm) is needed in EBSD scans to detect beta phase texture efficiently. However, in order to get a quantitative estimate of alpha texture, larger area needs to be scanned that in turn makes impractical to detect beta phase using a smaller step size. Hence, the entire study is focused on the texture of the alpha phase that constitutes about 90% of these alloys.

[2] *QUANTA 200, FEI, The Netherlands*
[3] *FEG-SEM, Sirion XL-40, FEI, The Netherlands*
[4] *TSL Crystallography, AMETEK Inc., USA*

3. Results and Discussions:

3.1 Flow stress and Flow curves:

Table 1 shows the variation of flow stress with respect to temperature and strain rate for all three kinds of materials, namely Ti64, Ti64+B-axial and Ti64+B-radial. The flow stress was taken as the stress at a true strain of 0.5. This was so chosen in order to avoid the rate dependent microstructural changes which may occur at higher values of strain. It can be seen from the table that for all three materials flow stress increases with strain rate at a fixed temperature and decreases with temperature at a pre-defined strain rate. This can be explained with the help of factors that controls the high temperature deformation. As can be easily understood, plastic deformation is always governed by the ease of dislocation motion. Anything that hinders the dislocation motion can cause the plastic deformation difficult and can increase the flow stress. The strain rate is related to dislocation motion by the following relation [7],

$$\varepsilon' = \rho b v \quad \text{..... (1)}$$

Where, έ = strain rate, ρ = dislocation density, b = burger vector, □ = dislocation velocity

Similarly, strain rate can be related to flow stress by the relation,

$$\sigma = C(\varepsilon')^m \text{, for } \varepsilon, T = \text{constant} \quad \text{..... (2)}$$

Where σ = flow stress, m = strain rate sensitivity, ε = true strain, and T = temperature

So, in turn, dislocation velocity is related to flow stress as,

$$v = C(\sigma')^{m'} \quad \text{..... (3)}$$

Therefore, any increase in strain rate will manifest itself in an increased dislocation velocity (provided the dislocation density remains constant during the process). The increase in dislocation velocity needs more amount of stress input so that the flow stress will increase with increasing strain rate.

With temperature increase, the diffusion rate increases which helps the edge dislocations to climb up and screw dislocations to climb over the barriers (e.g. precipitates, second phase particles etc.). Increased temperature also helps in grain boundary sliding above equi-cohesive temperature [7, 8], which is an important deformation mechanism at high temperature. Over and above, increased temperature promotes recovery and recrystallization which assists in reducing the stress required to cause further deformation. All these factors together reduce the flow stress with increasing temperature.

Comparing the effect of boron addition on the flow stress, it can be concluded that the flow stresses are almost comparable for Ti64 and Ti64+B for almost all strain rates and temperatures. Also, there is not much difference in flow stresses between Ti64+B-axial and Ti64+B-radial for all of the working conditions.

Fig. 3 shows the true stress-true strain flow curves of Ti64 for various strain rates at a fixed test temperature. The main features of each of these curves are discussed bellow.

At 750^{o}C, stress increases with strain up to a maximum value and decreases to a lower value afterwards. The strain at which this peak stress occurs differs from different strain rates, however, it occur near to $\varepsilon = 0.05$. At lower strain rate (10^{-3} S^{-1} and 10^{-2} S^{-1}), deformation occur as a steady state process with the curves become almost parallel to the strain axis. This is because of the ease of dynamic recovery during high temperature deformation. The longer deformation time for low strain rate deformation provides ample time for the temperature to equilibrate, so that flow localization due to adiabatic heating does not take place. However, for higher strain rates (10^{-1} S^{-1} and 1 S^{-1}), stress to cause further strain increases continuously after attaining the peak stress and subsequent flow softening. This is more pronounced in case of 1 S^{-1} strain rate deformation, where a large hump is evident in the flow curve. This kind of flow softening after peak stress and presence of humps in the flow curve is typically characteristics of instability (e.g. shear crack at grain boundary, cavitations at grain boundary triple junctions etc.) formation due to disproportionate grain boundary sliding during deformation [6]. Instability causes sudden release of energy, which produces adiabatic heating and subsequent flow localization and flow softening. Since adiabatic heating is more pronounced at higher strain

rates due to smaller time for energy dissipation, this kind of large hump in flow curves is not seen at lower strain rates.

At 800°C, the flow curves are similar to that obtained at 750°C. The only difference is that now at higher strain rate also, flow stress starts saturating after the initial flow softening. This can be attributed to the increased amount of dynamic recovery at higher temperature, which can compensate for the work hardening. A large amount of flow softening can be noticed at 10 S^{-1} strain rates. This is probably because of the shorter deformation time which induces profound instability formation and flow localization. At 850°C, the flow curves are similar to that obtained at 750°C and 800°C except for the fact that steady state flow after peak stress can be observed even for 10^{-1} S^{-1} strain rate. Similar to 800°C, this also can be attributed to increased dynamic recovery. As far as instability formation and flow localization is concerned, increased temperature helps in more and more grain boundary sliding. Additional possibility is dynamic recrystallization of grain boundary alpha phase which also can minimize strain concentration at grain boundaries. Therefore flow instability and flow localization gets minimized at higher temperatures even for higher strain rates. Thus, the hump in the flow curve is only present in 1 S^{-1} strain rate at 850°C.

At 900°C, steady state is achieved after peak stress and flow softening even at 1 S^{-1} strain rate. However, the basic shape of the curves does not differ much from that of the corresponding curves at 850°C. At 10 S^{-1} strain rate, however, large flow softening is observed even up to a very high value of strain. This is possibly because of the adiabatic conditions prevailed at this high strain rates which gives rise to flow localization and flow softening. The flow curves at 950°C are quite different from that of the lower temperatures. Wherein for 1 S^{-1} strain rate, a large decrease in flow stress after the peak stress is seen, both at 10^{-2} S^{-1} and 1 S^{-1} strain rates, a continuous flow softening with increasing strain can be observed. To a little approximation this kind of flow curve can be a signature of dynamic recrystallization occurring at higher strain. At 1000°C, the flow curves are closely similar to that of 950°C. The flow curve at 10 S^{-1} strain rate is similar to that observed at 800°C with the difference that after the peak stress, a steady state flow is followed with flow softening occurring only at very high strain.

Fig. 4 shows the true stress-true strain flow curves of Ti64+B-axial for various strain rates at a fixed test temperature. The main features of each of these curves are discussed bellow.

At 750°C, flow curves are similar to that obtained for Ti64 at 750°C except for 1 S^{-1} strain rate one where no large hump is observed. At lower strain rate (10^{-3} S^{-1} and 10^{-2} S^{-1}), the flow curves show almost steady state flow stress with increasing strain. However, for higher strain rates (10^{-1} S^{-1} and 1 S^{-1}), stress to cause further strain increases continuously after attaining the peak stress. At 800°C, flow curves are similar to that obtained for Ti64 at 800°C with steady state flow dominates after peak stress for low strain rate deformation (10^{-3} S^{-1} and 10^{-2} S^{-1}). However, at higher train rates, flow stress increases continuously with strain. The flow curve of 1 S^{-1} shows usual hump after initial peak stress. Interesting behavior can be seen in case of 10 S^{-1} strain rate, where initially flow stress increases with strain, but at higher strain values it decreases to lower value and again increases afterwards. This sudden drop in flow stress is also observed for Ti64 at 1000°C, 10 S^{-1} deformation. Probably this flow softening is because of instability and adiabatic conditions.

At 850°C, the flow curves are similar to that obtained at 850°C for Ti64 with steady state flow after peak stress even for 10^{-1} S^{-1} and 1 S^{-1} strain rate. The flow curve of 1 S^{-1} shows usual hump after initial peak stress. At 900°C, the flow curves are similar to that obtained at 850°C for Ti64 with steady state flow after peak stress for almost all the strain rates. At 10 S^{-1}, however the flow curve is similar to that of Ti64 at 900°C with flow softening after a peak stress and steady state flow up to ~0.4 strain and subsequent increase in flow stress with further strain. At 950°C, the flow curves are different from those of Ti64 at the same temperature. The difference is more prominent for a $1S^{-1}$ strain rate. The large hump in the curve is followed by steady state flow at higher strain. This is typical for a hot deformation with dynamic recrystallization being the dominant mechanism. Flow curves at 1000°C are again different from those of Ti64 at the same temperature. However the curves are similar to those obtained at 900°C with flow curve of 1 S^{-1} showing usual hump and that of 10 S^{-1} showing flow softening at higher strain.

Fig. 5 show the true stress-true strain flow curves of Ti64+B-radial for various strain rates at a fixed test temperature. The main features of each of these curves are discussed bellow.

At 750°C, flow curves are similar to that obtained for Ti64+B-axial at 750°C except for the fact that almost steady state flow with increasing strain is observed even at higher strain rates like 10-1 S-1. However, at 1 S^{-1} strain rate, stress to cause further strain increases continuously after attaining the peak stress. At 800°C, flow curves are similar to that obtained for Ti64+B-axial at 800°C with steady state flow dominates after peak stress for low strain rate

deformation for all strain rates. The flow curve of 1 S^{-1} does not show usual hump after initial peak stress. The flow curve at 1000°C, 10 S^{-1} is also similar to that obtained for Ti64+B-axial sample. At 850°C, the flow curves are similar to that obtained at 850°C for Ti64+B-axial with steady state flow after peak stress even for 10^{-1} S^{-1} and 1 S^{-1} strain rate. The flow curve of 1 S^{-1} shows usual hump after initial peak stress.

At 900°C, the flow curves are similar to that obtained at 850°C for Ti64+B-axial with steady state flow after peak stress for almost all the strain rates. The flow curve of 1 S^{-1} shows usual hump after initial peak stress. At 10 S^{-1}, however the flow curve is similar to that of Ti64+B-axial at 900°C with flow softening after a peak stress and steady state flow up to ~0.4 strain and subsequent increase in flow stress with further strain. The flow softening is not that intense as in the case of Ti64+b-axial at 900°C. At 950°C, the flow curves are very similar to those of Ti64+B-axial at the same temperature. The large hump in the curve is followed by steady state flow at higher strain. This is typical for a hot deformation with dynamic recrystallization being the dominant mechanism. Flow curves at 1000°C are again very similar to those of Ti64+B-axial at the same temperature.

In order to find out the effect of test temperature on the flow behavior of different materials, stress-strain curves were plotted at a particular strain rate for different temperatures for all three materials (see Fig. 6). In case of Ti64, up to 900°C, all the flow curves are of similar shape i.e. they have a peak stress after which a steady flow is followed by a flow softening and thereby producing a hump in the flow curve up to a strain of ~0.2. However, as the temperature increases, the flow behavior at higher strain level becomes more and more steady state. The presence of this large hump and subsequent steady state flow is typical characteristics of dynamic recrystallization (DRx), which is possibly the domination mechanism up to 900°C. At still higher temperatures the flow softening occurs right after the attainment of the peak stress and at high strain level, steady state flow is observed. This kind of flow curves signifies some softening mechanism which is different from DRx. The shape and nature of flow curves for Ti64+B-axial and Ti64+B-radial are very similar to that of Ti64. The only difference is that in case of Ti64+B, hump in the flow curve is observed even at very high temperatures i.e. 950°C and 1000°C. Also, the steady state flow after the hump starts at much lower strain level and much lower temperature (at ε = around 0.15 and T = around 850°C) than that of Ti64.

3.2 Kinetic Analysis:

The temperature and strain rate dependence of flow stress in hot deformation is generally expressed in terms of a kinetic rate equation given by [7, 8],

$$\dot{\varepsilon} = A\sigma^n \exp\left(-\frac{Q}{RT}\right) \quad \text{..... (4)}$$

Where $\dot{\varepsilon}$ = Strain rate, σ = flow stress, A = Frequency factor, Q = Apparent activation energy, R = Gas constant, T = Temperature in Kelvin, and n = Stress exponent = 1/m, where m=Strain rate sensitivity.

In order to identify the mechanism(s) of hot deformation, the kinetic parameters, n and Q are to be evaluated. The variation of flow stresses with strain rates at different temperatures are shown in Fig. 7 on a log–log scale. The slope of the linear fit between the flow stress and strain rate represents the strain rate sensitivity, m, for that particular temperature. It can be seen that m is strain rate dependent for a few test temperatures when considered over the entire range of strain rate employed in this study. In those cases, m value is calculated at each of the strain rate ranges and averaged. Table 2 summarizes the strain rate sensitivity of all three materials at each of the working conditions. The error in linear fitting, standard deviation in fitting and regression coefficient, all of them signify for the quality of linear fitting. A god linear fitting should show a regression coefficient not less than 0.98 with error value much less than 0.01. This kind of quality fitting is obtained for most of the working conditions other than only a very few exceptions. The poor quality of fitting is observed mostly at higher temperatures in case of Ti64 and Ti64+B-radial. The fitting quality is excellent, however, for Ti64+B-axial at all test temperatures. For Ti64+B-axial and Ti64+B-radial, the strain rate sensitivity value changes from a higher to a lower value at 10^{-1} S^{-1} strain rate. This behavior is especially visible in case of 800°C and 900°C working temperatures where sufficient number of flow stress data is available at different strain rates.

The strain rate sensitivity is quite low (~0.1) at 750°C and 800°C for all three materials with Ti64+B (both axial and radial) showing slightly higher m value than Ti64 (see Table 3). Strain rate sensitivity increases above 850°C and remains almost constant thereafter. For all

three materials, at high temperatures, m value is around 0.15-0.17. For Ti64 with and without boron addition, strain rate sensitivity is quite comparable with an exceptionally high m value being obtained at 1000°C in case of Ti64+B-radial.

Similar to strain rate sensitivity, activation energies at different deformation conditions are calculated using the slope of the linear fitting of flow stress vs. inverse of working temperature (expressed in terms of absolute temperature) in a log-log scale. The activation energy is calculated from the slope using the following relation,

$$Slope = \frac{mQ}{2.303R} \quad \text{, ... (5)}$$

This ultimately gives,

$$Q = \frac{2.303R}{m \times slope} \quad \text{..... (6)}$$

It can be seen that activation energy depends strongly upon strain rate and test temperature (see Table 5). Also, multiple activation energy values are possible for a particular strain rate, which accounts for the fact that the slope is different in different temperature ranges. Table 4 summarizes the slope of flow stress-inverse temperature plot of all three materials at each of the working conditions. The error in linear fitting, standard deviation in fitting and regression coefficient, all of them signify for the quality of linear fitting. Satisfactory quality fitting is obtained for most of the working conditions other than a very few exceptions. The poor quality of fitting is observed mostly at lower strain rate (at 10^{-3} and 10^{-2} S-1 in case of Ti64 and at 10^{-3} S^{-1} for Ti64+B (for both axial and radial). Both for Ti64 and Ti64+B, a change in the slope of the flow stress-inverse temperature curve (and hence in activation energy) occurs around 900°C. This transition in the activation energy signifies the change in operating deformation mechanism at that temperature. This behavior is especially visible in case of 10^{-2} and 1 S^{-1} strain rates were sufficient number of flow stress data is available at different temperatures.

Table 6 summarizes the activation energies of three materials at different working conditions. In case of Ti64, activation energy is particularly high at all strain rates. It decreases to a lower value as the temperature increase up to 850°C. Activation energy jumps back to a very high value at 900°C and decreases afterwards indicating that a completely different

deformation mechanism being dominated at this temperature. Any such correlation between activation energy and strain rate is difficult to find out. However, at very low and high strain rates (10^{-3} and 1 S^{-1}, respectively) at any particular test temperature, activation energy is quite low as compared to the other strain rates at that temperature. For Ti64+ B-axial and Ti64+B-radial, the general trend of activation energy as seen in case of Ti64 is maintained although in most of the working conditions, activation energy for Ti64+B is higher than that of Ti64. In case of Ti64+B, activation energy at different strain rates decreases initially with temperature and jumps to a very high value after a certain temperature. This temperature is found to be around 900°C for Ti64+B-axial and around 850°C for Ti64+B-radial. In case of the later material, activation energy decreases with temperature after 850°C for almost all strain rates. However a marked difference between the activation energies Ti64+B-radial and Ti64+B-axial can be observed at different strain rates. For example, activation energy is quite low at 10^{-3} S^{-1} strain rate in case of Ti64+B-axial, but it is quite high for Ti64+B-radial at that strain rate. Similarly, lower activation energy of Ti64+B-radial at 1 S^{-1} strain rate is complemented by higher activation energy for Ti64+B-axial.

As reported by previous researchers, in case of α-titanium, activation energy estimated for lattice diffusion is 150 kJ/mole [9], wherein apparent activation energy of 242 kJ/mole was reported for power-law creep [10]. These values are relatively low when compared to the range of activation energies that has been obtained in the present study. However, under certain working conditions, especially at low strain rates like 10^{-3} S^{-1}, the experimental activation energies are quite comparable to that reported in literature for different deformation mechanisms of α-titanium. Thus it can be concluded that at low strain rates and low temperatures, deformation is controlled by diffusion through alpha lattice i.e. it is mostly dominated by recovery through cross slip and climb of dislocations. It should be noted that the presence of substantial amount of beta (~10 wt%) can change the operational deformation mechanism and hence the activation energy in case of (α+β) alloys like Ti-6Al-4V. Table 6 displays typical strain rate sensitivity and activation energy values obtained by earlier researchers for Ti64 using the constitutive equation described above. It can be seen that for Ti64, at most of the working conditions, activation energy values correlate well with that given in literature, especially at moderate to high strain rates (0.01to 1 S^{-1}) and moderate temperatures (800°-900°C). This observation supports the conclusion that globularization of lamellar alpha phase may be the dominant deformation mechanism in these working conditions. In case of Ti64+B-higher activation energies are observed which may be attributed to the presence of additional titanium-boride phases. The

strain rate sensitivity values reported in the literature, however, are way too far different from that obtained in the present study for bothTi64 and Ti64+B.

Continuing the analysis on the basis of the kinetic rate equation, the temperature compensated strain rate parameter, Zener-Holloman parameter (Z), is given by [8],

$$Z = \dot{\varepsilon} \exp\left(-\frac{Q}{RT} \right) \quad \text{..... (7)}$$

It is evaluated on the basis of the apparent activation energy and showed as a function of flow stress in Table 7, 8, and 9. In case of Ti64 (see table 7) Z-values exhibits a good correlation with flow stress. It can be noticed that increasing temperature actually decreases the Z parameter and it is related to a continual increase in the flow stress. However, at 900°C, Z value increases again and decreases afterwards indicating a different deformation mechanism operating at that condition. Other than 10^{-3} S^{-1}, strain rate seems to have a limited effect on Z parameter. Similar such correlation between Z parameter, temperature and flow stress holds true for Ti64+B-axial and Ti64+B-radial at almost all strain rates (see Table 8 and 9). In this case also, Z value is quite high at 900°C and decreases afterwards. The variation of flow stress with Zener-Holloman parameter confirms that the kinetic rate equation is obeyed in the limited temperature and strain rate range being considered in the present study.

It should be noted here that the beta volume fraction and alpha grain size (or rather colony size) are not constant over the experimental range of temperature and strain rate. As observed by previous researchers [5, 6], beta volume fraction in an (α+β) alloy initially increase slowly with temperature. After certain transition temperature, beta volume fraction shots up and increases rapidly with temperature to a value of ~90% near the beta transus. This variation in beta volume fraction with temperature is usually monitored using the beta approach curve developed for different alloys. The constitutive equation used by the earlier researchers as well as in the present study does not include the influence of these factors (i.e. increasing beta volume fraction with temperature and change in alpha colony size) on deformation kinetics. Therefore the constitutive equation is not sufficient to draw any conclusion regarding the deformation kinetics, especially in case of two phase alloys like Ti-6Al-4V. In view of these limitations, the flow stress data can be analyzed using thermal activation models proposed by Schőck et al [11] and Kocks et al [12], which consider the stress dependency of activation energy.

According to Schőck's model, the stress dependent activation energy U(σ) is given by the equation for thermally activated cross-slip as follows,

$$\dot{\varepsilon} = \dot{\varepsilon}_0 \exp\left[-\frac{U(\sigma)}{kT}\right], \quad \text{..... (8)}$$

and

$$U(\sigma) = \acute{A}\ln\left(\frac{\sigma}{\sigma_0}\right) \quad \text{..... (9)}$$

Where $\dot{\varepsilon}$ = constant (assumed to be 10^{-7} s^{-1}), U(σ) = stress-dependent activation energy, k = Boltzman's constant, Á = Temperature and stress-independent constant, and σ_0 = Stress required to overcome the activation barrier in the absence of any thermal activation. Using the plots of ln(έ) versus ln(σ), the threshold stress σ_o can be evaluated and the corresponding activation energy values can be estimated.

To understand the recovery mechanism, thermal activation model proposed by Kocks et al can be used as follows,

$$\frac{\sigma}{\mathrm{E}} = \frac{\sigma_{athermal}}{\mathrm{E}} + \frac{\sigma}{\mathrm{E}}\left(1 - \frac{kT}{g_o E b^3}\ln\frac{\dot{\varepsilon}}{\dot{\varepsilon}_o}\right) \quad \text{..... (10)}$$

Where, g_0 = normalized total activation free enthalpy, b = Burgers vector, σ/E = normalized flow stress, $\sigma_{athermal}$ = Athermal component of the flow stress due to long-range obstacles, and σ_0 and $\acute{\varepsilon}_0$ have the same meaning as in equation 8 and 9. The activation energies are evaluated at high temperature where $\sigma_{athermal}$ will be very small and can be neglected. A plot of (σ/E) vs. (kT/Eb^3) $\ln(\acute{\varepsilon}_0/\acute{\varepsilon})$ is used to evaluate σ_0/E value by extrapolation from which the apparent activation energy can be determined.

3.3 Microstructure Evolution:

The SEM micrographs shown from Figure 9 to Figure 31 are of Ti64 samples deformed at various temperature-strain rate combinations. The direction of compression axis is shown in the micrographs. The main microstructural features of each of the samples are discussed bellow.

At working condition of 750°C, 10^{-3} S^{-1}, the SEM micrographs show a completely deformed microstructure with lath bending and kinking as the primary deformation mechanism (see Fig. 9a and 9b). There is no sign of instability in the form of adiabatic shear banding, although some cavities can be seen inside the alpha colonies which are quite unexpected. The micrographs do not reveal any evidence of globularization or recrystallization at this condition. At working condition of 750°C, 10^{-2} S^{-1}, the SEM micrographs again show deformed microstructure without the sign of either instability formation or globularization (see Fig. 10). SEM micrographs at working condition of 750°C, 10^{-1} S^{-1} show lath bending along with large cavitation inside the alpha colonies (see Fig. 11). SEM micrographs at working condition of 750°C, $1S^{-1}$, show instabilities like cavities and shear cracks at prior beta boundaries (see Fig. 12b & 12c). This can be seen mostly in the two sides of the sample where secondary tensile stresses prevail. Otherwise the microstructure shows usual deformed structure with lath bending.

At working condition of 800°C, 10^{-3} S^{-1}, SEM micrographs show cavities and shear cracks at prior beta boundaries (see Fig. 13a & 13c) in the two side regions. Rest of the places where only primary compressive stresses was present, microstructure shows usual deformed structure. At working condition of 800°C, 10^{-2} S^{-1}, the SEM micrographs again show deformed microstructure (see Fig. 14). In this case, the colonies bend at successive places and form some kind of wavy structure. Similar features can be found for samples worked at 800°C, 10^{-1} S^{-1} condition (see Fig. 15). Cracking and cavities at prior beta boundaries can be seen in case of samples worked at 800°C, 1 S^{-1} condition (see Fig. 18) in the tensile stress regions. At other places, a deformed structure can be found. Similar cavities can also be found in case of sample worked at 800°C, 10 S^{-1} conditions (see Fig. 16) in the same region.

The microstructures of the samples deformed at 850°C in different strain rates are almost similar to that of the samples worked at 750°C or 800°C in the sense that the primary

deformation mechanism is characterized by lath bending and kinking (see Fig 17 to Fig. 21). However, cracking and cavitations at prior beta boundaries is not visible in the region of tensile stress even at the highest strain rate condition. In some cases, newer small colonies can be seen in the microstructure, which can possibly be attributed to dynamic recrystallization during deformation.

At 900°C, the micrographs show usual deformed microstructure characterized by lath bending in almost all strain rates (see Fig. 22 to Fig. 26). However, cracking and cavitations at prior beta boundaries can be seen for most of the conditions. An interesting observation is that at this temperature, the beta phase starts protruding into the alpha laths. This indicates the beginning of globularization. Closer observation of Fig. 24d and Fig 26a reveals the fact that the bigger alpha laths are now divided into smaller sections surrounded by beta phase from all sides. In fact at this temperature, simply deformed alpha colonies coexists with globularized colonies (see Fig. 26b).

The coexistence of deformation by lath bending and initiation of globularization further extended up to 950°C at all strain rates tested (see Fig. 27 & 28). The amount of lath bending is however, quite less compared to that at lower temperatures. The cracking and cavitations at prior beta boundaries continues at this temperature also. At 1000°C, the microstructure of deformed samples exhibit completely globularized structure with colony alpha structure being transformed to an equiaxed one. Lath bending can be seen only at higher strain rate of 10 S^{-1}, although the amount of colonies showing deformed structure is quite less. Any kind of instabilities in terms of cracking and cavitations at prior beta boundaries are absent in this case.

The SEM micrographs shown from Figure 32 to Figure 54 are of Ti64+B-Axial samples deformed at various temperature-strain rate combinations. The direction of compression axis is shown in the micrographs. The main microstructural features of each of the samples are discussed bellow.

At working condition of 750°C, the SEM micrographs show a completely deformed microstructure with lath bending and kinking as the primary deformation mechanism (see Fig. 32 to 35) for all the strain rates. As the prior beta grain size as well as the alpha colony size is comparatively small for Ti64+B samples, the amount of lath bending is also less compared to that in the case of Ti64. There is no sign of instability in the form of adiabatic shear banding, cracking and cavitations at prior beta grain boundaries is any of the samples all over the microstructure. The interesting difference between the deformed microstructures of Ti64 and

Ti64+B-Axial is the presence of cavities around the hard and brittle titanium boride particles present at the prior beta grain boundaries. These cavities are formed during etching, as the eloctropolished samples do not show any such feature in the microstructure. This is possibly because of the strain accumulation around the Ti-B particles which leads to excessive material removal during etching. Titanium boride compounds, being hard and brittle particles do not deform in the same rate as does the ductile metal matrix phase. Therefore, a strain accumulation because of dislocation pile ups around the particles occurs which leads to the cavity formation.

The microstructures of the samples deformed at 800^{o}C in different strain rates are almost similar to that of the samples worked at 750^{o}C in the sense that the primary deformation mechanism is characterized by lath bending and kinking (see Fig 36 to Fig. 40). Here also cavities around Ti-B particles are clearly visible. The interesting observation from Fig. 38a is that near to Ti-B particles, laths do not bent as much as they do away from the particles. This shows that near the particles, most of the applied strain is absorbed by the particles themselves and very little strain is experienced by the alpha colonies. Similar to 750^{o}C, no visible cracking, cavitations or shear banding is observed in the present case.

SEM micrographs taken from the samples deformed at 850^{o}C showed usual deformed microstructure of lath bending at all strain rates (see Fig. 41 to 44). Cavitations around Ti-B particles are visible as well as the absence of shear cracking and cavitations at prior beta boundaries. The anchoring effect of hard Ti-B particles on the alpha laths can also be seen (see Fig. 41b). The interesting observation at this temperature is the fragmentation of bigger alpha laths into small equiaxed alpha grains surrounded by beta phase (see Fig. 44). This is more prominent at higher strain rate deformation like 1S^{-1}. Typical effect of deformation like lath bending and kinking is also very less in this case as compared to the other strain rates. This is possibly the initiation of globularization. This effect is more prominent adjacent to the Ti-B particles, wherein deformed structure can mostly be seen in the grain interior. The additional strain effective around the Ti-B particles is expected to help in beta phase penetration through alpha laths and as an effect initiates globularization. Similar to this condition, at 900^{o}C, the micrographs show more of a globularized structure than a typical deformed one (see Fig. 45 to 49). The noticeable feature is that at these temperatures, the amount of beta phase present in the microstructure is much more than that remains in the samples of Ti64 deformed in corresponding temperatures. This is possibly because of the lowering of beta transus by boron addition, wherein beta volume fraction of Ti64+B at any given temperature will be more than

that of Ti64 at that temperature. Additional observation is that at 900°C, globularization takes place even at lower strain rates as oppose to 850°C and in case of higher strain rates like $1S^{-1}$ and $10S^{-1}$, globularized grains are much more prominent and almost equiaxed. At both these temperatures, neither cracking nor cavitations can be seen at prior beta grain boundaries at the two side regions of the samples.

At 950°C, the microstructure of the samples deformed at various strain rates can be characterized by three distinctly different features (see Fig 50 and 51), namely (i) well developed equiaxed alpha grains formed due to globularization, (ii) small amount of deformed structure showing lath bending and kinking and (iii) fine, acicular alpha laths forming small, un-deformed alpha colonies inside the prior beta boundaries. The acicular alpha laths and colonies are typical signature of beta working. Possibly, the local heating due to adiabatic rise helps the material to cross its beta transus and while cooling, (fast air cooling) acicular laths were produced instead of Widmanstatten plates. Deformation at 1000°C produces completely beta worked structure at all strain rates (see Fig 52, 53 and 54). This indirectly signifies for the fact that the beta transus of Ti64+B possibly lies between 950°-1000°C. The prior beta boundaries can be identified from the locations of Ti-B particles wherein the beta grains after working are clearly visible. The worked beta grains are quite finer (~50 microns) than that of the prior beta grains. The alpha laths are totally acicular in shape signifying for the effect of faster cooling rate during air cooling. Extending the discussion further, the deformed microstructure indeed shows a basket-weave structure rather than a Widmanstatten one. At both these temperatures, cracking or cavitations cannot be seen at prior beta grain boundaries even at the two side regions of the samples.

The SEM micrographs of Ti64+B-Radial samples deformed at various temperature-strain rate combinations show (see Fig. 55 to 78) exactly the same microstructural features for each of the conditions as those of the Ti64+B-Axial samples. It can then be concluded that texture does not play any crucial role in terms of microstructure evolution in case of Ti64+B.

3.4 Texture Evolution

The results obtained from the EBSD analysis of some of the specimens deformed under various temperature-strain rate conditions re summarized from Fig. 79-81. The alpha colony size refines substantially from the as cast condition in both Ti64 and Ti64+B. wwherein the colony size

ranging around 70 μm for Ti64 and 50 μm for Ti64+B, after deformation, the colony sizes come down to around 15-20 μm for Ti64 and less than 10 μm for Ti64+B for all the deformation conditions studied. The miss-orientation distribution plots show the predominant presence of log angle colony boundaries which is typical characteristics of deformed structure without any sigh of dynamic restoration processes occurring. In another words, presence of low angle boundaries during deformation signifies for the formation of sub-grains surrounded by dislocation arrays forming low angle boundaries. The texture evolved in the deformed samples markedly differs from their as cast counterpart in case of both the materials. The texture of deformed Ti64 samples is different from that of Ti64+B, although there is no difference between the texture of the longitudinal and radial samples. The primary texture component in Ti64 that evolved after deformation varies from {11-20> to {11-21> as the temperature and strain rate increases. In case of Ti64+B, the texture always remains near to {10-10> for all the temperature-strain rate combinations studied.

4. Conclusions

In the present study, deformation of boron modified Ti-6Al-4V alloy has been carried out in the limited temperature range of 750°-900°C and strain rate of 10^{-3} to 1 S^{-1}. On the basis of the flow curves and microstructural analysis, the following conclusions can be drawn:

1. Steady state flow and substantial flow softening for low strain rates at all temperatures and for high strain rates at high temperatures.
2. Kinetic analysis shows the possibility of dynamic recovery in the alpha phase during low strain rate deformation as well as dynamic recrystallization at higher strain rate and temperature.
3. Deformation causes the α-lath bending and kinking to accommodate the strain.
4. Cavity can be formed around the boride particles due to strain mismatch during deformation.
5. No sign of instability can be seen during the deformation process for Ti64+B, possibly due to the ease of nucleation at boride particles during dynamic recrystallization.
6. Presence of low angle grain boundary as well as remarkable difference in texture can be observed in EBSD analysis.

References:

1. *T. Seshacharyulu , S.C. Medeiros, W.G. Frazier, and Y.V.R.K. Prasad, "Microstructural mechanisms during hot working of commercial grade Ti–6Al–4V with lamellar starting structure", Mat. Sc. Engg. A 325, 112 (2002)*
2. *S.L. Semiatin, V. Seetharaman, I. Weiss, "Flow behavior and globularization kinetics during hot working of Ti–6Al–4V with a colony alpha microstructure", Mat. Sc. Engg. A 263 (1999) 257–271*
3. *T. Seshacharyulu, S.C. Medeiros, J.T. Morgan, J.C. Malas, W.G. Frazier, and Y.V.R.K. Prasad, "Hot deformation mechanism in ELI grade Ti-6Al-4V", Scripta Materialia, 41(3), 283 (1999)*
4. *P. D. Nicolaou, J. D. Miller, and S. L. Semiatin, "Cavitation during Hot-Torsion Testing of Ti-6Al-4V, Metallurgical and Materials Transactions, 36(12), 3461 (2005)*
5. *T. Seshacharyulu, S.C. Medeiros, J.T. Morgan, J.C. Malas, W.G. Frazier, and Y.V.R.K. Prasad, "Hot deformation and microstructural damage mechanisms in extra-low interstitial (ELI) grade Ti–6Al–4V", Materials Science and Engineering A, 279 289 (2000)*
6. T. *Seshacharyulu, S.C. Medeiros, W.G. Frazier, and Y.V.R.K. Prasad, "Hot working of commercial Ti–6Al–4V with an equiaxed α-β microstructure: materials modeling considerations", Mat. Sc. Engg. A 284, 184 (2000)*
7. *G. E. Diieter, and D. Bacon, "Mechanical Metallurgy", McGraw-Hill Book Co., 1998B.*
8. *Verlinden, J. Driver, I. Samajdar, and R. D. Doherty, "Thermo-Mechanical Processing of Metallic Materials", Elesevier Ltd., 2007*
9. *F. Dyment and C.M. Libanati, "Self-diffusion of Ti, Zr, and Hf in their hcp phases, and diffusion of Nb^{95} in hcp Zr", J. Mater. Sci. 3, 349 (1968)*
10. *M. Doner and H. Conrad, "Deformation mechanisms in commercial Ti (0.5 at. pct) at intermediate and high temperatures (0.3 - 0.6 T_m)", Metall. Trans. 4, 2809 (1973)*
11. *G. Schöck, in ed. F.R.N. Nabarro, Dislocations in Solids, vol. 3, p. 63, North-Holland, Amsterdam (1980)*
12. *U.F. Kocks, A.S. Argon, and M.F. Ashby, "Thermal Activation", Progress in Mater. Sci. 21, 110 (1975)*

SUMMARY

Titanium alloys like Ti-6Al-4V are the backbone materials for aerospace, energy, and chemical industries. Hypoeutectic boron addition Ti-6Al-4V alloy produces a reduction in as-cast grain size by roughly an order of magnitude resulting in the possibility of avoiding ingot breakdown step and thereby tremendously reducing the processing cost. In the present study, ISM processed as-cast boron added Ti-6Al-4V alloy showed identical, although refined microstructure and largely randomized/weak texture compared to normal Ti-6Al-4V alloy. When deformed in (α+β)-phase field, α-lath bending and globularization seemed to be the dominating deformation mechanisms at lower and higher temperatures, respectively for both these materials. Wherein normal Ti-6Al-4V showed flow instabilities (cavitations, cracking etc.) at low temperatures, boron added materials possessed enhanced workability under all processing conditions. The texture evolved during deformation was, however, completely different in these two kinds of alloys, suggesting a difference in the operating deformation mode that produces the end stable orientations.

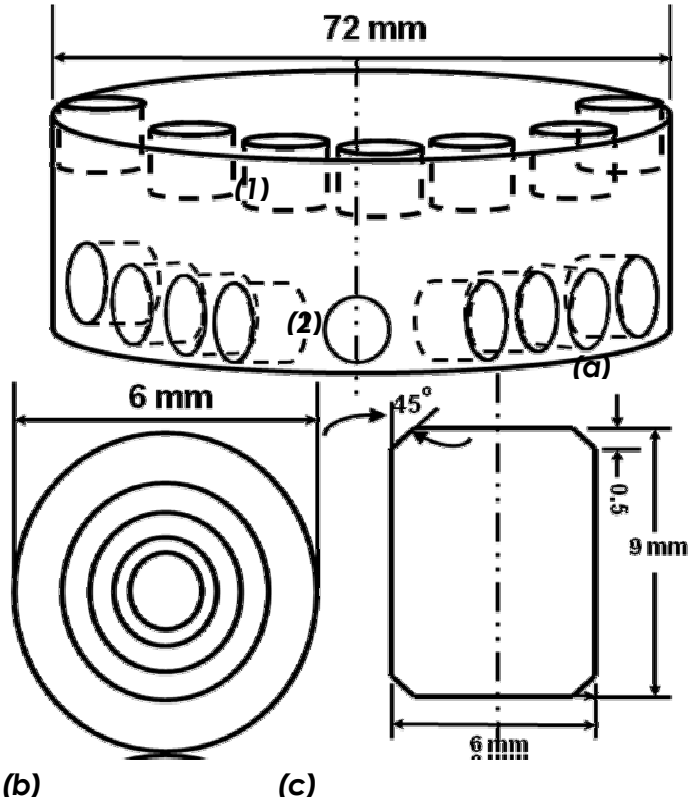

Fig. 1: (a) Schematic showing as-cast ingot and the way compression samples were made from the original ingot, (1) In case of Ti64 and Ti64+B-Axial, the compression sample axis is parallel to the original ingot axis, and (2) in case of Ti64+B-Radial, , the compression sample axis is perpendicular to the original ingot axis; (b) schematic showing the top view of the compression sampless, and (c) schematic showing the side view of the compression sampless

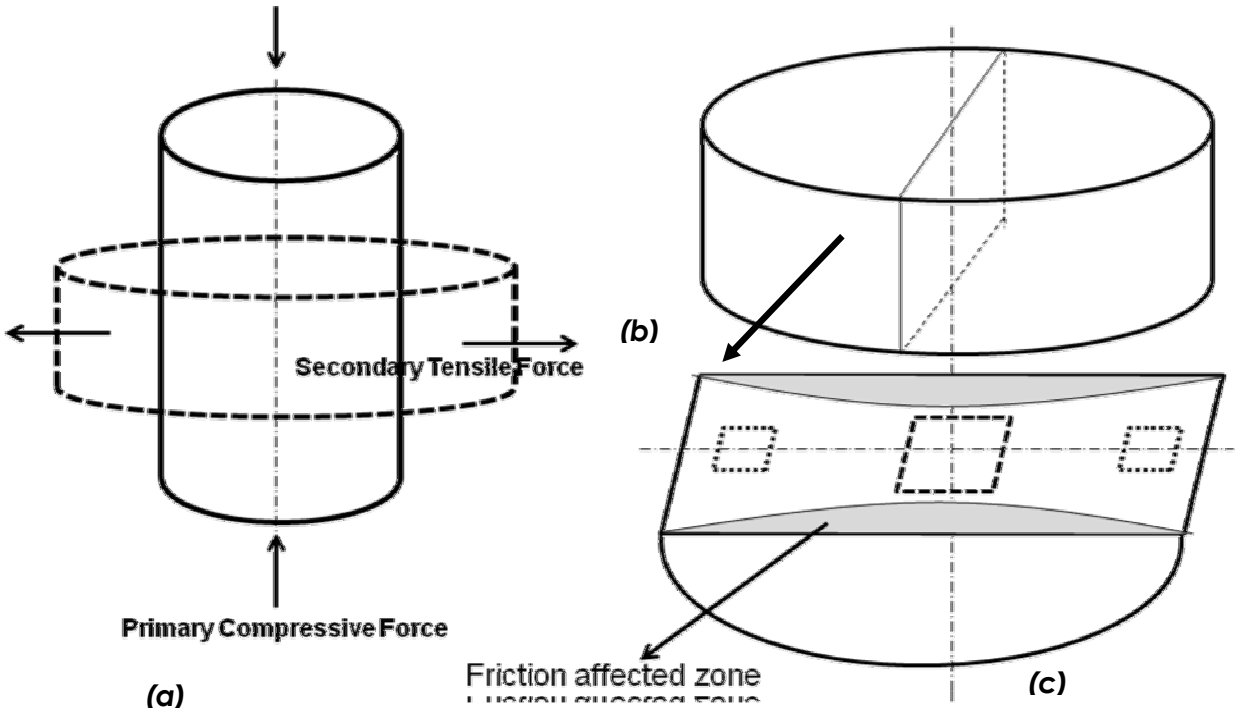

Fig. 2: Schematic showing the way the compressed samples were prepared for microstructure and texture studies; (a) the directions of different forces applied to the original sample, (b) compressed samples were cut longitudinally, and (c) areas were selected for examination from the mid thickness region, at both the sides and at the middle.

Table 1: Compression test matrix of as-cast samples.

Temp.	Strain Rate				
	$10^{-3}\ S^{-1}$	$10^{-2}\ S^{-1}$	$10^{-1}\ S^{-1}$	$1\ S^{-1}$	$10\ S^{-1}$
750°C	Yes	Yes	Yes	Yes	No
800°C	Yes	Yes	Yes	Yes	Yes
850°C	Yes	Yes	Yes	Yes	No
900°C	*Yes*	*Yes*	*Yes*	*Yes*	*Yes*
950°C	No	Yes	No	Yes	No
1000°C	No	Yes	No	Yes	Yes

Table1: Flow Stress of different materials at various temperature-strain rate combinations.

Material	***Temperature***	***Flow Stress***				
		Strain Rate				
		$10^{-3}\ S^{-1}$	***$10^{-2}\ S^{-1}$***	***$10^{-1}\ S^{-1}$***	***$1\ S^{-1}$***	***10 S-1***
Ti64	**750**	**205.93**	**278.2**	**317.48**	**414.72**	
	800	**105.98**	**153.5**	**230.87**	**254.4**	**308.9**
	850	**75.24**	**156.18**	**179.6**	**175.15**	
	900	**57.38**	**88.52**	**135**	**183.34**	**249.47**
	950		**52.2**		**64.03**	
	1000		**29.96**		**50.34**	**109.3**
Ti64+B-Axial	**750**	**189.88**	**264.94**	**311**	**439.56**	
	800	**161.4**	**161.6**	**210.63**	**288.2**	**385.66**
	850	**95.64**	**135.65**	**185.48**	**240**	
	900	**34.934**	**85.41**	**147.14**	**188**	**245.6**
	950		**58.01**		**129.38**	
	1000		**31.02**		**69.46**	**86.5**
Ti64+B-Radial	**750**	**184.22**	**255.63**	**281.96**	**374**	
	800	**123.42**	**184.54**	**278.44**	**338**	**385.8**
	850	**109.35**	**138.88**	**182.79**	**273.51**	
	900	**60.88**	**97.3**	**133.82**	**222.91**	**245.72**
	950		**59.01**		**129.5**	
	1000		**20.02**		**89.49**	**87.79**

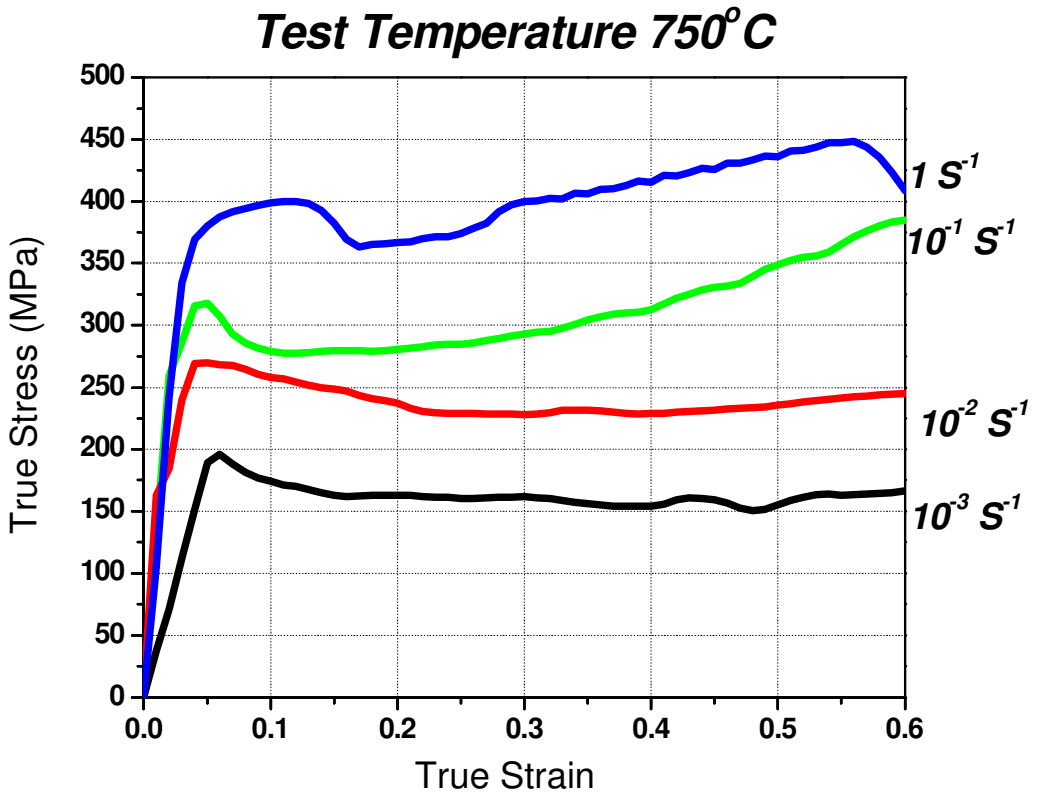
Test Temperature 750°C
True Stress (MPa)
True Strain
1 S-1
10-1 S-1
10-2 S-1
10-3 S-1

(a)

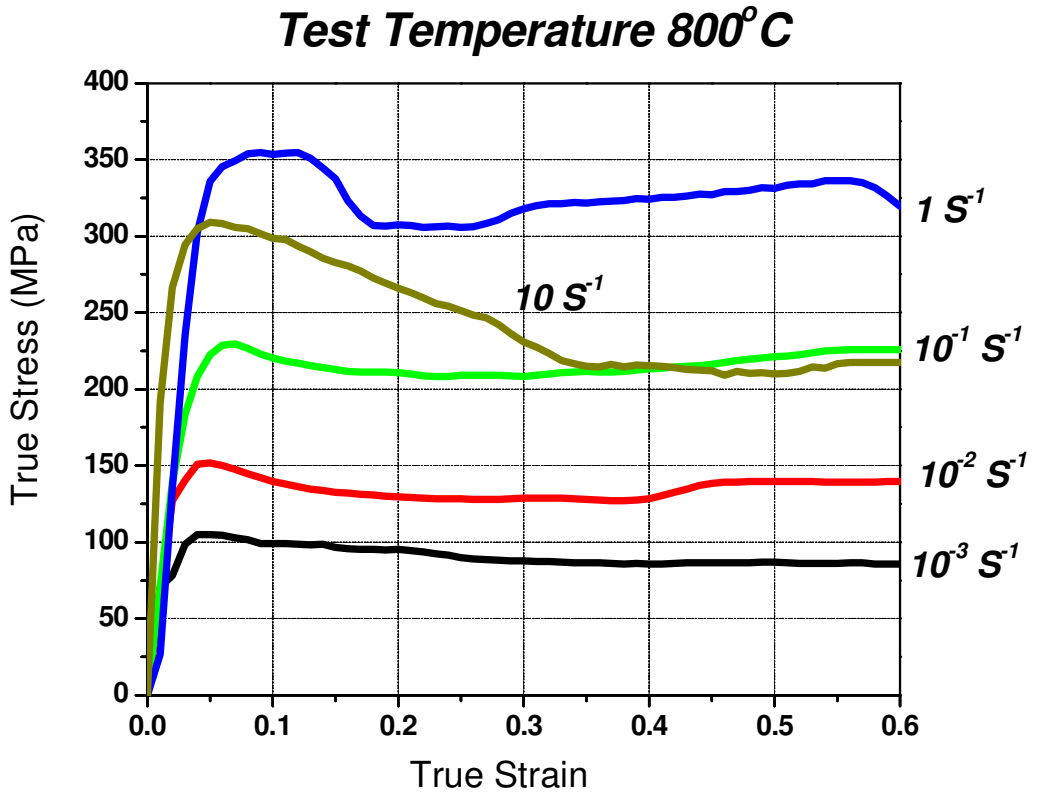
Test Temperature 800°C
True Stress (MPa)
True Strain
1 S-1
10 S-1
10-1 S-1
10-2 S-1
10-3 S-1

(b)

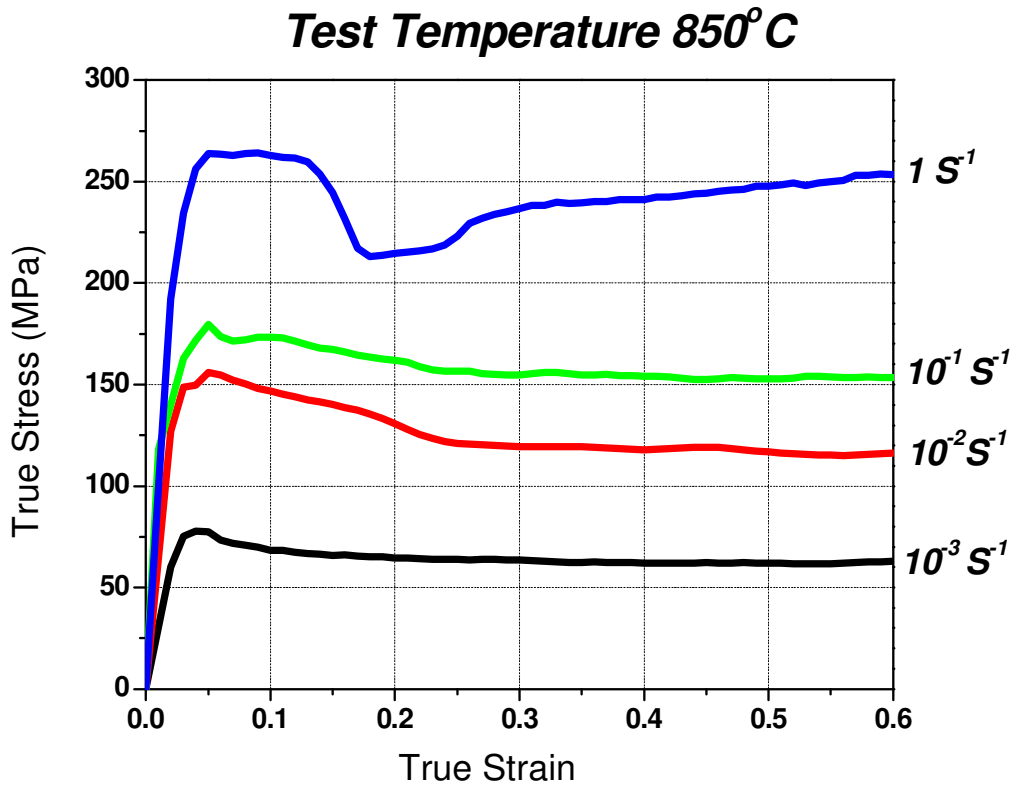
Test Temperature 850°C
True Stress (MPa)
True Strain
1 S-1
10-1 S-1
10-2S-1
10-3 S-1

(c)

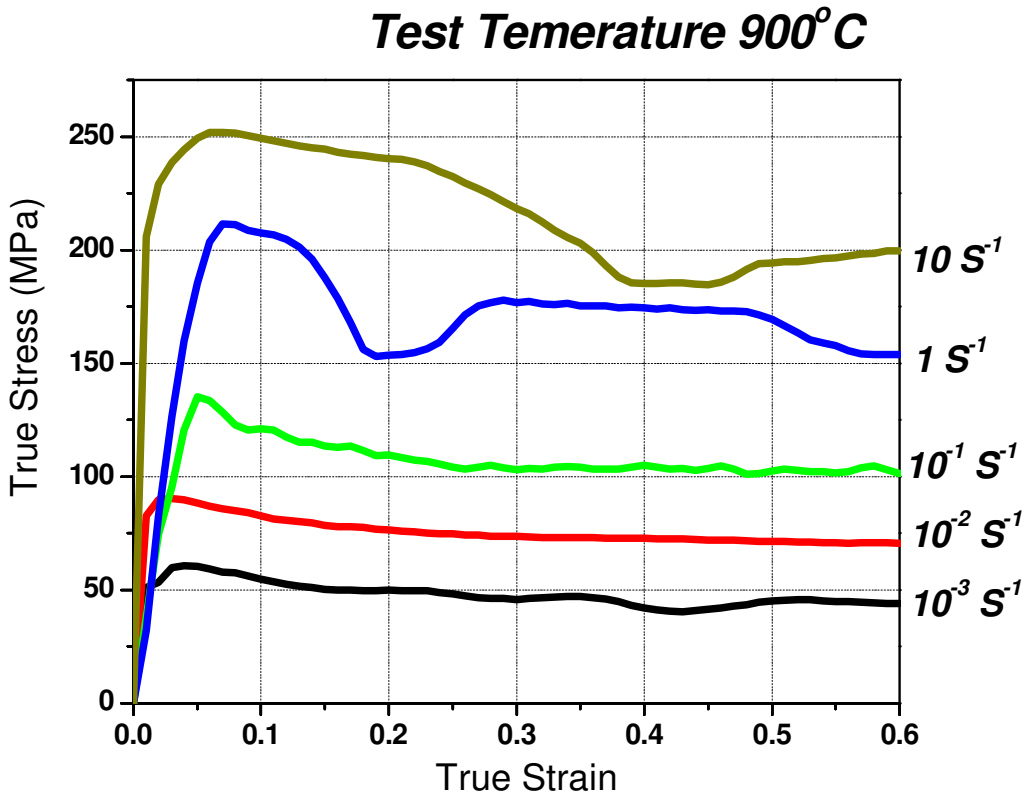
Test Temerature 900°C
True Stress (MPa)
True Strain
10 S-1
1 S-1
10-1 S-1
10-2 S-1
10-3 S-1

(d)

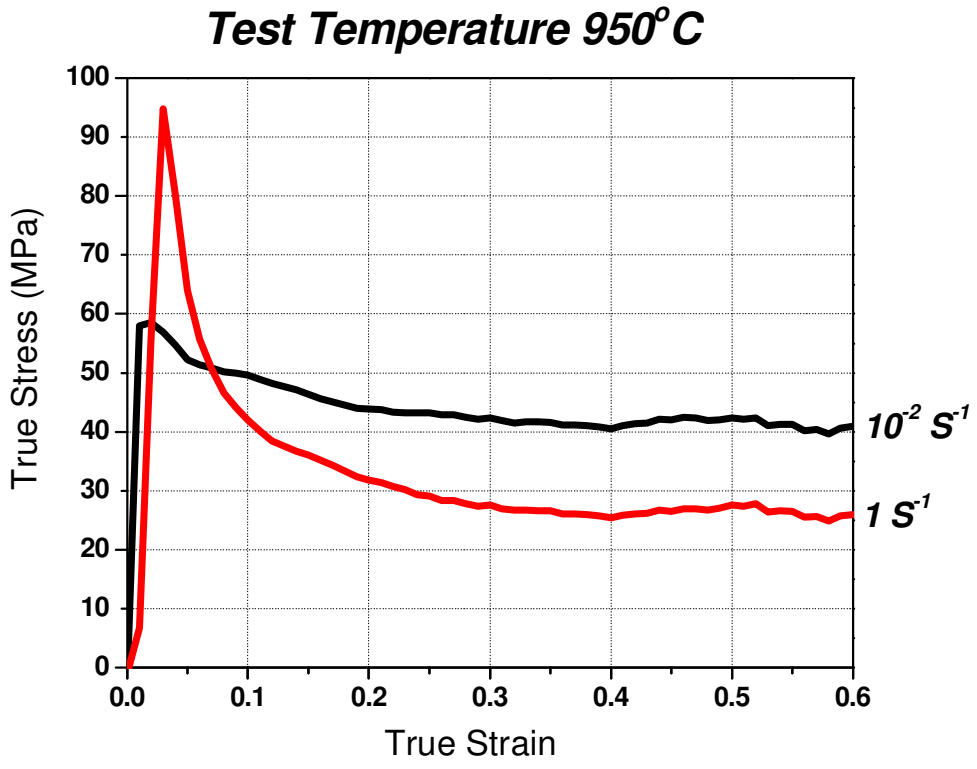

(e)

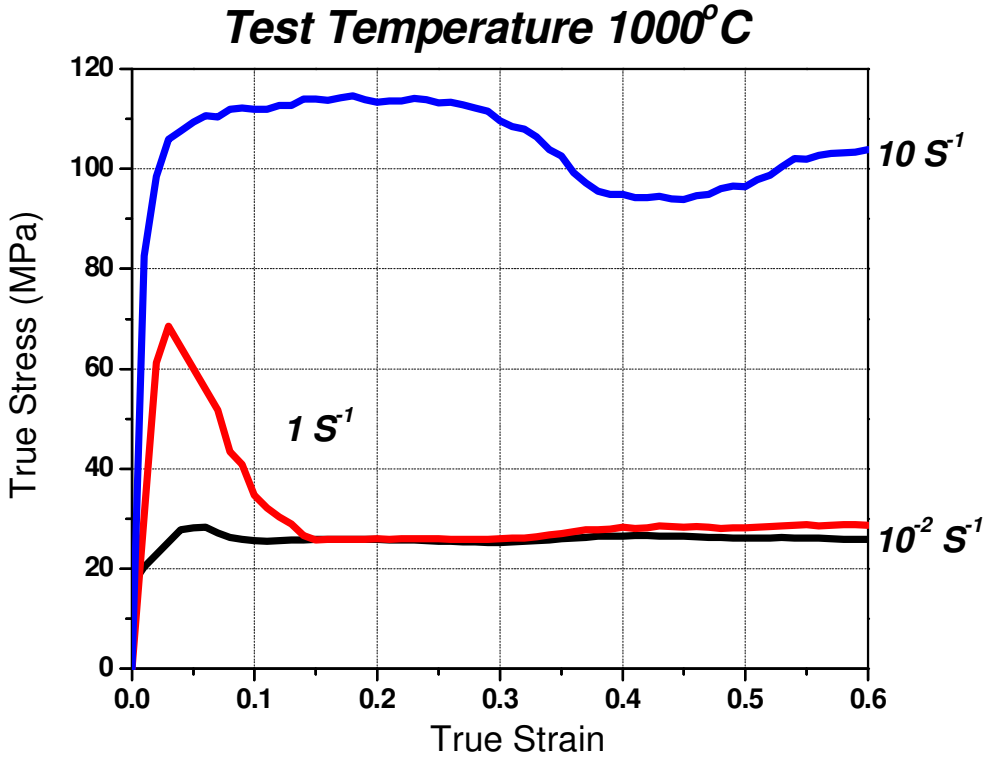

(f)

Fig. 3: Flow curves Ti64 at various strain rates for the test temperatures of (a) 750°C, (b) 800°C, (c) 850°C, (d) 900°C, (e) 950°C, and (f) 1000°C.

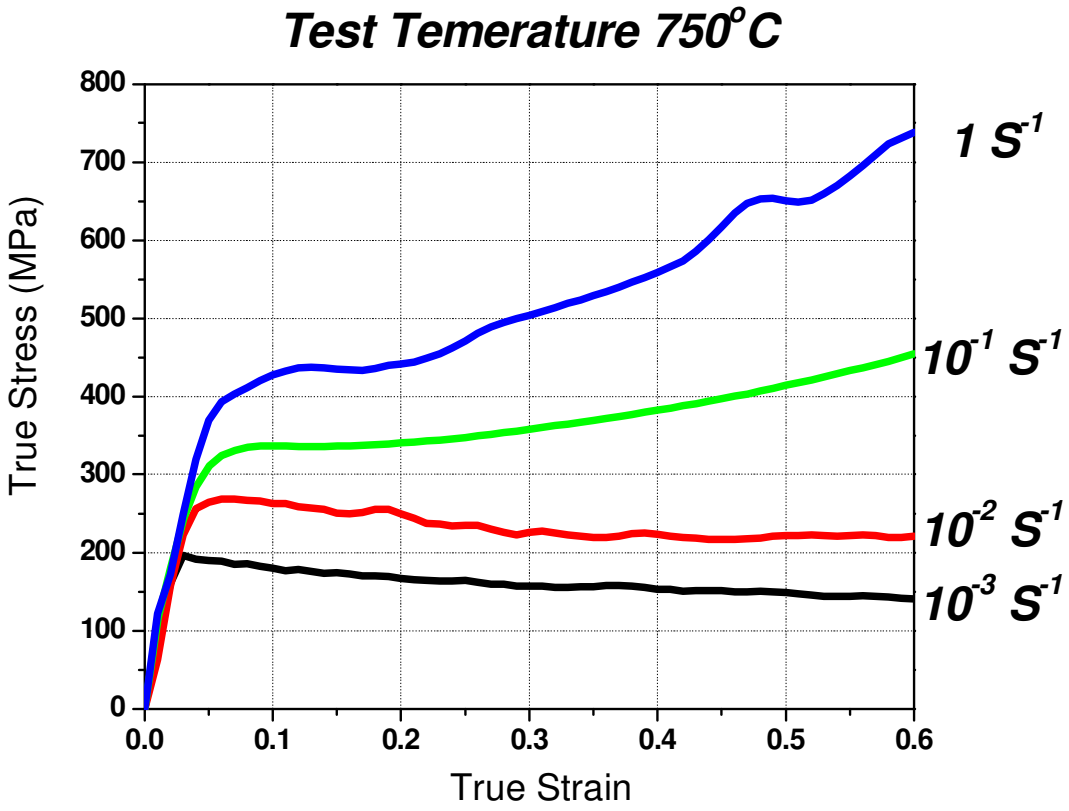
Test Temerature 750°C
True Stress (MPa)
True Strain
1 S-1
10-1 S-1
10-2 S-1
10-3 S-1

(a)

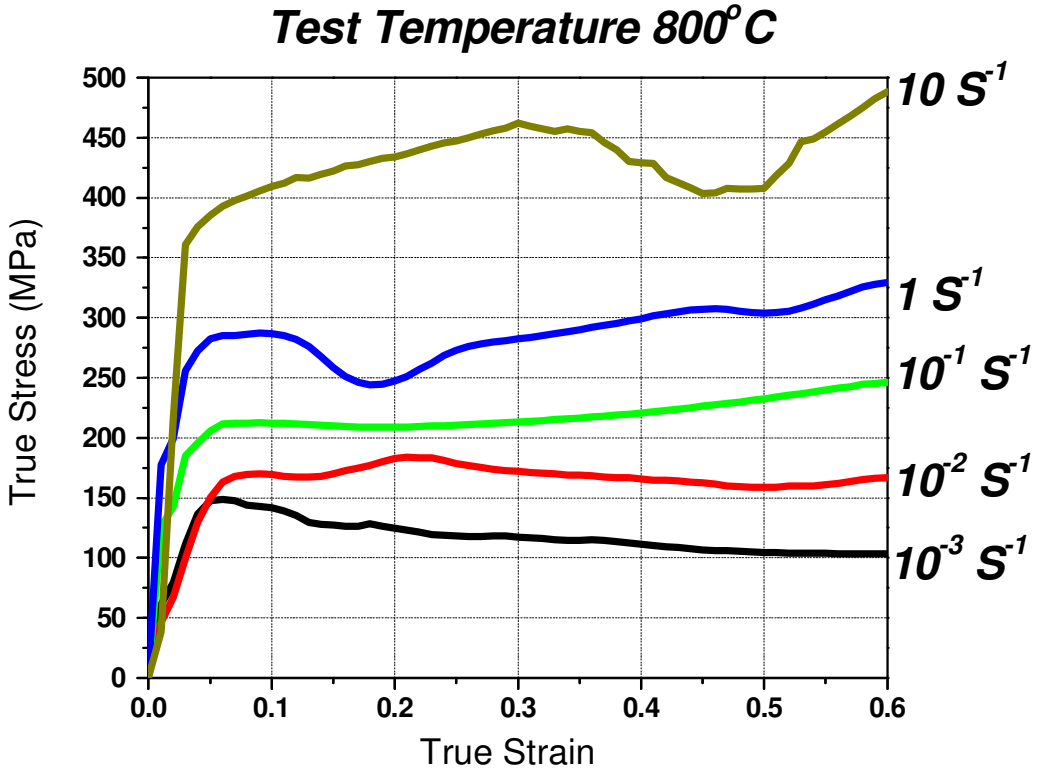
Test Temperature 800°C
True Stress (MPa)
True Strain
10 S-1
1 S-1
10-1 S-1
10-2 S-1
10-3 S-1

(b)

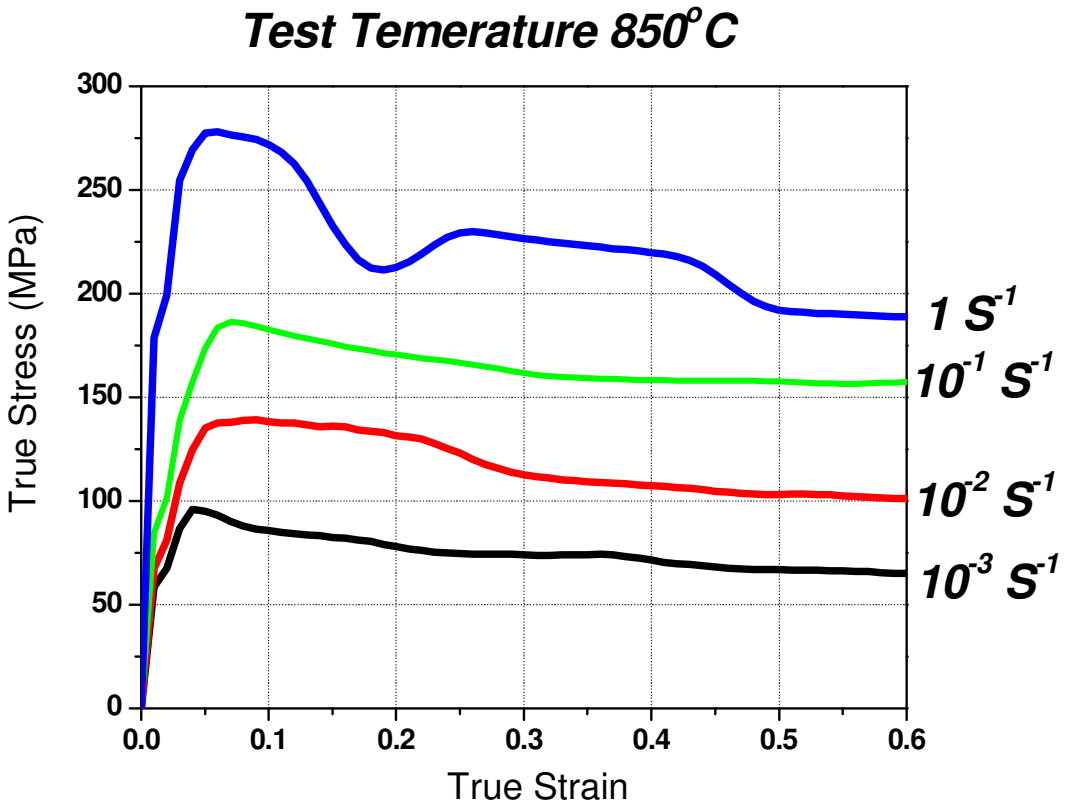
Test Temerature 850°C
True Stress (MPa)
True Strain
0
50
100
150
200
250
300
0.0
0.1
0.2
0.3
0.4
0.5
0.6
1 S-1
10-1 S-1
10-2 S-1
10-3 S-1

(c)

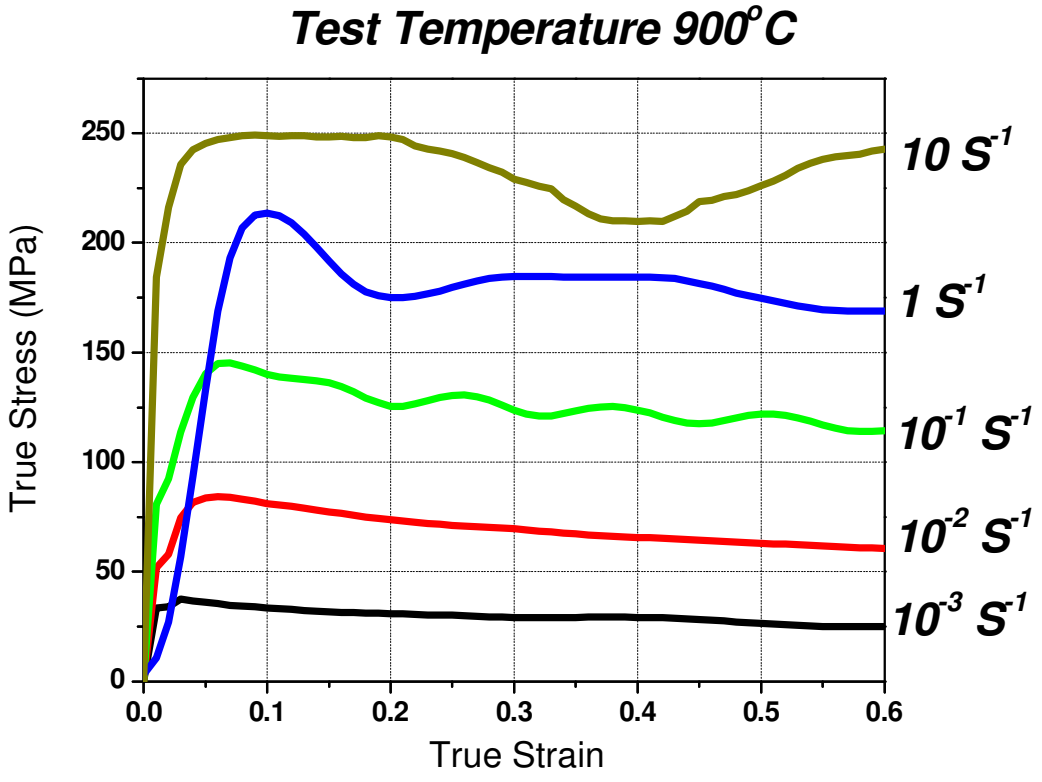
Test Temperature 900°C
True Stress (MPa)
True Strain
0
50
100
150
200
250
0.0
0.1
0.2
0.3
0.4
0.5
0.6
10 S-1
1 S-1
10-1 S-1
10-2 S-1
10-3 S-1

(d)

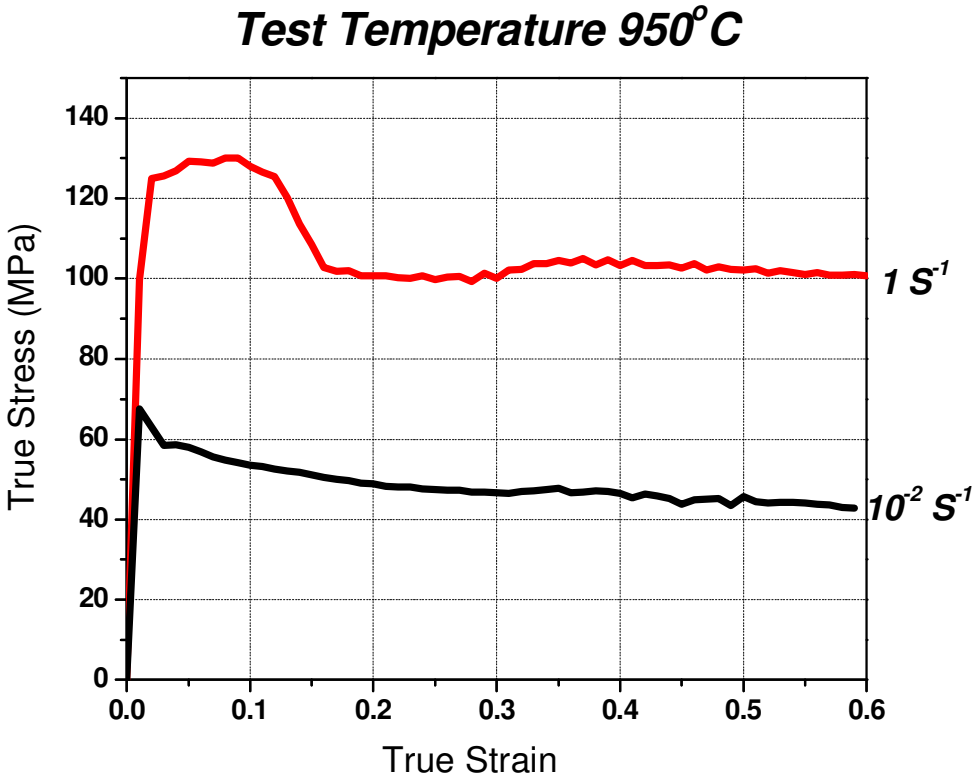

(e)

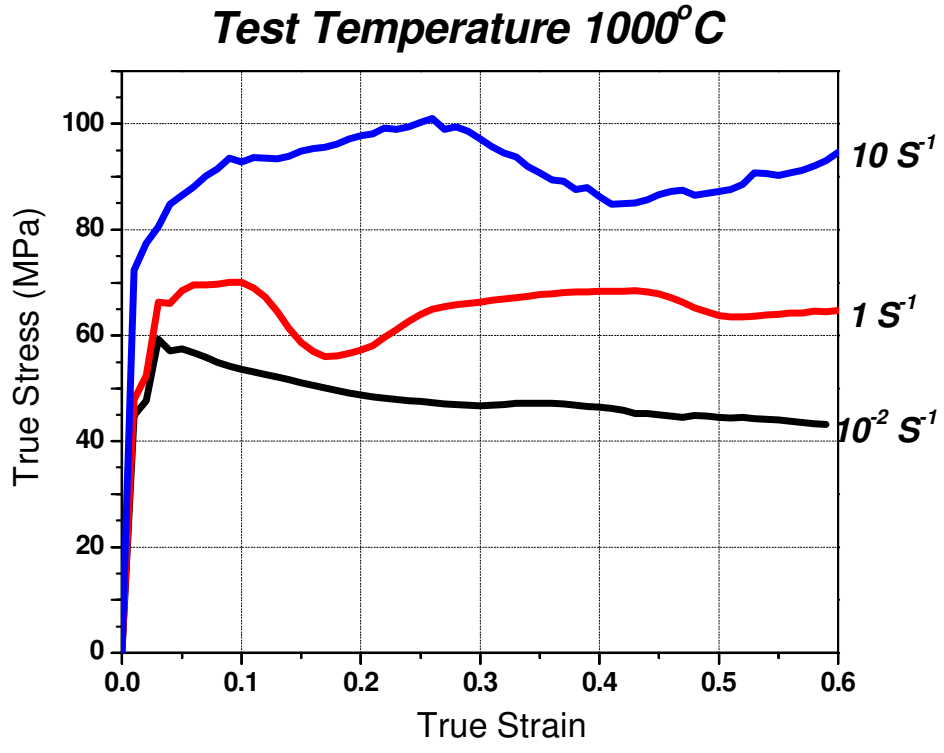

(f)

Fig. 4: Flow curves Ti64+B-Axial at various strain rates for the test temperatures of (a) 750°C, (b) 800°C, (c) 850°C, (d) 900°C, (e) 950°C, and (f) 1000°C.

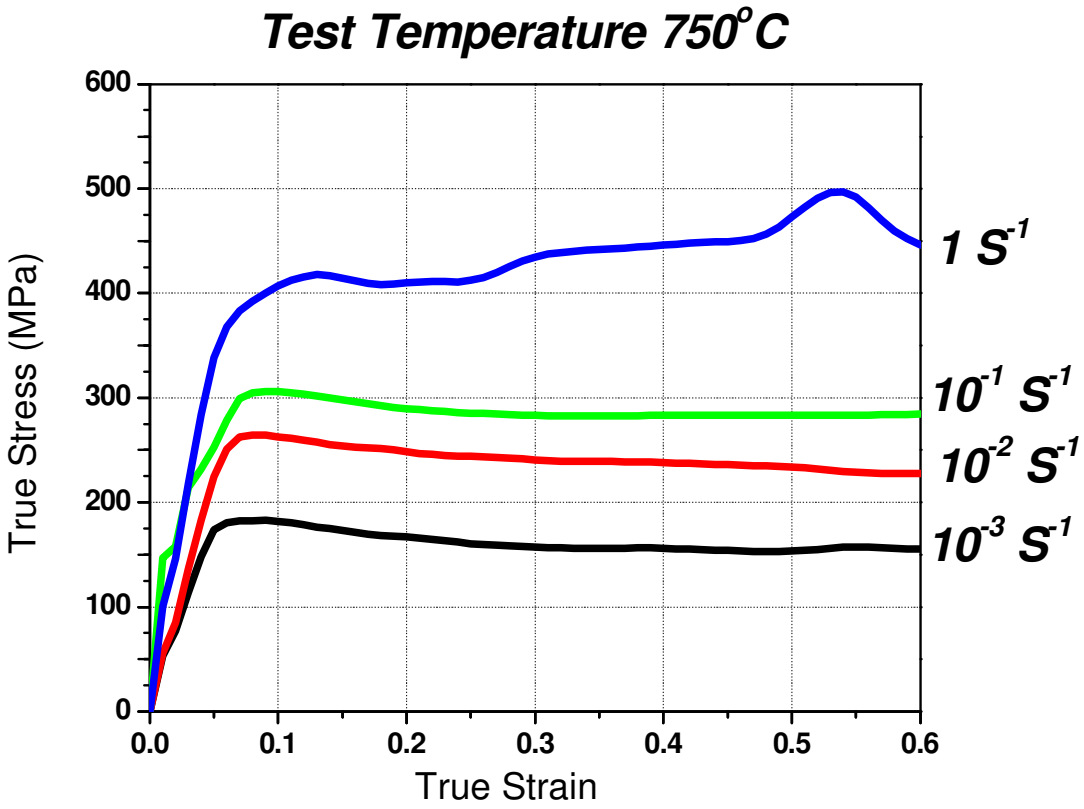
Test Temperature 750°C
True Stress (MPa)
True Strain
1 S-1
10-1 S-1
10-2 S-1
10-3 S-1

(a)

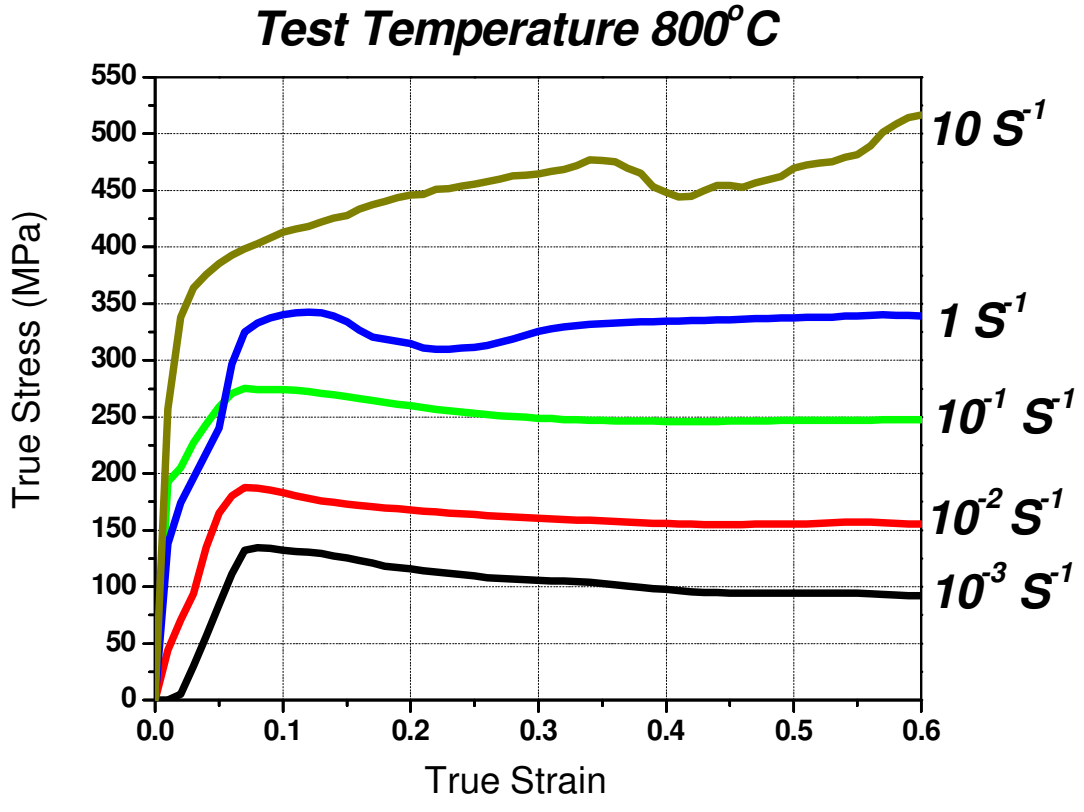
Test Temperature 800°C
True Stress (MPa)
True Strain
10 S-1
1 S-1
10-1 S-1
10-2 S-1
10-3 S-1

(b)

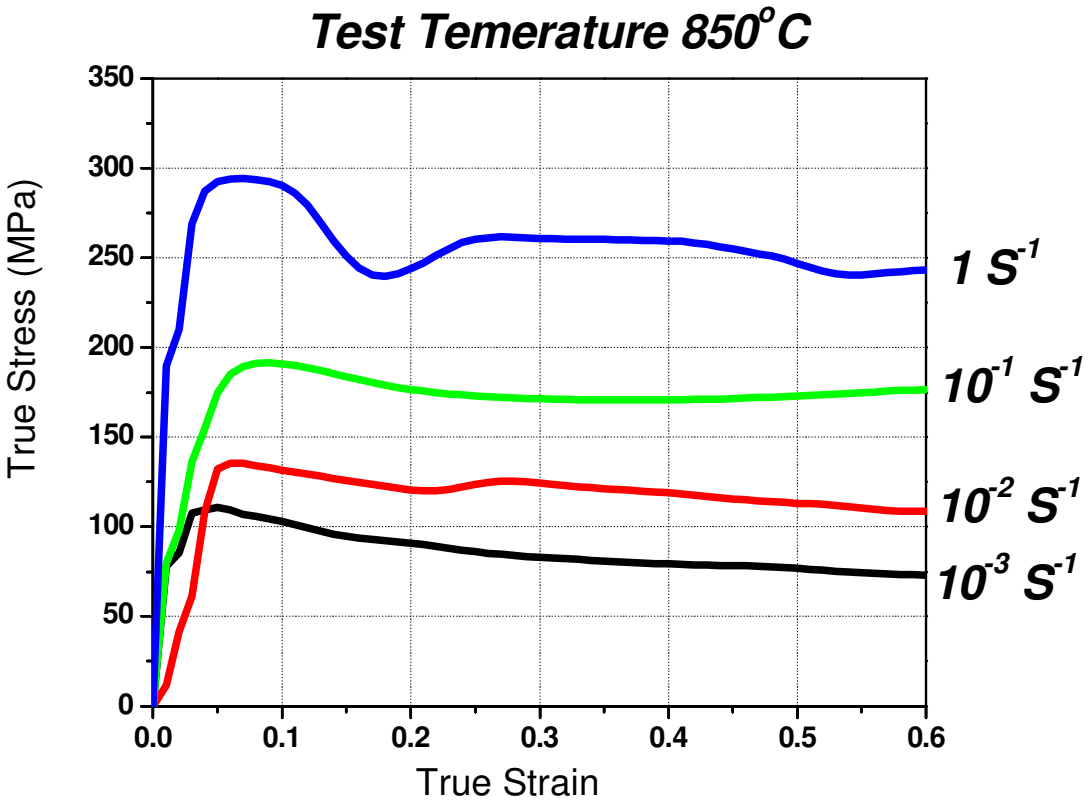
Test Temerature 850°C
True Stress (MPa)
True Strain
0
50
100
150
200
250
300
350
0.0
0.1
0.2
0.3
0.4
0.5
0.6
1 S-1
10-1 S-1
10-2 S-1
10-3 S-1

(c)

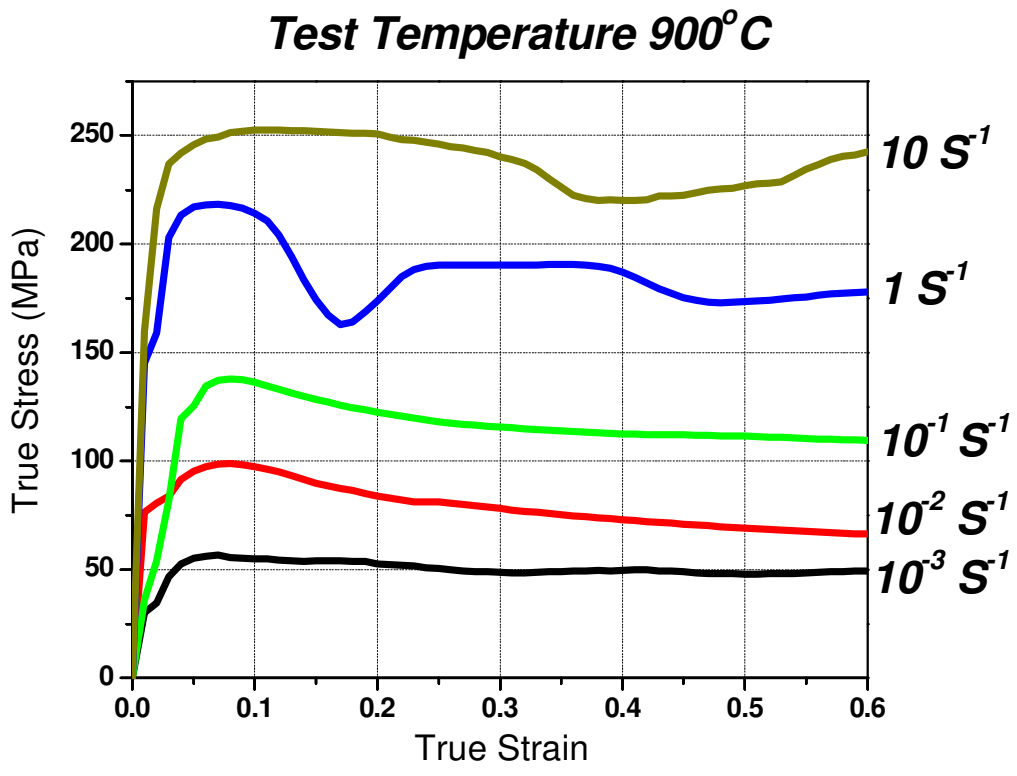
Test Temperature 900°C
True Stress (MPa)
True Strain
0
50
100
150
200
250
0.0
0.1
0.2
0.3
0.4
0.5
0.6
10 S-1
1 S-1
10-1 S-1
10-2 S-1
10-3 S-1

(d)

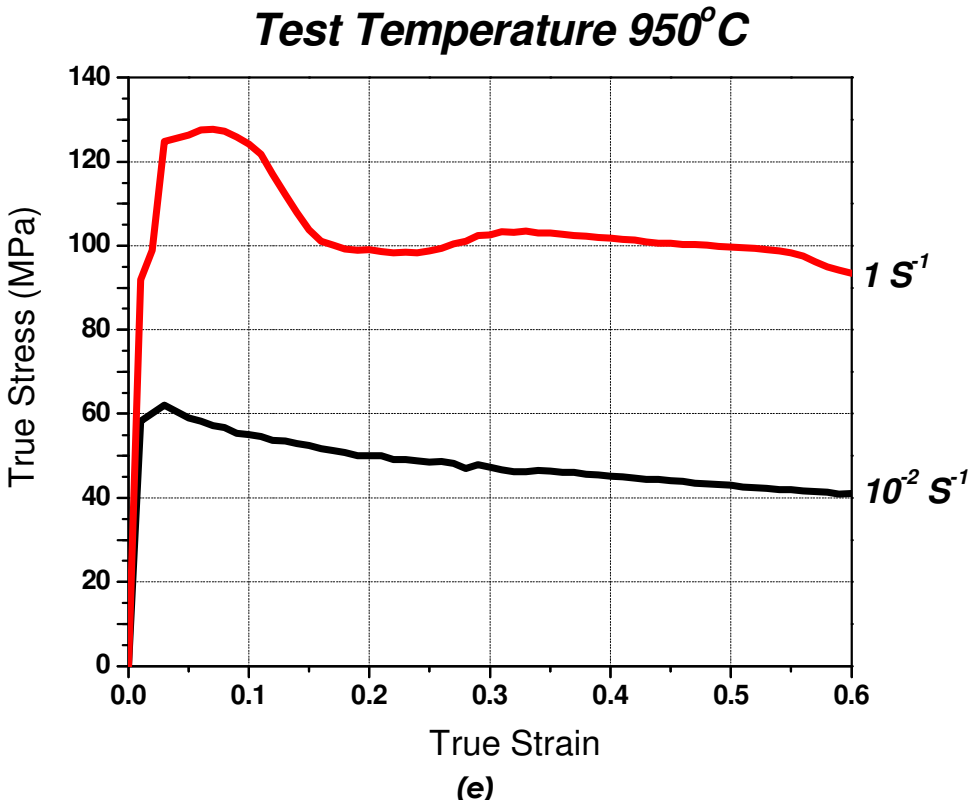

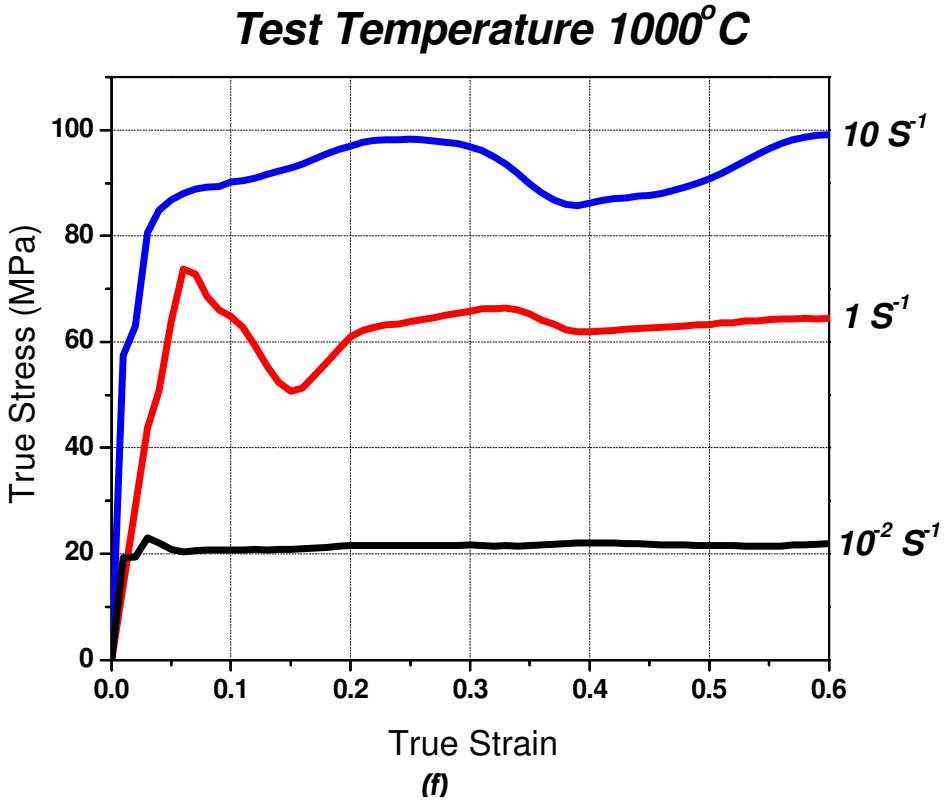

Fig. 5: Flow curves Ti64+B-Radial at various strain rates for the test temperatures of (a) 750°C, (b) 800°C, (c) 850°C, (d) 900°C, (e) 950°C, and (f) 1000°C.

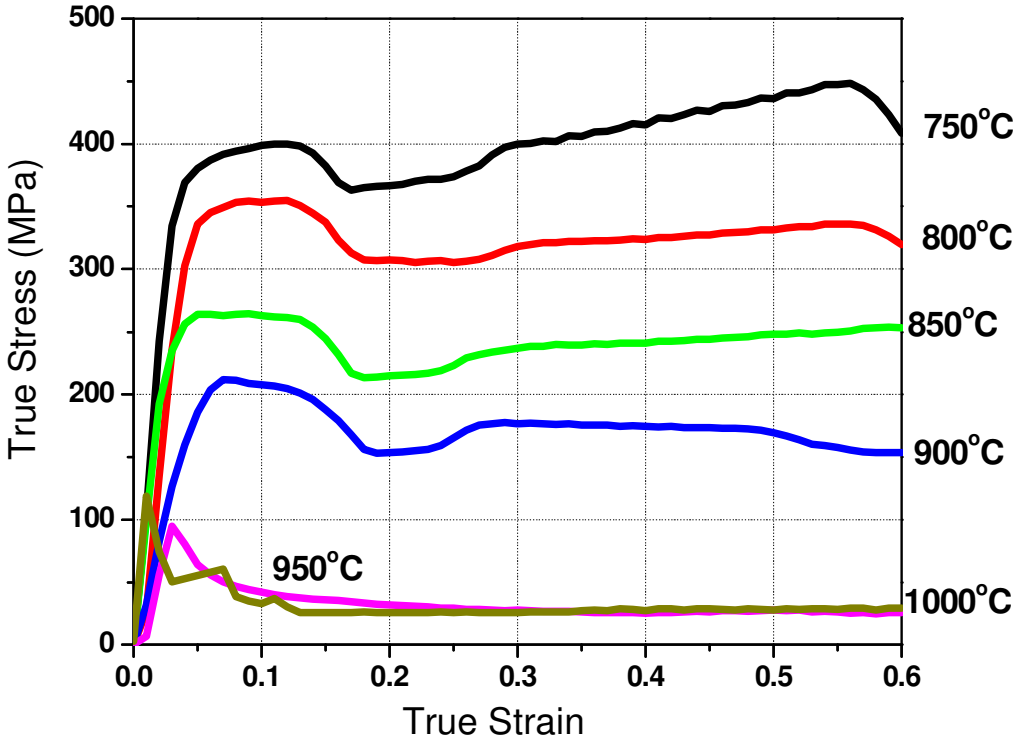
True Stress (MPa)
True Strain
750°C
800°C
850°C
900°C
950°C
1000°C

(a)

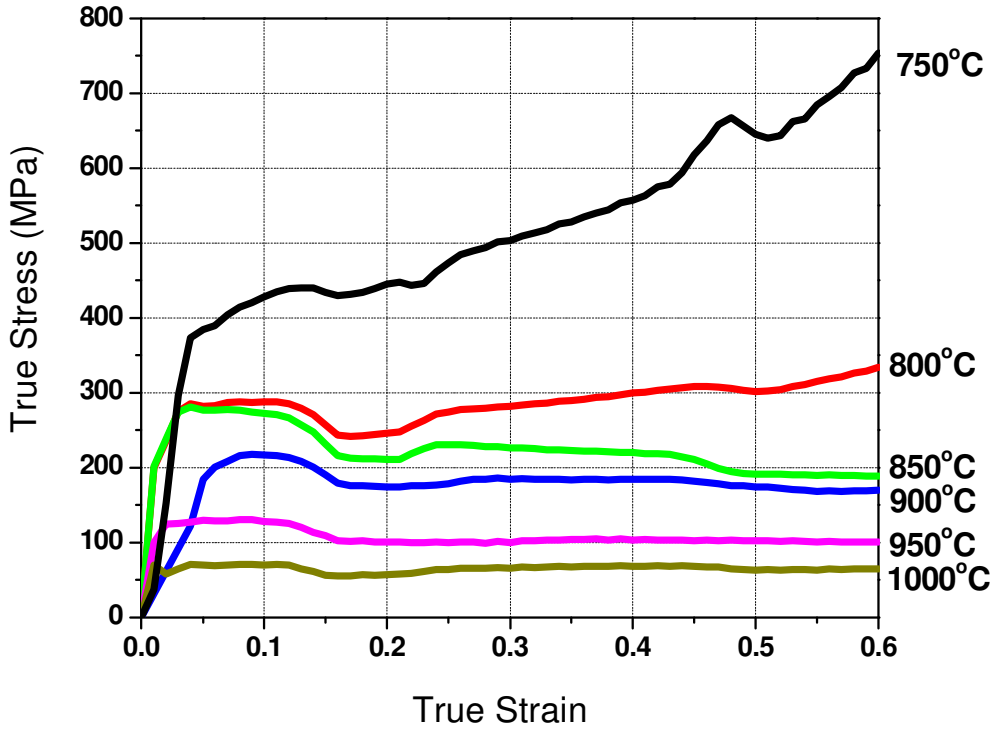
True Stress (MPa)
True Strain
750°C
800°C
850°C
900°C
950°C
1000°C

(b)

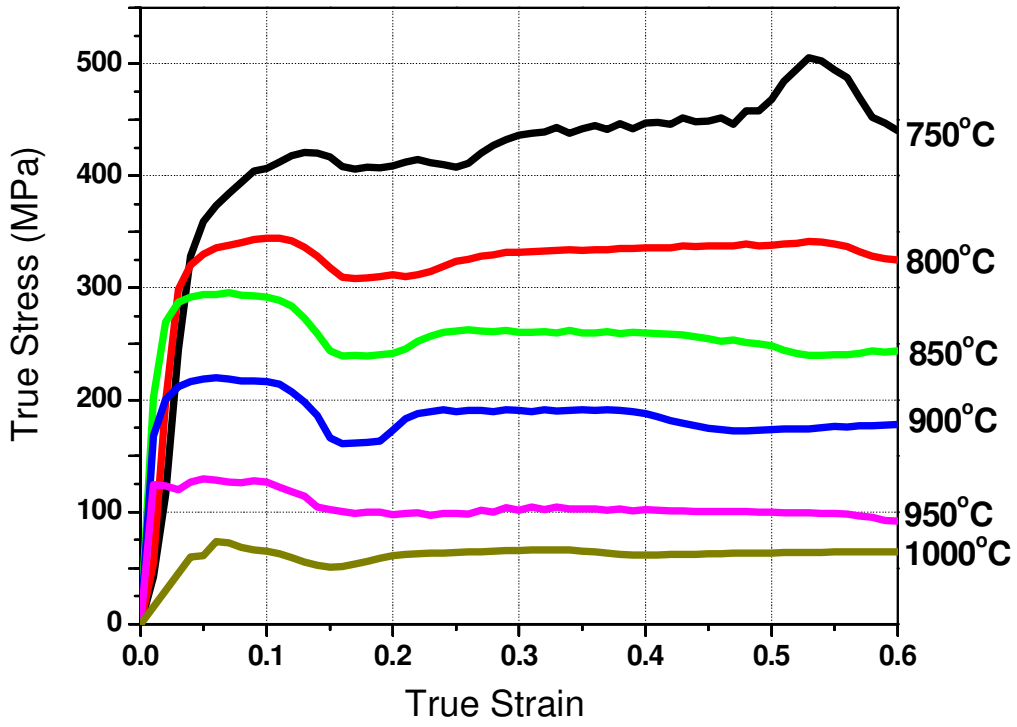

(c)

Fig. 6: Flow curves at various test temperatures for 1 S^{-1} strain rates for (a) Ti64, (b) Ti64+B-Axial, and (c) Ti64+B-Radial.

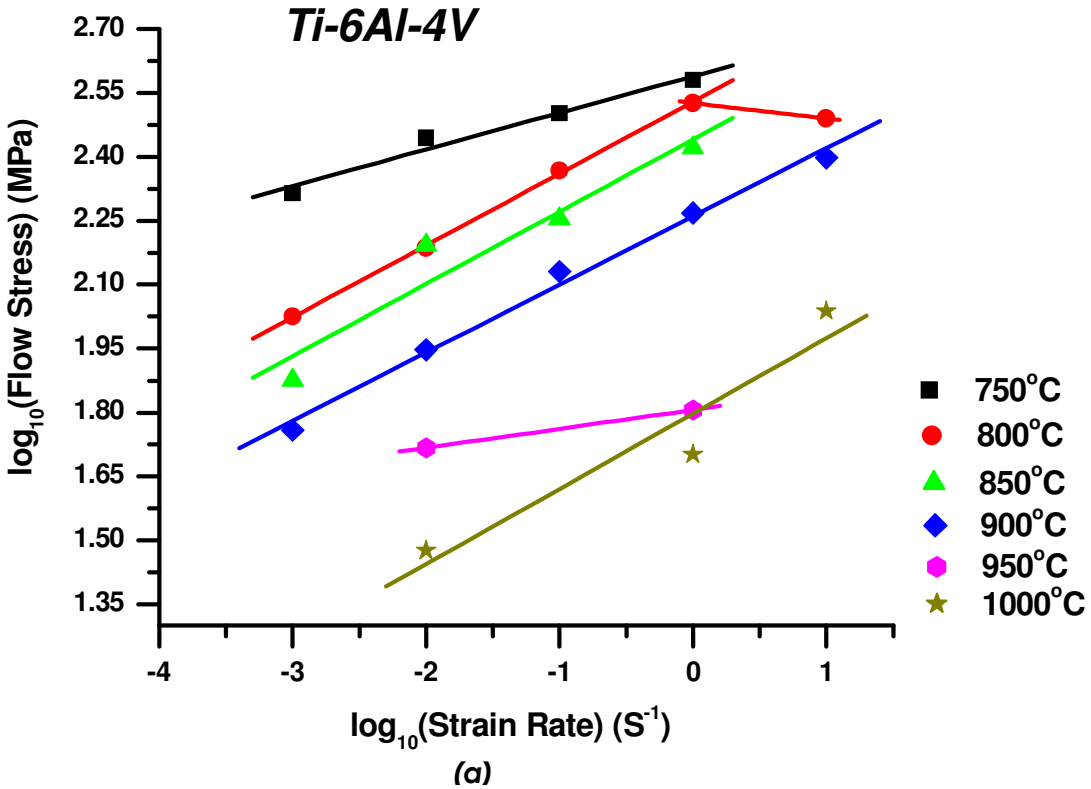

(a)

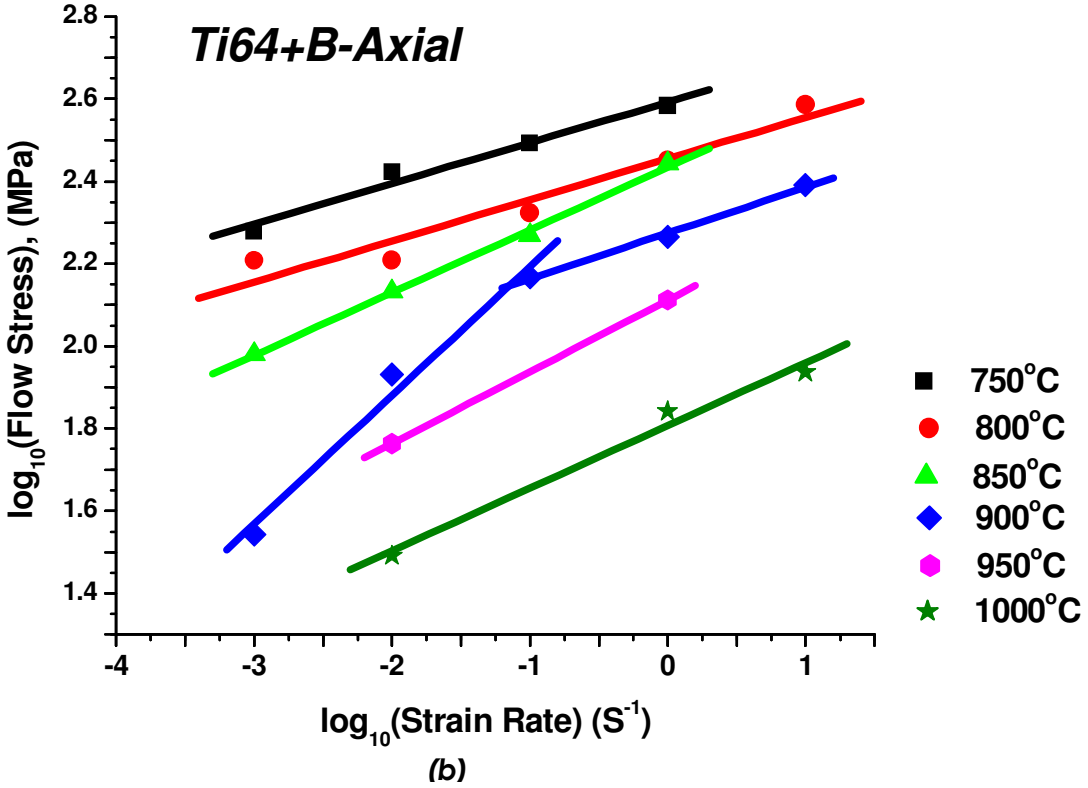

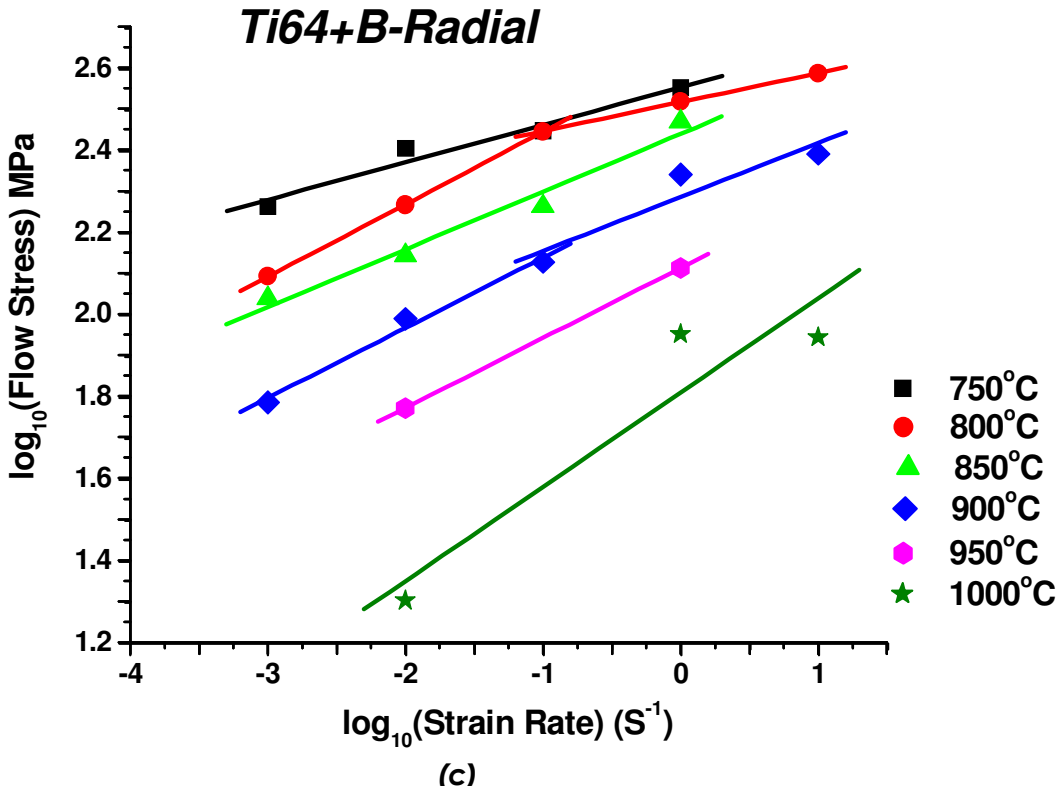

Fig. 7: $\log_{10}$(Flow Stress) vs. $\log_{10}$(Strain Rate) plots for (a) Ti64, (b) Ti64+B-Axial, and (c) Ti64+B-Radial.

Table 2: Details of Strain rate sensitivity calculation by linear fitting of $\log_{10}$(Flow Stress) vs. $\log_{10}$(Strain Rate) plots. Error, regression coefficient and standard deviation values signify the quality of fitting.

Material	Temp.	Strain Rate	Strain rate sensitivity (m)	Error in linear fitting	Regression Coefficient (R)	Standard Deviation	Avg. m
Ti64	750	10^{-3} to 1	0.0857	0.01061	0.98503	0.02371	
	800	10^{-3} to 1	0.16844	0.00316	0.99965	0.00706	0.1023
		1 to 10	0.03631		1		
	850	10^{-3} to 1	0.16951	0.03496	0.96	0.07817	
	900	10^{-3} to 10	0.1598	0.00824	0.99603	0.02607	
	950	10^{-2} and 1	0.04438		1		
	1000	10^{-2}, 1 and 10	0.17668	0.05541	0.95418	0.1197	
Ti64+B-Axial	750	10^{-3} to 1	0.09869	0.01085	0.98813	0.02426	
	800	10^{-3} to 10	0.0999	0.01522	0.96691	0.04812	
	850	10^{-3} to 1	0.15223	0.00527	0.9988	0.01179	
	900	10^{-3} to 10^{-1}	0.31224	0.0439	0.99026	0.06208	0.2117
		10^{-1} to 10	0.11125	0.00768	0.99763	0.01086	
	950		0.17418		1		
	1000	10^{-3} to 10	0.15224	0.01973	0.99171	0.04262	
Ti64+B-Radial	750	10^{-3} to 1	0.09121	0.01289	0.9806	0.02882	
	800	10^{-3} to 10^{-1}	0.17667	0.00114	0.99998	0.00161	0.1237
		10^{-1} to 10	0.07082	0.00177	0.99969	0.0025	
	850	10^{-3} to 1	0.14076	0.01698	0.98576	0.03796	
	900	10^{-3} to 10^{-1}	0.17101	0.01884	0.99399	0.02664	0.1514
		10^{-1} to 10	0.13196	0.04705	0.94192	0.06654	
	950		0.17066		1		
	1000	10^{-2}, 1 and 10	0.3251	0.0825	0.9412	0.17822	

Table 3: Strain rate sensitivity values of different materials at various temperature-strain rate combinations.

Material	Temperature	Strain Rate Sensitivity (m)				
		Strain Rate				
		$10^{-3}\ S^{-1}$	$10^{-2}\ S^{-1}$	$10^{-1}\ S^{-1}$	$1\ S^{-1}$	10 S-1
Ti64	750	0.09869	0.09869	0.09869	0.09869	
	800	0.0999	0.0999	0.0999	0.0999	0.0999
	850	0.15223	0.15223	0.15223	0.15223	
	900	0.31224	0.31224	0.221747	0.11125	0.11125
	950		0.17418		0.17418	
	1000		0.15224		0.15224	0.15224
Ti64+B-Longitudinal	750	0.09121	0.09121	0.09121	0.09121	
	800	0.17667	0.17667	0.123745	0.07082	0.07082
	850	0.14076	0.14076	0.14076	0.14076	
	900	0.17101	0.17101	0.151485	0.13196	0.13196
	950		0.17066		0.17066	
	1000		0.3251		0.3251	0.3251
Ti64+B-Radial	750	0.0857	0.0857	0.0857	0.0857	
	800	0.16844	0.16844	0.16844	0.123745	0.03631
	850	0.16951	0.16951	0.16951	0.16951	
	900	0.1598	0.1598	0.1598	0.1598	0.1598
	950		0.04438		0.04438	
	1000		0.17668		0.17668	0.17668

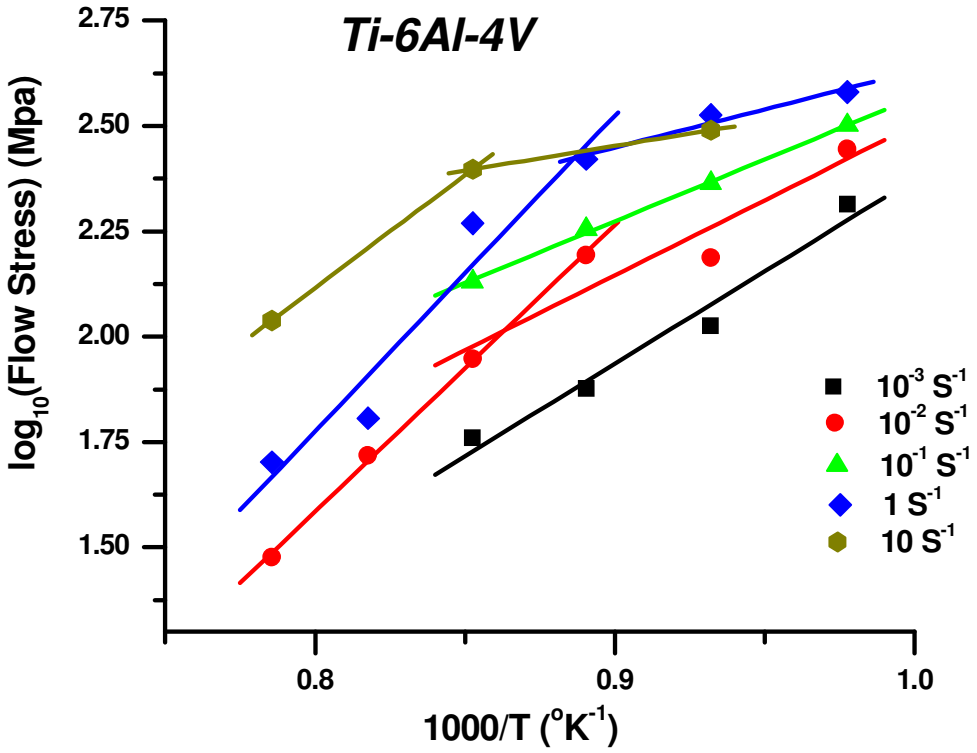
Ti-6Al-4V
log10(Flow Stress) (Mpa)
2.75
2.50
2.25
2.00
1.75
1.50
0.8
0.9
1.0
1000/T (°K-1)
10-3 S-1
10-2 S-1
10-1 S-1
1 S-1
10 S-1

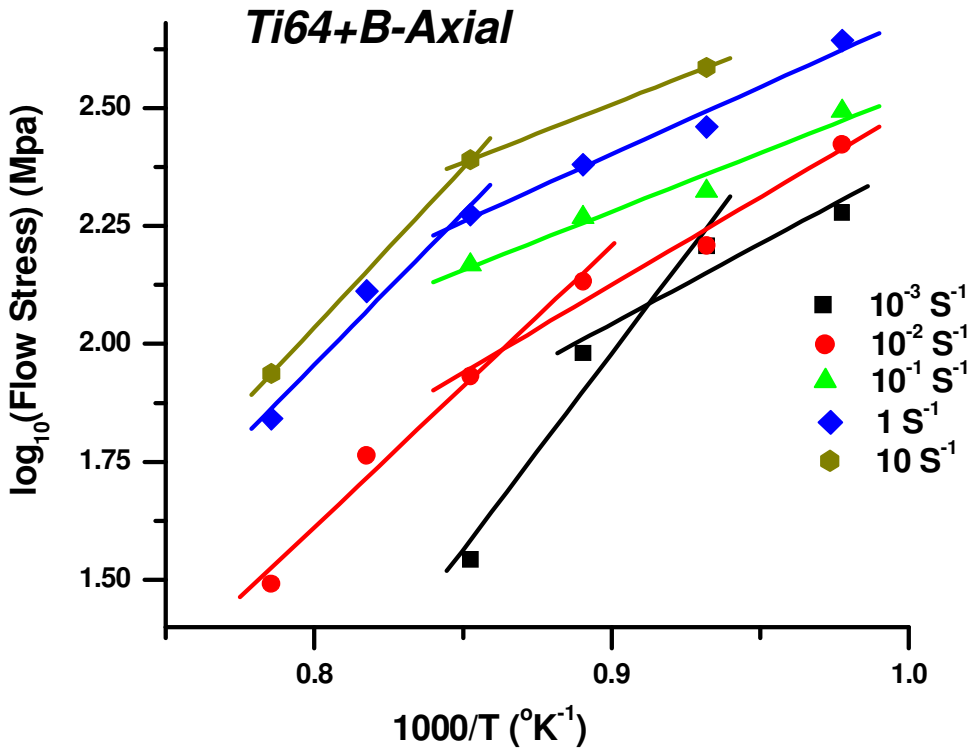
Ti64+B-Axial
log10(Flow Stress) (Mpa)
2.50
2.25
2.00
1.75
1.50
0.8
0.9
1.0
1000/T (°K-1)
10-3 S-1
10-2 S-1
10-1 S-1
1 S-1
10 S-1

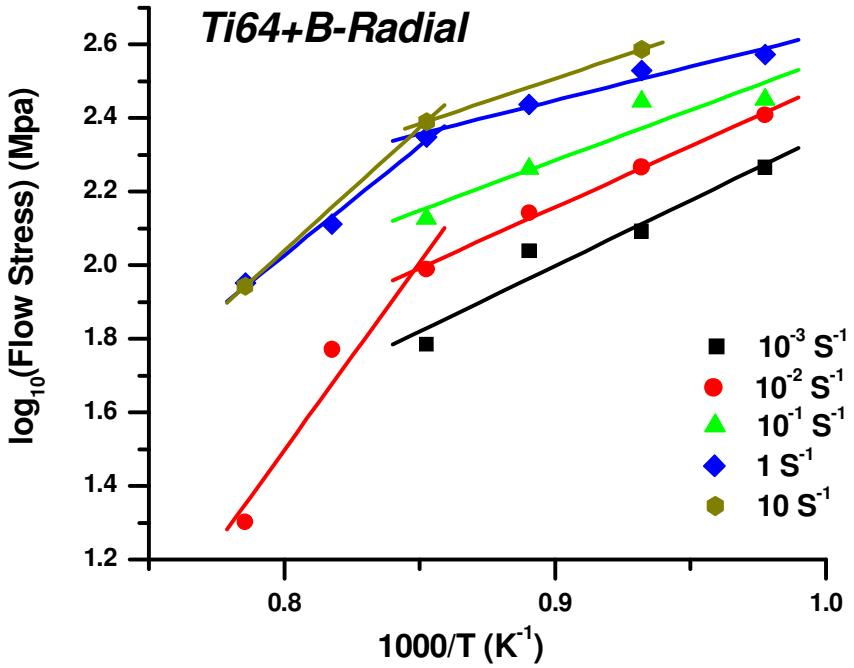

Fig. 8: Activation Energy determination from $\log_{10}$(Flow Stress) vs. 1000/T plots for (a) Ti64, (b) Ti64+B-Axial, and (c) Ti64+B-Radial.

Table 4: Details of activation energy calculation by linear fitting of $\log_{10}$(Flow Stress) vs. $\log_{10}$(Strain Rate) plots. Error, regression coefficient and standard deviation values signify the quality of fitting.

Material	Strain Rate	Temp.	Slope of log(σ) vs 1000/T curve	Error in linear fitting	Regression Coefficient (R)	Standard Deviation
Ti64	10^{-3} S^{-1}	750°C to 900°C	4.3847	0.55232	0.9845	0.05148
	10^{-2} S^{-1}	750°C to 850°C	3.56215	0.8807	0.94396	0.08209
		850°C to 1000°C	6.80094	0.16396	0.99942	0.01283
	10^{-1} S^{-1}	750°C to 900°C	2.93311	0.0774	0.9993	0.00721
	1	750°C to 850°C	1.81614	0.38545	0.97821	0.02373
		850°C to 1000°C	7.49339	1.35421	0.96866	0.10627
	10	800°C to 900°C	1.168		1	
		900°C to 1000°C	5.35171		1	
Ti64+B-Axial	10^{-3} S^{-1}	750°C to 850°C	3.39094	1.13055	0.94866	0.06961
		800°C to 900°C	8.32094	1.74106	0.9788	0.09785
	10^{-2} S^{-1}	750°C to 900°C	3.72135	0.44721	0.98586	0.04168
		850°C to 1000°C	5.95384	0.55008	0.99157	0.04304
	10^{-1} S^{-1}	750°C to 900°C	2.48563	0.32829	0.983	0.0306
	1	750°C to 900°C	2.86023	0.30382	0.9889	0.02832
		900°C to 1000°C	6.43154	1.08153	0.98615	0.05123
	10	800°C to 900°C	2.46661		1	
		900°C to 1000°C	6.7675		1	

Ti64+B-Radial	10^{-3} S^{-1}	750°C to 900°C	3.56723	0.68084	0.96545	0.06346
	10^{-2} S^{-1}	750°C to 900°C	3.30979	0.16563	0.99751	0.01544
		900°C to 1000°C	10.19622	2.41557	0.97307	0.11442
	10^{-1} S^{-1}	750°C to 900°C	2.73646	0.68893	0.94207	0.06421
	1	750°C to 900°C	1.82652	0.2399	0.98318	0.02236
		900°C to 1000°C	5.93052	0.50975	0.99633	0.02415
	10	800°C to 900°C	2.46593		1	
		900°C to 1000°C	6.67467		1	

Table 5: Strain rate sensitivity values of different materials at various temperature-strain rate combinations.

Material	***Temperature***	***Activation Energy (Q), KJ/Mole***				
		Strain Rate				
		10^{-3} S^{-1}	***10^{-2} S^{-1}***	***10^{-1} S^{-1}***	***1 S^{-1}***	***10 S^{-1}***
Ti64	750	425.41	795.87	655.37	405.80	
	800	216.44	404.93	333.44	206.46	615.97
	850	215.08	402.27	331.34	205.15	
	900	228.14	814.95	351.47	897.93	641.29
	950					
	1000		737.09		812.14	580.02
Ti64+B-Longitudinal	750	285.69	722.01	482.29	554.97	
	800	282.23	713.26	476.44	548.25	472.80
	850	454.48	608.47	312.66	359.78	
	900	221.58	296.66	152.44	492.31	794.7

	950		654.50		707.06	
	1000		748.83		808.96	851.22
Ti64+B-Radial	750	748.91	694.86	574.50	383.46	
	800	386.64	358.74	518.25	493.87	666.75
	850	485.28	450.26	372.26	248.48	
	900	399.44	756.16	562.81	562.81	663.2
	950				665.43	
	1000		600.57		349.31	393.15

Table 6: Strain rate sensitivity and activation energy of Ti64 as reported by previous researchers.

	Material	*Working region*	*Deformation condition*	*Deformation mechanism*	*Strain Rate Sensitivity (m=1/n)*	*Activation Energy (Q) kJ/mole*
Seshacharyulu et al [3, 4, 5]	ELI Grade Ti-6Al-4V with Widmanstätten type microstructure	(α+β)	T = 850°–950°C; $\dot{\varepsilon}$ = 0.001–0.1 S^{-1}	Globularization of lamellae	0.217	453
		Beta	T = 980°–1100°C $\dot{\varepsilon}$ = 0.001 – 100 S^{-1}	Large grained Super-plasticity (LGSP)	0.33	
	Commercial Ti-6Al-4V with equiaxed α-β microstructure	(α+β)	T = 750°–1000°C; $\dot{\varepsilon}$ = 0.0003–100 S^{-1}	Fine-grained super-plasticity	0.278	330
		Beta	T = 1000° - 1100°C; $\dot{\varepsilon}$ = 0.0003–100 S^{-1}	Dynamic recrystallization	0.278	210
	Commercial Ti–6Al–4V with lamellar starting structure	(α+β)	T = 800° – 975°C; $\dot{\varepsilon}$ = 3×10^{-4}–10^{-2} S^{-1}	Globularization of lamellae	0.278	455
		Beta	T = 1000° – 1100°C; $\dot{\varepsilon}$ = 10^{-3} – 10^{-1} S^{-1}	Dynamic recrystallization	0.278	172±10
Semiatin et al [6]	Ti–6Al–4V with a colony alpha microstructure	(α+β)	T = 815° – 955°C; $\dot{\varepsilon}$ = 0.001 -10 S^{-1}	Globularization of lamellae	0.25	

Table 7: The correlation between Zener-Holloman parameter and flow stress for Ti64.

Strain Rate (ε̇)	Temperature	Z = ε̇*exp(Q/RT)	log(Z)	Flow Stress	log(Flow Stress)
0.001	750	4.35552E+18	18.639	205.93	2.314
	800	31367596.84	7.496	105.98	2.025
	850	9249581.286	6.966	75.24	1.876
	900	13202985.27	7.121	57.38	1.759
0.01	750	3.04072E+38	38.483	278.2	2.444
	800	4.34009E+17	17.637	153.5	2.186
	850	1.32393E+25	25.122	156.18	2.194
	900	1.42084E+34	34.153	88.52	1.947
	950			52.2	
	1000	1.34873E+28	28.130	29.96	1.477
0.1	750	2.16899E+32	32.336	317.48	2.502
	800	1.48087E+15	15.171	230.87	2.363
	850	2.25549E+14	14.353	179.6	2.254
	900	3.90659E+14	14.592	135	2.130
1	750	4.38078E+20	20.642	414.72	2.618
	800	1.70024E+28	28.231	254.4	2.406
	850	2.31893E+24	24.365	175.15	2.243
	900	6.81832E+39	39.834	183.34	2.263
	950			64.03	1.806
	1000	1.57664E+33	33.198	50.34	1.702
10	800	7.44905E+30	30.872	308.9	2.490
	900	2.80994E+29	29.449	249.47	2.397
	1000	5.12149E+24	24.709	109.3	2.397

Table 8: The correlation between Zener-Holloman parameter and flow stress for Ti64+B-Axial.

Strain Rate (ἐ)	Temperature	Z = ἐ*exp(Q/RT)	log(Z)	Flow Stress	log(Flow Stress)
0.001	750	3.40407E+11	11.532	189.88	2.278
	800	48644665065	10.687	161.4	2.208
	850	1.14592E+18	18.059	95.64	1.981
	900	6755532.101	6.830	34.934	1.543
0.01	750	5.32096E+34	34.726	264.94	2.423
	800	3.89296E+32	32.590	161.6	2.208
	850	1.56517E+26	26.195	135.65	2.132
	900	1.44655E+11	11.160	85.41	1.932
	950	7.04185E+25	25.848	58.01	1.764
	1000	4.07211E+28	28.610	31.02	1.492
0.1	750	3.40656E+23	23.532	311	2.493
	800	1.27482E+22	22.105	210.63	2.324
	850	3.07375E+13	13.488	185.48	2.268
	900	578753.2895	5.762	147.14	2.168
1	750	1.69543E+28	28.229	439.56	2.643
	800	3.87213E+26	26.588	288.2	2.460
	850	4.68877E+16	16.671	240	2.380
	900	2.98332E+35	35.475	188	2.274
	950	1.21342E+30	30.084	129.38	2.112
	1000	1.16881E+33	33.068	69.46	
10	800	8.49032E+23	23.929	385.66	2.586
	900	1.79565E+36	36.254	245.6	2.390
	1000	3.0538E+33	33.485	86.5	1.937

Table 9: The correlation between Zener-Holloman parameter and flow stress for Ti64+B-Radial.

Temp. (ŧ)	Strain Rate (ἐ)	Z = ἐ*exp(Q/RT)	log(Z)	Flow Stress	log(Flow Stress)
0.001	750	1.24249E+35	35.094	184.22	2.265
	800	5.62997E+15	15.751	123.42	2.091
	850	3.06429E+19	19.486	109.35	2.039
	900	5.24598E+14	14.720	60.88	1.784
0.01	750	2.21294E+33	33.345	255.63	2.408
	800	2.49728E+15	15.397	184.54	2.266
	850	7.3049E+18	18.864	138.88	2.143
	900	3.50367E+31	31.545	97.3	1.988
	950	0.01	-2.000	59.01	1.771
	1000	3.54336E+22	22.549	20.02	1.301
0.1	750	1.66993E+28	28.223	281.96	2.450
	800	1.35853E+24	24.133	278.44	2.445
	850	1.77559E+16	16.249	182.79	2.262
	900	9.27243E+23	23.967	133.82	2.127
1	750	3.20035E+19	19.505	374	2.573
	800	8.92762E+23	23.951	338	2.529
	850	3.26416E+11	11.514	273.51	2.437
	900	9.27243E+24	24.967	222.91	2.348
	950	2.05464E+28	28.313	129.5	2.112
	1000	1.89975E+14	14.279	89.49	
10	800	2.16137E+33	33.335	385.8	2.586
	900	2.63428E+30	30.421	245.72	2.390
	1000	1.17689E+17	17.071	87.79	1.943

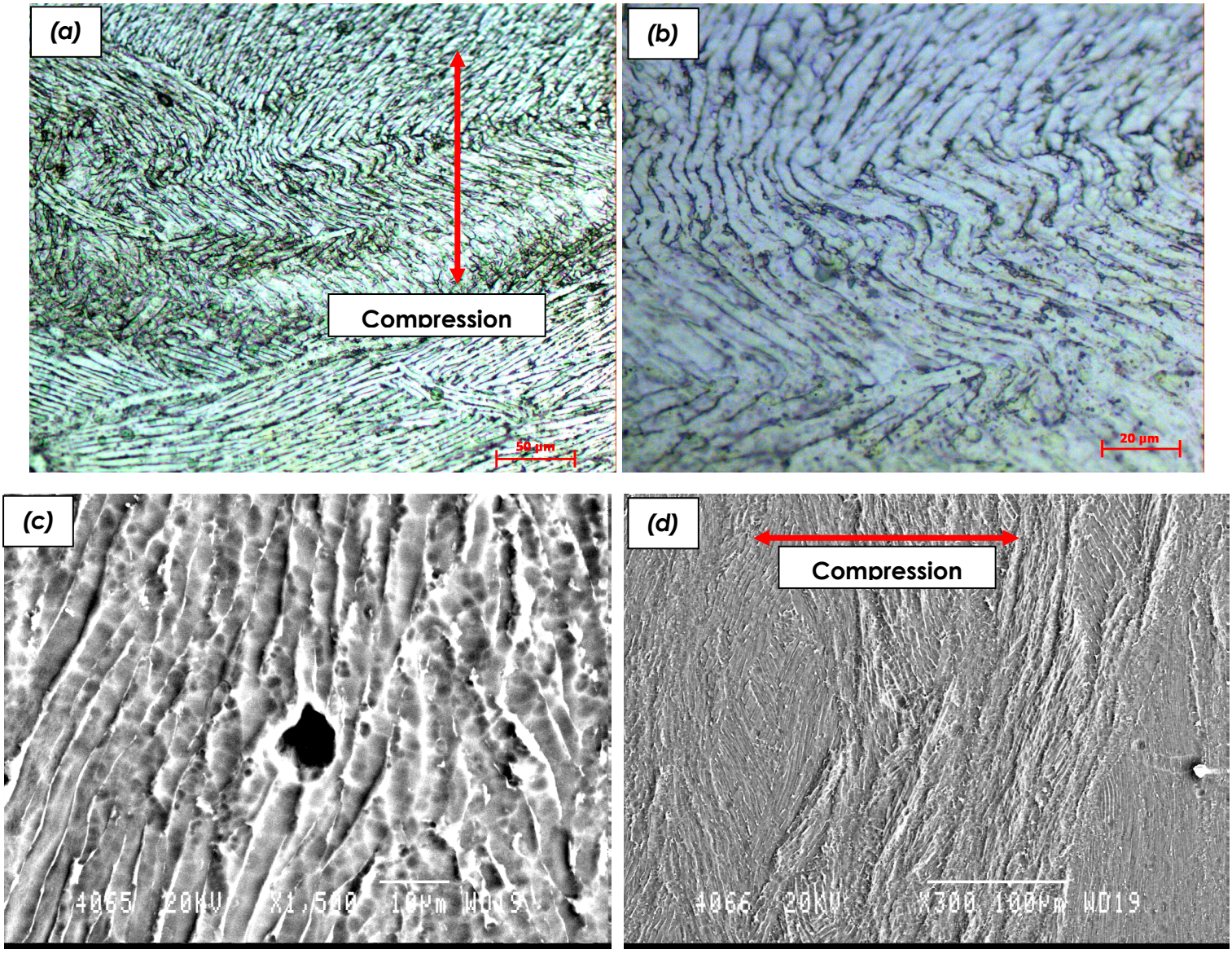

Fig. 9: SEM micrographs of hot compressed Ti64 samples (Working condition: temperature 750°C, strain rate 10^{-3} S^{-1})

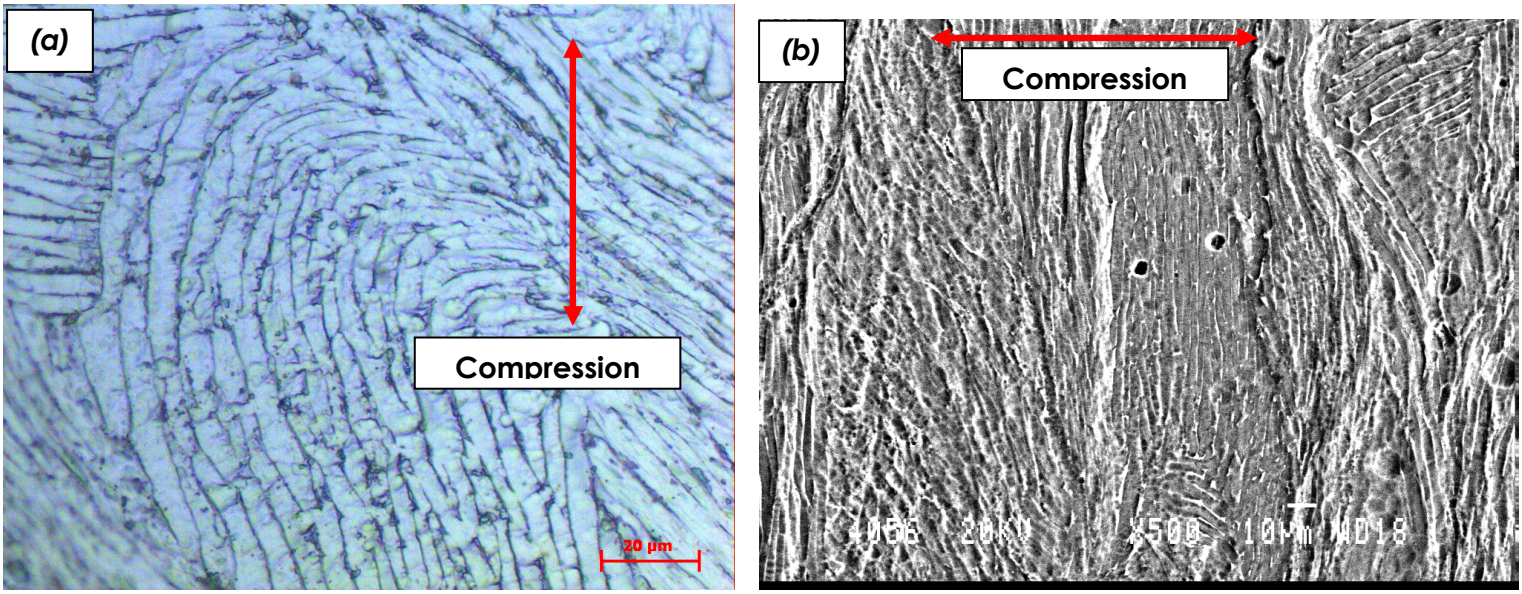

Fig. 10: SEM micrographs of hot compressed Ti64 samples (Working condition: temperature 750°C, strain rate 10^{-2} S^{-1})

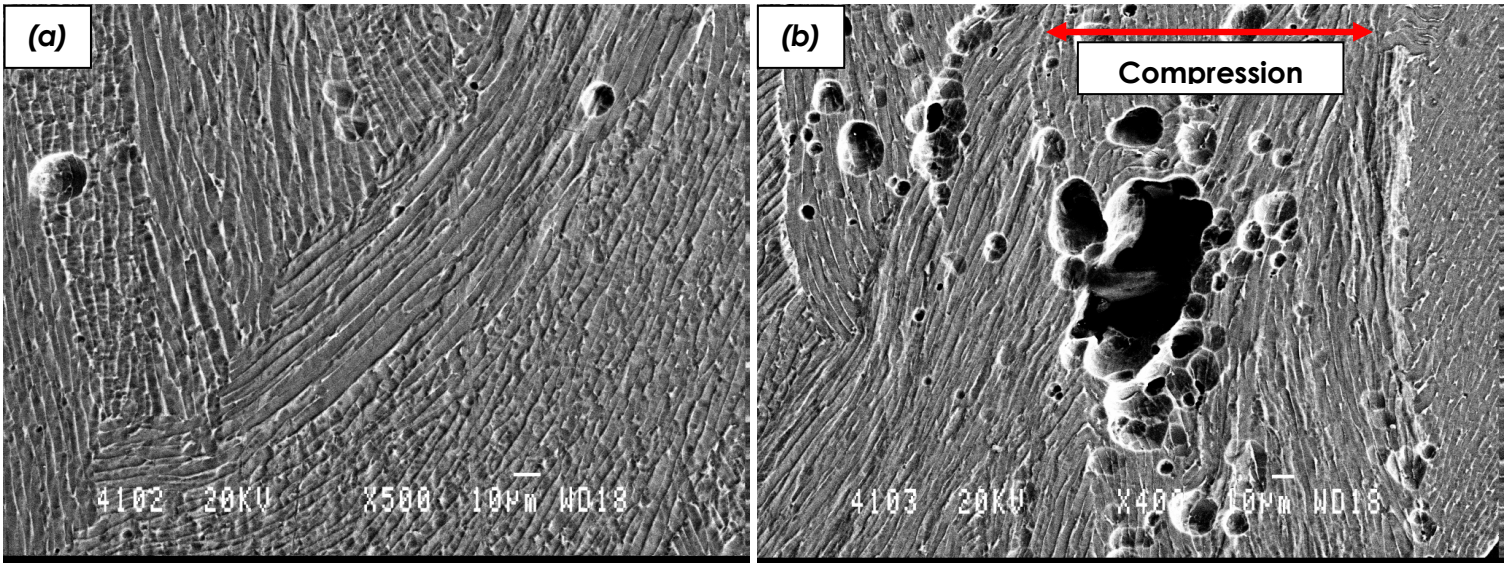

Fig. 11: SEM micrographs of hot compressed Ti64 samples (Working condition: temperature 750°C, strain rate 10^{-1} S^{-1})

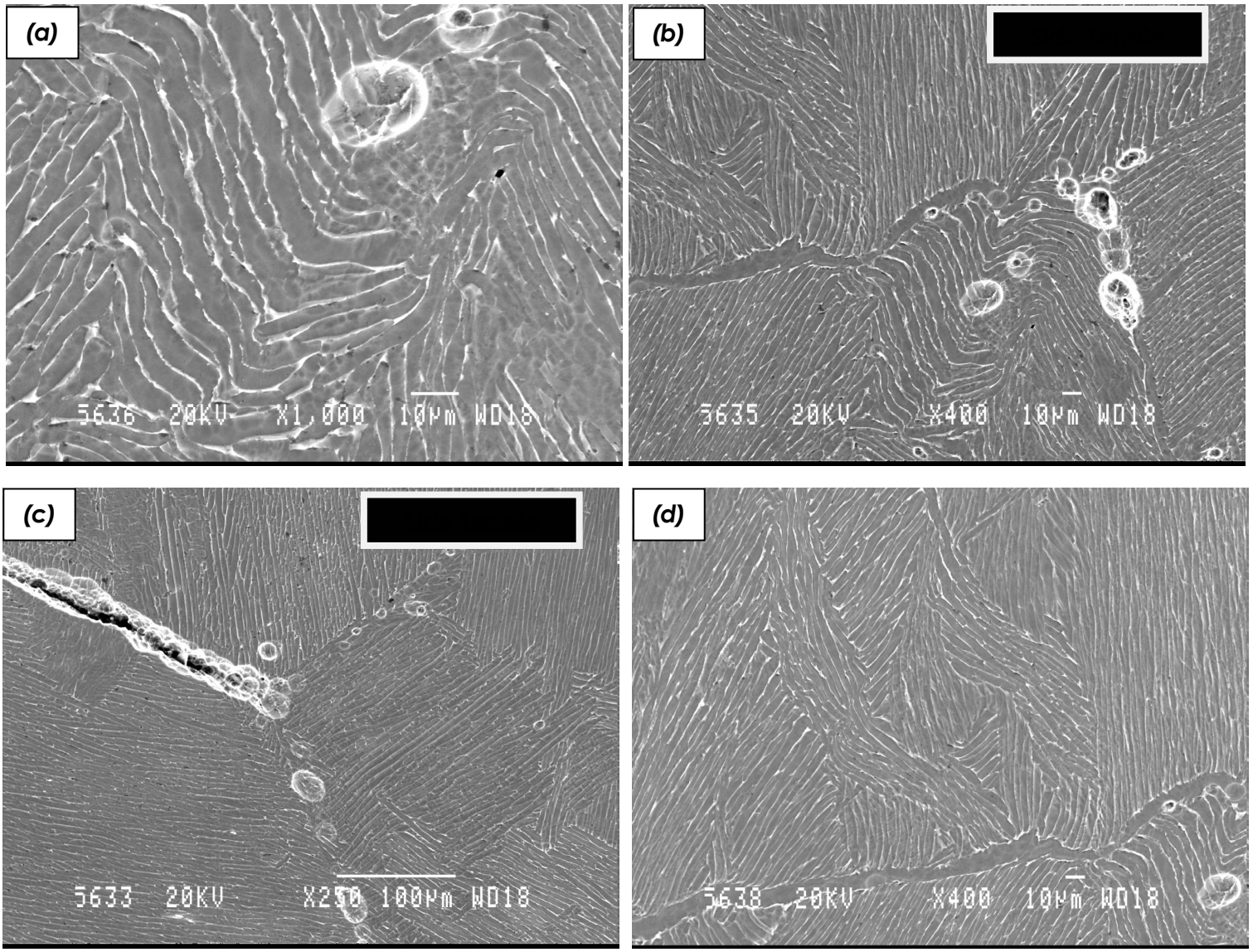

Fig. 12: SEM micrographs of hot compressed Ti64 samples (Working condition: temperature 750°C, strain rate 1 S^{-1})

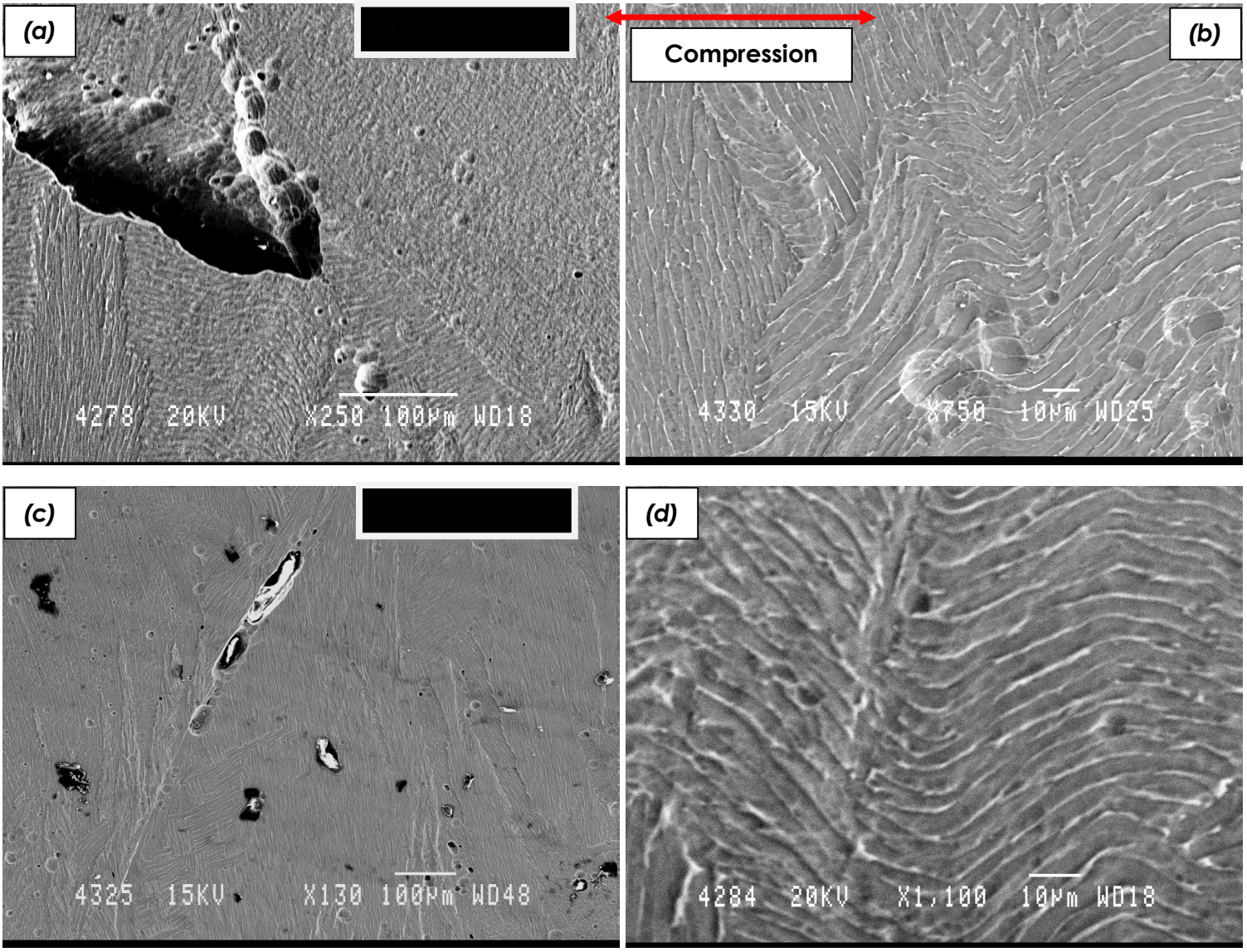

Fig. 13: SEM micrographs of hot compressed Ti64 samples (Working condition: temperature 800°C, strain rate 10^{-3} S^{-1})

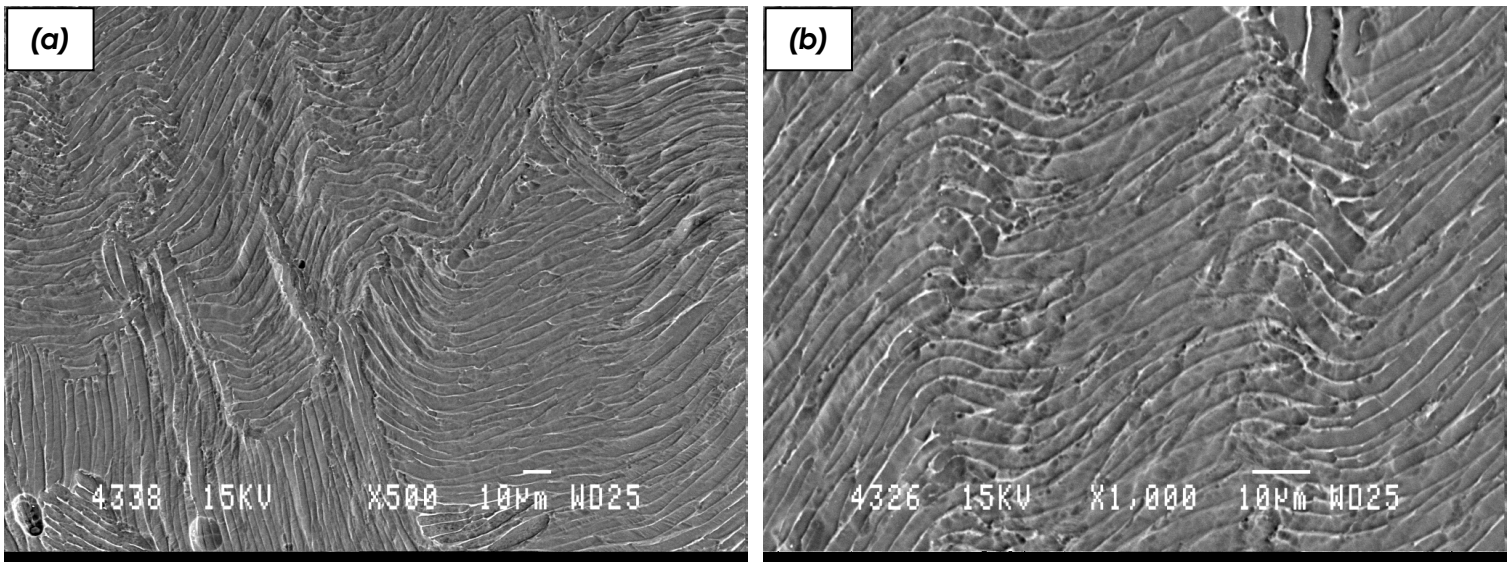

Fig. 14: SEM micrographs of hot compressed Ti64 samples (Working condition: temperature 800°C, strain rate 10^{-2} S^{-1})

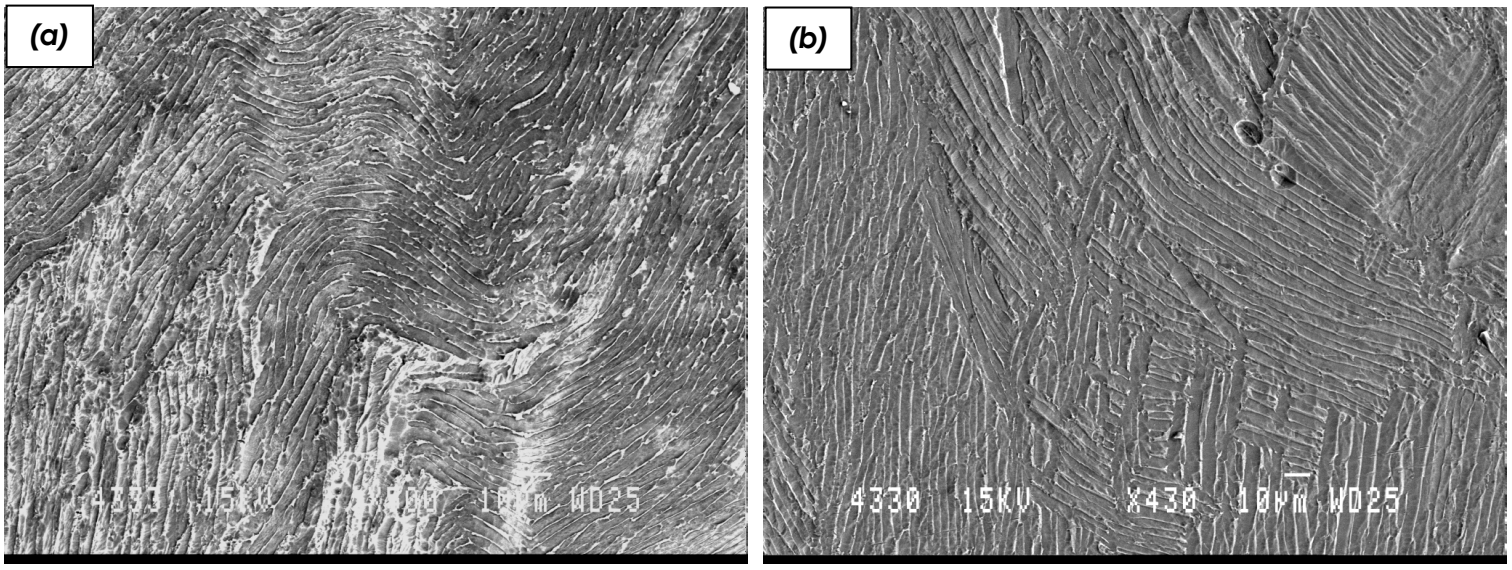

Fig. 15: SEM micrographs of hot compressed Ti64 samples (Working condition: temperature 800°C, strain rate 10^{-1} S^{-1})

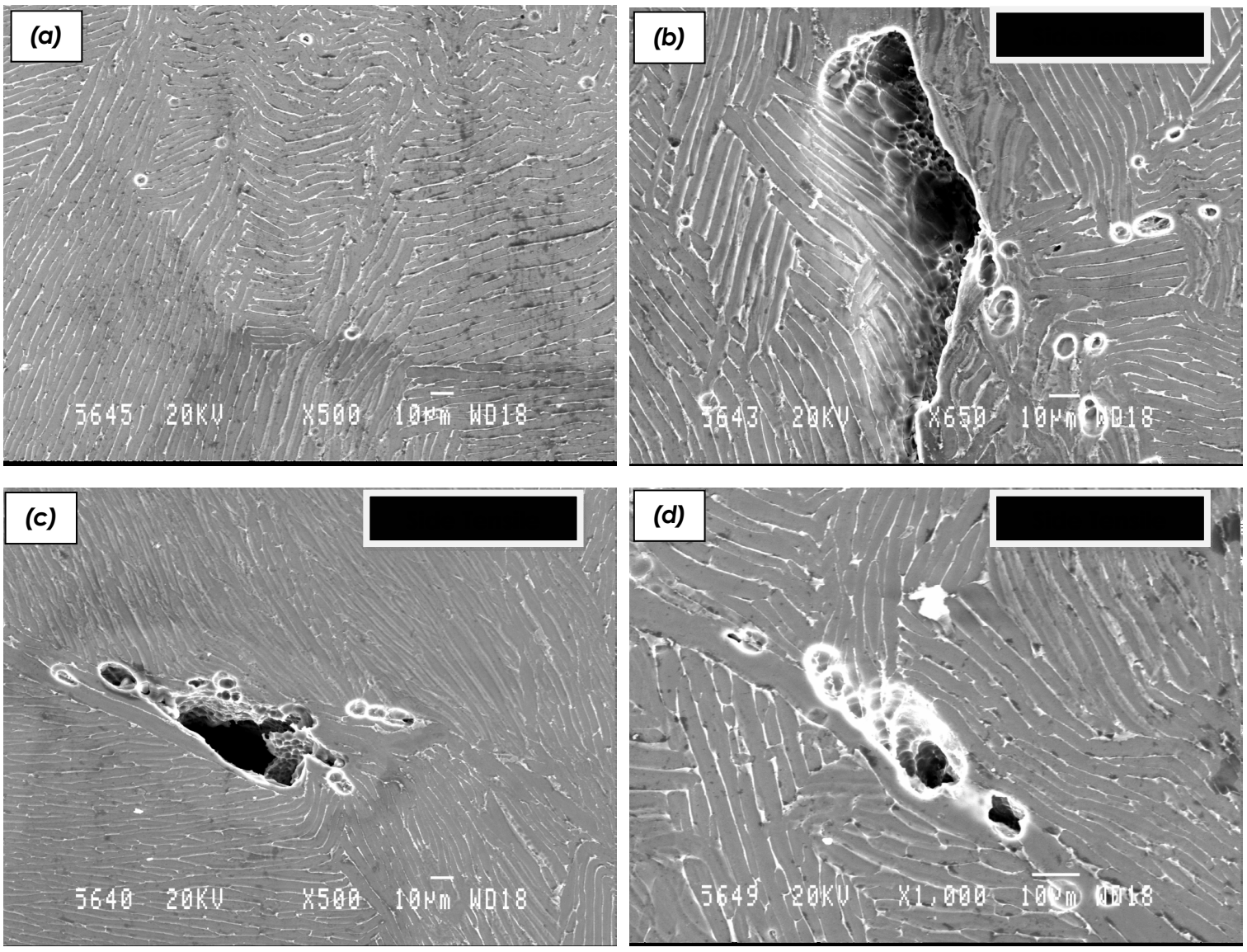

Fig. 16: SEM micrographs of hot compressed Ti64 samples (Working condition: temperature 800°C, strain rate 1 S^{-1})

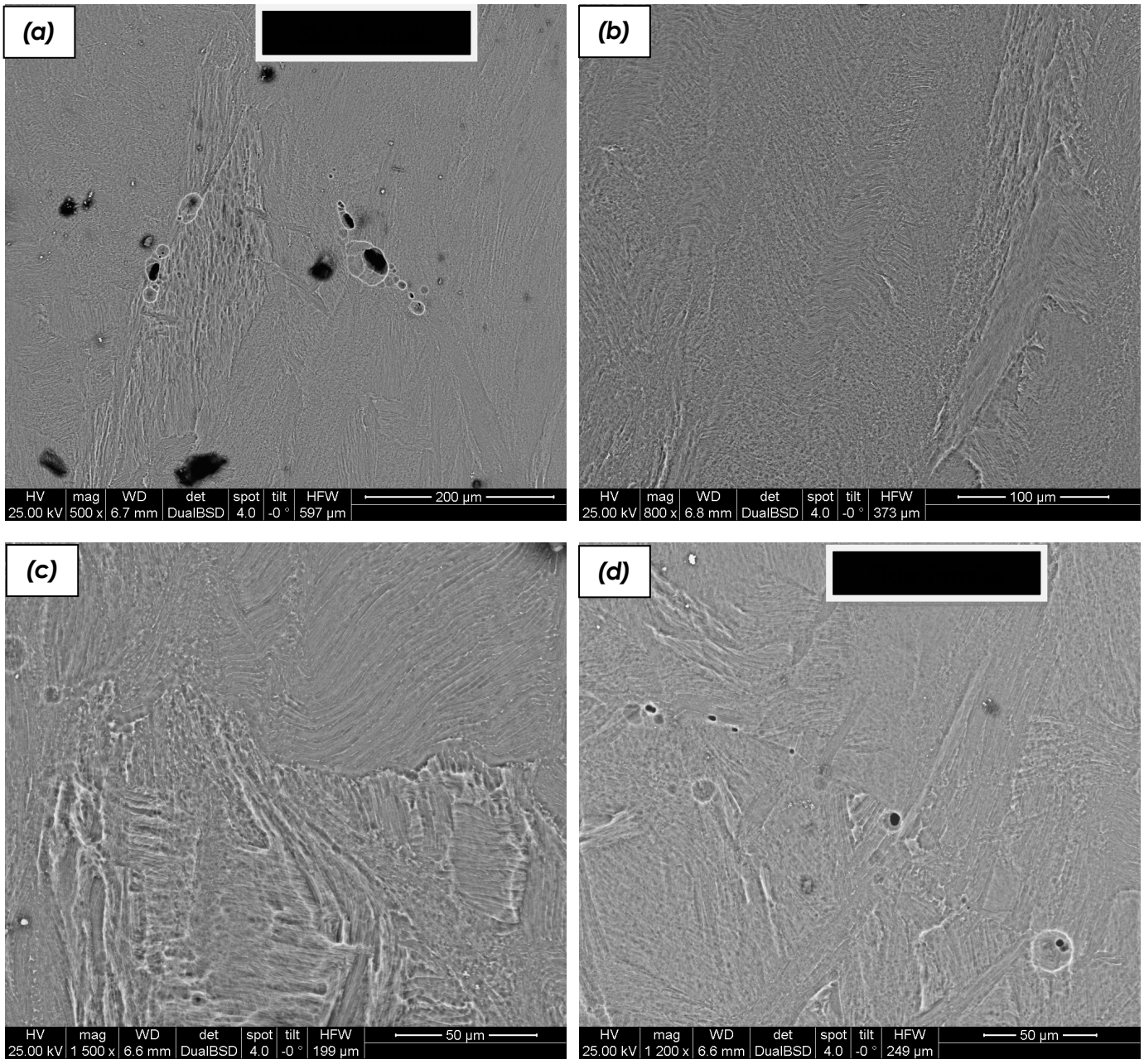

Fig. 17: SEM micrographs of hot compressed Ti64 samples (Working condition: temperature 800°C, strain rate 10 S^{-1})

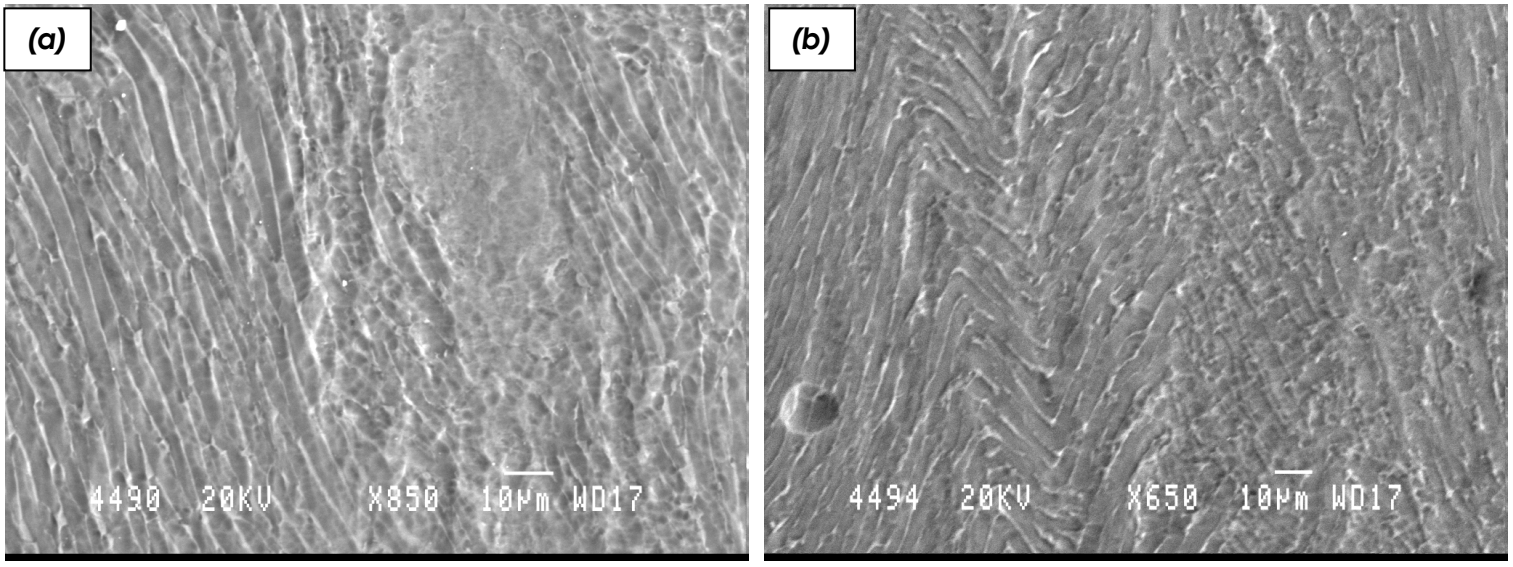

Fig. 18: SEM micrographs of hot compressed Ti64 samples (Working condition: temperature 850°C, strain rate 10^{-3} S^{-1})

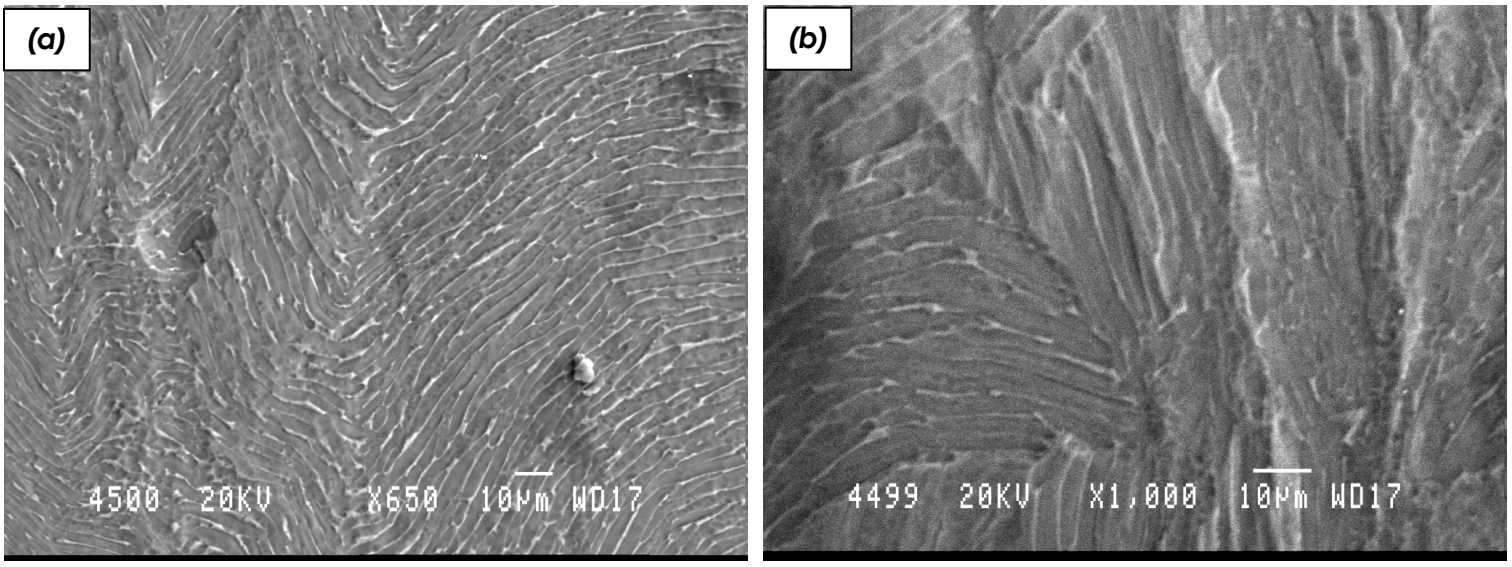

Fig. 19: SEM micrographs of hot compressed Ti64 samples (Working condition: temperature 850°C, strain rate $10^{-2}S^{-1}$)

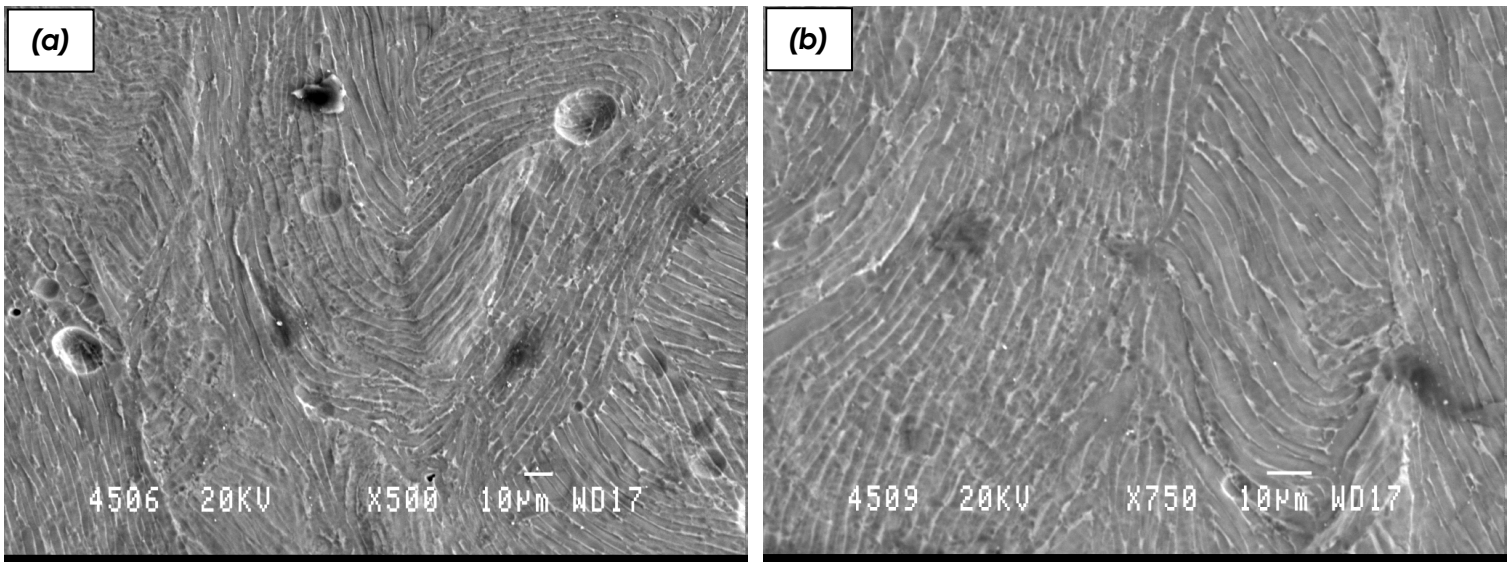

Fig. 20: SEM micrographs of hot compressed Ti64 samples (Working condition: temperature 850°C, strain rate 10^{-1} S^{-1})

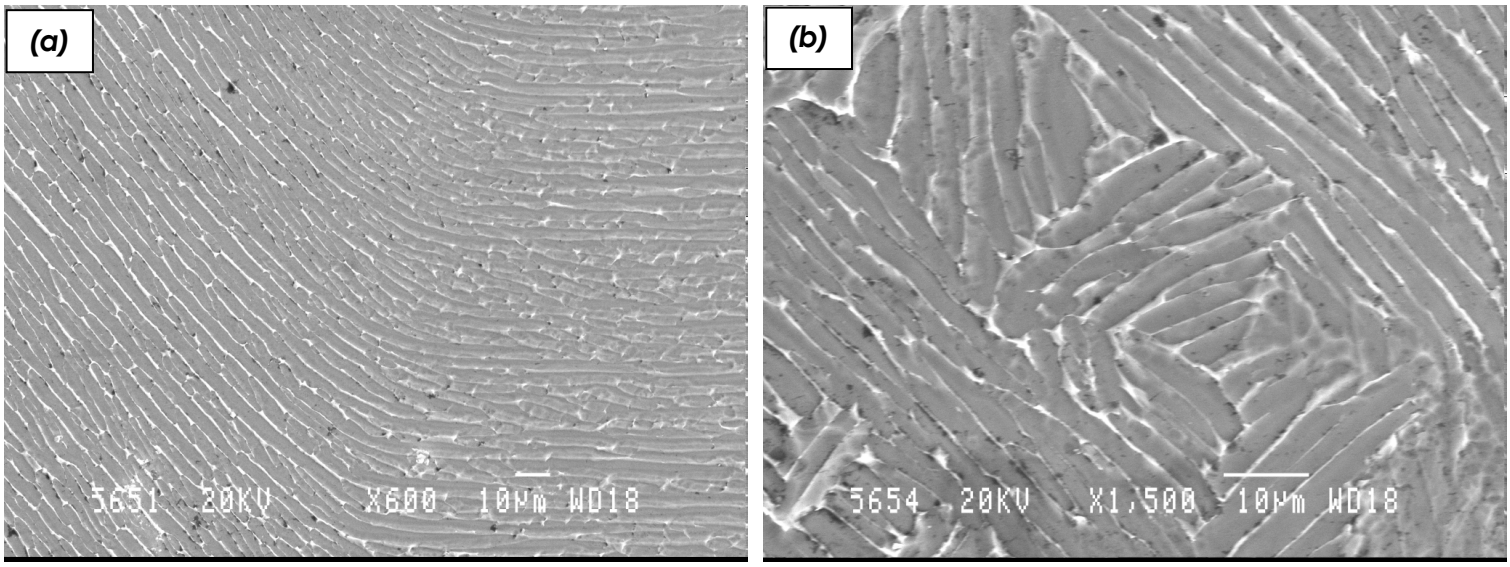

Fig. 21: SEM micrographs of hot compressed Ti64 samples (Working condition: temperature 850^{o}C, strain rate 1 S^{-1})

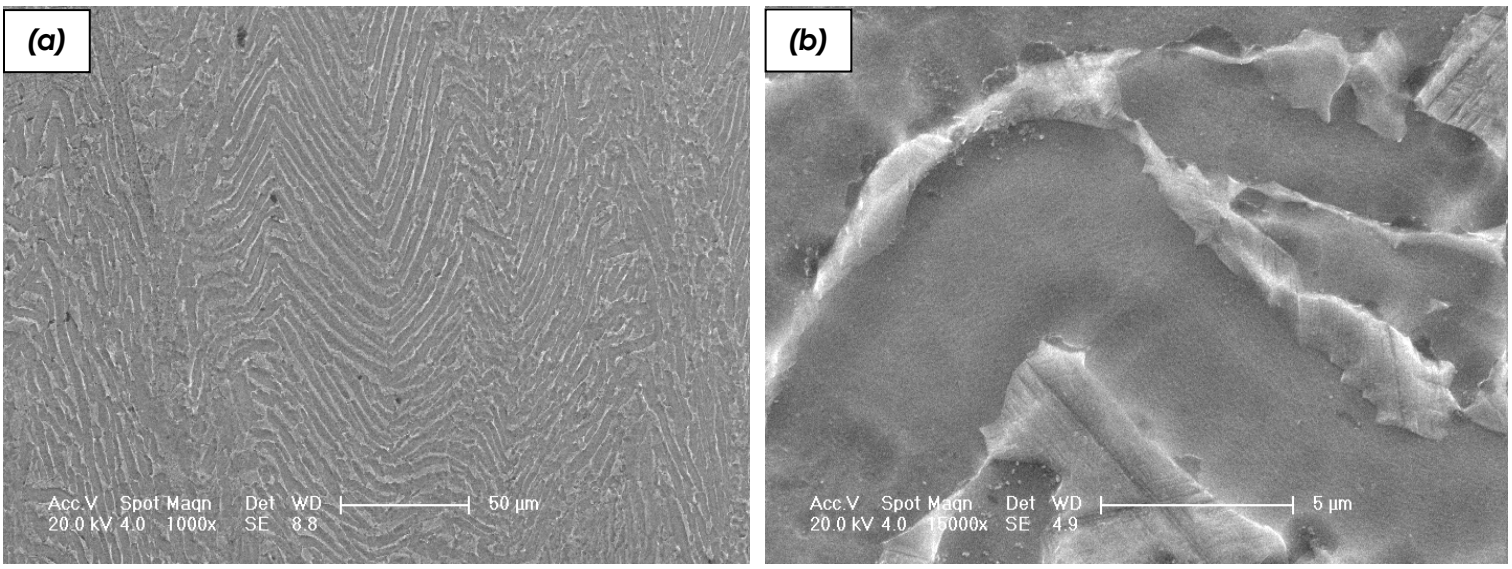

Fig. 22: SEM micrographs of hot compressed Ti64 samples (Working condition: temperature 900^{o}C, strain rate 10^{-3} S^{-1})

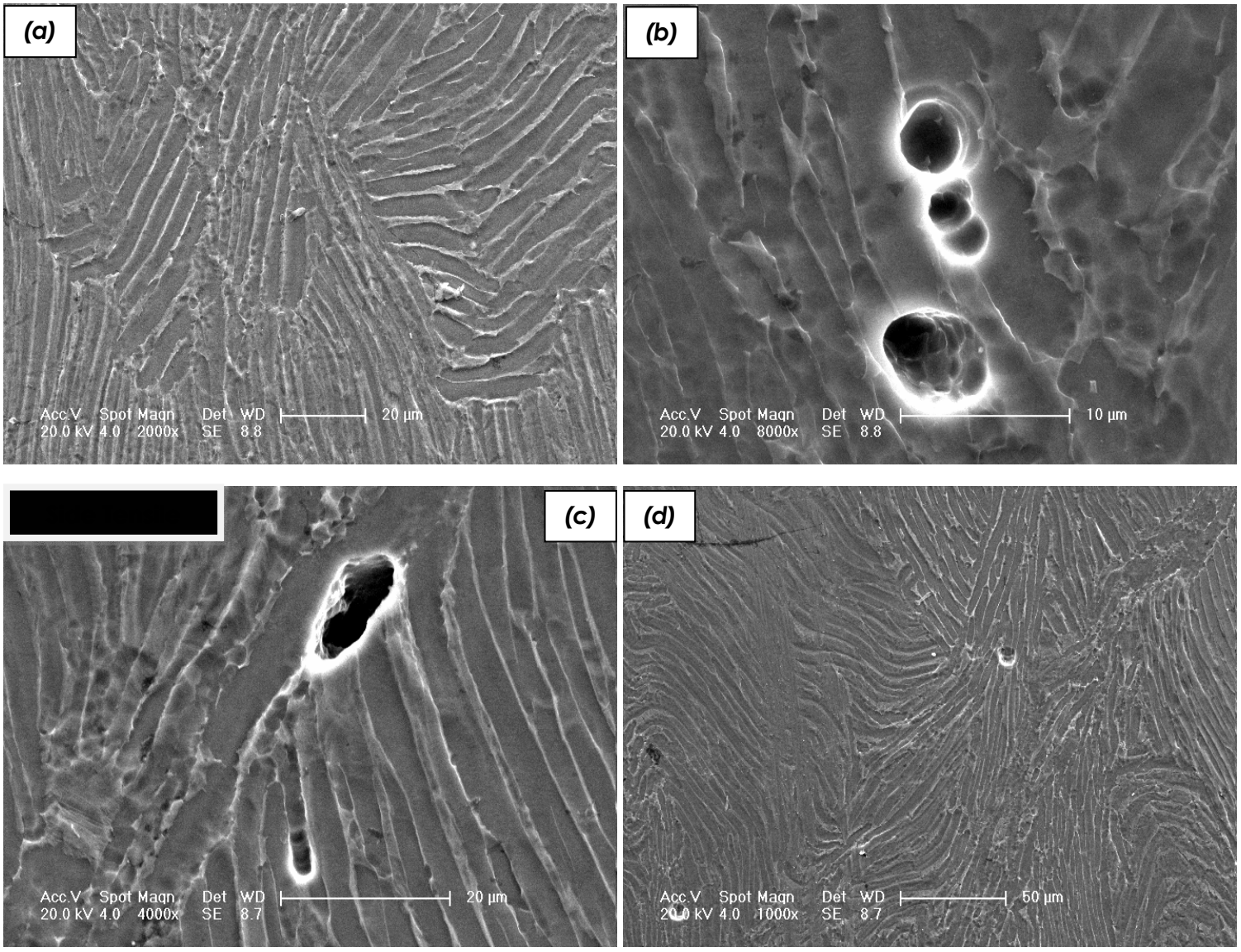

Fig. 23: SEM micrographs of hot compressed Ti64 samples (Working condition: temperature 900°C, strain rate 10^{-2} S^{-1}

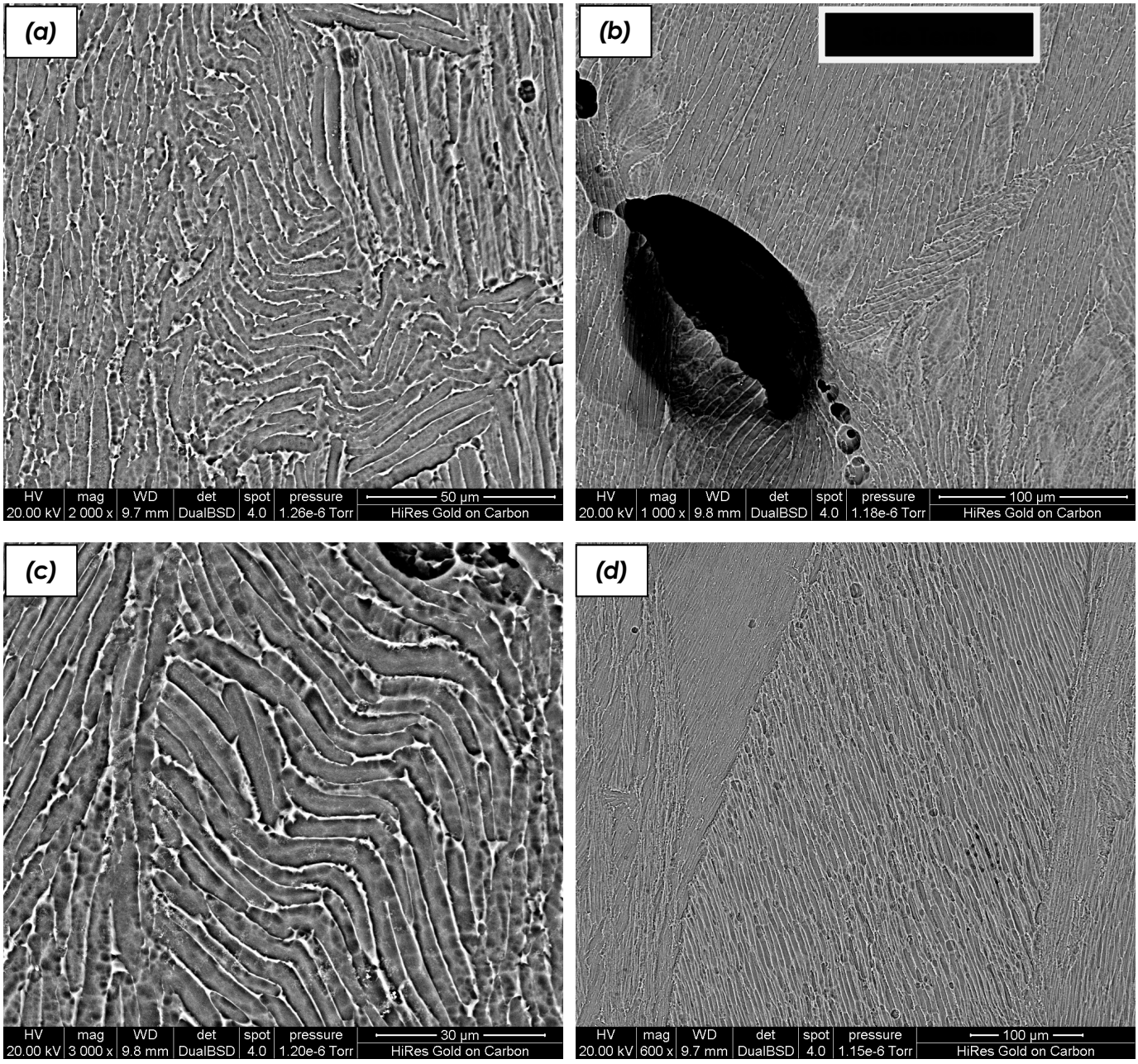

Fig. 24: SEM micrographs of hot compressed Ti64 samples (Working condition: temperature 900^{o}C, strain rate 10^{-1} S^{-1}

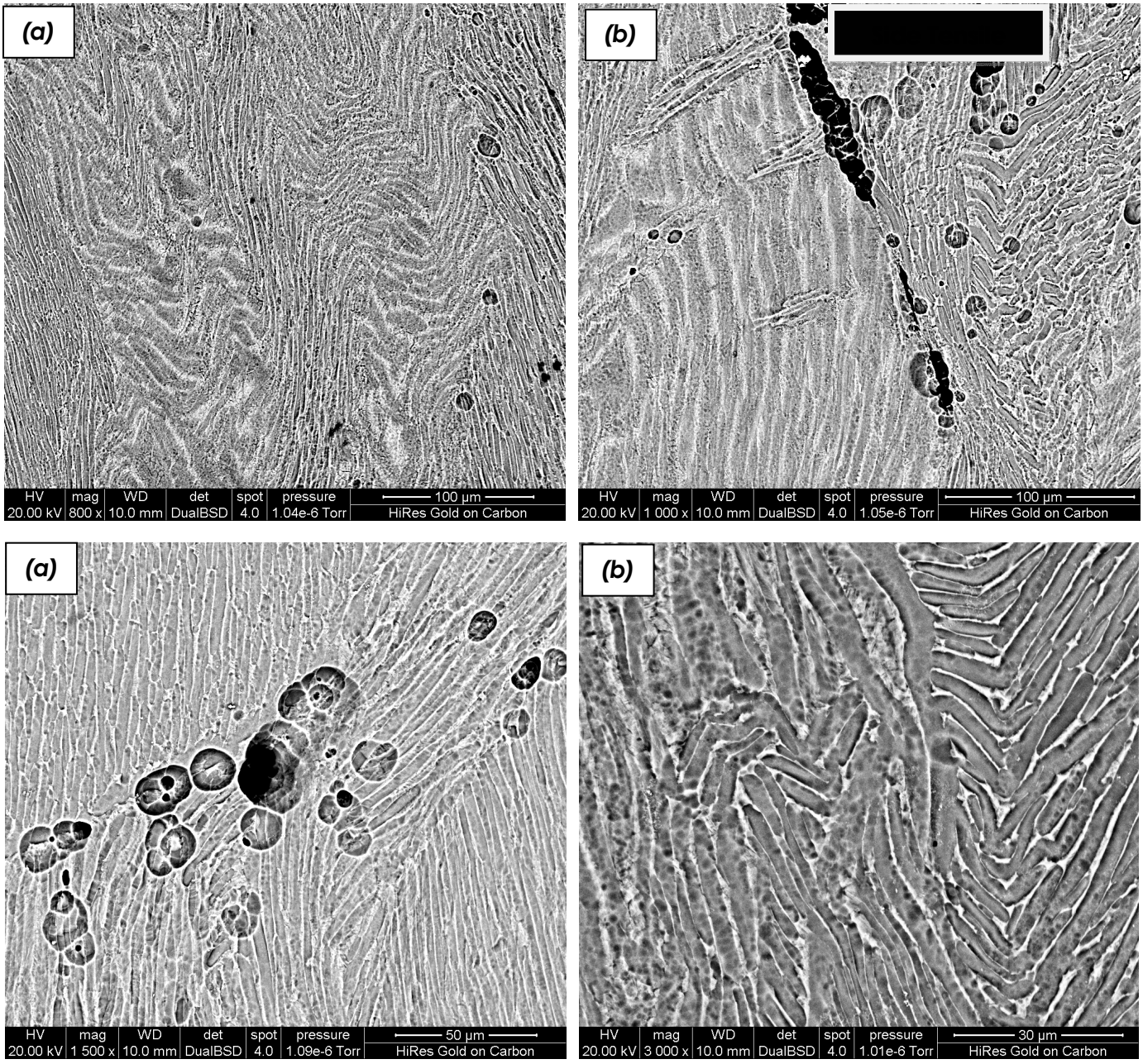

Fig. 25: SEM micrographs of hot compressed Ti64 samples (Working condition: temperature 900°C, strain rate 1 S^{-1}

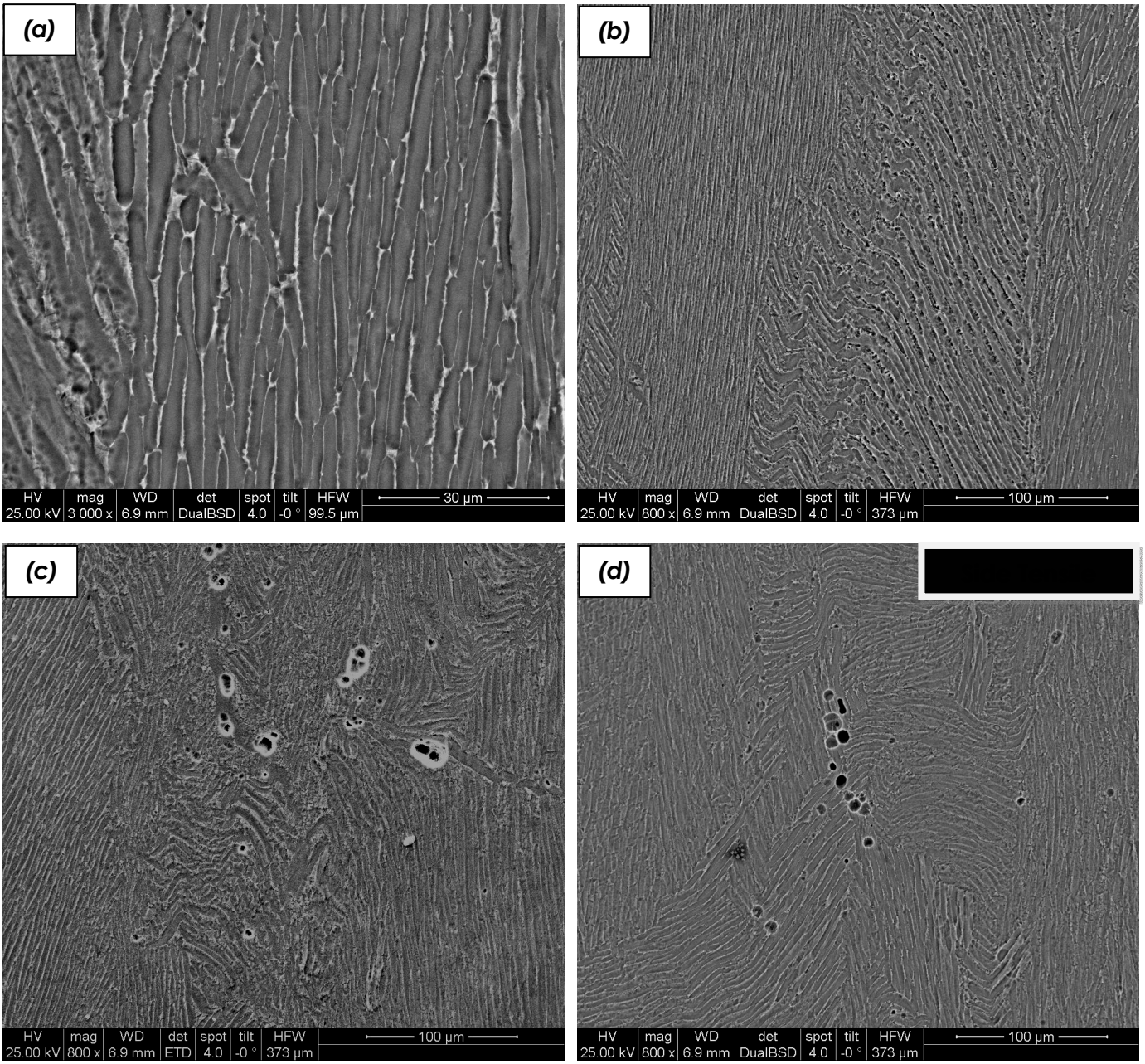

Fig. 26: SEM micrographs of hot compressed Ti64 samples (Working condition: temperature 900^{o}C, strain rate 10 S^{-1}

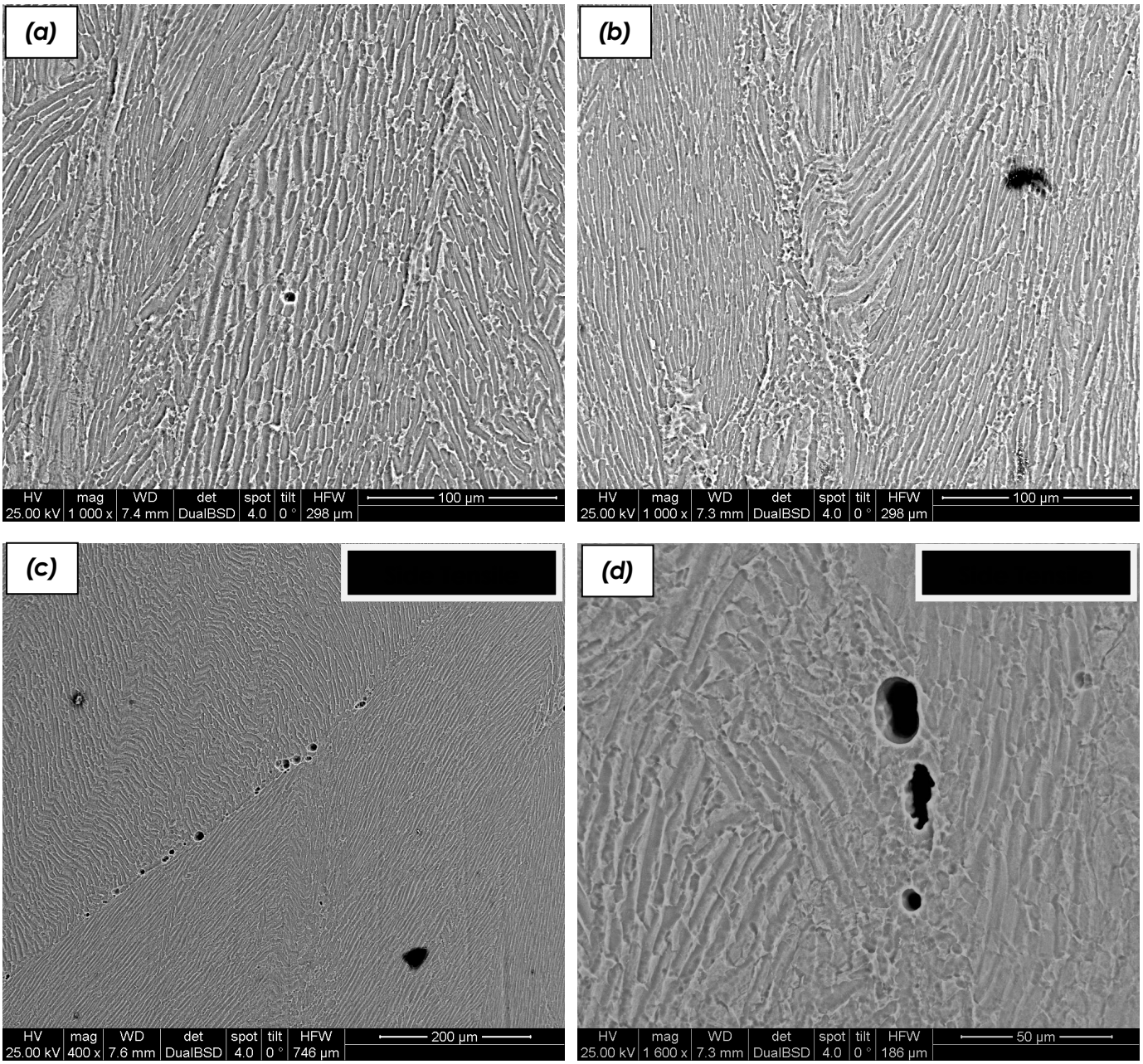

Fig. 27: SEM micrographs of hot compressed Ti64 samples (Working condition: temperature 950°C, strain rate 10^{-2} S^{-1}

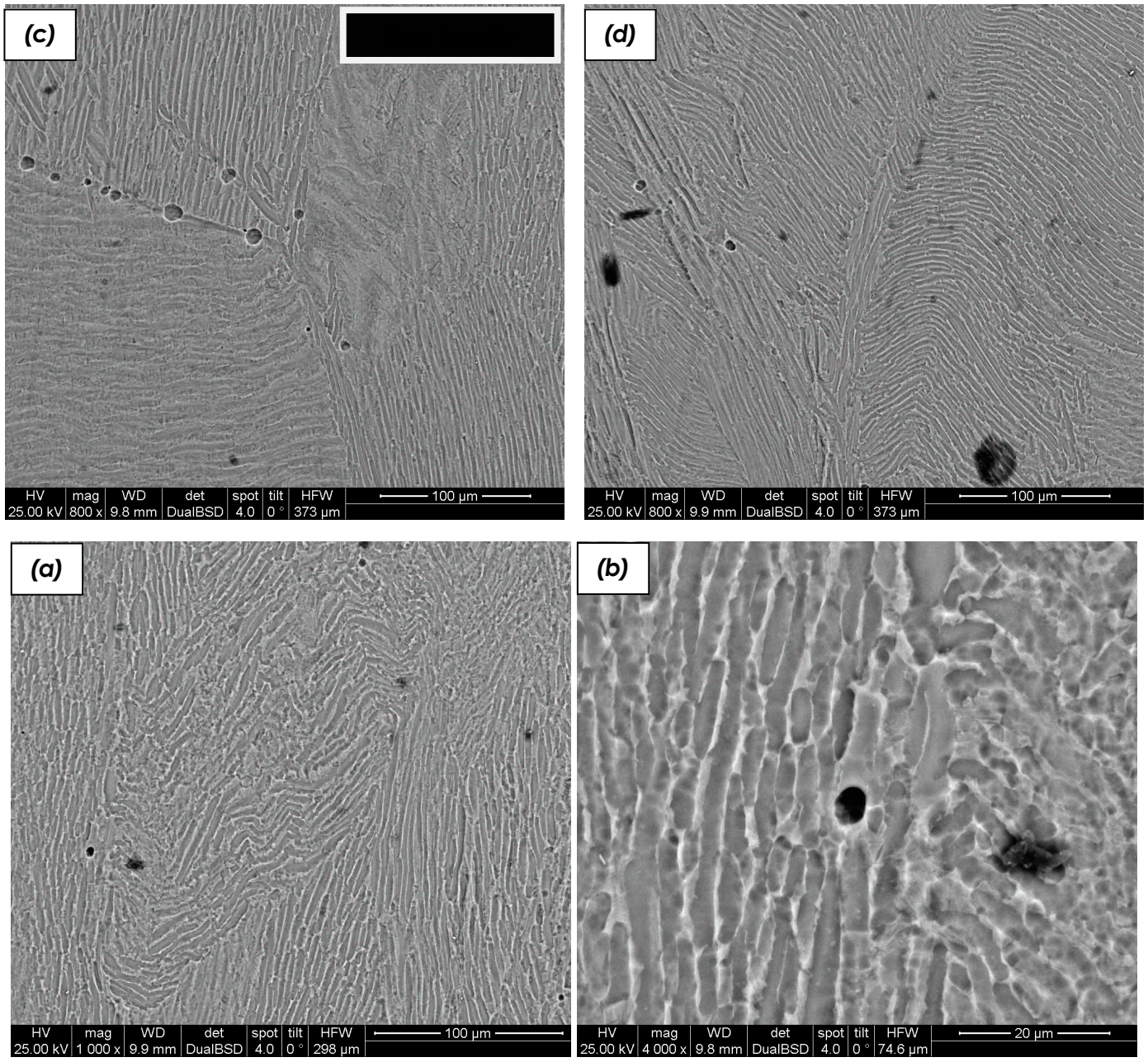

Fig. 28: SEM micrographs of hot compressed Ti64 samples (Working condition: temperature 950°C, strain rate 1 S^{-1}

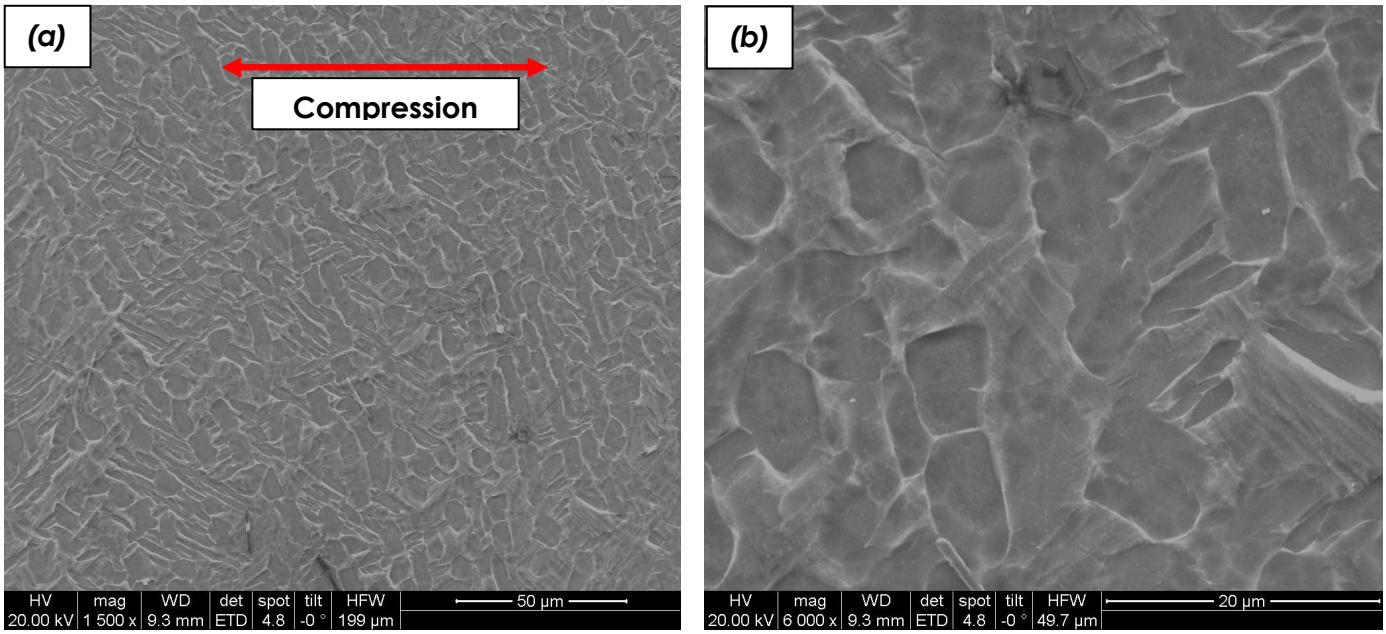

Fig. 29: SEM micrographs of hot compressed Ti64 samples (Working condition: temperature 1000°C, strain rate 10^{-2} S^{-1}

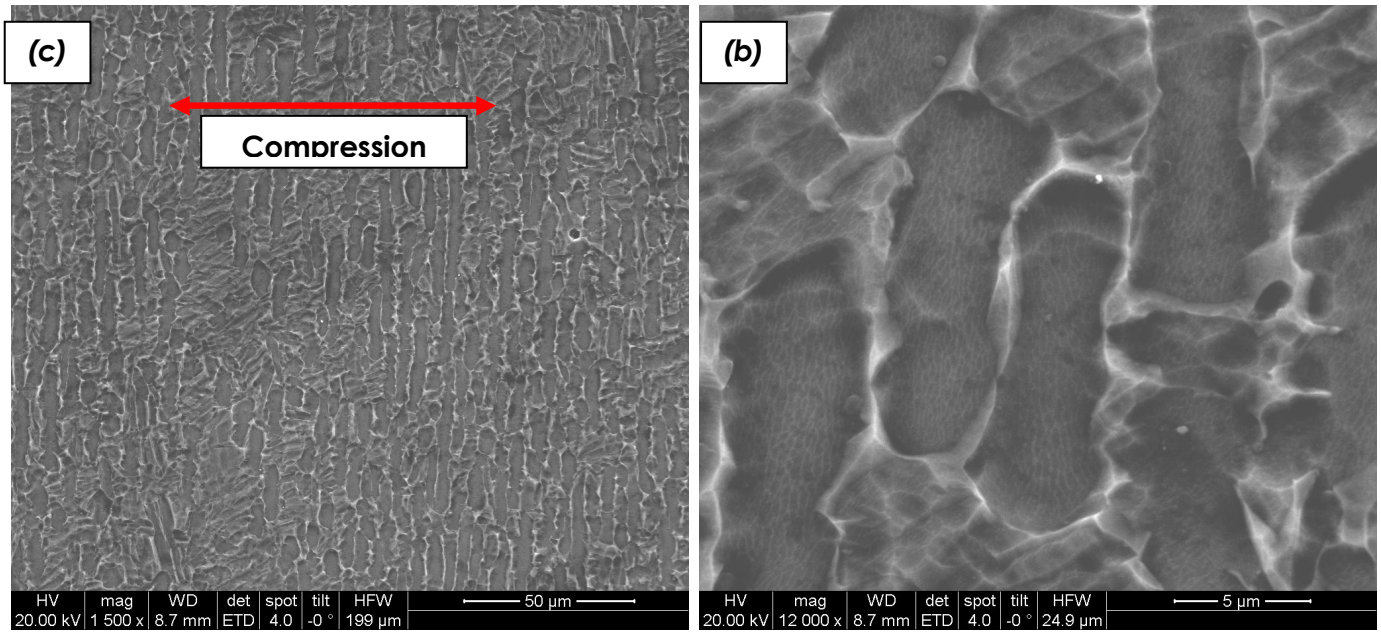

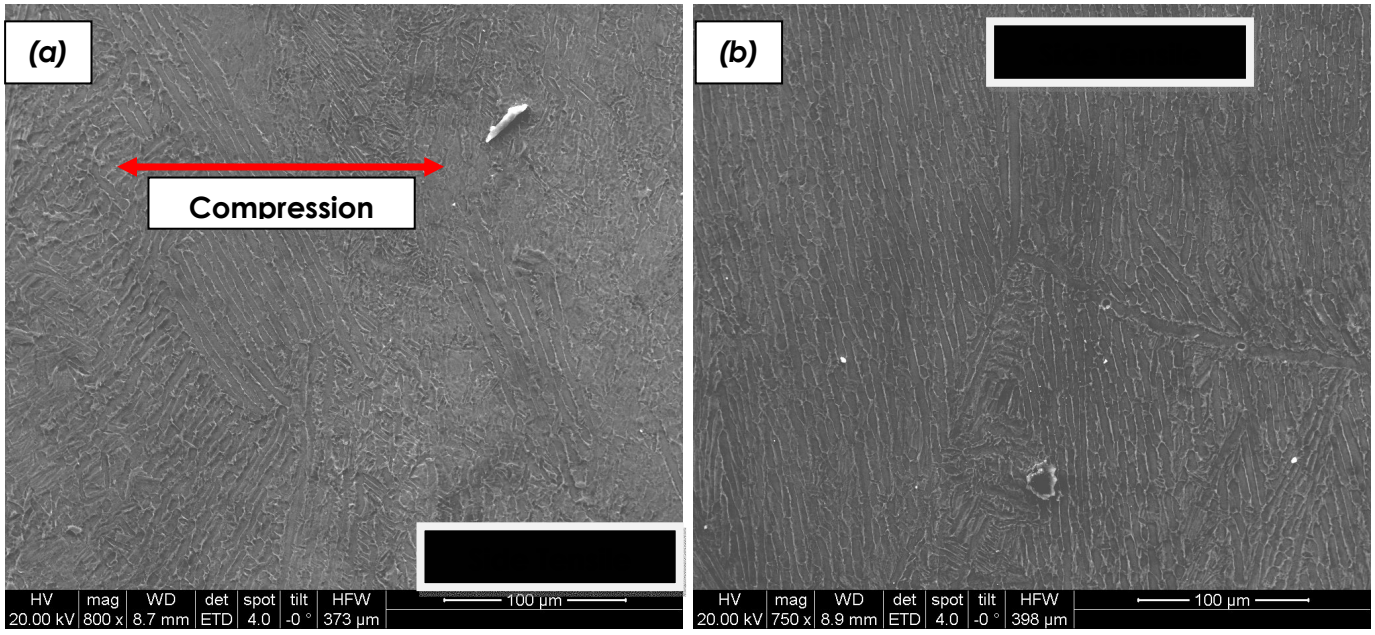

Fig. 30: SEM micrographs of hot compressed Ti64 samples (Working condition: temperature 1000°C, strain rate 1 S^{-1}

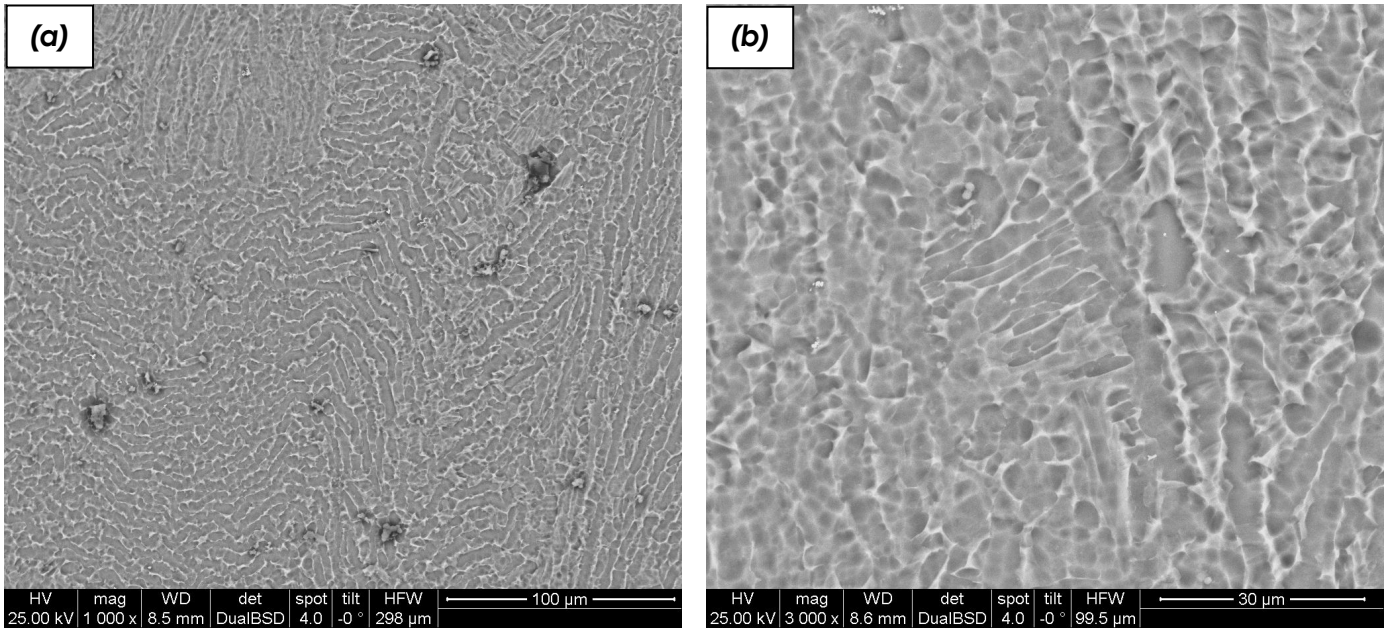

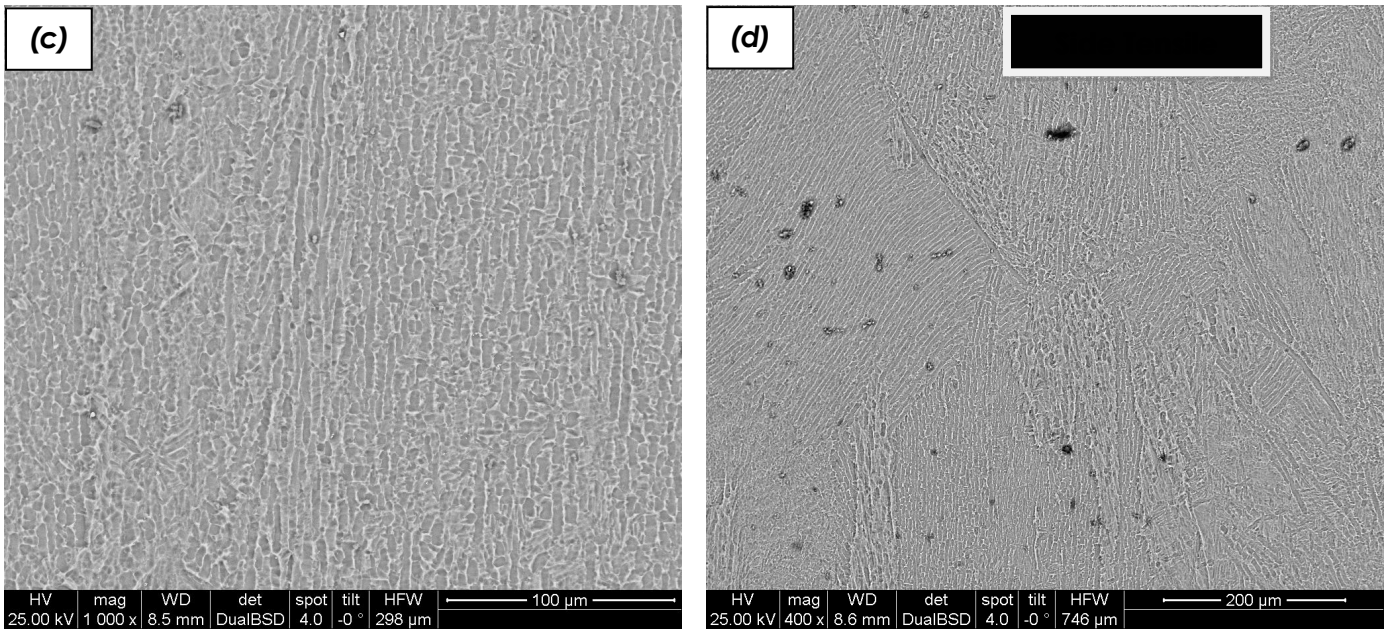

Fig. 31: SEM micrographs of hot compressed Ti64 samples (Working condition: temperature 1000°C, strain rate 10 S^{-}

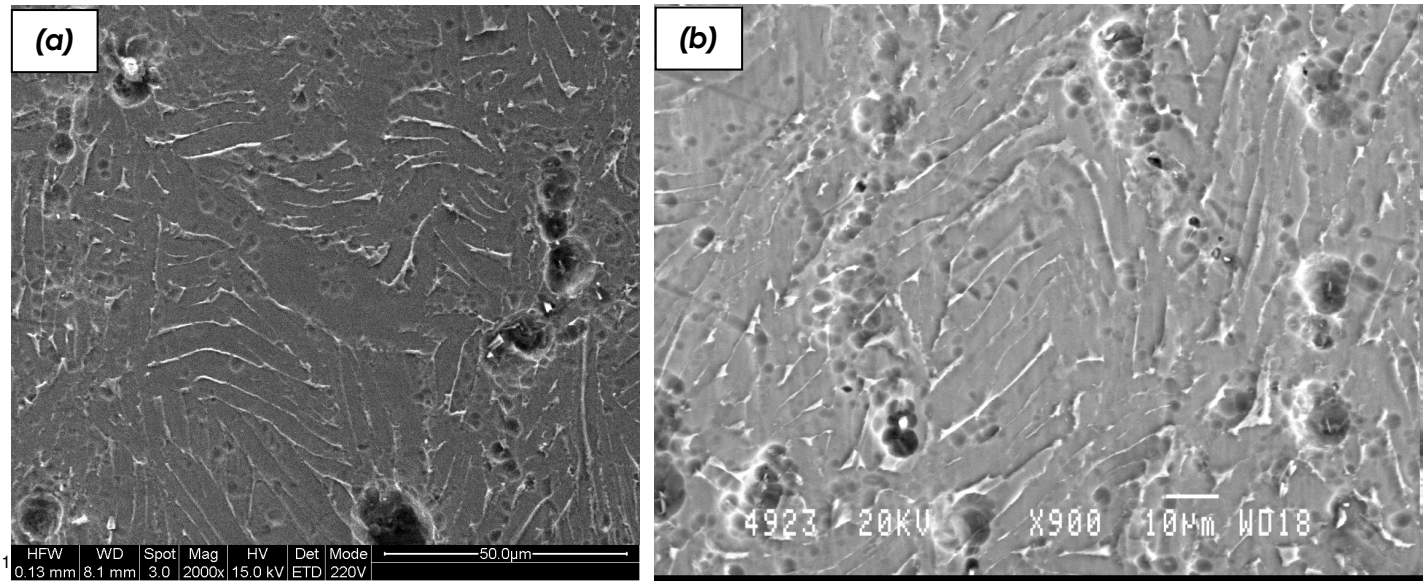

Fig. 32: SEM micrographs of hot compressed Ti64+B-Axial samples (Working condition: temperature 750°C, strain rate 10^{-3} S^{-1})

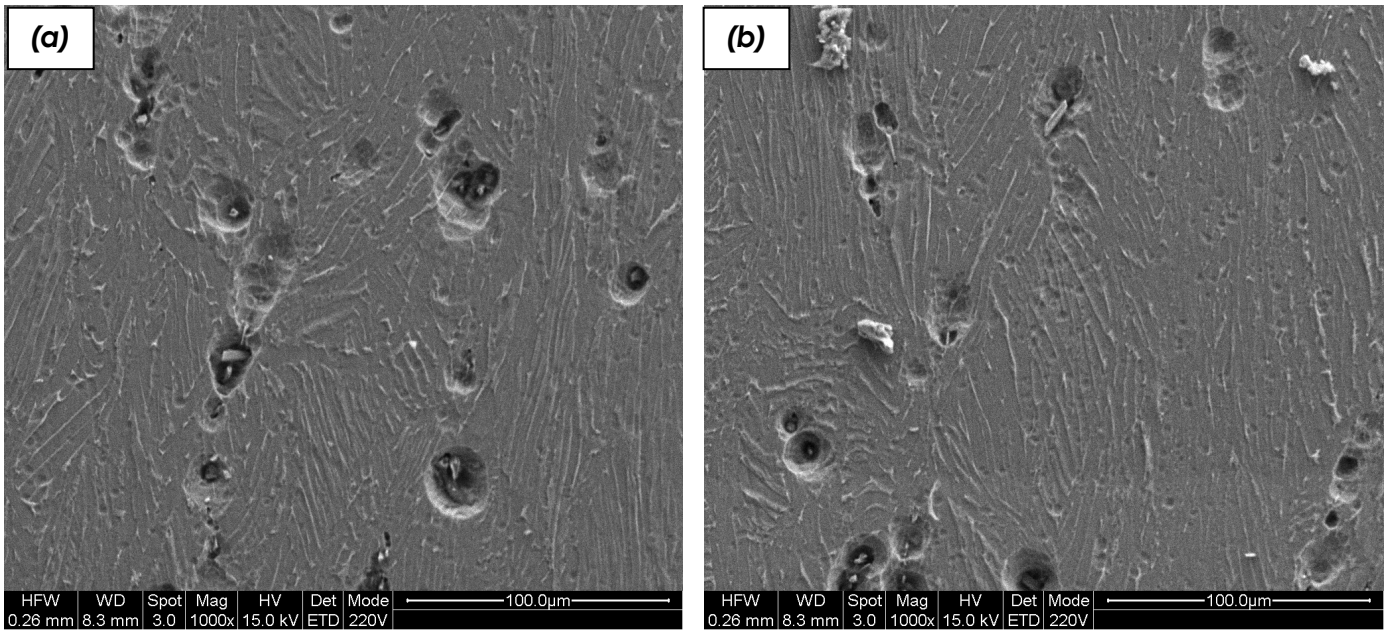

Fig. 33: SEM micrographs of hot compressed Ti64+B-Axial samples (Working condition: temperature 750^{o}C, strain rate 10^{-2} S^{-1})

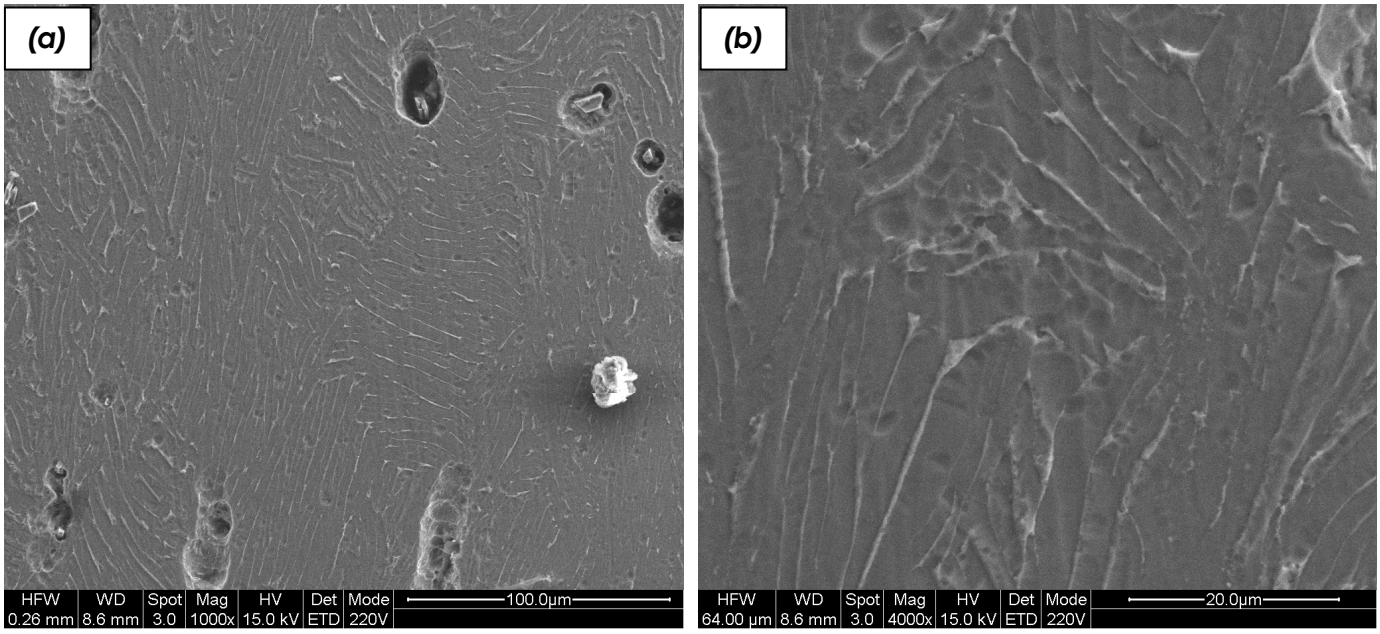

Fig. 34: SEM micrographs of hot compressed Ti64+B-Axial samples (Working condition: temperature 750^{o}C, strain rate 10^{-1} S^{-1})

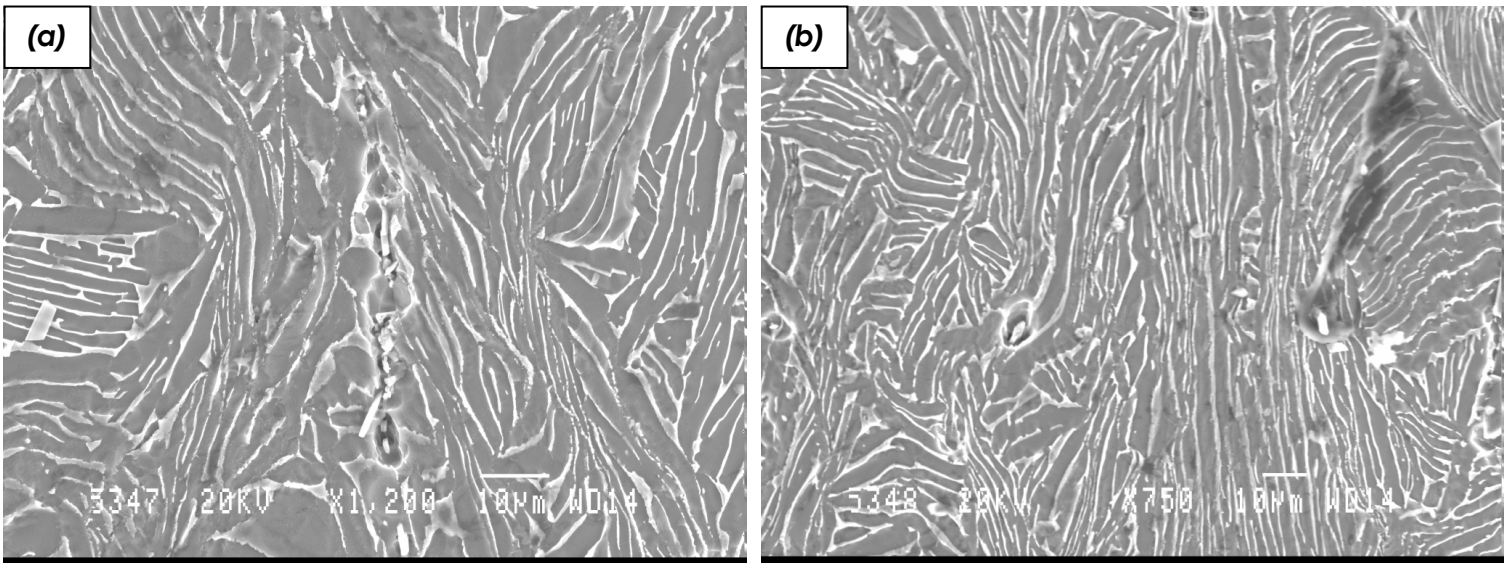

Fig. 35: SEM micrographs of hot compressed Ti64+B-Axial samples (Working condition: temperature 750^{o}C, strain rate 1 S^{-1})

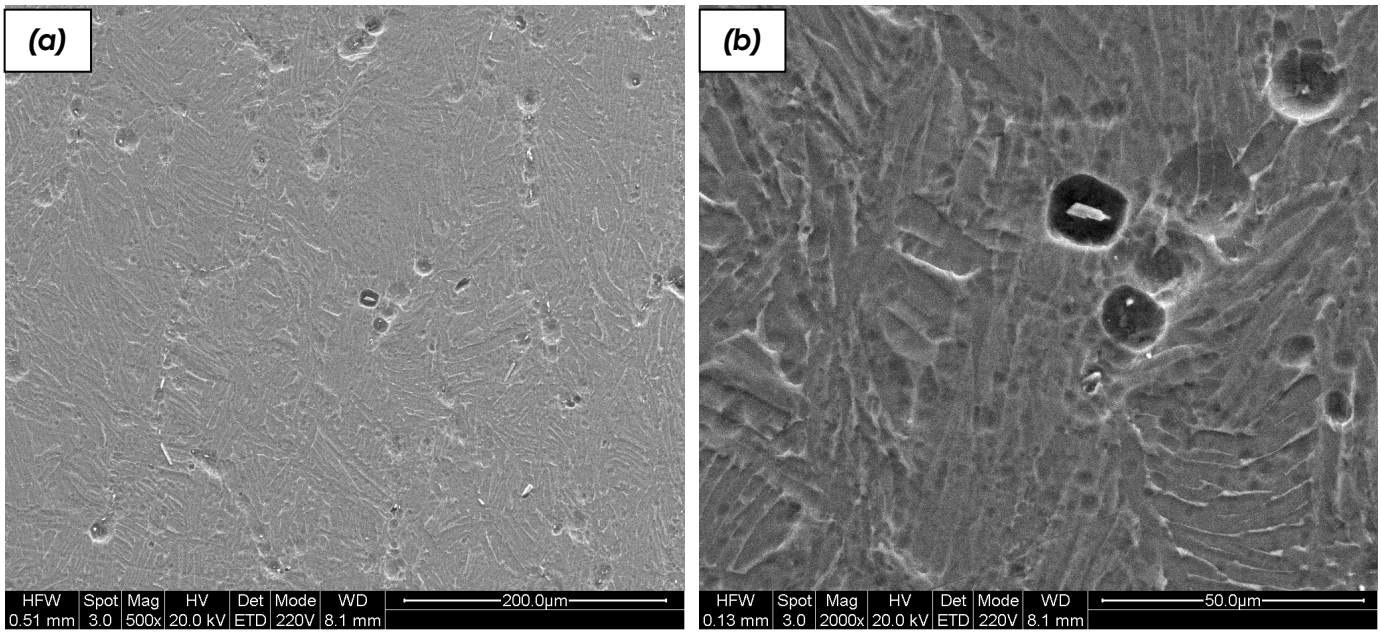

Fig. 36: SEM micrographs of hot compressed Ti64+B-Axial samples (Working condition: temperature 800^{o}C, strain rate 10^{-3} S^{-1})

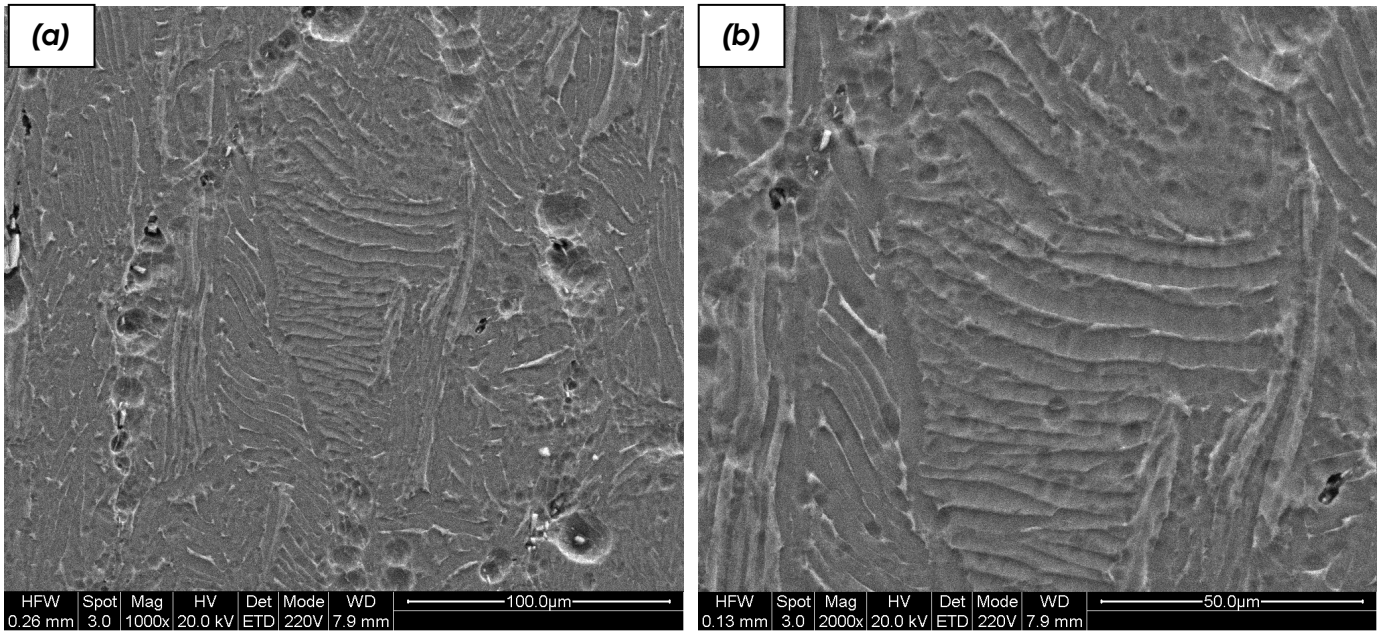

Fig. 37: SEM micrographs of hot compressed Ti64+B-Axial samples (Working condition: temperature 800^{o}C, strain rate 10^{-2} S^{-1})

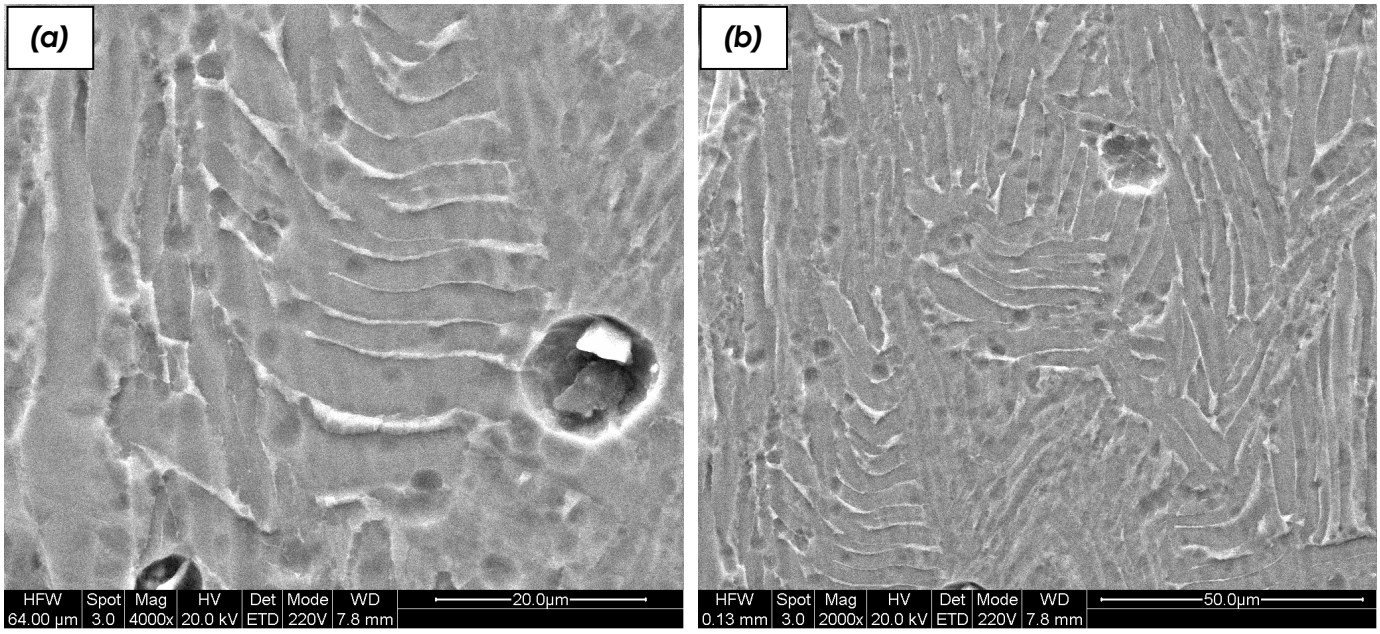

Fig. 38: SEM micrographs of hot compressed Ti64+B-Axial samples (Working condition: temperature 800^{o}C, strain rate 10^{-1} S^{-1})

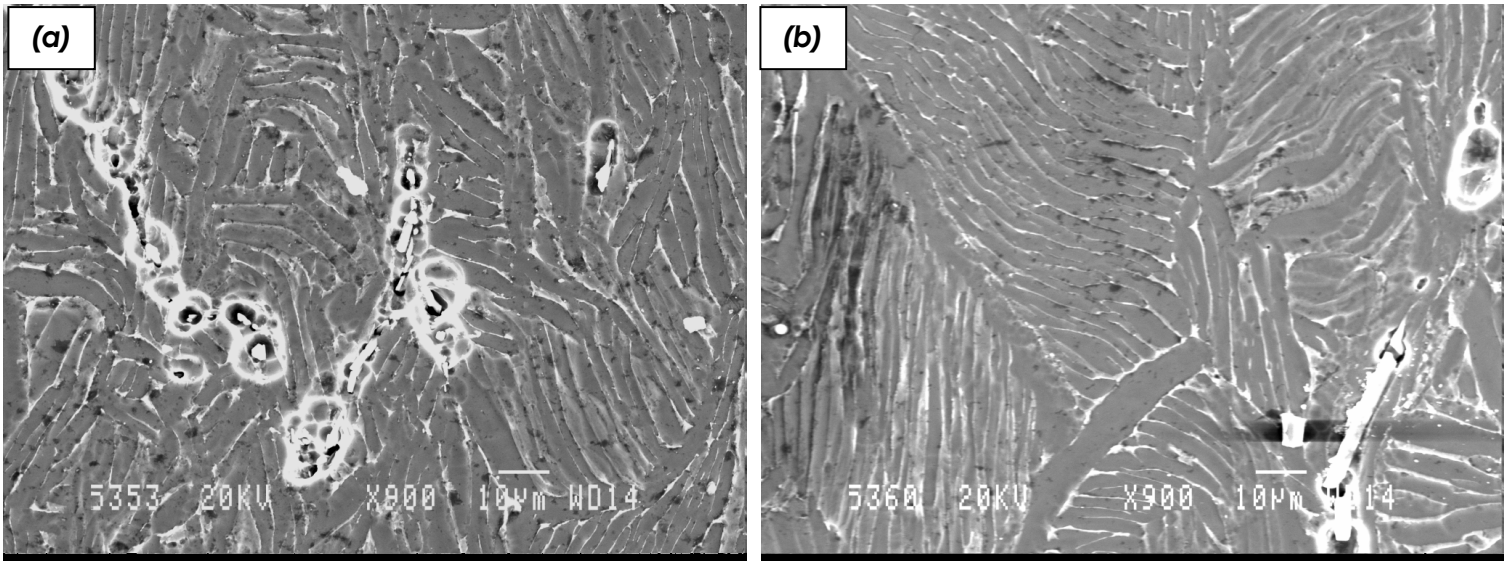

Fig. 39: SEM micrographs of hot compressed Ti64+B-Axial samples (Working condition: temperature 800^{o}C, strain rate 1 S^{-1})

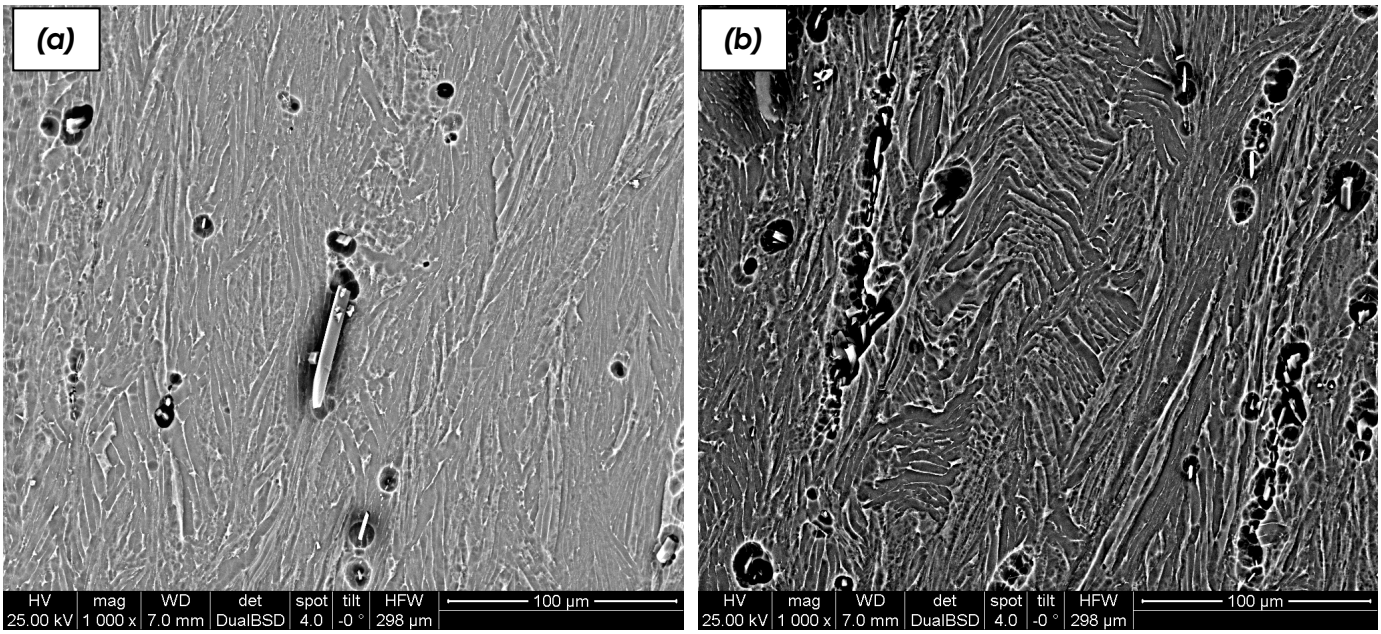

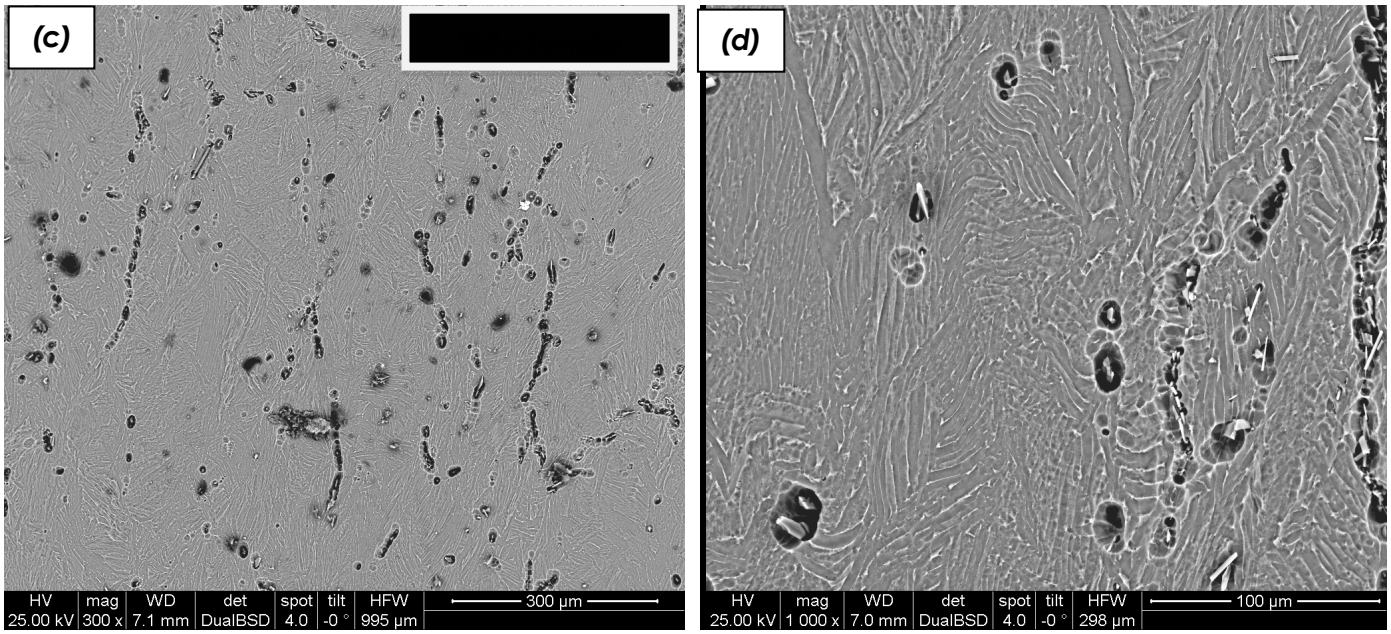

Fig. 40: SEM micrographs of hot compressed Ti64+B-Axial samples (Working condition: temperature 800^{o}C, strain rate 10 S^{-1})

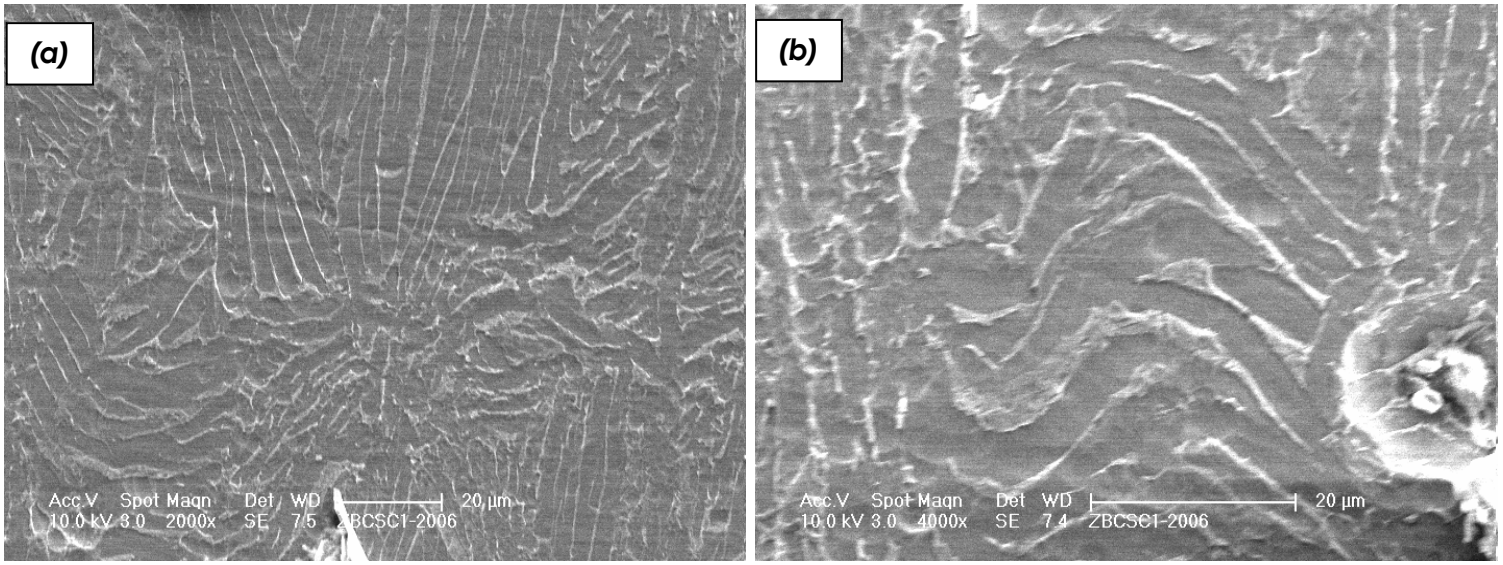

Fig. 41: SEM micrographs of hot compressed Ti64+B-Axial samples (Working condition: temperature 850^{o}C, strain rate 10^{-3} S^{-1})

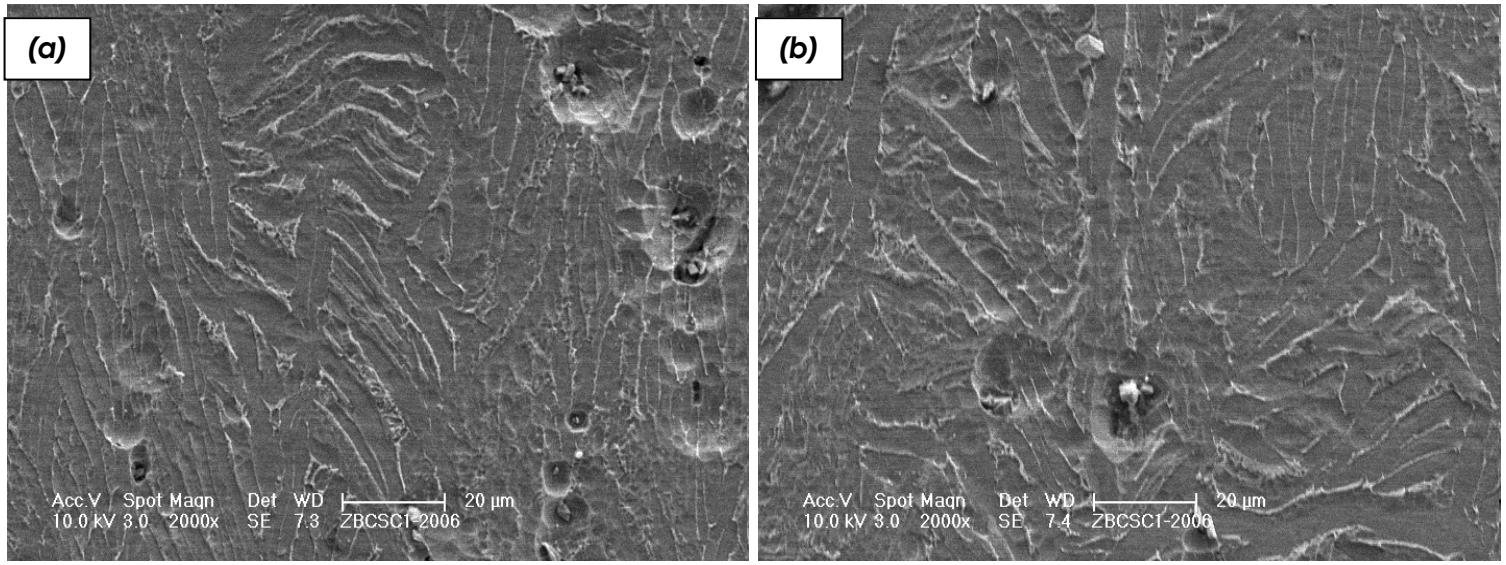

Fig. 42: SEM micrographs of hot compressed Ti64+B-Axial samples (Working condition: temperature 850^{o}C, strain rate 10^{-2} S^{-1})

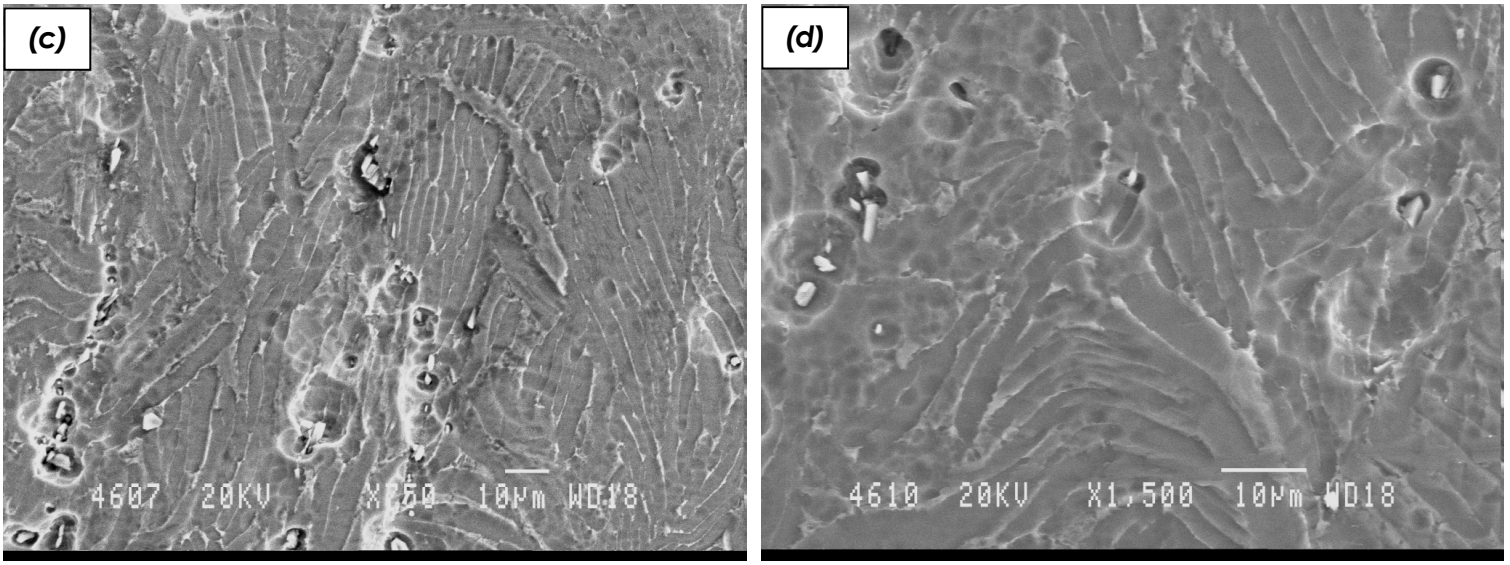

Fig. 43: SEM micrographs of hot compressed Ti64+B-Axial samples (Working condition: temperature 850^{o}C, strain rate 10^{-1} S^{-1})

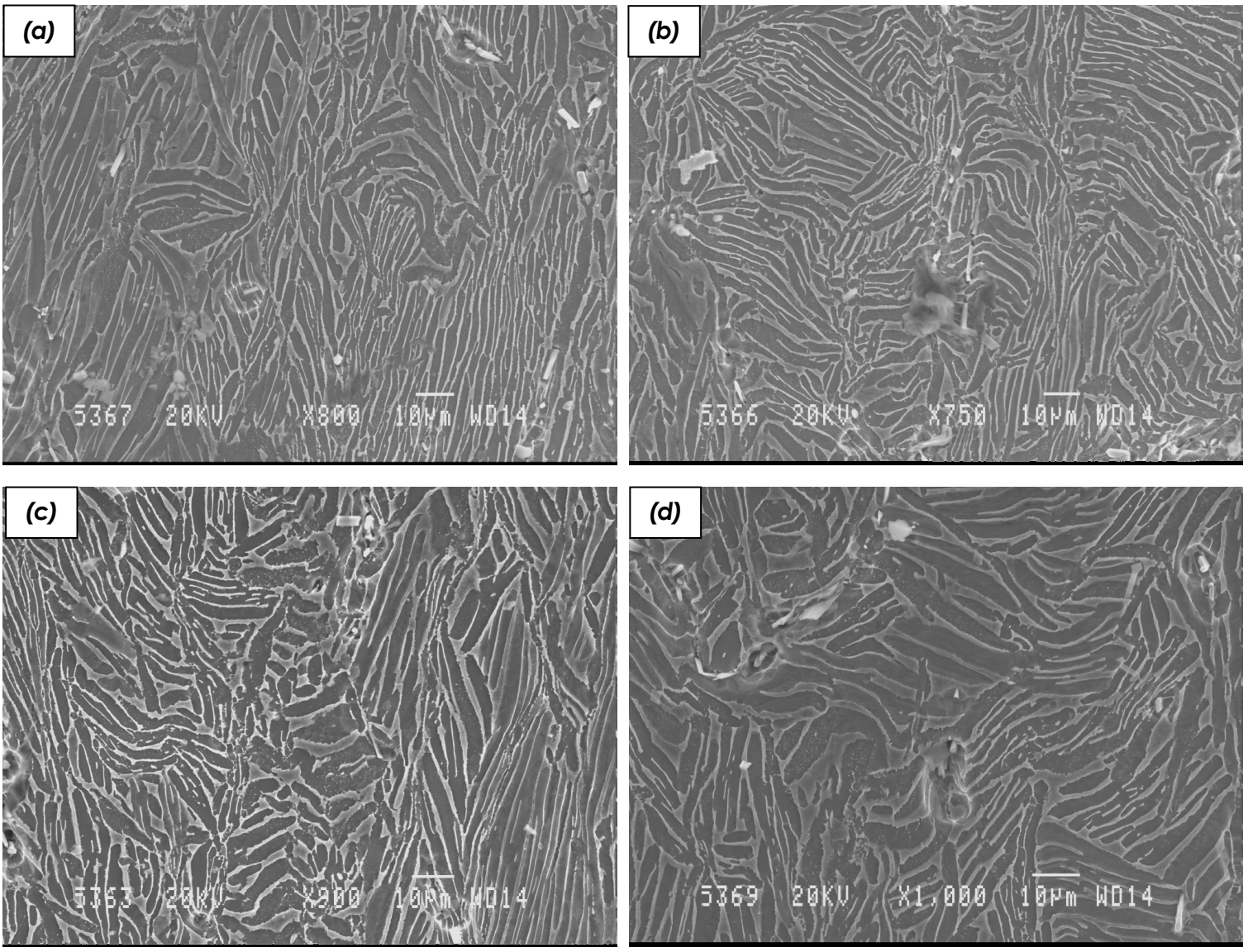

Fig. 44: SEM micrographs of hot compressed Ti64+B-Axial samples (Working condition: temperature 850^{o}C, strain rate 1 S^{-1})

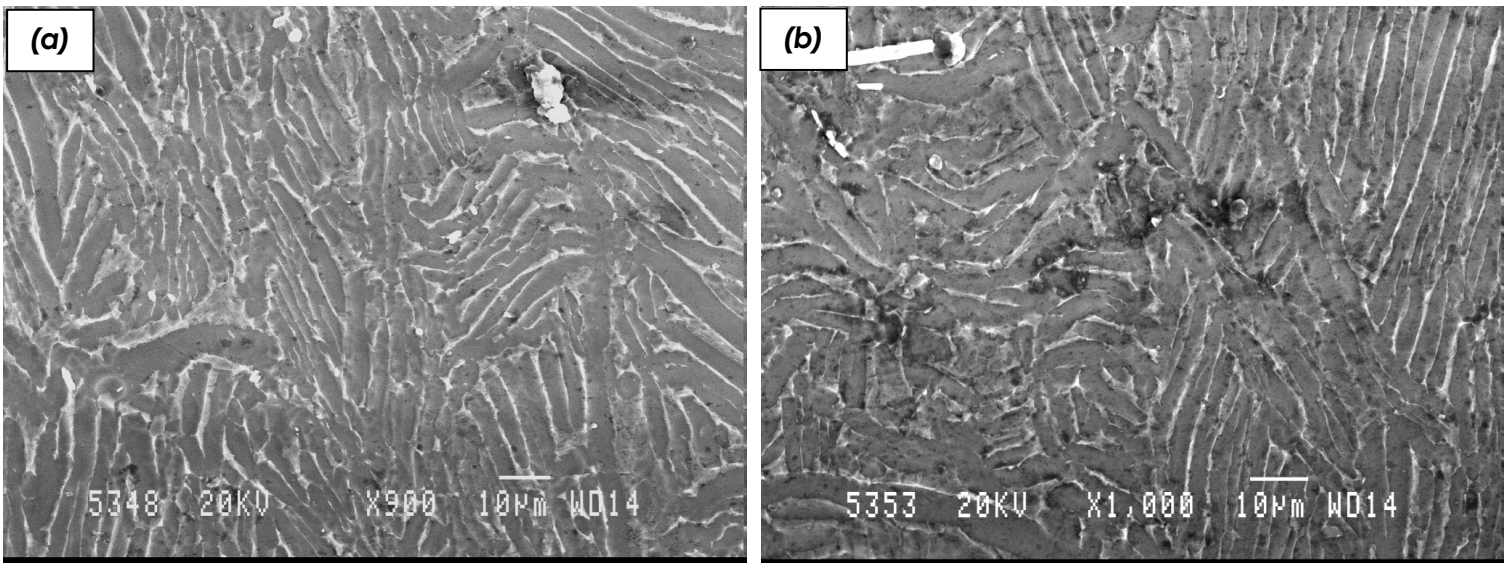

Fig. 45: SEM micrographs of hot compressed Ti64+B-Axial samples (Working condition: temperature 900^{o}C, strain rate 10^{-3} S^{-1})

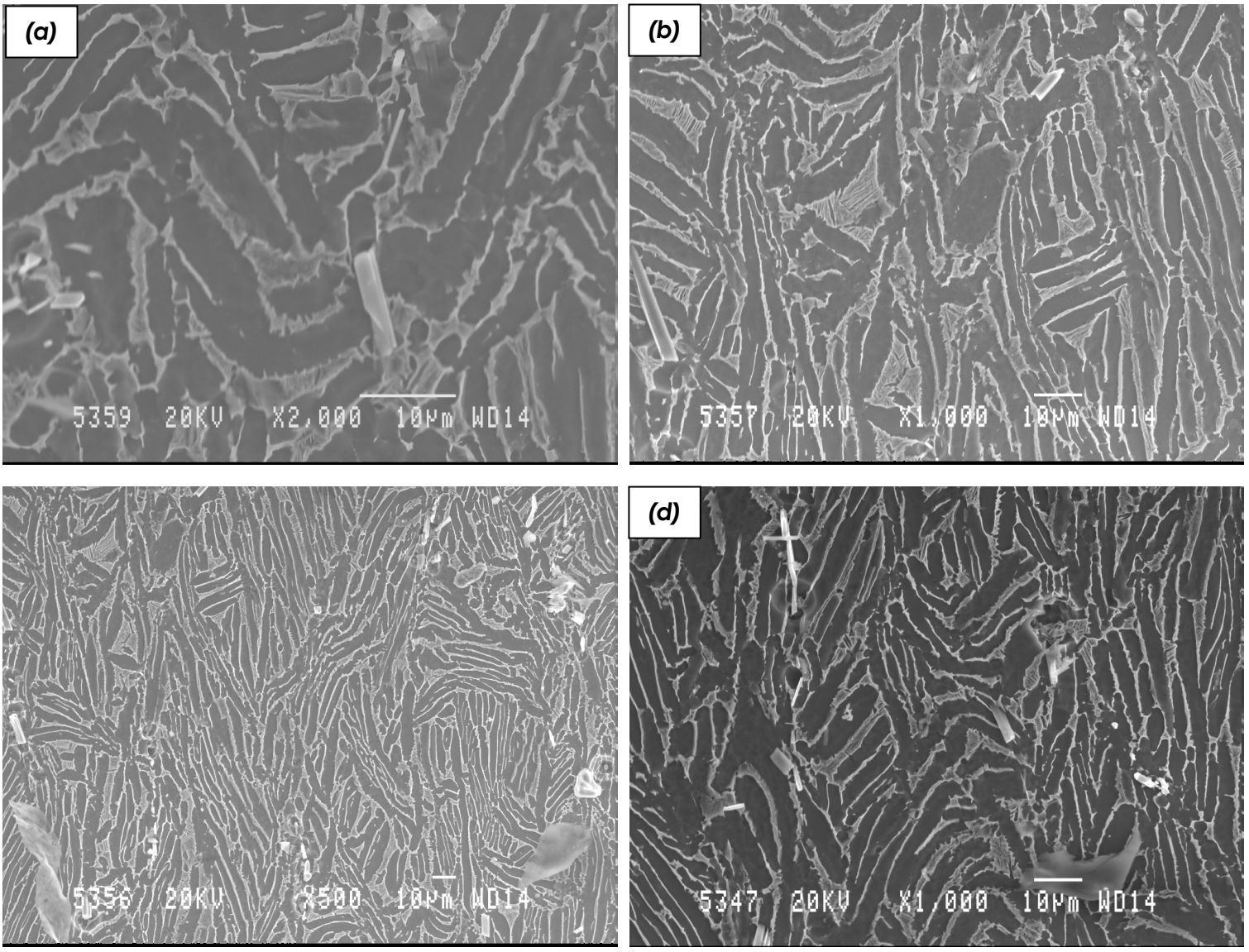

Fig. 46: SEM micrographs of hot compressed Ti64+B-Axial samples (Working condition: temperature 900^{o}C, strain rate 10^{-2} S^{-1})

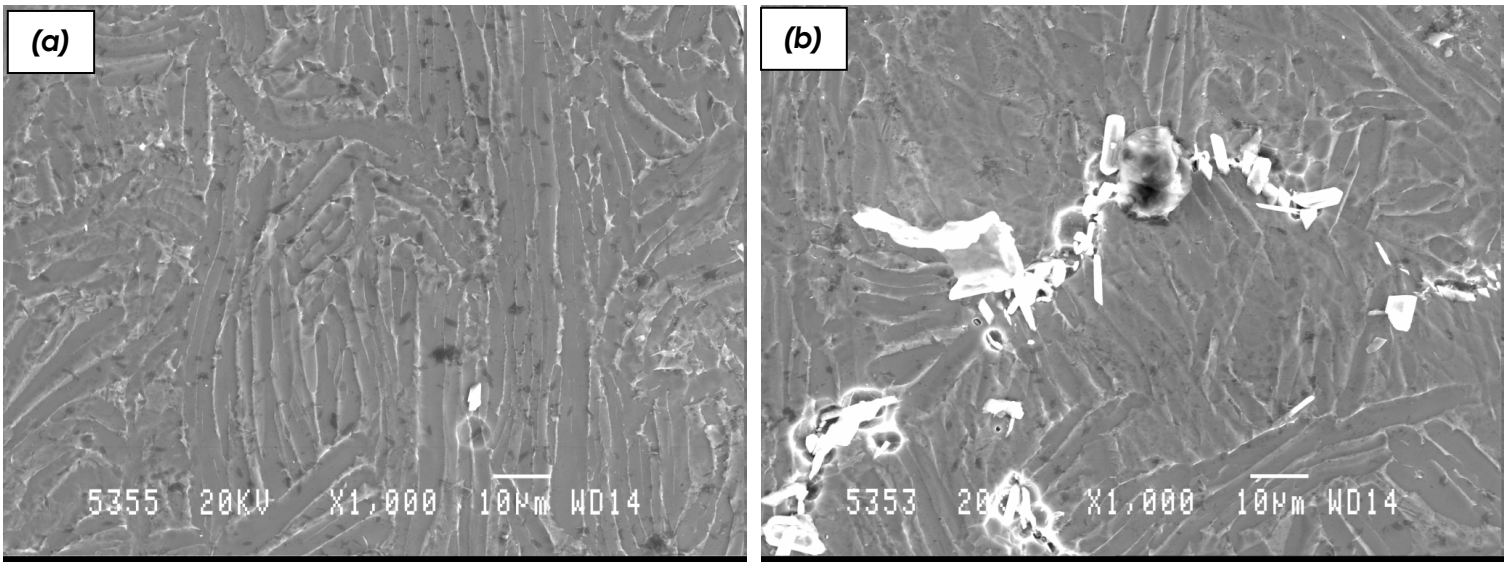

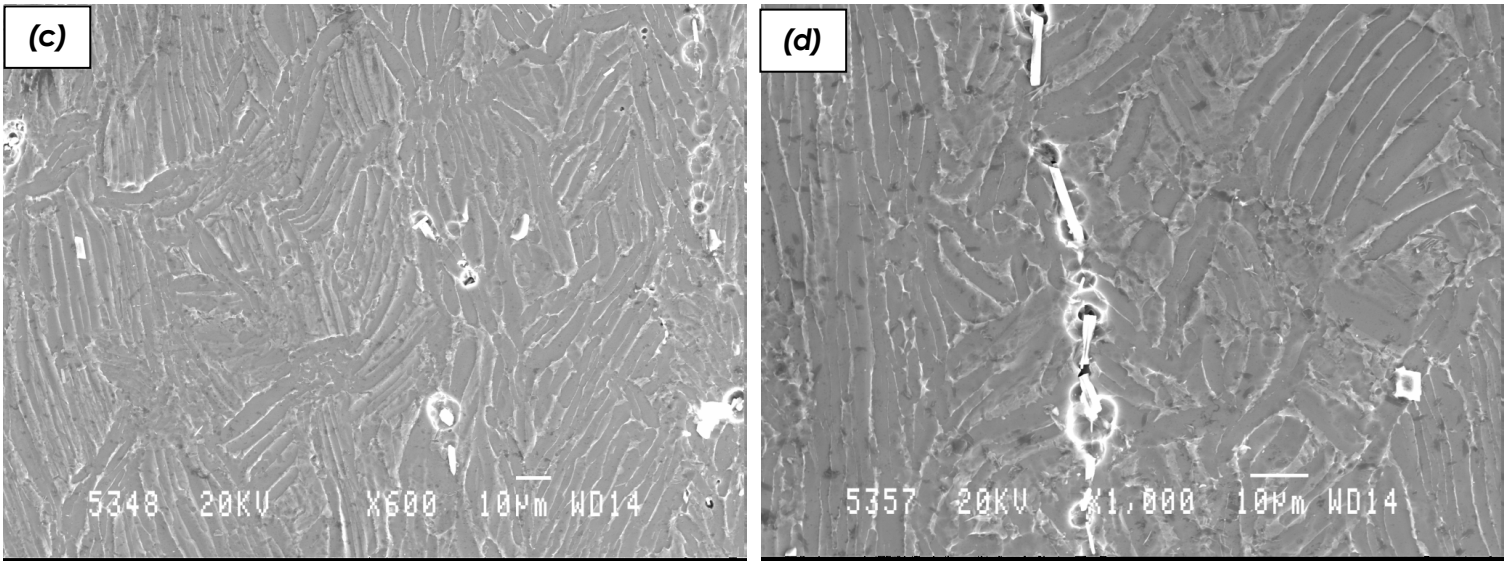

Fig. 47: SEM micrographs of hot compressed Ti64+B-Axial samples (Working condition: temperature 900^{o}C, strain rate 10^{-1} S^{-1})

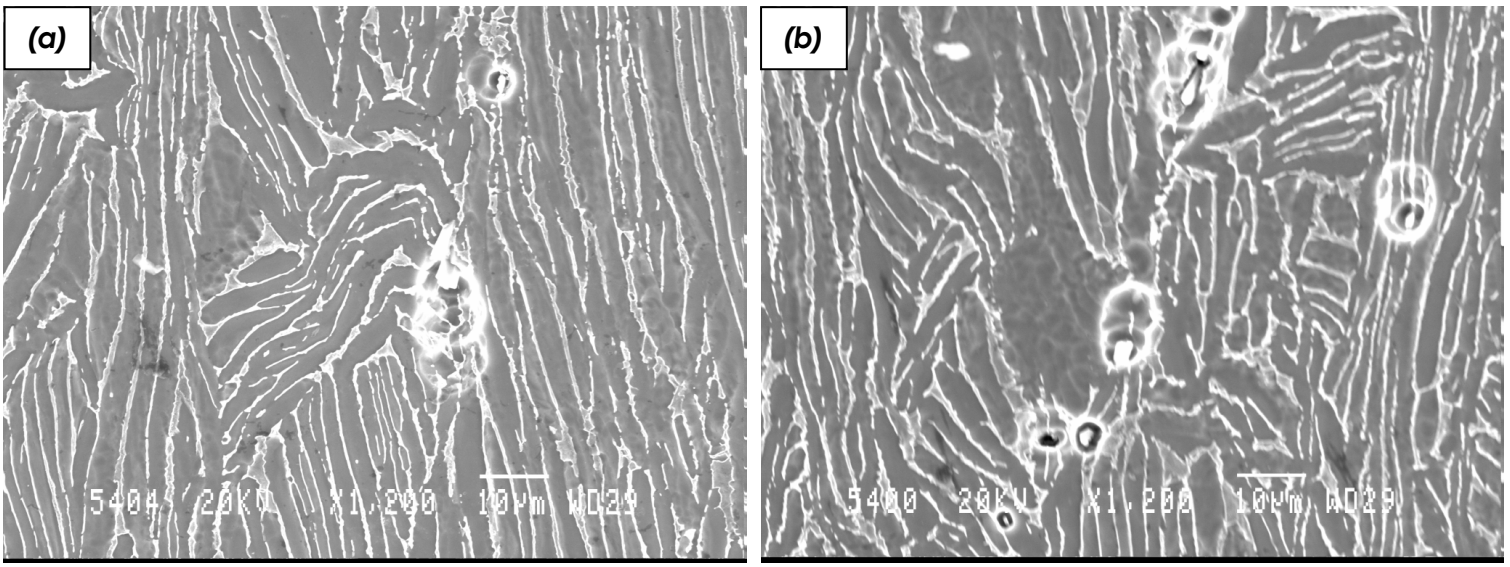

Fig. 48: SEM micrographs of hot compressed Ti64+B-Axial samples (Working condition: temperature 900^{o}C, strain rate 1 S^{-1})

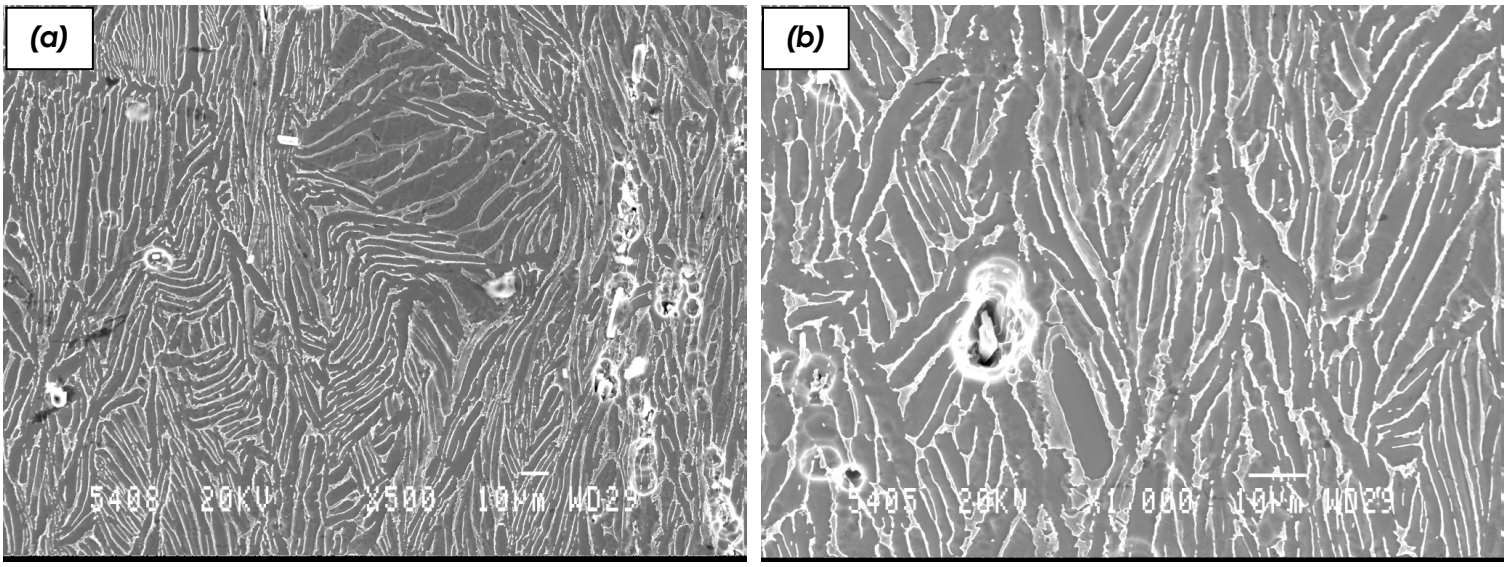

Fig. 49: SEM micrographs of hot compressed Ti64+B-Axial samples (Working condition: temperature 900^{o}C, strain rate 1 S^{-1})

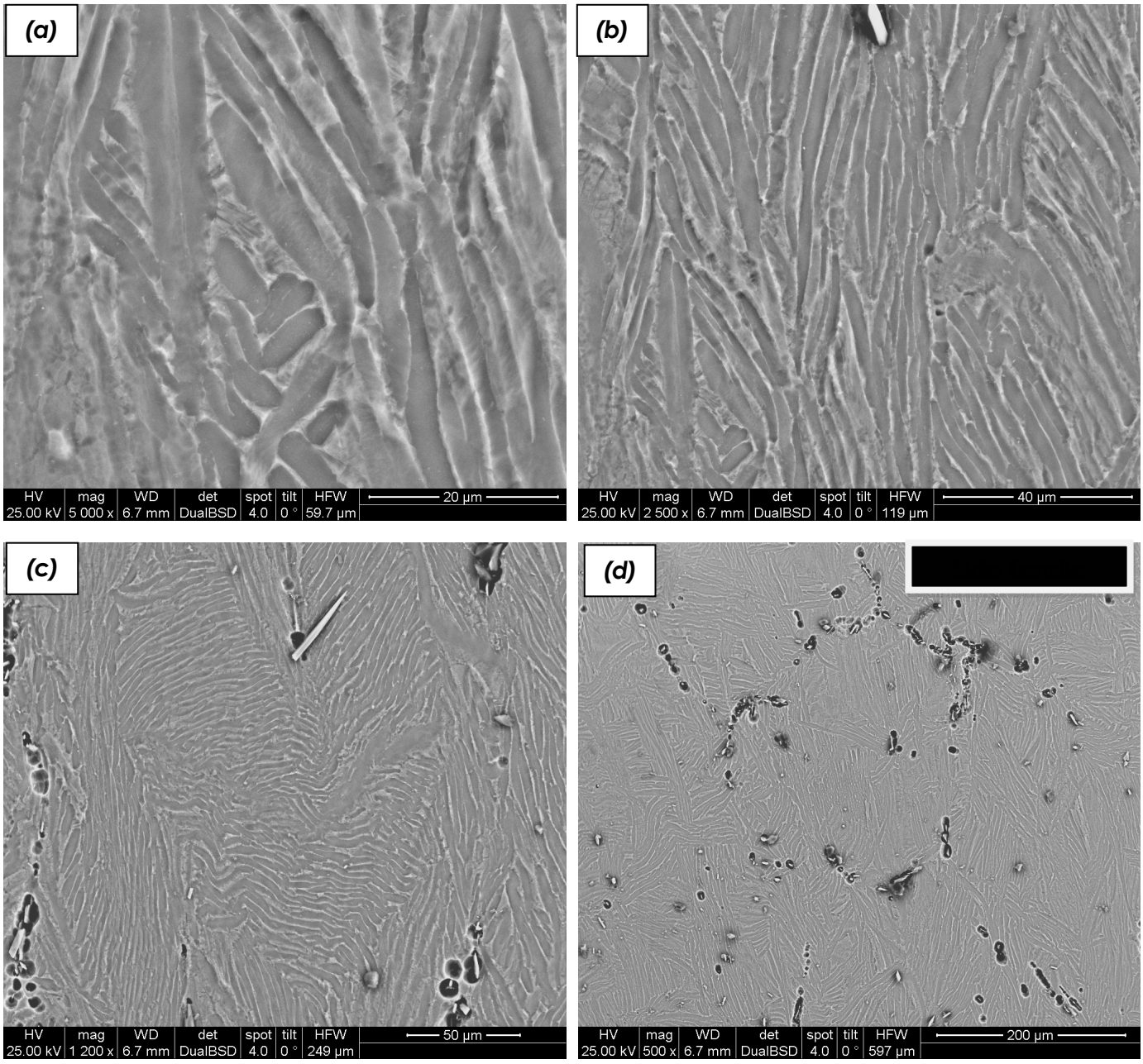

Fig. 50: SEM micrographs of hot compressed Ti64+B-Axial samples (Working condition: temperature 900^{o}C, strain rate 10 S^{-1})

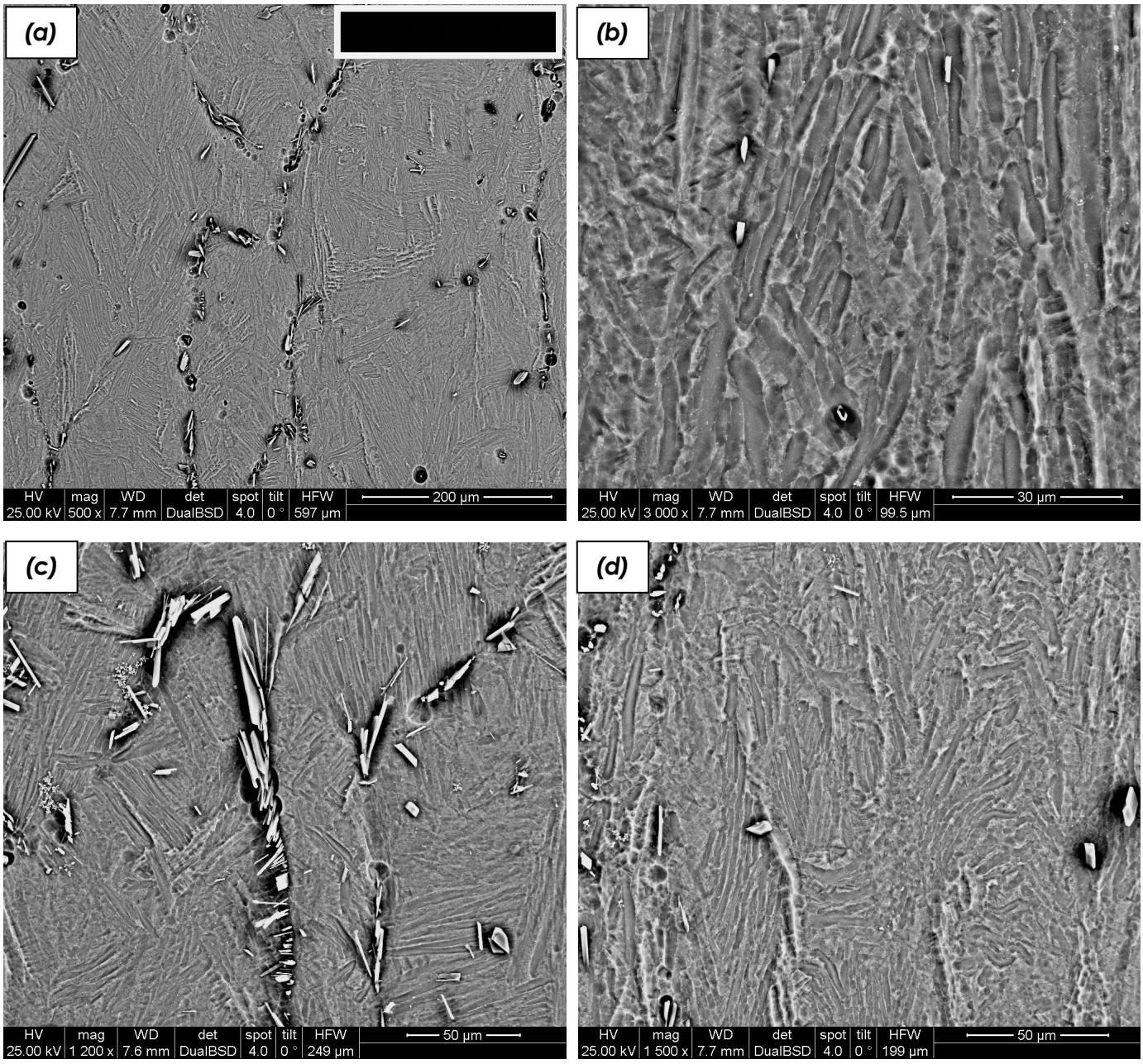

Fig. 51: SEM micrographs of hot compressed Ti64+B-Axial samples (Working condition: temperature 950^{o}C, strain rate 10^{-2} S^{-1})

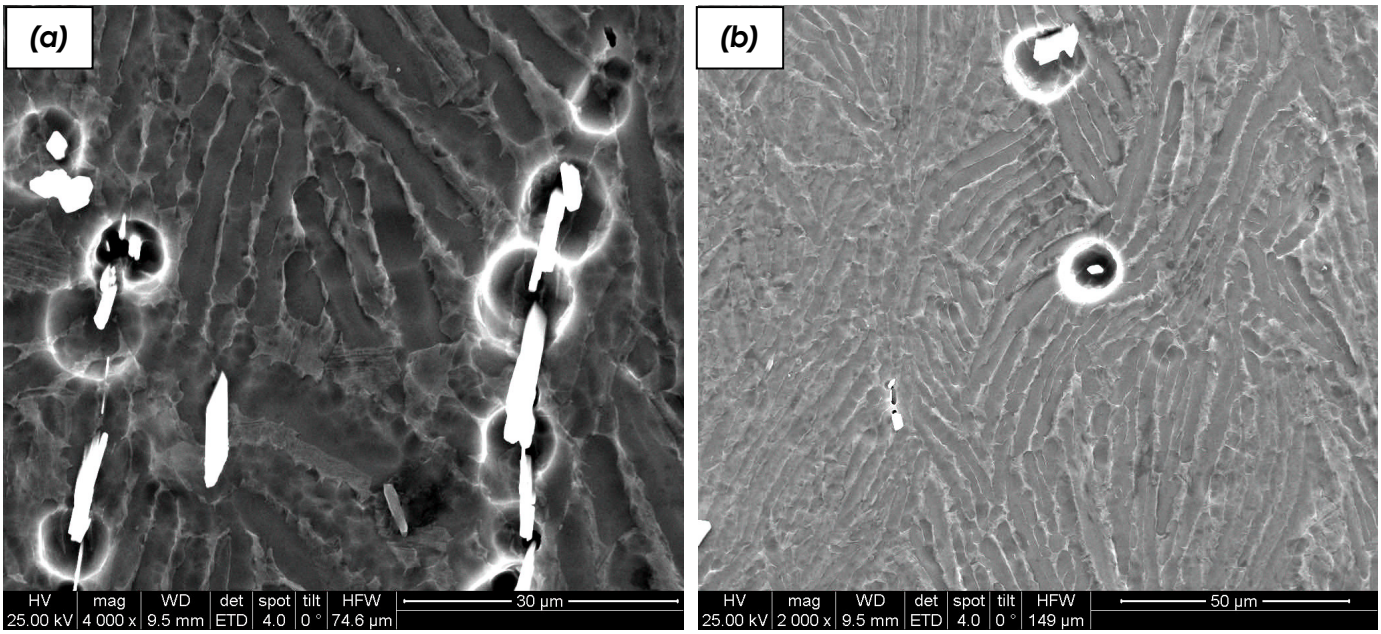

Fig. 52: SEM micrographs of hot compressed Ti64+B-Axial samples (Working condition: temperature 950^{o}C, strain rate 1 S^{-1})

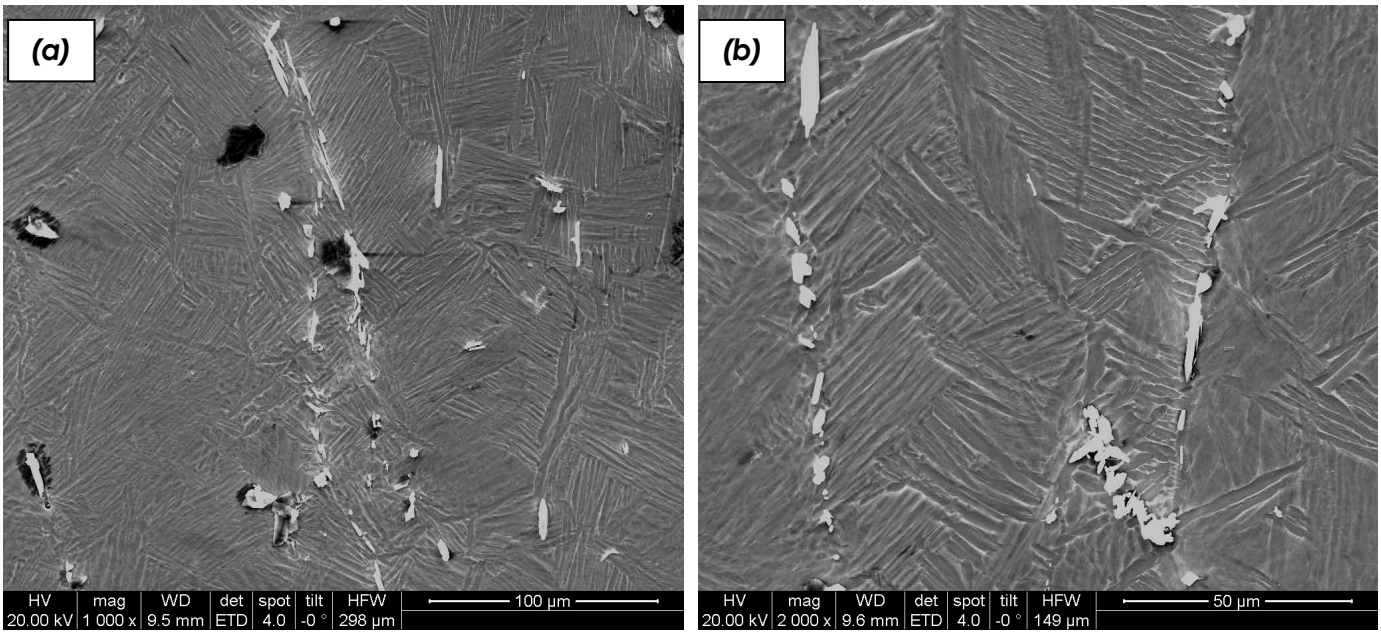

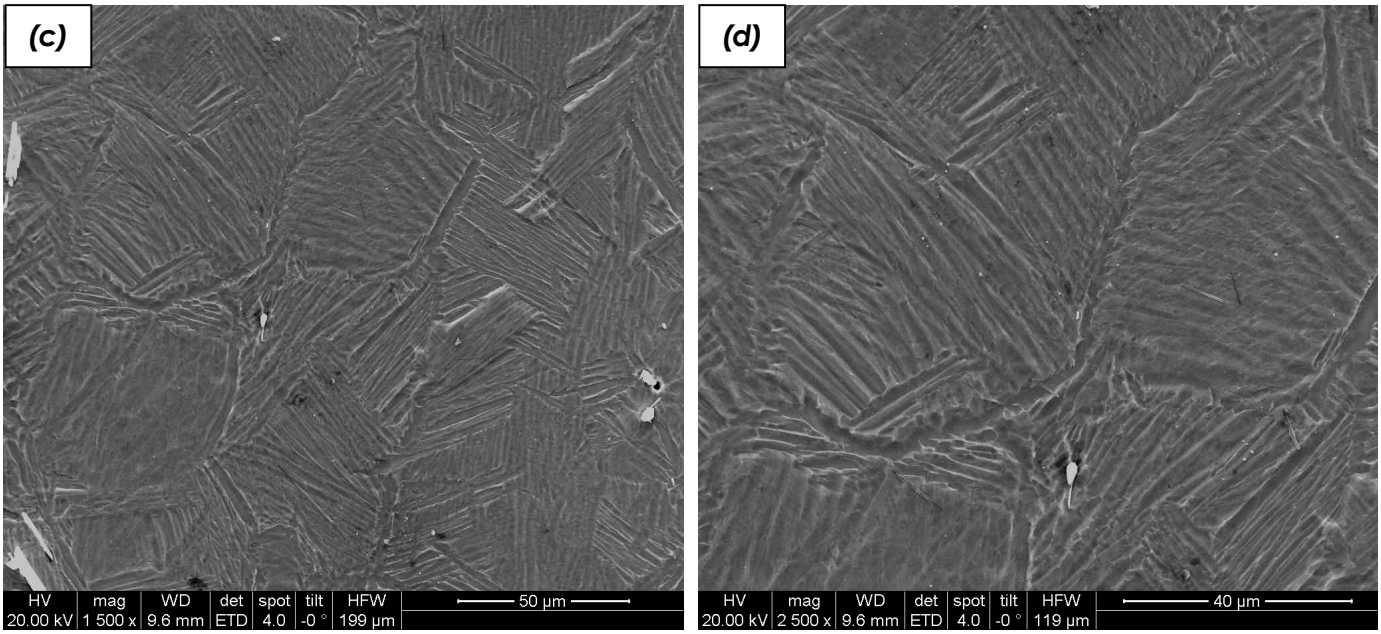

Fig. 53: SEM micrographs of hot compressed Ti64+B-Axial samples (Working condition: temperature 1000^{o}C, strain rate 10^{-2} S^{-1})

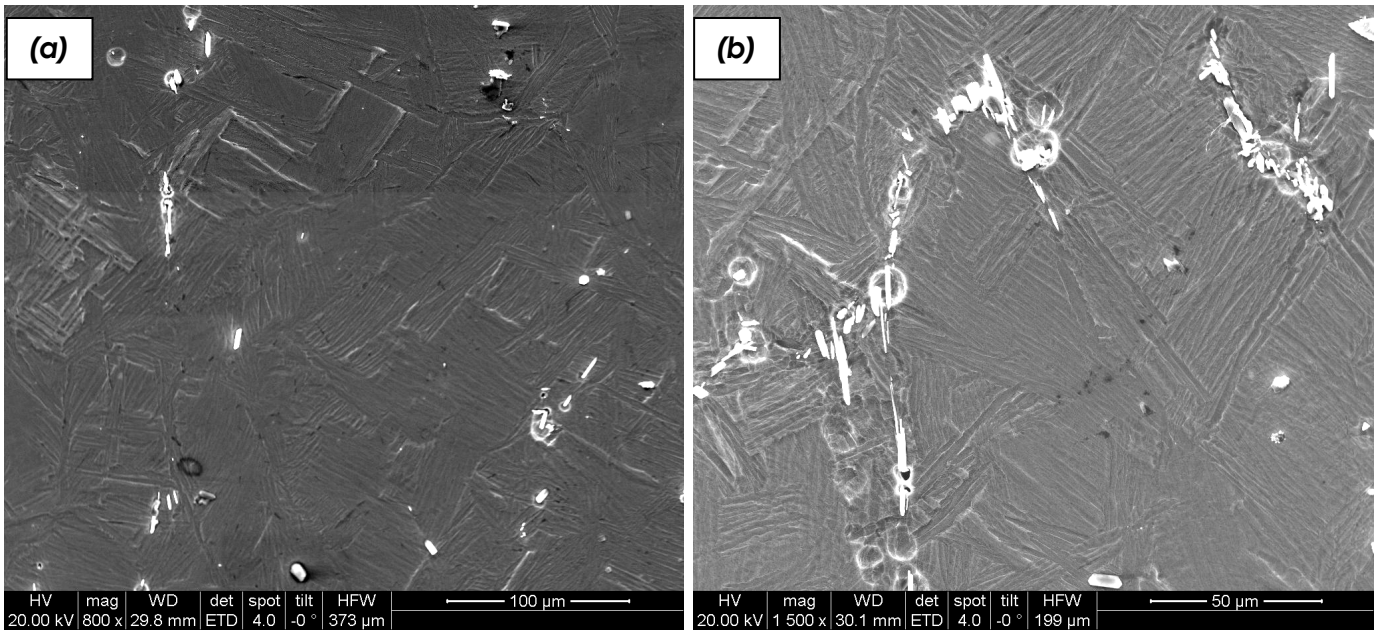

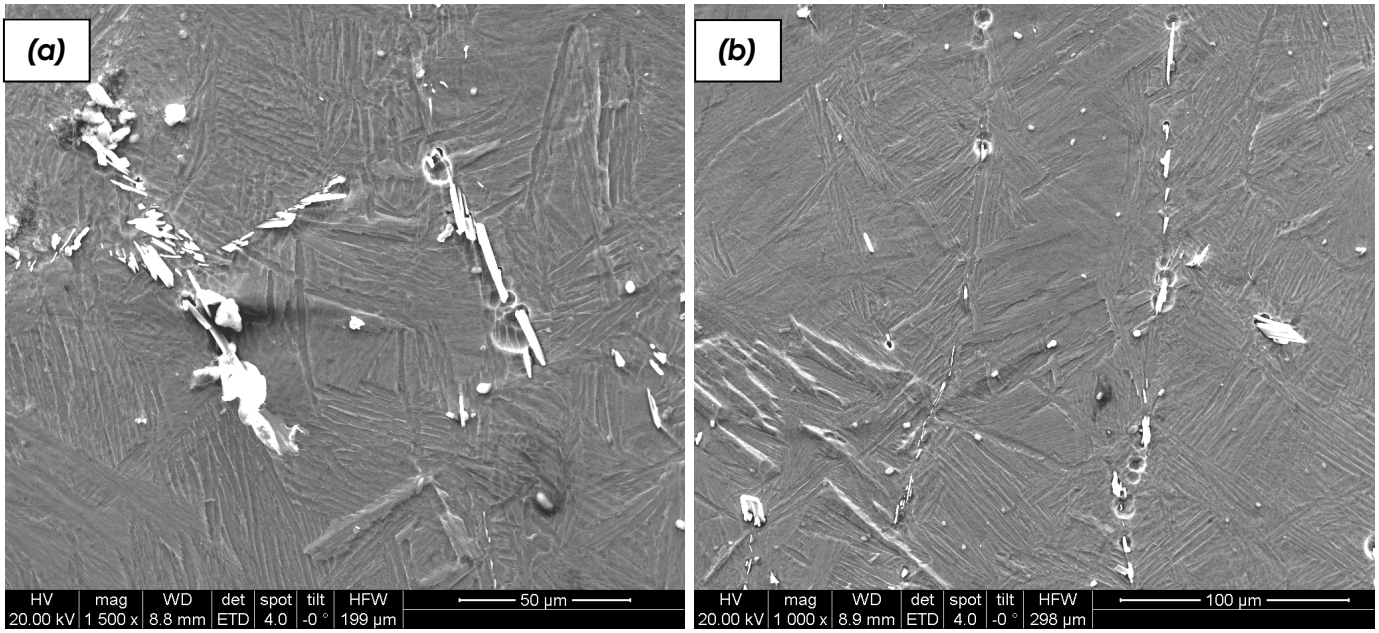

Fig. 54: SEM micrographs of hot compressed Ti64+B-Axial samples (Working condition: temperature 1000^{o}C, strain rate 1 S^{-1})

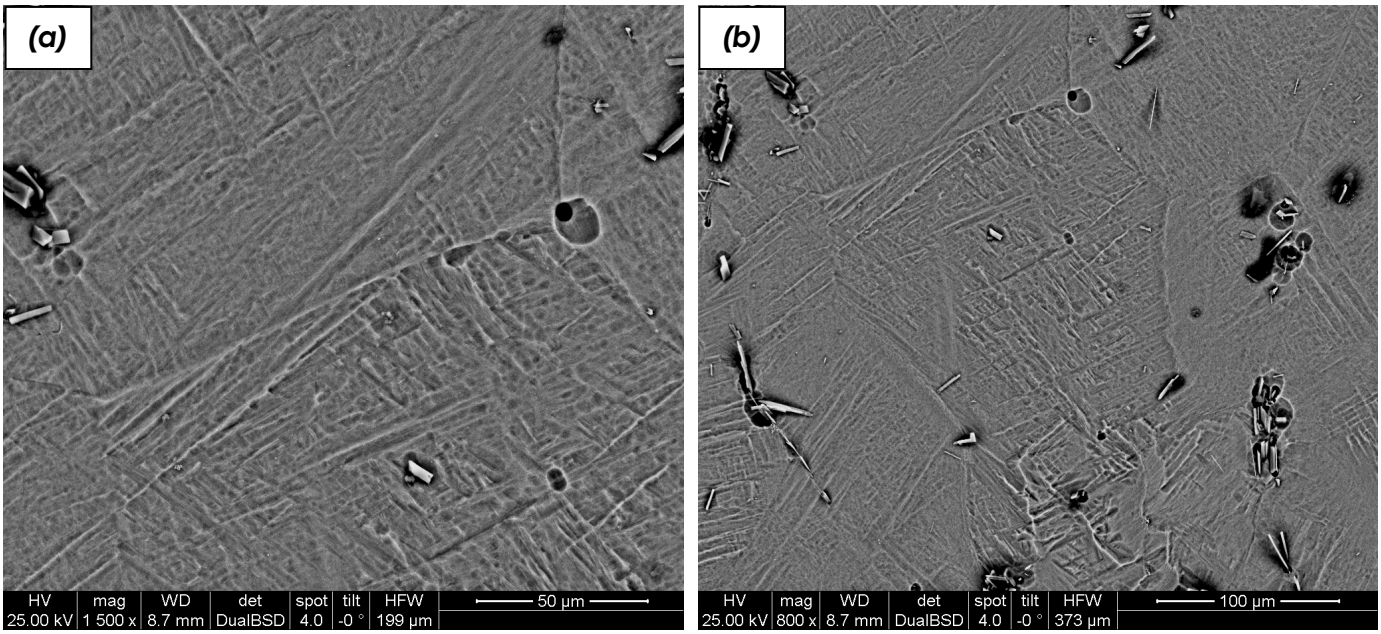

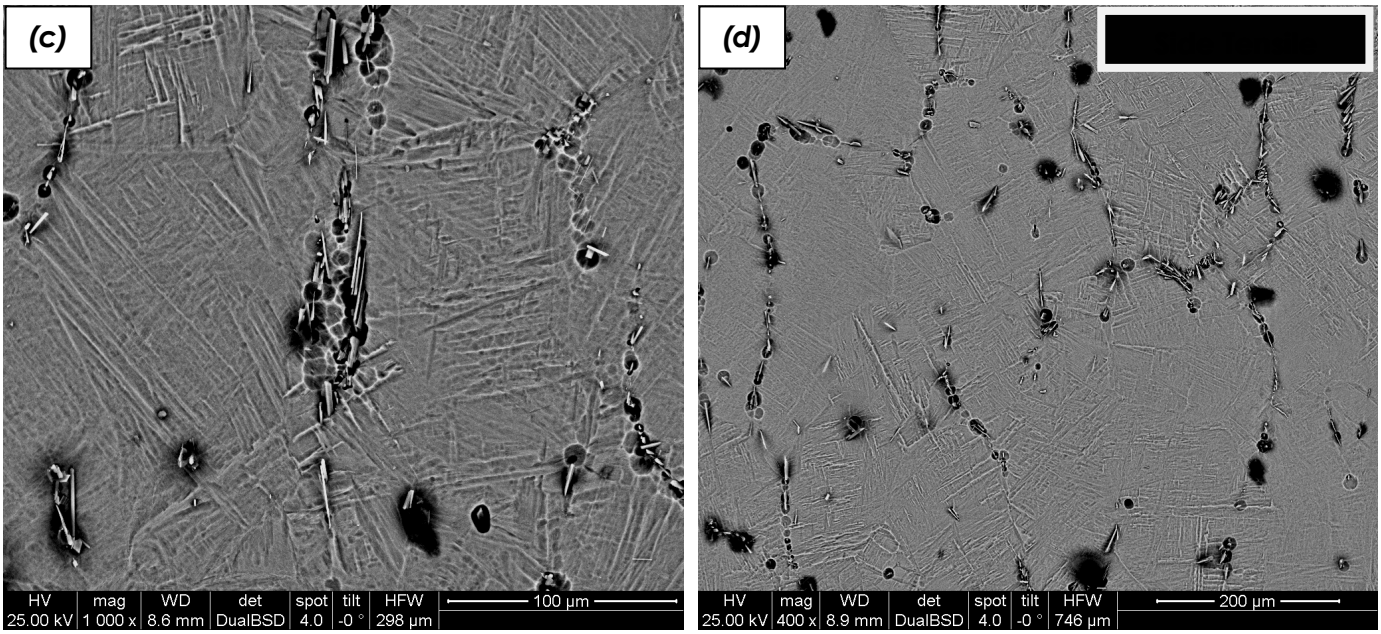

Fig. 55: SEM micrographs of hot compressed Ti64+B-Axial samples (Working condition: temperature 1000^{o}C, strain rate 10 S^{-1})

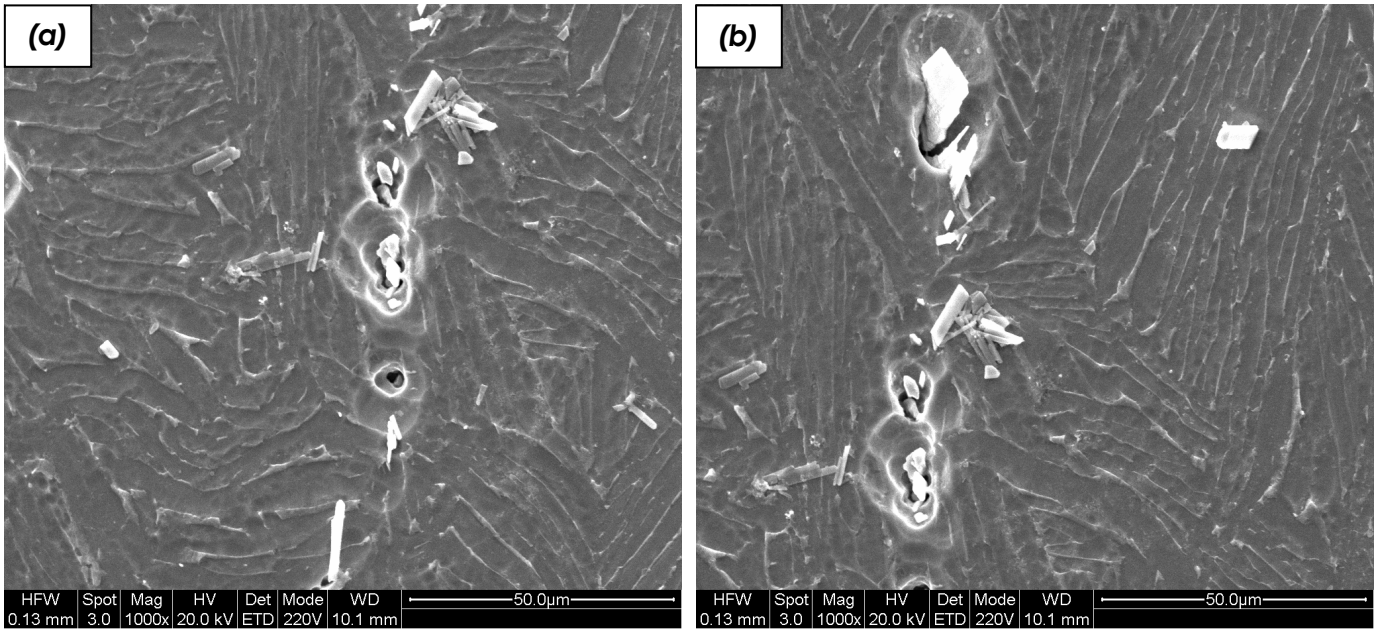

Fig. 56: SEM micrographs of hot compressed Ti64+B-Radial samples (Working condition: temperature 750^{o}C, strain rate 10^{-3} S^{-1})

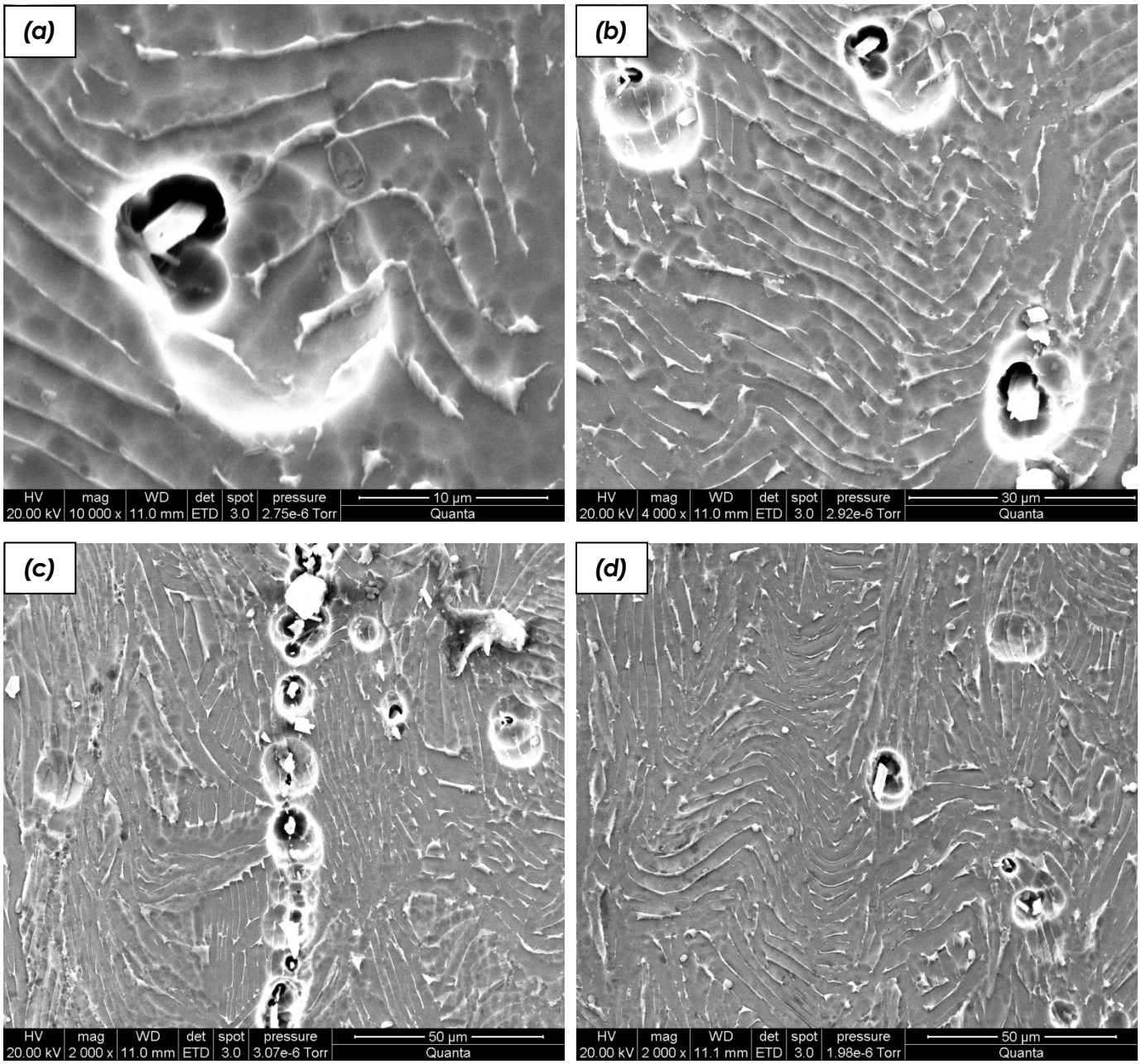

Fig. 57: SEM micrographs of hot compressed Ti64+B-Radial samples (Working condition: temperature 750^{o}C, strain rate 10^{-2} S^{-1})

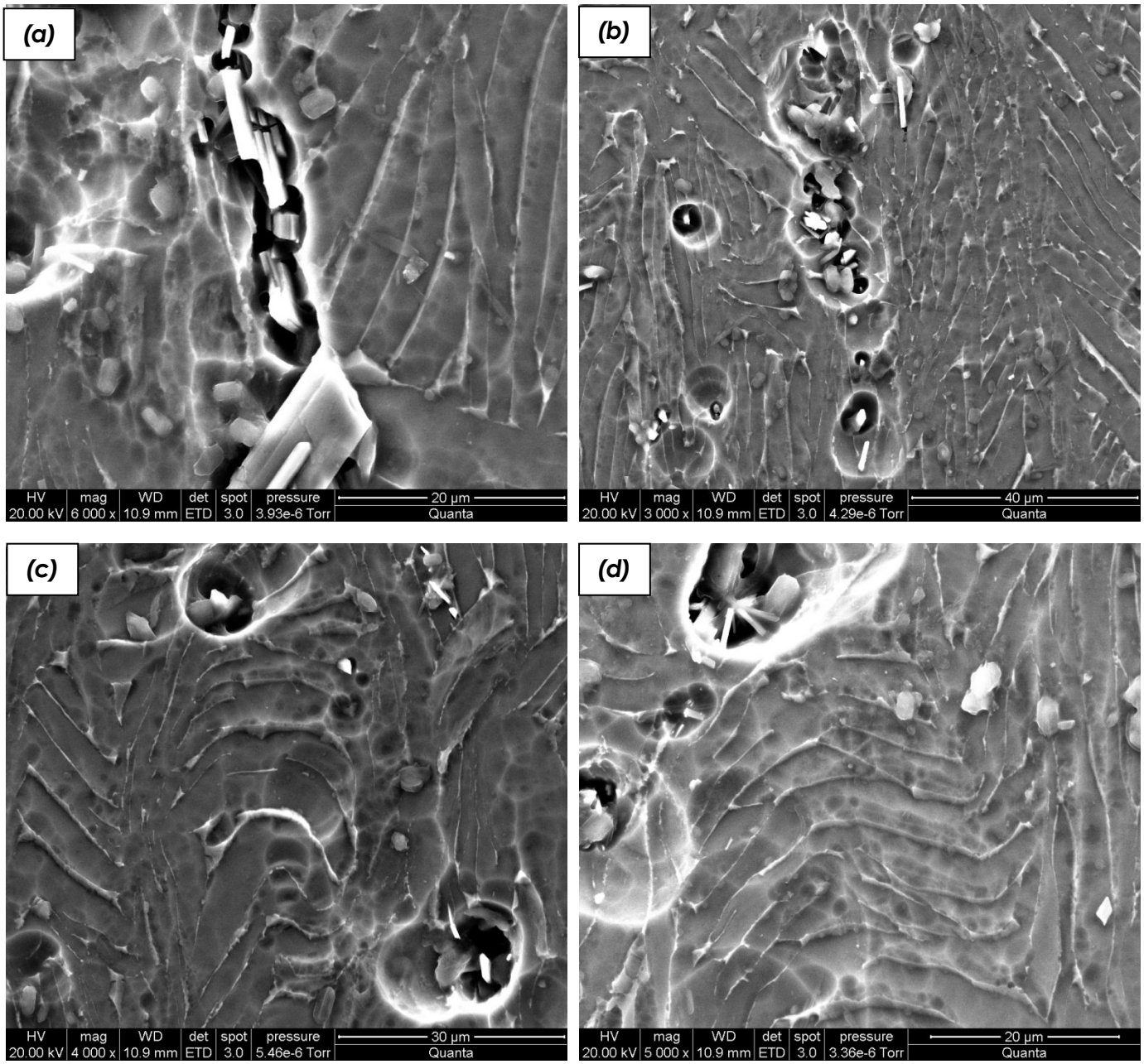

Fig. 58: SEM micrographs of hot compressed Ti64+B-Radial samples (Working condition: temperature 750^{o}C, strain rate 10^{-1} S^{-1})

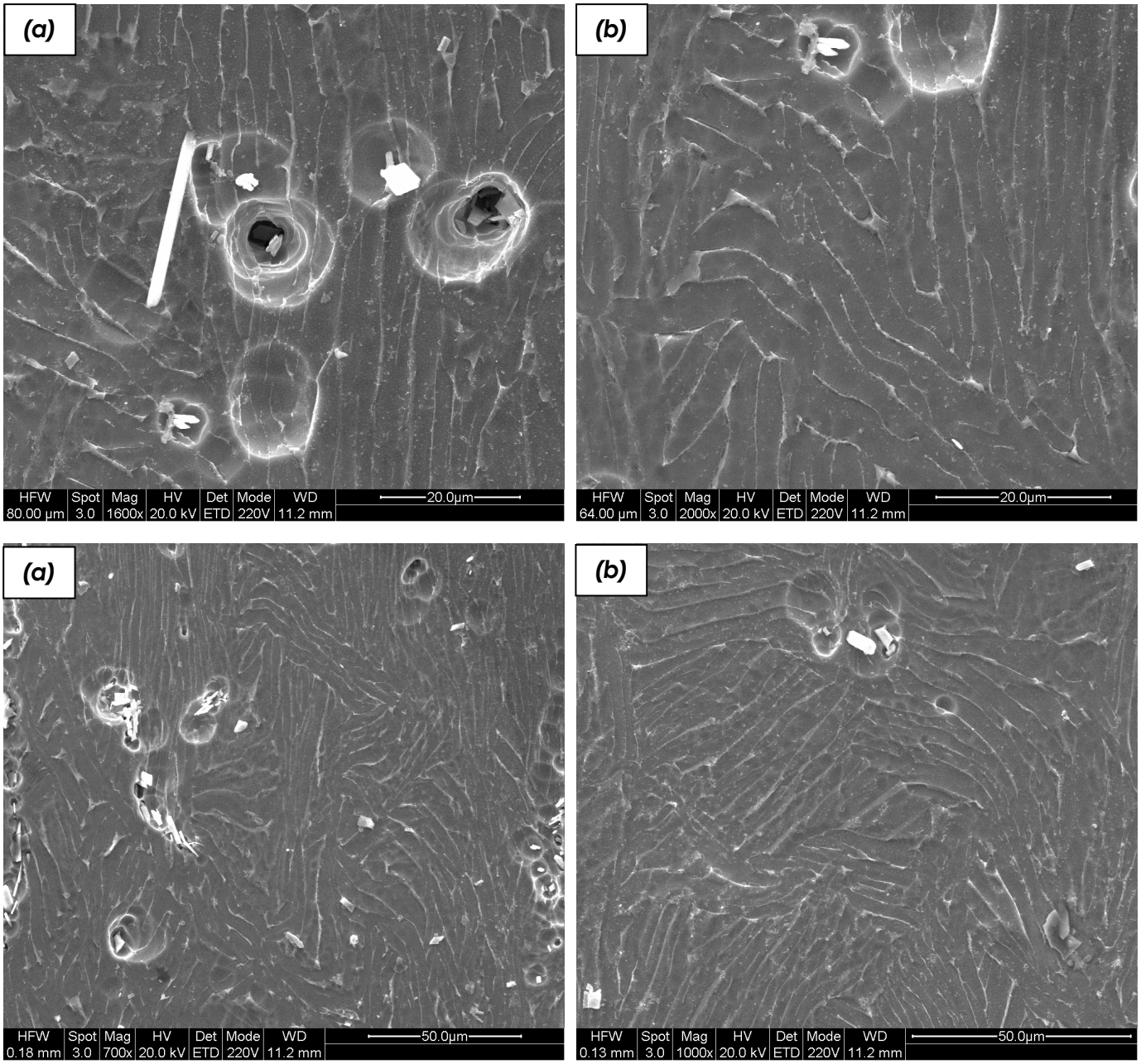

Fig. 59: SEM micrographs of hot compressed Ti64+B-Radial samples (Working condition: temperature 750^{o}C, strain rate 1 S^{-1})

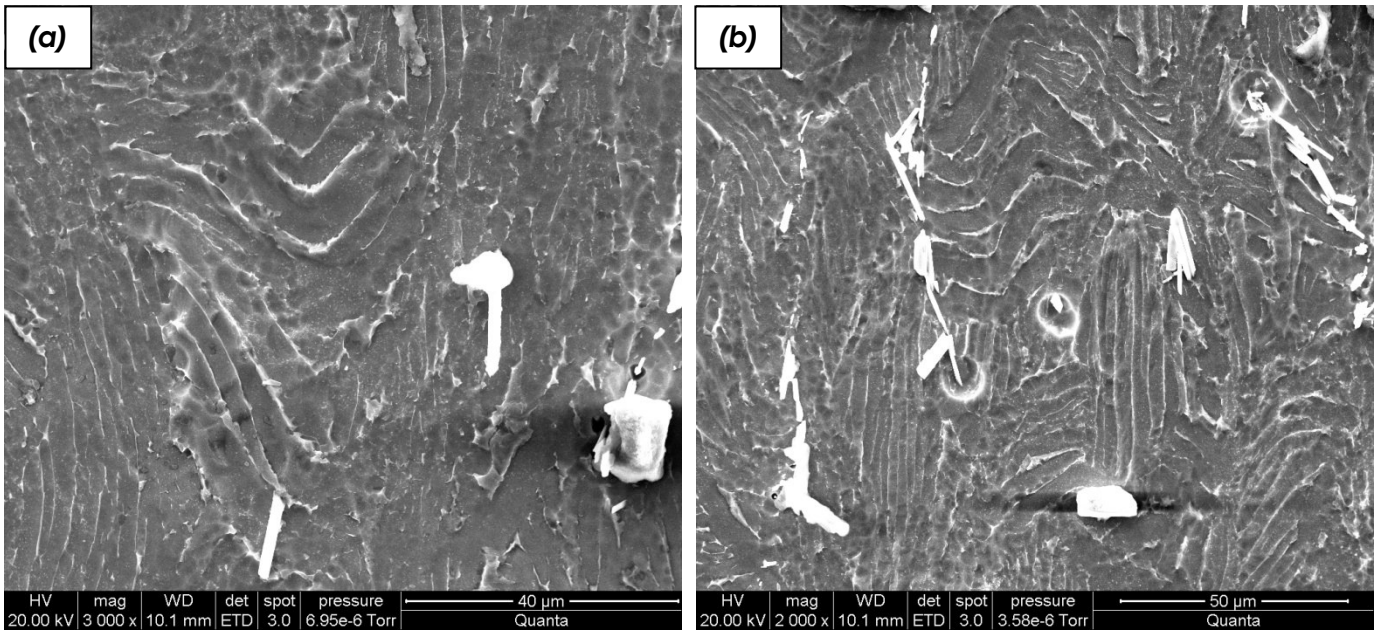

Fig. 60: SEM micrographs of hot compressed Ti64+B-Radial samples (Working condition: temperature 800^{o}C, strain rate 10^{-3} S^{-1})

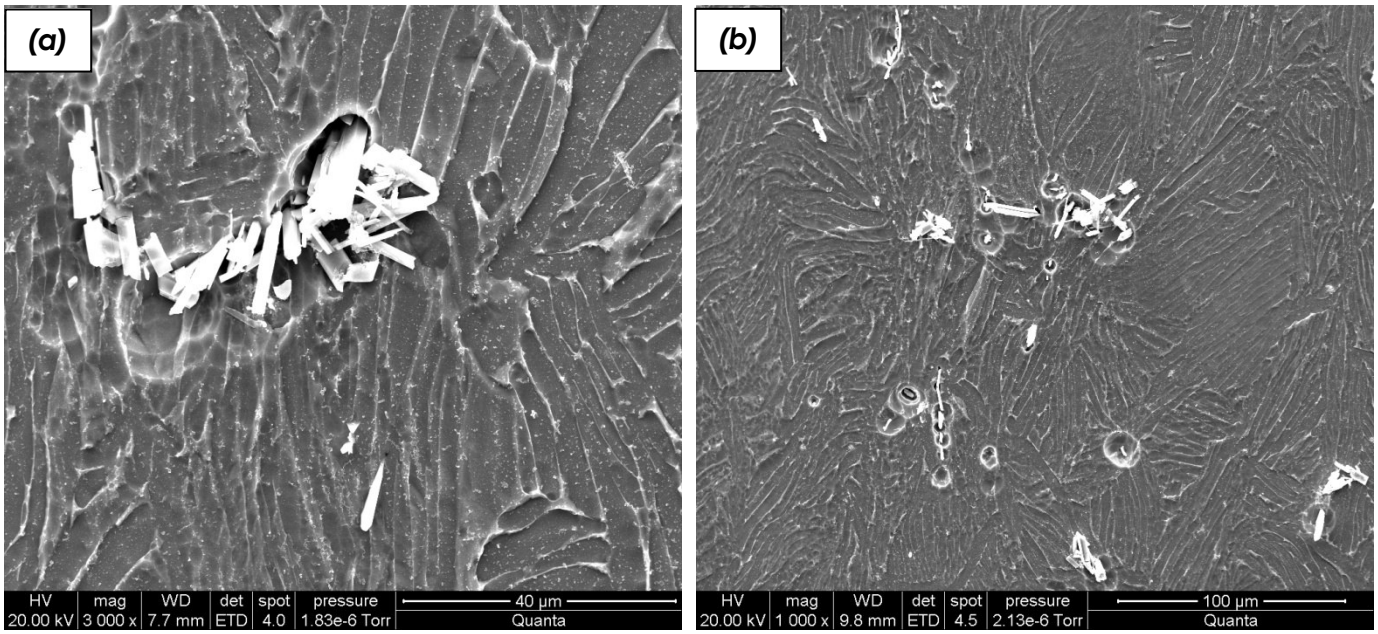

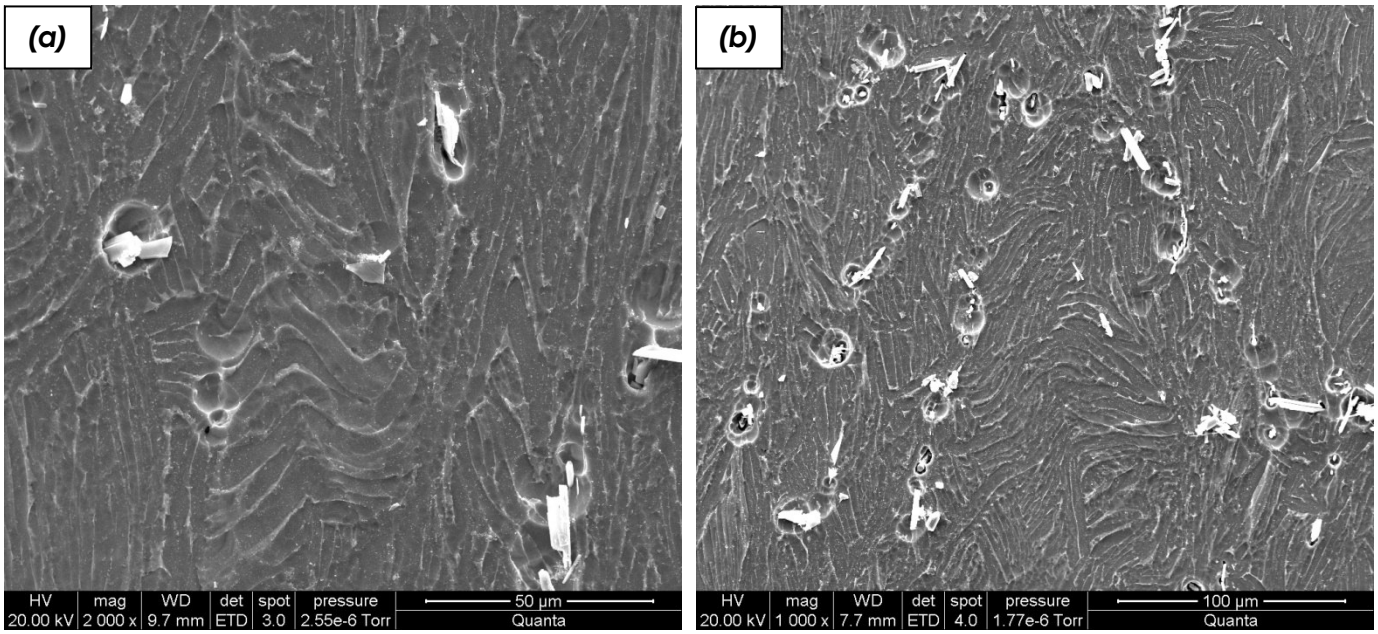

Fig. 61: SEM micrographs of hot compressed Ti64+B-Radial samples (Working condition: temperature 800^{o}C, strain rate 10^{-2} S^{-1})

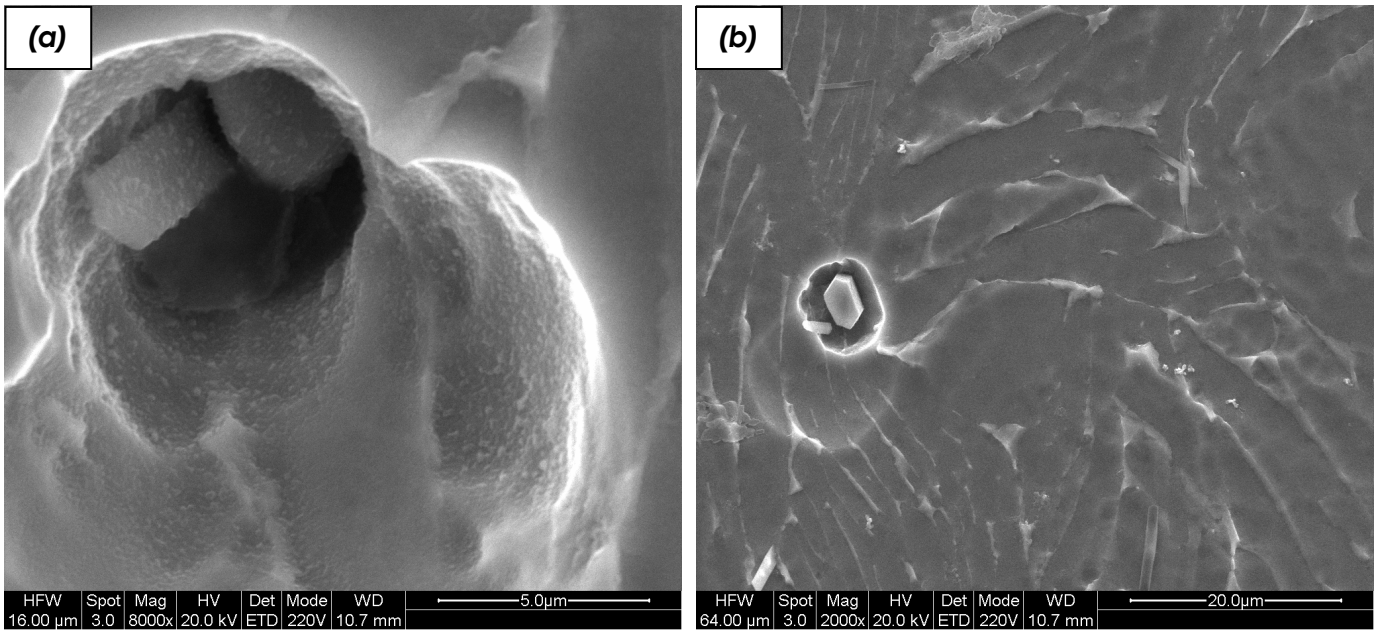

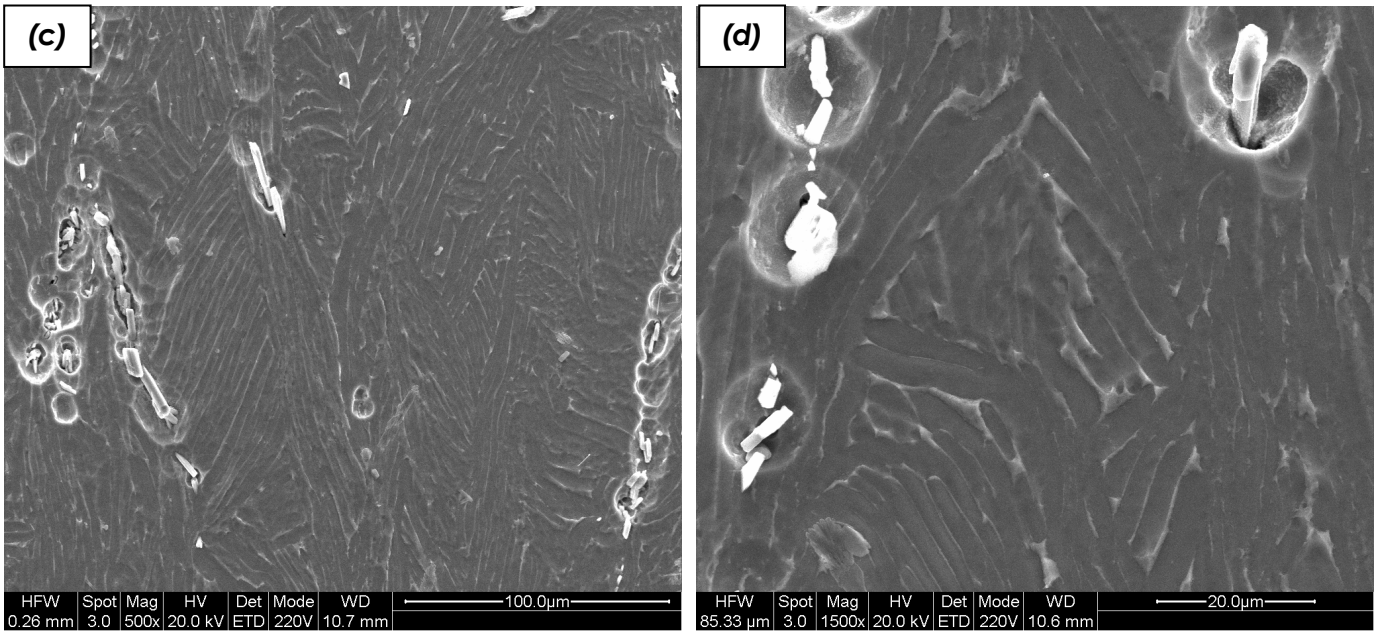

Fig. 62: SEM micrographs of hot compressed Ti64+B-Radial samples (Working condition: temperature 800^{o}C, strain rate 10^{-1} S^{-1})

Fig. 63: SEM micrographs of hot compressed Ti64+B-Radial samples (Working condition: temperature 800^{o}C, strain rate 1 S^{-1})

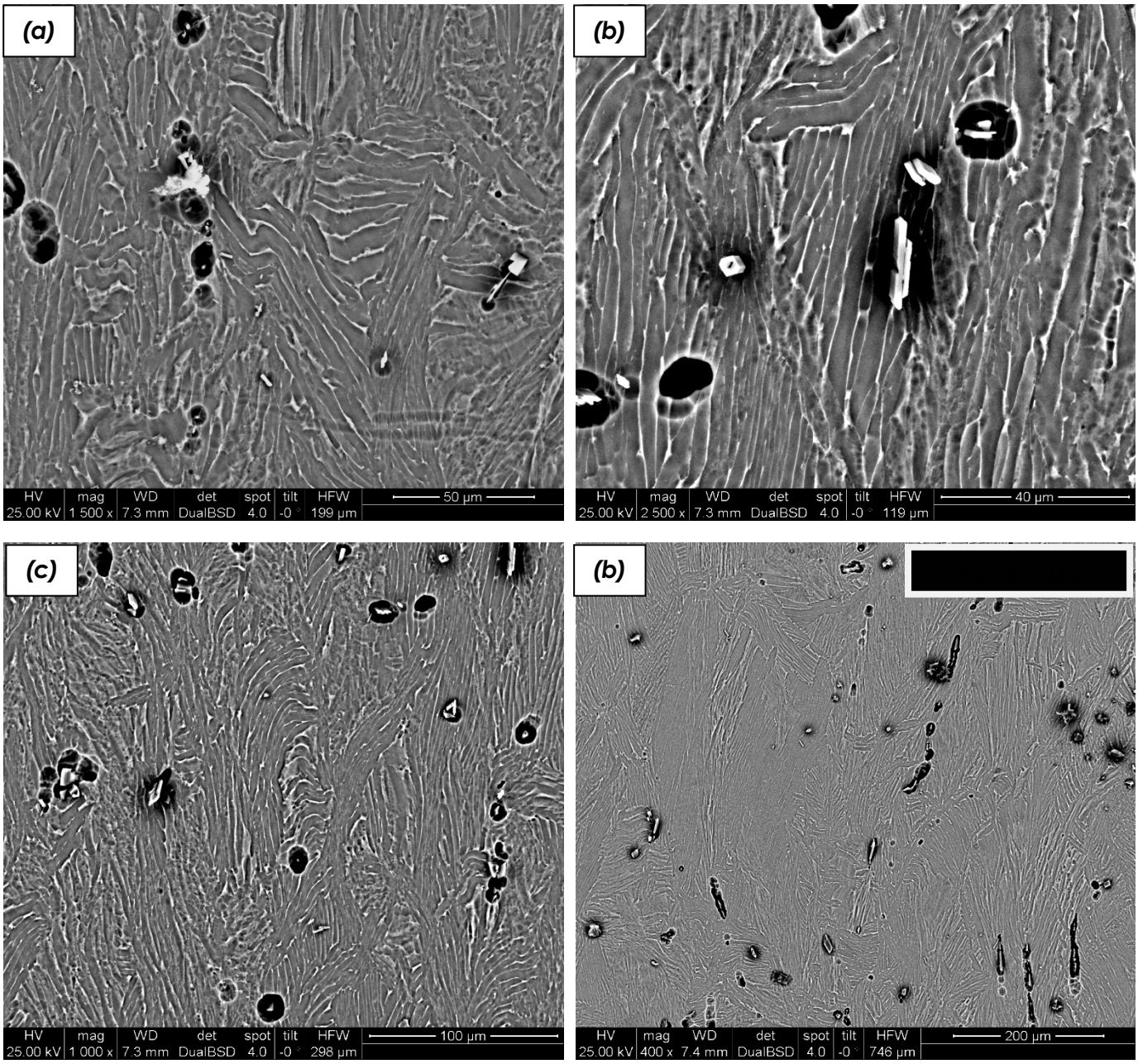

Fig. 64: SEM micrographs of hot compressed Ti64+B-Radial samples (Working condition: temperature 800^{o}C, strain rate 10 S^{-1})

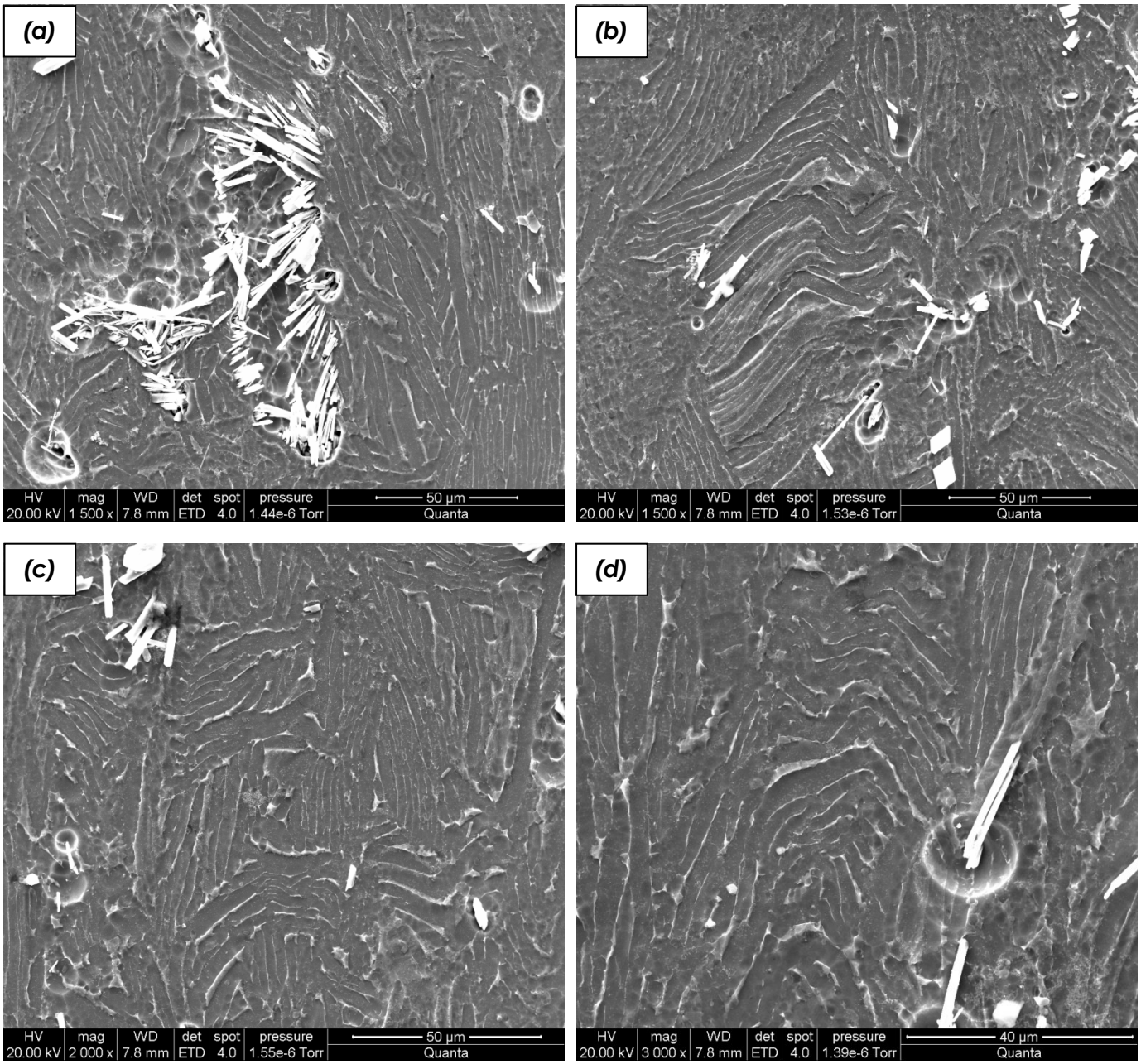

Fig. 65: SEM micrographs of hot compressed Ti64+B-Radial samples (Working condition: temperature 850^{o}C, strain rate 10^{-3} S^{-1})

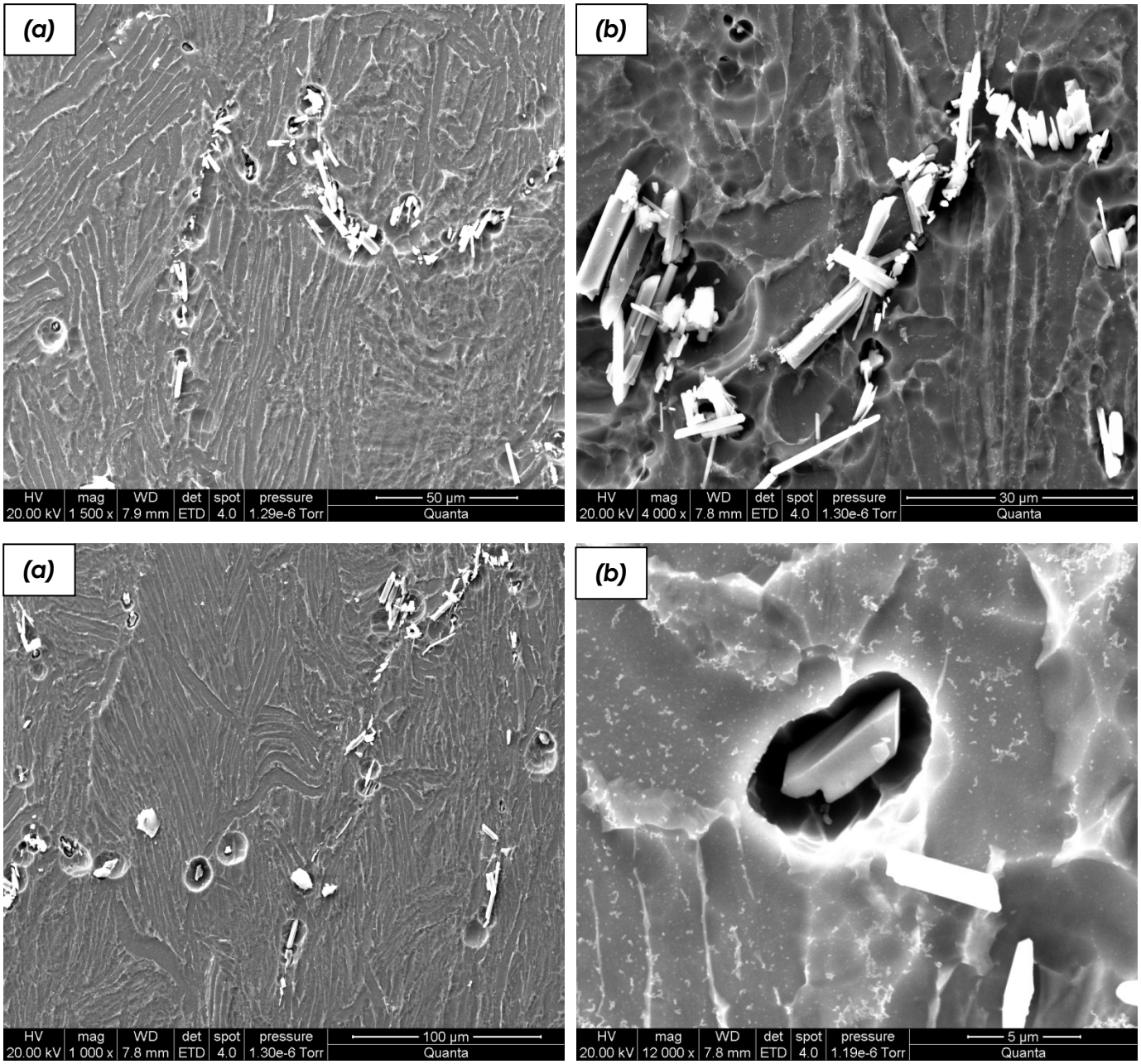

Fig. 66: SEM micrographs of hot compressed Ti64+B-Radial samples (Working condition: temperature 850^{o}C, strain rate 10^{-2} S^{-1})

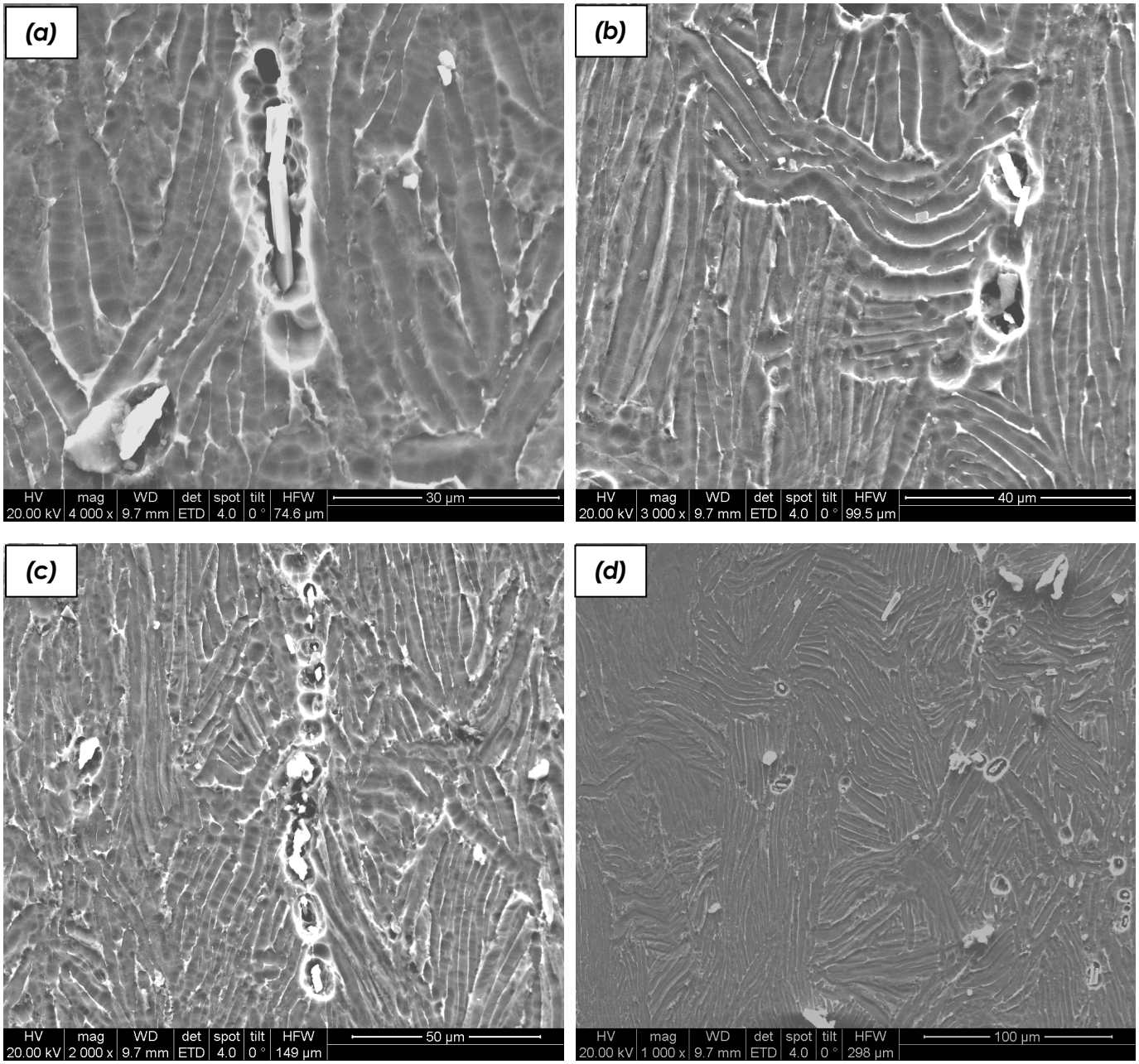

Fig. 67: SEM micrographs of hot compressed Ti64+B-Radial samples (Working condition: temperature 850^{o}C, strain rate 10^{-1} S^{-1})

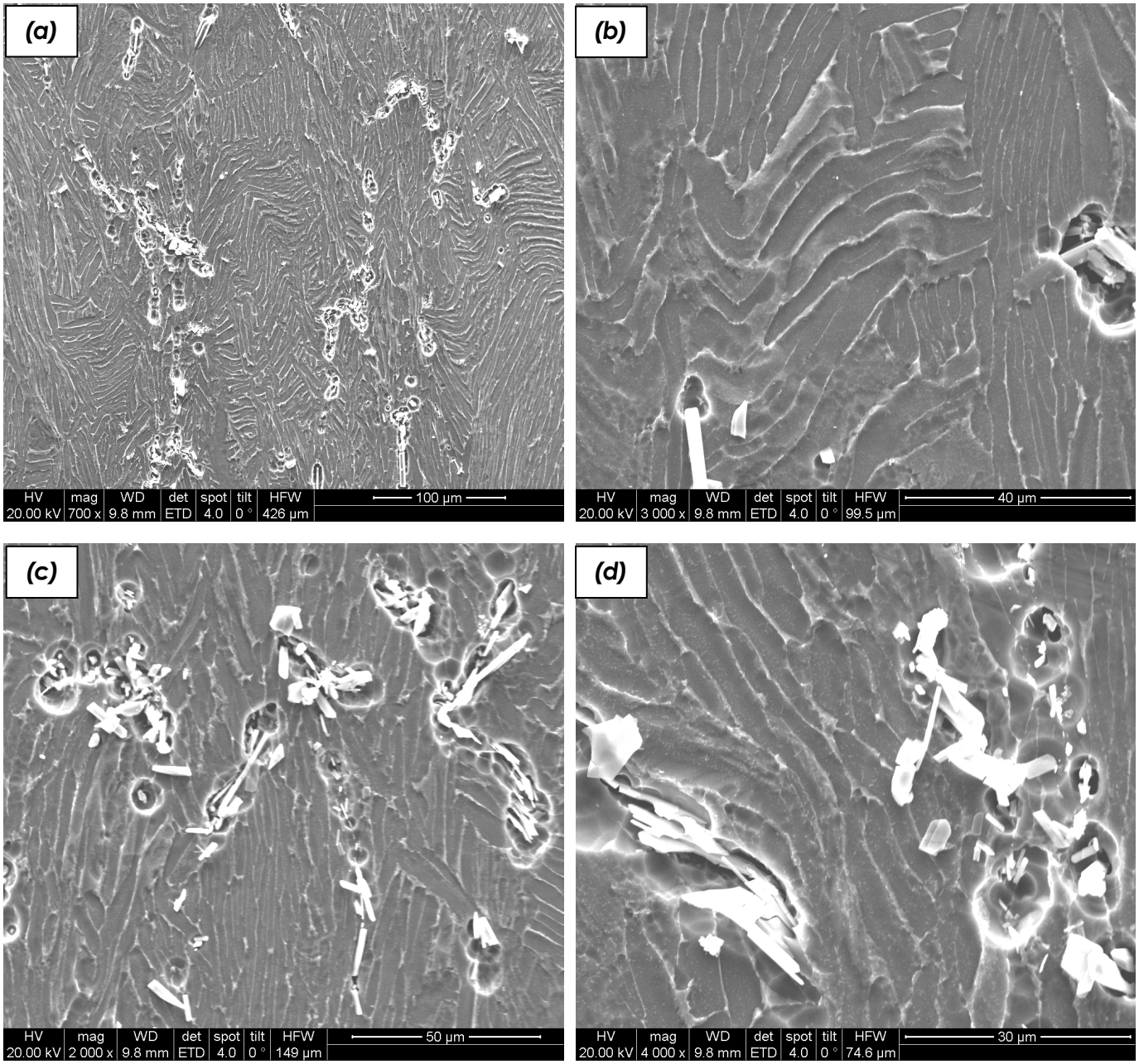

Fig. 68: SEM micrographs of hot compressed Ti64+B-Radial samples (Working condition: temperature 850^{o}C, strain rate 1 S^{-1})

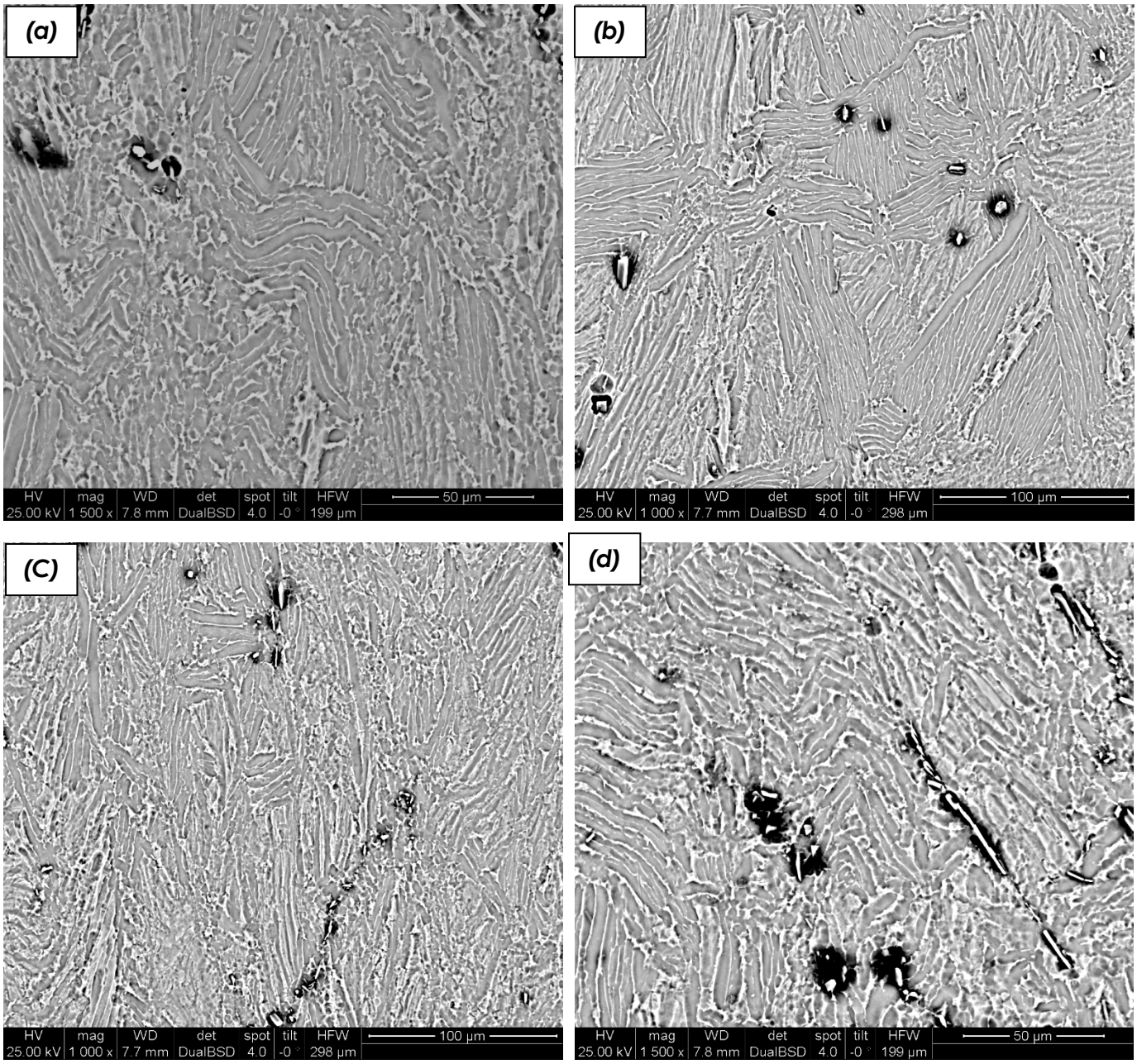

Fig. 69: SEM micrographs of hot compressed Ti64+B-Radial samples (Working condition: temperature 900^{o}C, strain rate 10^{-3} S^{-1})

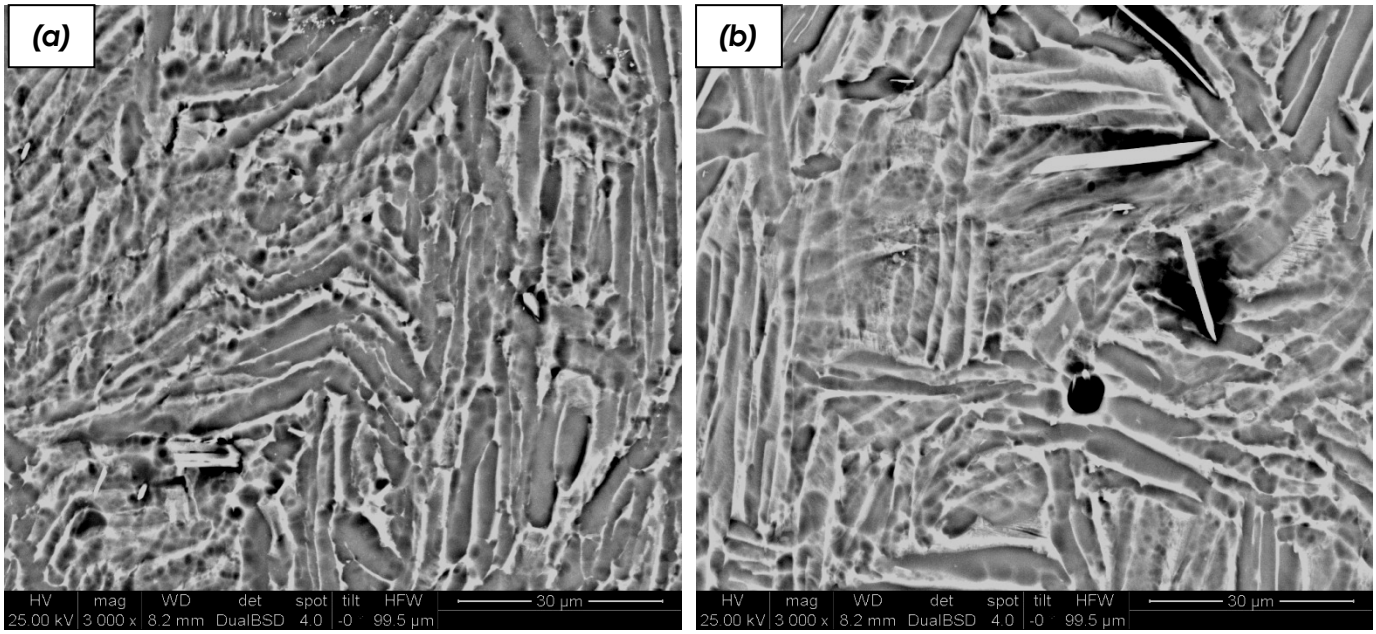

Fig. 70: SEM micrographs of hot compressed Ti64+B-Radial samples (Working condition: temperature 900^{o}C, strain rate 10^{-2} S^{-1})

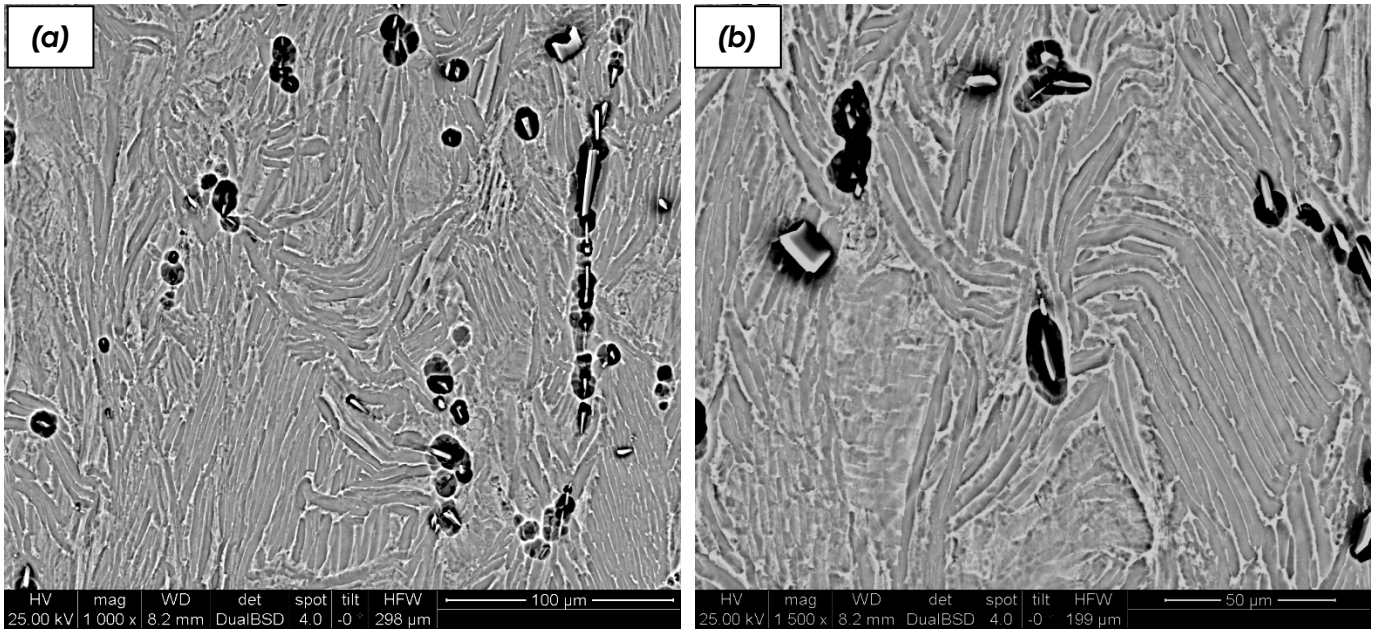

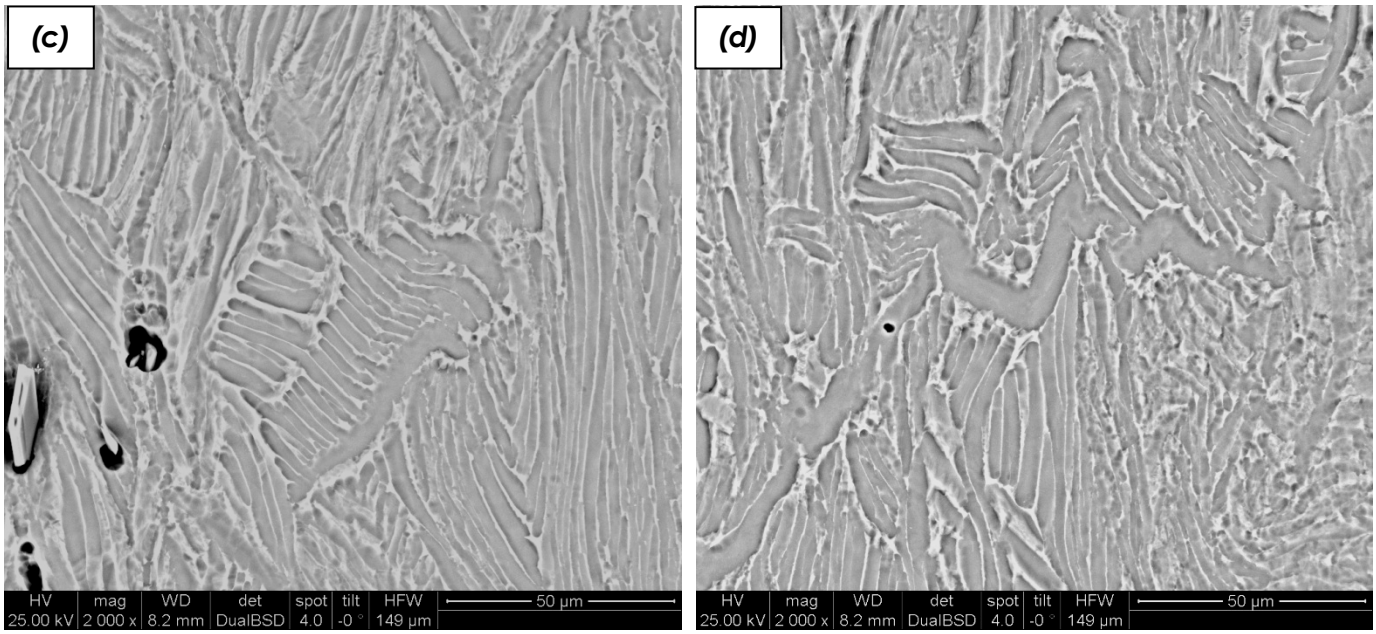

Fig. 71: SEM micrographs of hot compressed Ti64+B-Radial samples (Working condition: temperature 900^{o}C, strain rate 10^{-1} S^{-1})

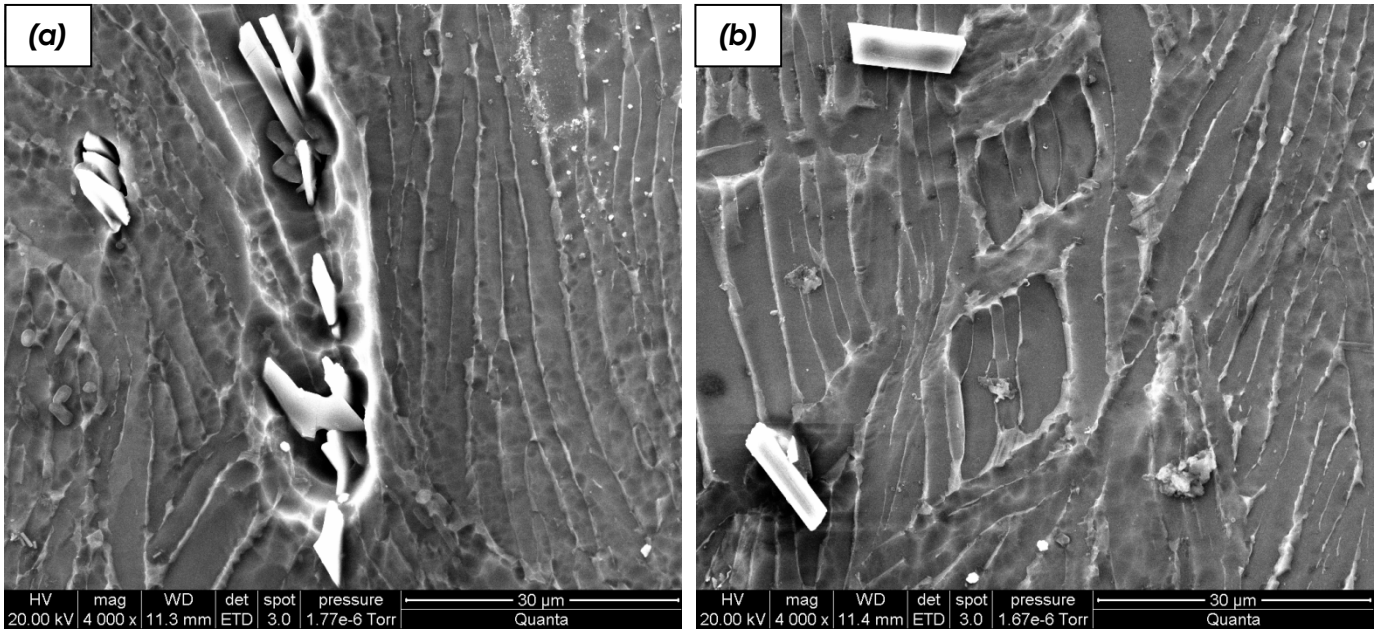

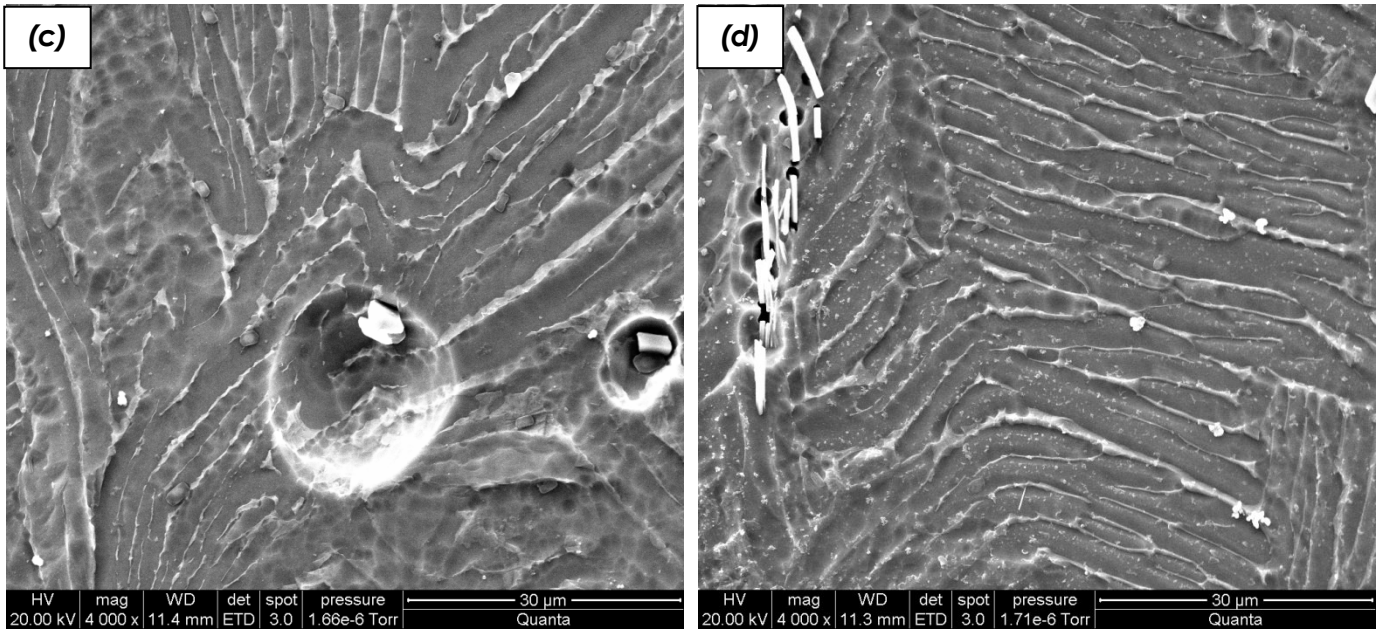

Fig. 72: SEM micrographs of hot compressed Ti64+B-Radial samples (Working condition: temperature 900^{o}C, strain rate 1 S^{-1})

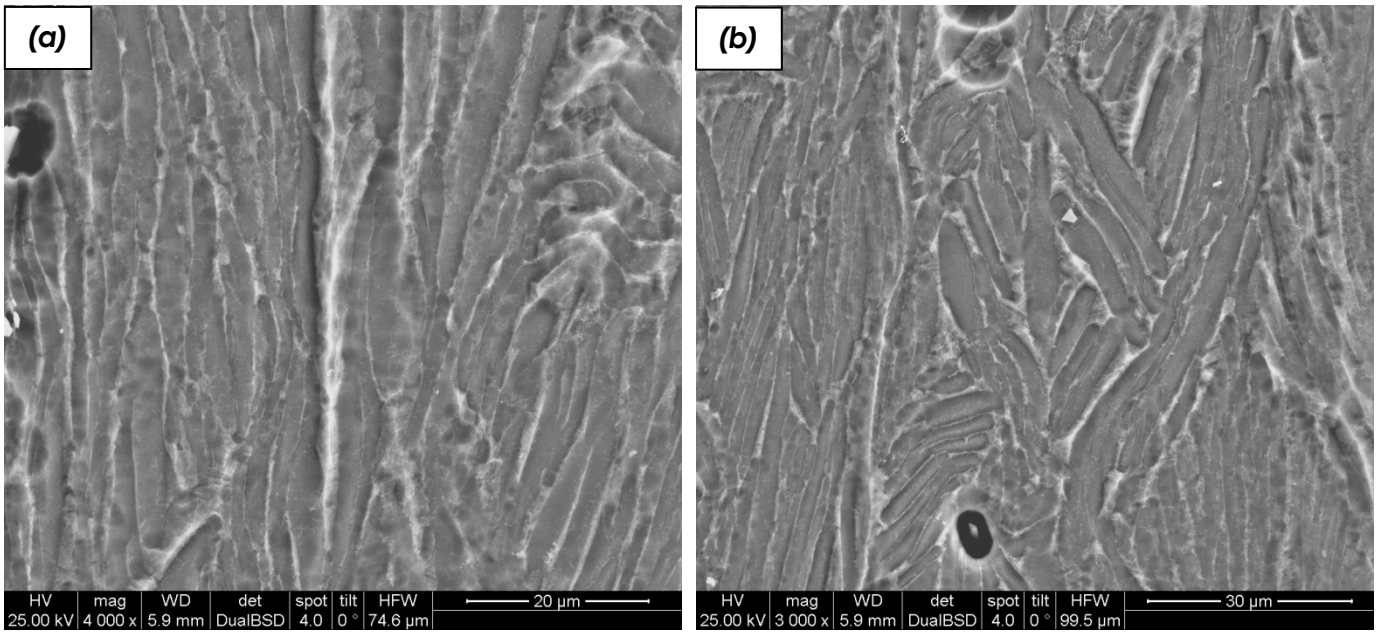

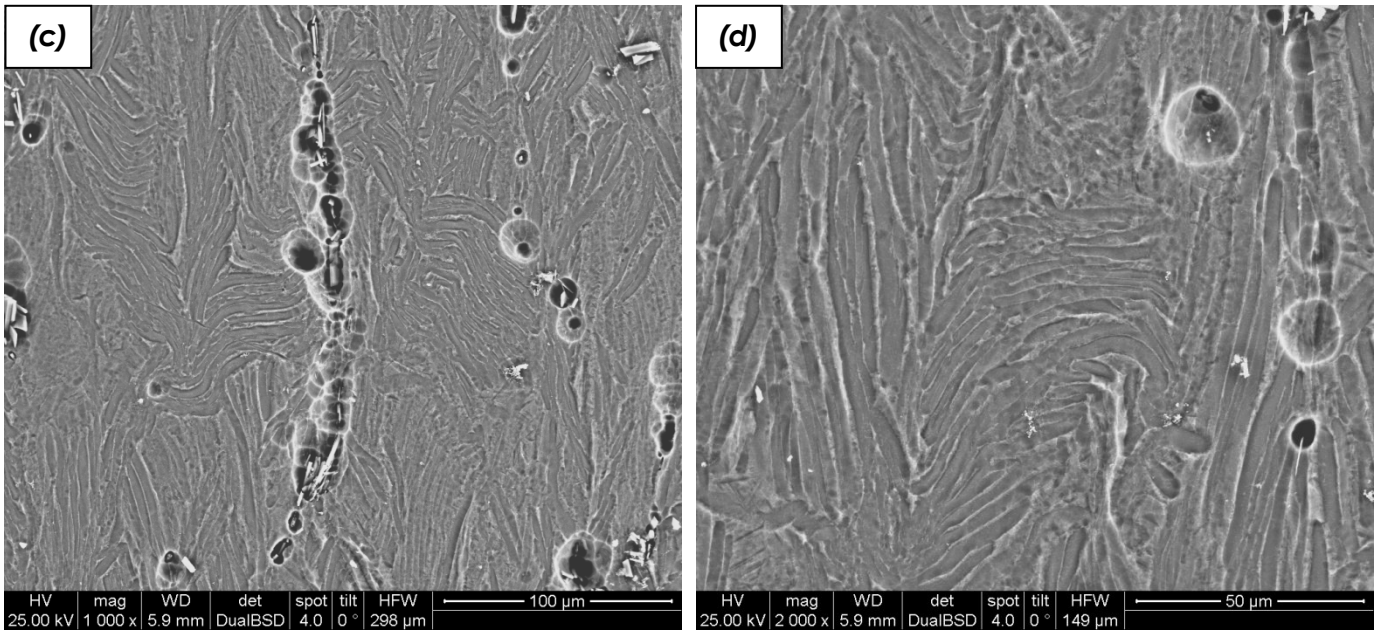

Fig. 73: SEM micrographs of hot compressed Ti64+B-Radial samples (Working condition: temperature 900^{o}C, strain rate 10 S^{-1})

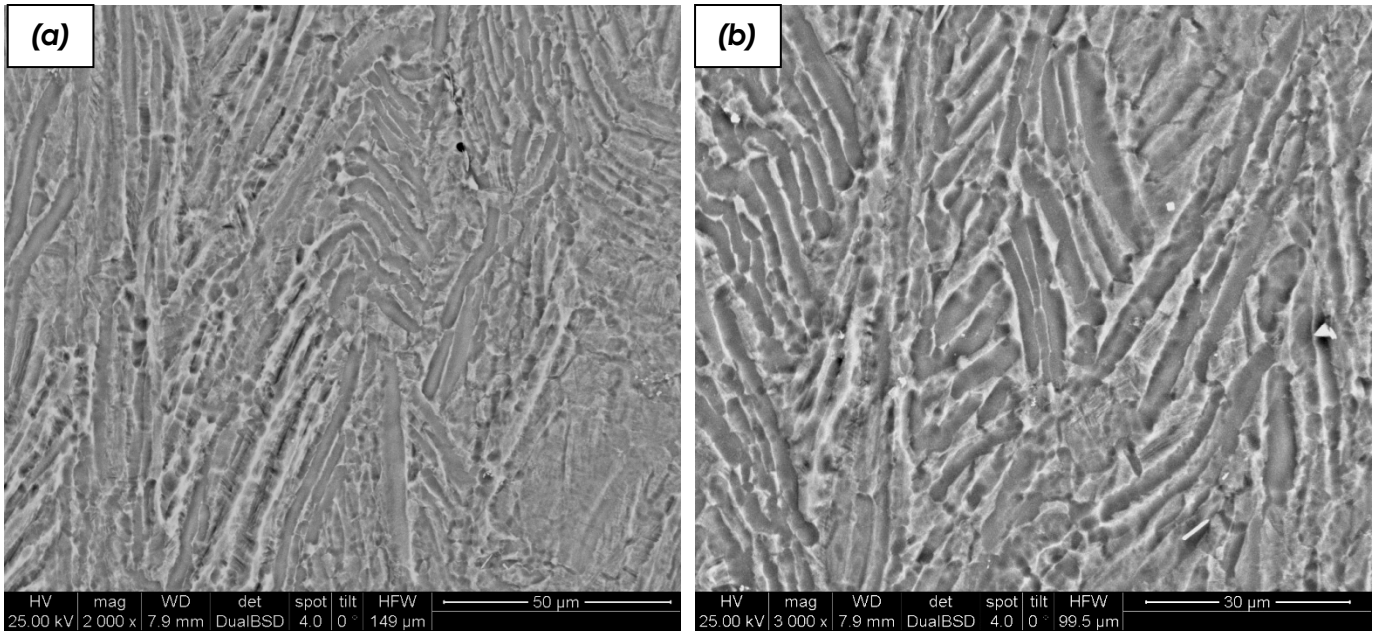

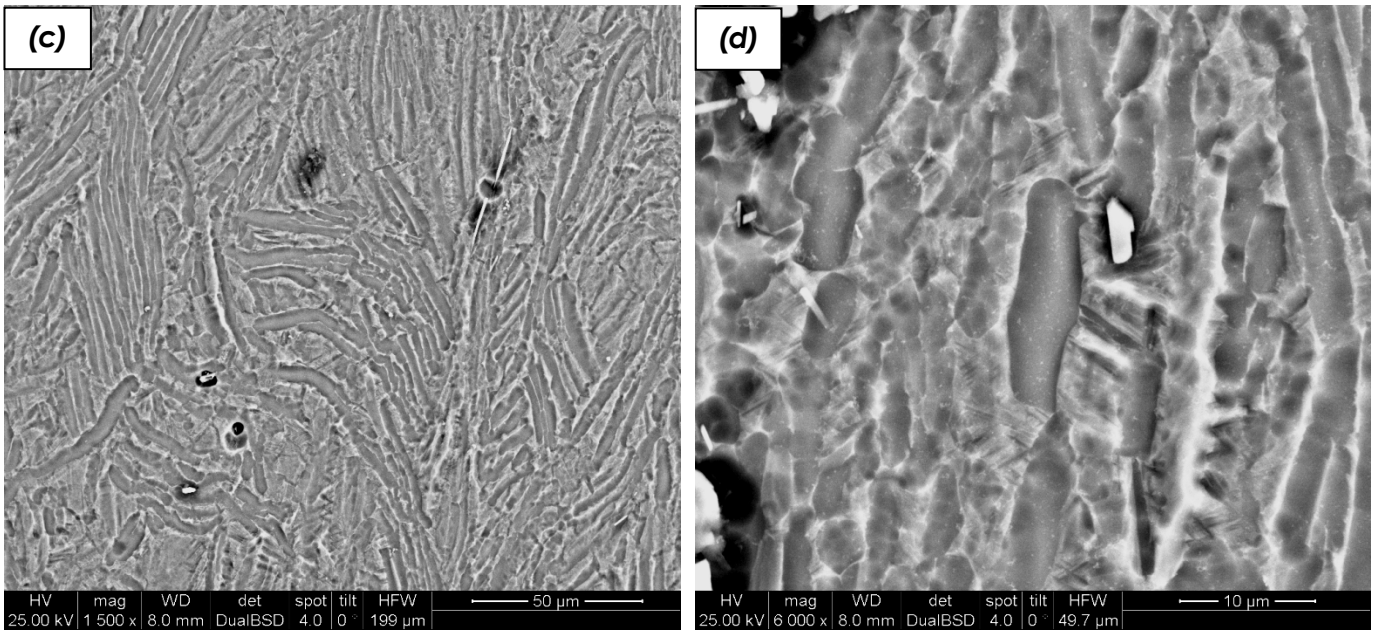

Fig. 74: SEM micrographs of hot compressed Ti64+B-Radial samples (Working condition: temperature 950^{o}C, strain rate 10^{-2} S^{-1})

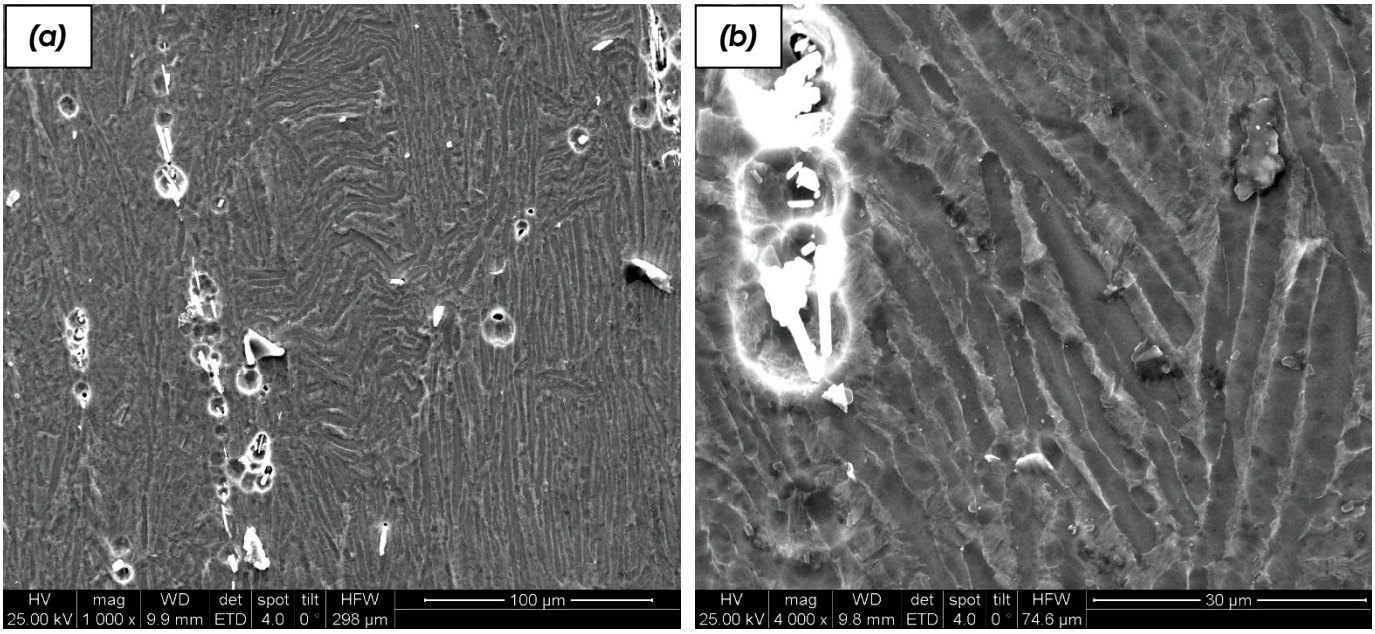

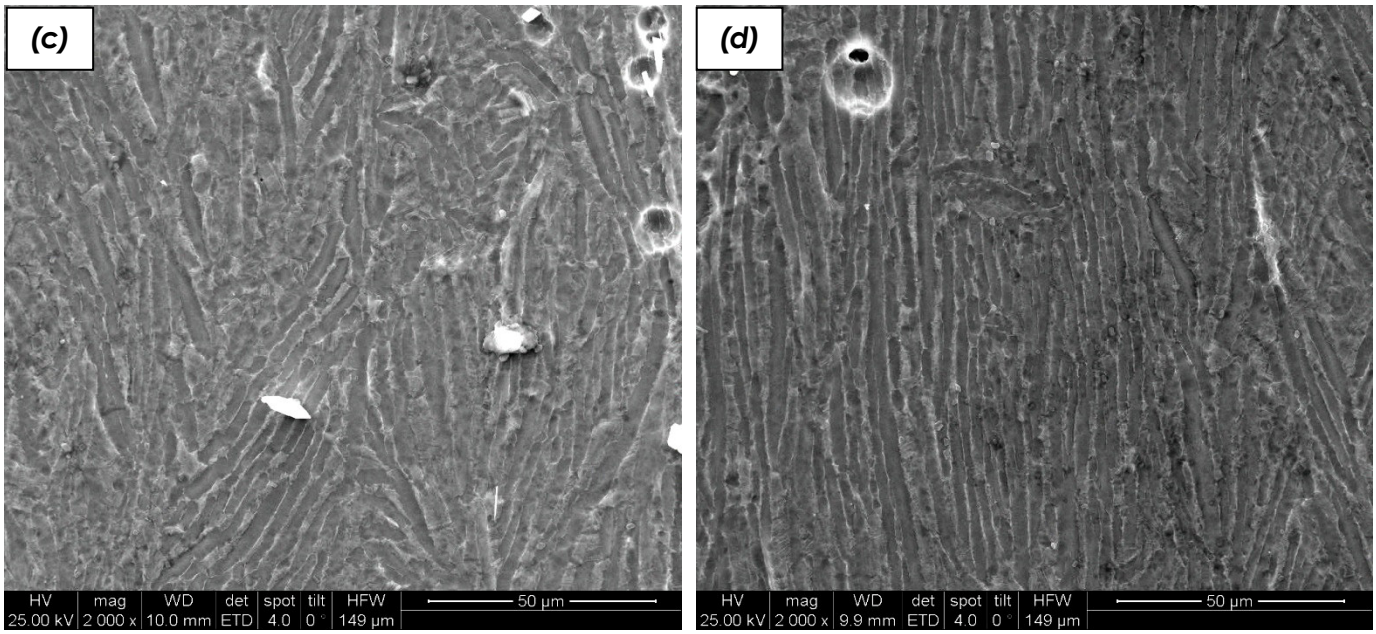

Fig. 75: SEM micrographs of hot compressed Ti64+B-Radial samples (Working condition: temperature 950^{o}C, strain rate 1 S^{-1})

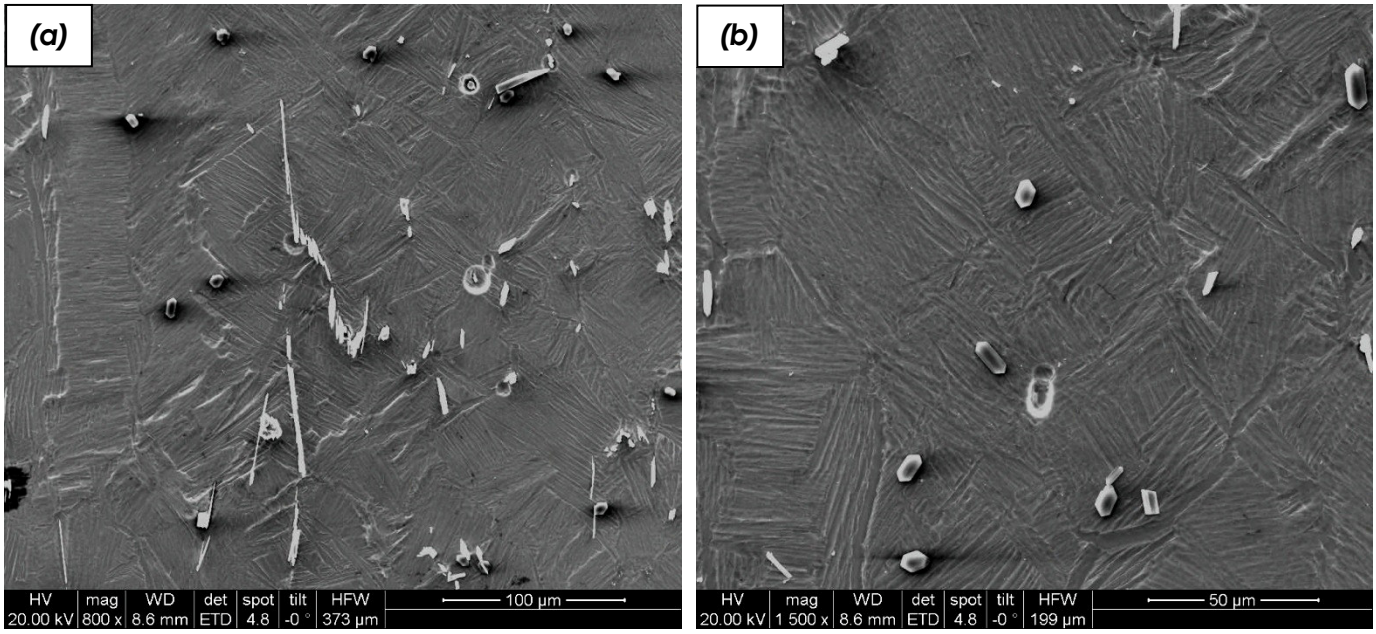

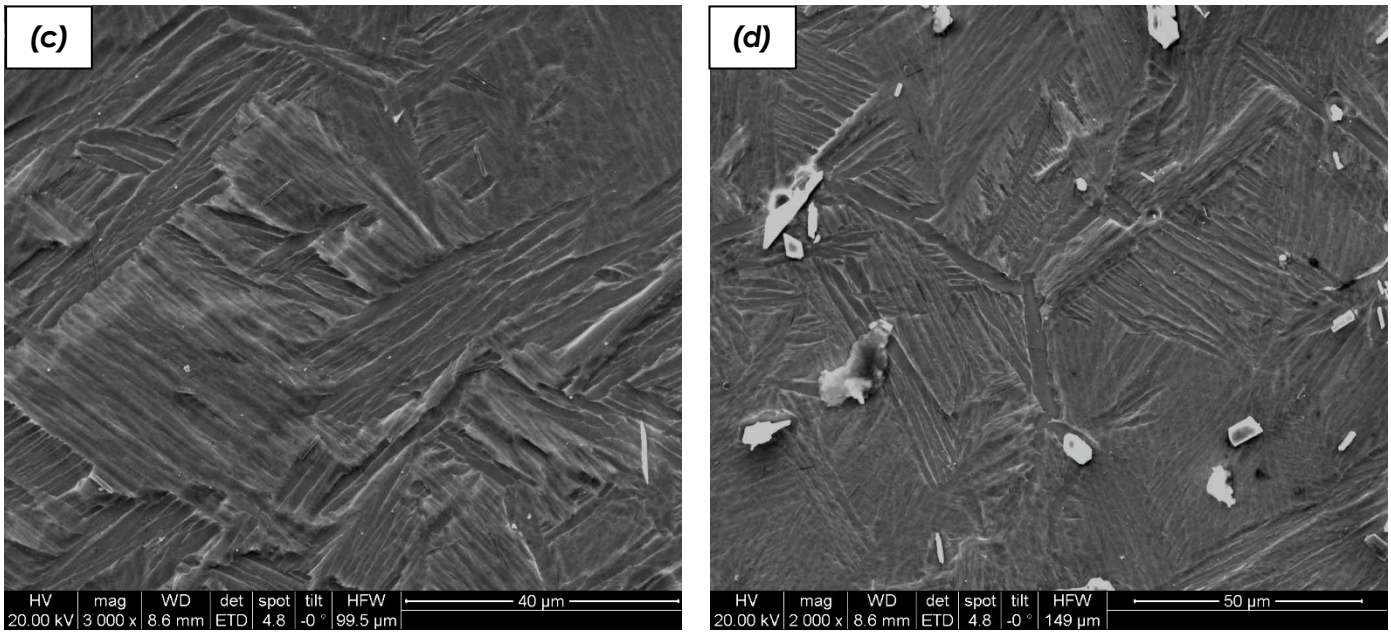

Fig. 76: SEM micrographs of hot compressed Ti64+B-Radial samples (Working condition: temperature 1000^{o}C, strain rate 10^{-2} S^{-1})

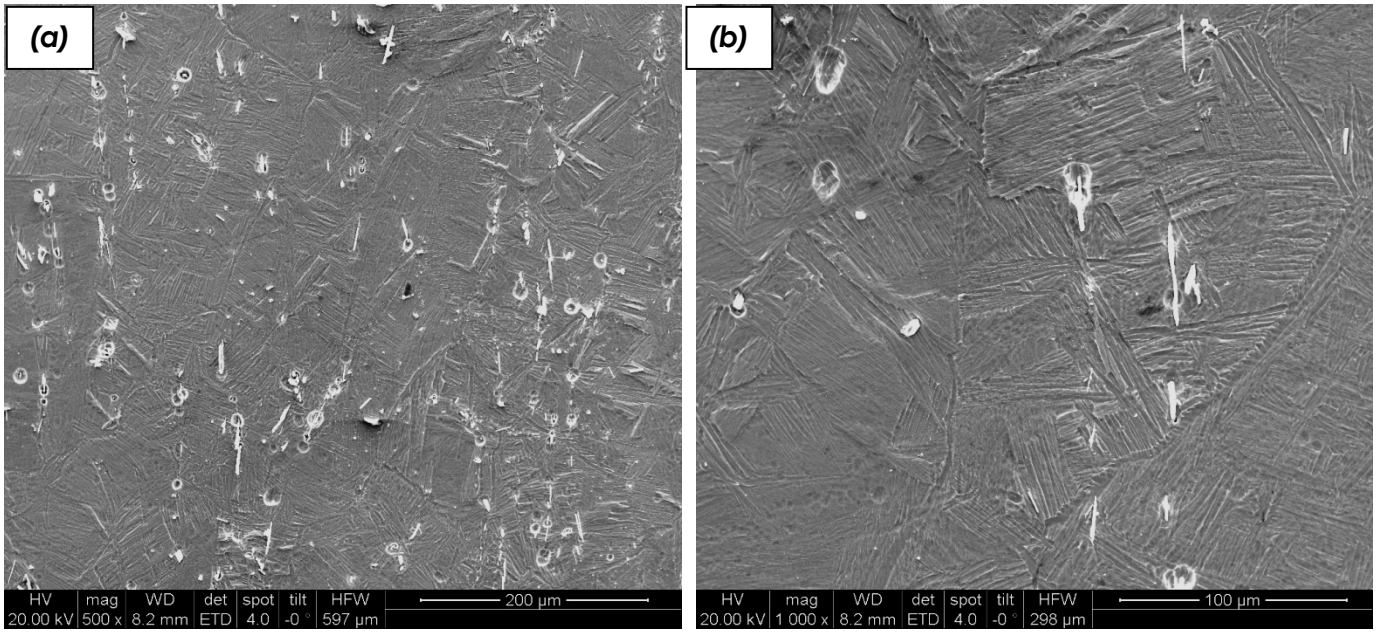

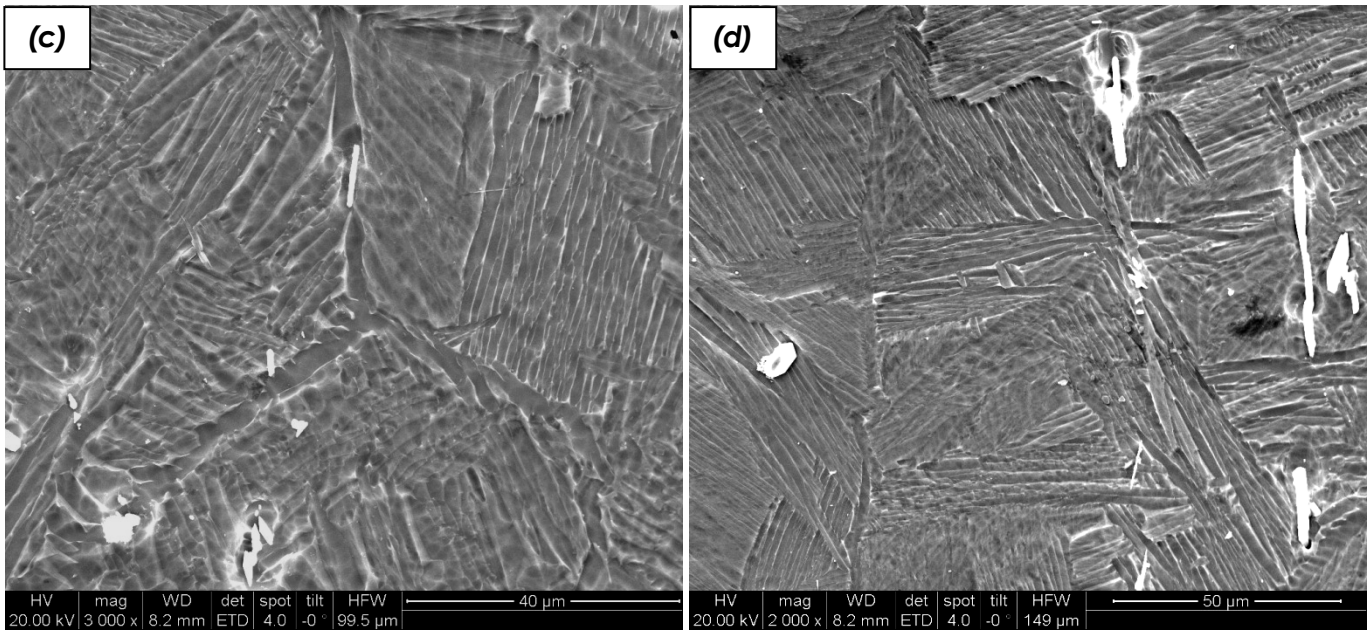

Fig. 77: SEM micrographs of hot compressed Ti64+B-Radial samples (Working condition: temperature 1000^{o}C, strain rate 1 S^{-1})

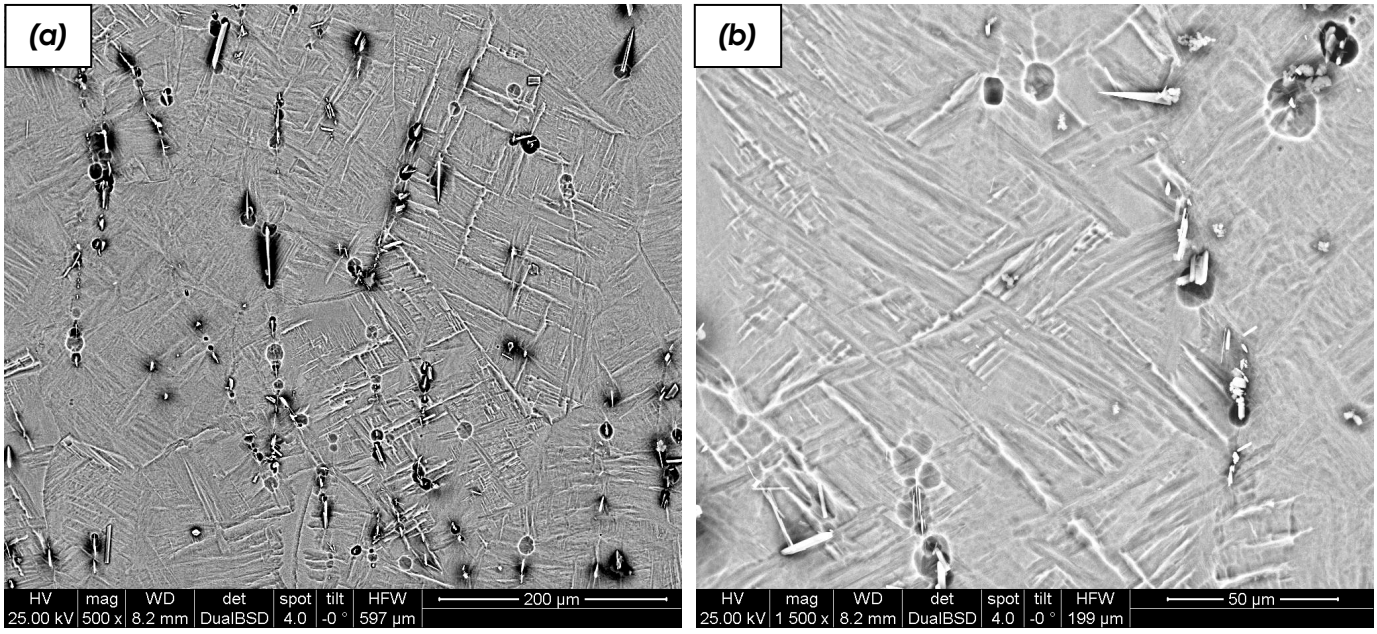

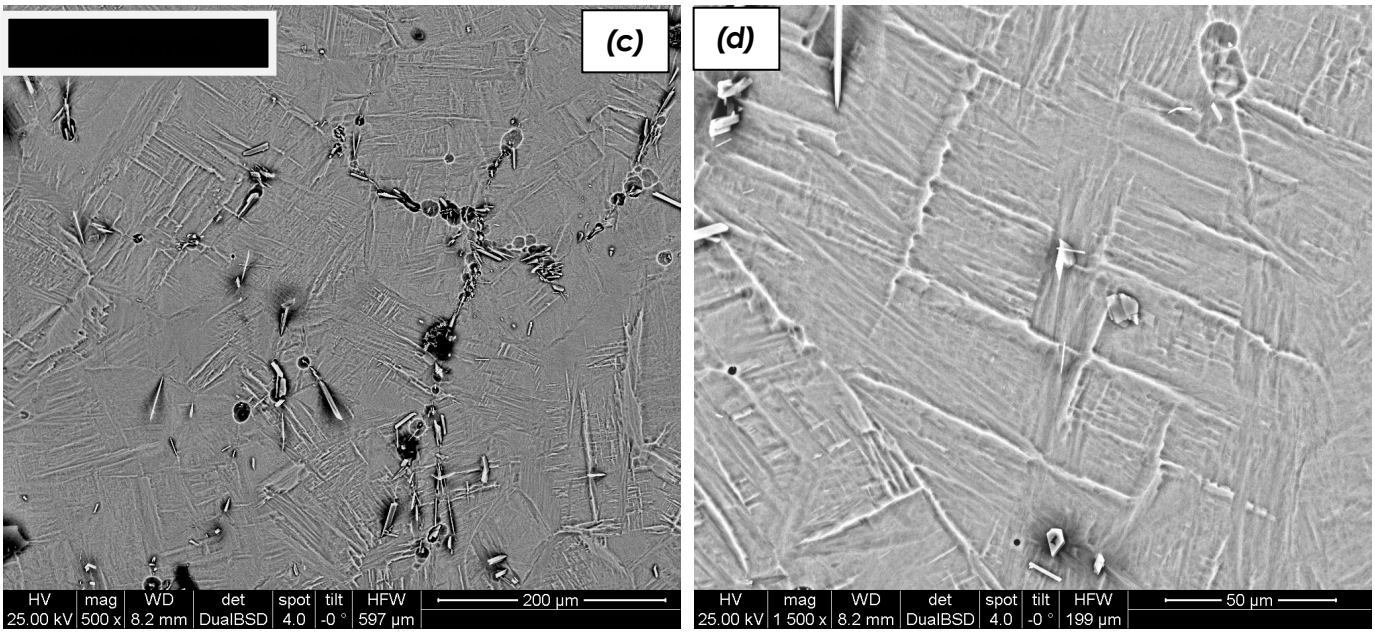

Fig. 78: SEM micrographs of hot compressed Ti64+B-Radial samples (Working condition: temperature 1000^{o}C, strain rate 10 S^{-1})

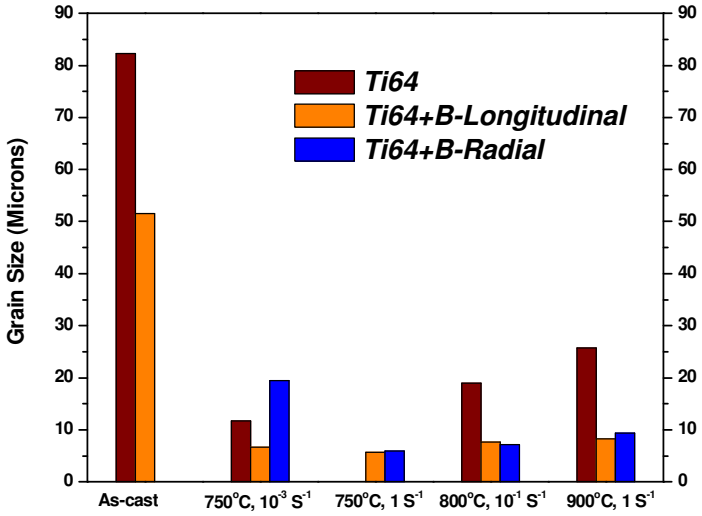

Fig. 79: Comparative colony sizes of the samples deformed under various temperature-strain rate combinations with respect to the initial materials.

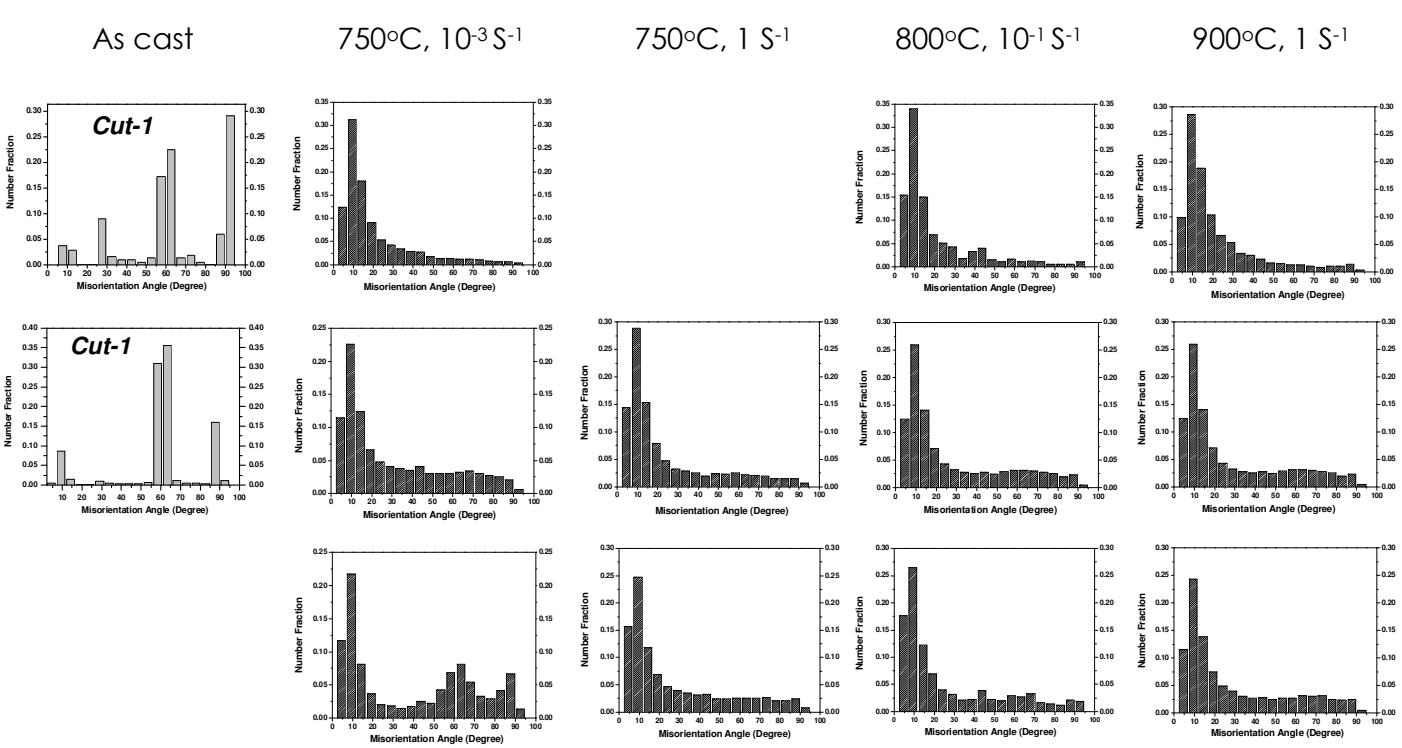

Fig. 80: Comparative miss-orientation angle distribution of the samples deformed under various temperature-strain rate combinations with respect to the initial materials.

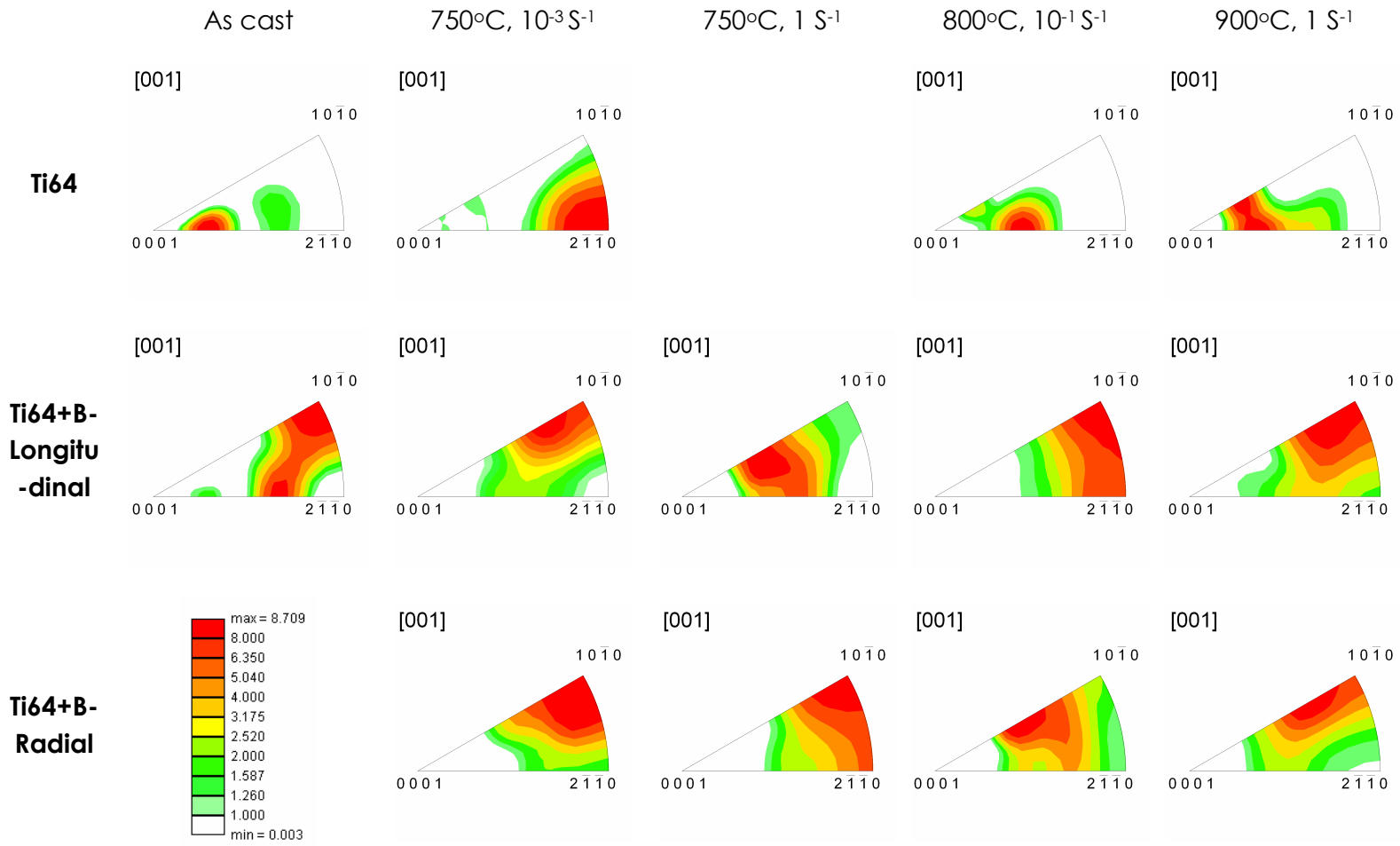

Fig. 81: Comparative ND inverse pole figures of the samples deformed under various temperature-strain rate combinations with respect to the initial materials.